

**NONLINEAR BEHAVIOUR OF THE RESISTIVE TEARING  
INSTABILITY IN PLASMAS**

**INCLUDING : COALESCENCE, REGENERATION,  
SATURATION, BIFURCATION, FORCED RECONNECTION  
AND MODE-LOCKING.**

by

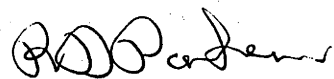
**RITCHIE DAVID PARKER**

A thesis submitted for the degree of Doctor of Philosophy  
of The Australian National University.

December 1987

## Preface

The work presented in this thesis represents original research produced by myself, in close collaboration with my supervisor Dr. R.L. Dewar. Any material which was not produced by me is clearly identified as such by reference to the original source from which it came.

A handwritten signature in black ink, appearing to read 'R.D. Parker', written in a cursive style.

Ritchie David Parker.

## Abstract

An investigation is made of the nonlinear behaviour of the resistive tearing instability which is a limiting factor in the performance of fusion oriented plasmas as well as being highly significant in astrophysical plasmas.

The thesis is divided into two main parts. The first represents an attempt to resolve the general properties of the magnetic islands produced by a tearing mode on a current sheet, while the second is more concerned with relating the properties of the instability to the Mirnov oscillation activity observed in tokamak plasmas such as LT-4.

Using a time evolution code with periodic boundary conditions, the visco-resistive magnetohydrodynamic equations describing an (initially) almost planar current sheet have been evolved for times long enough to reach steady state. Using the periodicity length as a control parameter two new bifurcations have been found, in addition to the standard one occurring at the minimum unstable tearing mode wavelength : A symmetry breaking bifurcation to a left or right going asymmetric travelling island chain; and a period doubling bifurcation to a state with alternating large and small islands. The complex transient behaviour leading to these states, which involves a competition between secondary current sheet instability and coalescence, is described in detail. This includes a parameter study of the dependence of these phenomena on the resistivity, viscosity, wall separation and periodicity length.

A quasi-linear delta-prime theory, in cylindrical geometry, has been used to calculate the amplitude of the poloidal magnetic field oscillations produced by a rotating, saturated,  $m=2/n=1$  magnetic island. Using radial safety factor profiles inferred from experimental electron temperature data from LT-4, amplitudes have been calculated in good agreement with observed MHD activity although occurring over a broader range of values of the safety factor at the edge of the plasma. It was found that this discrepancy could be reduced by invoking a mechanism of mode-locking onto an external field perturbation such as would be produced by the limiter or LT-4's single-armed iron core.

Corrugated conducting wall boundary conditions and a finite plasma drift have also been implemented in the evolution code to investigate the formation of magnetic islands *via* forced reconnection in a flowing plasma. It has been found, that, for high enough flow velocities, the plasma will transform from a state in which the flow is diverted around the island to one in which the island is reduced in width to a thin filament with the flow uniformly distributed across the whole plasma – the transition velocity being critically dependent on the viscosity and conductivity of the plasma.

Preliminary simulations in tearing unstable plasmas with flow have also demonstrated instances of full and partial mode-locking of tearing mode magnetic islands to the static corrugation in a manner which may explain the stop-start nature of the MHD activity observed on the LT-4 tokamak.

## CONTENTS :

	<u>Page</u>
TITLE	1
ABSTRACT	2
CONTENTS	4
ACKNOWLEDGEMENTS	6
FIGURE CAPTIONS	7
<u>PART I-1</u>	<u>REVIEW</u>
I-1.1	Introduction to the Resistive Tearing Instability 13
I-1.2	Review of Nonlinear Behaviour 22
<u>PART I-2</u>	<u>MODELLING TEARING MODES ON A CURRENT SHEET</u>
I-2.1	Mathematical Model 26
I-2.2	Numerical Scheme 37
I-2.3	Convergence 50
I-2.4	Numerical Stability 53
<u>PART I-3</u>	<u>RESULTS</u>
I-3.1	Simple Nonlinear Tearing Mode Evolution 58
I-3.2	Saturated Behaviour - Evidence of a 'Preferred' Island Length 63
I-3.3	Secondary Island Generation 67
I-3.4	Coalescence 75
I-3.5	Long Time Behaviour with Symmetry Breaking and Period Doubling Bifurcations 80
I-3.6	Reconnection Rates 91
I-3.7	Summary and Conclusions 97

	<u>Page</u>	
<u>PART II-1</u>	<u>TEARING MODES AND MHD ACTIVITY</u>	
II-1.1	Introduction : Tearing Modes, MHD Activity and Mode- Locking.	103
<u>PART II-2</u>	<u>QUASI-LINEAR DELTA-PRIME THEORY</u>	
II-2.1	A Quasi-Linear Delta-Prime Model for Poloidal Magnetic Field Oscillations	111
II-2.2	Results : Comparison with LT-4 MHD Activity	117
II-2.3	Discussion of Results and Conclusions	122
<u>PART II-3</u>	<u>TEARING MODES AND FORCED RECONNECTION IN A FLOWING PLASMA</u>	
II-3.1	Corrugated Conducting Wall Boundary Conditions	127
II-3.2	Forced Reconnection in a Flowing Plasma	133
II-3.3	Mode Locking : Preliminary Simulations	141
II-3.4	Final Remarks	145
REFERENCES		146

## Acknowledgements

I wish to thank my supervisor Dr. R.L. Dewar for his guidance and patient support during the course of my thesis and for always being happy to give generously of his time and knowledge. Much of the research for this thesis has benefited from his direction and invaluable insight, and it is through his encouragement and constructive criticism of my efforts that I have been able to bring this work to fruition. I have also greatly enjoyed his pleasant company during lunchtime runs beside the lake, as well as Friday afternoons at the pub, and will always value his friendship.

I am grateful to Prof. S.M. Hamberger for his advice and encouragement, and to Dr. A.D. Cheetham, Dr. H. Kuwahara, Dr. L.E. Sharp, Mr. R. Nazikian and other members of the Plasma Physics Laboratory for valuable technical discussions and for making available to me data and results from the LT-4 experiment.

Thanks must also go to Prof. K.J. Le Couteur for giving me the opportunity to come and work in the Department of Theoretical Physics, R.S. Phys. S., to Dr. B.A. Robson for his continual support and encouragement, to Dr. W.N-C. Sy for useful discussions and to the other members of the department for providing a friendly and stimulating environment in which to work. I have also benefited from discussions with visitors to the department, especially with Prof. F. Troyon and Dr. J.A. Wesson.

Most of the simulation work was performed on the Cyber-205 super-computer, which was made available for this project under the CSIRO Computing Grants Scheme. For this I am truly grateful and to the Technical Support Group at CSIRONET. Without access to this machine very little of the work would have been possible.

My thanks also extend to the staff of the School Computer Unit, and in particular to Julie Dalco for cheerfully looking after all my peripheral computing needs. Her friendship and pleasant company during weekly swims and par coursing with Bob and myself will always be remembered fondly.

Last but not least, I would like to express my deepest appreciation to my parents for providing moral support and encouragement, especially during the writing up stage and for always being there when I needed them.

This work was supported by a Commonwealth Postgraduate Research Award.

## Figure Captions :

- Fig.1 The topology of the magnetic flux surfaces, as seen in cross-section, after an  $m=2/n=1$  magnetic island has formed as a result of a tearing mode instability.
- Fig.2 Schematic diagram showing the topology of (a) the type of secondary island found by Steinolfson and Van Hoven and here and (b) the type of secondary island found by Biskamp in between two coalescing islands.
- Fig.3 Schematic diagram of the plasma slab model.
- Fig.4 Ratio of the cpu time per timestep for the Vax-11/780 to that for the Cyber-205 versus the number of grid points for runs with 5 and 8 Fourier modes.
- Fig.5 The relative amplitudes of the Fourier modes of (a)  $\psi$ , (b)  $\phi$ , (c)  $J_z$  and (d)  $\zeta$  on the neutral line at saturation showing the dominance of low order modes.
- Fig.6 The number of Fourier modes,  $M$ , required for convergence of the vorticity as a function of the viscosity,  $\nu$ , for several values of the wall separation,  $X_w$
- Fig.7 The reconnected flux,  $\Delta\Psi$ , and its corresponding exponential growth rate,  $\gamma$ , versus time (in units of  $V_A$ ) showing the growth and saturation of a tearing mode for a simulation made with  $K_p = 0.35$ ,  $X_w = 4.0$ ,  $\nu = 0.01$  and  $S = 200$
- Fig.8 Contour plots of (a) the magnetic flux function,  $\psi$ , (b) the z-component of the current density,  $J_z$ , (c) the magnetic field magnitude,  $B$ , (d) the velocity stream function,  $\phi$ , (e) the z-component of the vorticity,  $\zeta$ , and (f) the velocity magnitude,  $V$ , at saturation for the simulation of fig.7.
- Fig.9 A series of 3-D perspective plots of the z-current density at several points during the growth of the tearing mode for a simulation made with :  $K_p = 0.35$   $X_w = 2.5$ ,  $\nu = 0.01$  and  $S = 10,000$
- Fig.10 A series of schematic diagrams describing the mechanism leading to the formation of tearing mode magnetic islands : - (a) shows the neutral line between two oppositely directed field components which (b) are perturbed so that the field lines are pinched together at regular intervals along the neutral line causing (c) reconnection of the field lines into localized elongated loops due to the intense dissipation there. The tension in the lines of force pulls, (d) and (e), the loop into a more nearly circular form. The plasma flows in from either side of the x-point, out along the neutral line and around to form a vortical plasma motion.
- Fig.11 A series of contour plots of (a)  $\psi$  and (b)  $J_z$  for increasing values of the periodicity length,  $L_p = 2\pi/K_p$  showing the invariance of the aspect ratio of the inner reconnected field loops and the increase in length of the x-point current sheets in proportion to  $L_p$  as  $L_p$  is increased beyond  $L_{pref}$ .



- Fig.12 Variation of the saturated island width with (a) periodicity length,  $L_p$ , and (b) periodicity wave number,  $K_p = 2\pi/L_p$ , for several values of the wall separation ( $X_w = 2.5, 4.0, 8.7, 12.0$ ) and the viscosity ( $\nu^{-1} = 100, 600$ ).
- Fig.13 Variation of the saturated reconnected flux with (a)  $L_p$  and (b)  $K_p$  for  $X_w = 2.5, 4.0, 8.7$  and  $12.0$  and  $\nu^{-1} = 100$  and  $600$ .
- Fig.14 Variation of (a) the reconnected flux, (b) the island width, (c) the number of Fourier modes required for convergence, (d) the linear growth rate and in (e) and (f) the first four Fourier modes of  $\psi$  on the neutral line versus the half wall separation,  $X_w$ , for  $K_p = 0.4$  and  $0.27$  at saturation showing the absence of wall effects for  $X_w > 10$ .
- Fig.15 Variation of the saturated reconnected flux with  $L_p$  and  $K_p$  for several values of the Lundquist number ( $S = 200., 1000., 2000.$ ) showing : the periodicity length corresponding to the preferred island length,  $L_{pref}$ , marked by  $\dagger$ ; the critical periodicity length,  $L_{crit}$ , for secondary tearing mode stability which also defines the transition to the asymmetric travelling wave solutions, marked by  $\lceil$ ; and the second critical periodicity length,  $L_{crit(2)}$ , for the transition to the double island states marked by the discontinuous jump in  $\Delta\Psi$ .
- Fig.16 Variation of the saturated island width with  $L_p, K_p$  for several values of  $S$  similar to that shown in fig.15 for  $\Delta\Psi$ .
- Fig.17 (a) Plot of  $L_{pref}$  and  $L_{crit}$  versus  $S$ . (b) Plot of  $L_{crit}$  versus  $S$  including data from Steinolfson and Van Hovens simulations.
- Fig.18 Evolution of a simulation made with  $K_p = 0.263, S = 200., \nu = 0.01$  and  $X_w = 2.5$  including a secondary island generation as described by : (a) the reconnected flux, (b) its corresponding exponential growth rate, (c) the position of the x and o points on the neutral line and (d) the amplitude of the first four fourier modes of  $\psi$  also on the neutral line.
- Fig.19 An isolated instance of secondary island generation during a simulation made with  $K_p = 0.23, S = 200., \nu = 0.01$  and  $X_w = 2.5$  described by the evolution of (a) the reconnected flux, (b) the exponential growth rate, (c) the first four Fourier amplitudes of  $\psi$  on the neutral line, (d) the position of the x and o points on the neutral line and (e) the magnetic island width.
- Fig.20 Contour plots of  $\psi, \phi$  and  $J_z$  at several points during the secondary island generation described in fig.19.
- Fig.21 3-D perspective plots of  $J_z$  at several points during the secondary island generation described in fig.19.
- Fig.22 The (a) length,  $\Delta$ , (b) width,  $\delta$ , and (c) aspect ratio,  $A$ , of the x-point current sheet as a function of the Lundquist number showing the following scalings:

$$\Delta \sim S^{-0.34}, \delta \sim S^{-0.25}, A \sim S^{-0.095}.$$

- Fig.23 The maximum flow velocity,  $V_{\max}$ , reached along the x-point current sheet as a function of Lundquist number showing that  $V_{\max} \sim S^{-0.73}$ .
- Fig.24 The (a) length,  $\Delta$ , (b) width,  $\delta$ , and (c) aspect ratio,  $A$ , of the x-point current sheet versus the periodicity length for several values of the Lundquist no.,  $S = 200, 1000, 2000$ . The small horizontal lines mark the length, width and aspect ratio at which the current sheets break up due to the secondary tearing instabilities.
- Fig.25 An isolated instance of coalescence during a simulation made with  $K_p = 0.23$ ,  $S = 200.$ ,  $\nu = 0.01$  and  $X_w = 2.5$  described by the evolution of (a) the reconnected flux, (b) the exponential growth rate, (c) the first 4 Fourier modes of  $\psi$  on the neutral line, (d) the position of the x and o points on the neutral line and (e) the magnetic island width.
- Fig.26 Contour plots of  $\psi$ ,  $\phi$  and  $J_z$  at several points during phase I or the Preparation phase of the coalescence process described in fig. 25.
- Fig.27 Contour plots of  $\psi$ ,  $\phi$  and  $J_z$  at several points during phase II or the Reconnection phase of the coalescence process described in fig. 25.
- Fig.28 Contour plots of  $\psi$ ,  $\phi$  and  $J_z$  at several points during phase III or the Relaxation phase of the coalescence process described in fig. 25.
- Fig.29 3-D perspective plots of  $J_z$  at a dozen points during the coalescence process described in fig. 25.
- Fig.30 The variation of (a) the reconnected flux, (b) the exponential growth rate, (c) the maximum island width, (d) the first four fourier modes of  $\psi$  on the neutral line and (e) the positions of the x and o points on the neutral line over the entire evolution of a simulation made with  $K_p = 0.25$ ,  $S = 200.$ ,  $\nu = 0.01$ , and  $X_w = 2.5$ , complete to saturation.
- Fig.31 Contour plots of  $\psi$  at several points during a section of evolution in which the coalescence and secondary island generation partially overlap to produce a peristaltic like squashing and stretching motion of the magnetic islands.
- Fig.32 Contour plots of  $\psi$  showing the three types of saturated configurations that have so far been found as a function of  $L_p$ . i.e. (I) the stationary symmetric islands that exist for  $L_p < L_{\text{crit}}$ , (II) the asymmetric travelling wave solutions that exist for  $L_{\text{crit}} < L_p < L_{\text{crit}(2)}$  and (III) the stationary modulated double island states that exist for  $L_{\text{crit}(2)} < L_p < L_{\text{crit}(3)}$ ?
- Fig.33 (a) The phase velocity of the islands as a function of  $L_p$  showing the parabolic bifurcation to the asymmetric travelling island solutions at  $L_p = L_{\text{crit}}$ , the period doubling bifurcation of the symmetric solution at  $L_p = L_{\text{PD}}$  and the

interchange of stability back to the zero phase velocity double island solution at  $L_{crit(2)}$ . (b) Schematic drawings of three types of bifurcation.

- Fig.34 Contour plots of  $J_z$  corresponding to the same values of  $L_p$  as in fig.32 showing clearly the increasing length and asymmetry of the current sheets with  $L_p$  and the transition to the double island state above  $L_{crit(2)}$ .
- Fig.35 3-D perspective plots of  $J_z$  for  $K_p = 0.25$  and  $0.12$  showing the similarity in shape but difference in orientation of the asymmetric current sheets in each case.
- Fig.36 Plots of (a) the first 4 Fourier modes of  $\psi$  on the neutral line as a function of wavenumber and (b) the first 9 Fourier modes of  $\psi$  over a smaller range of wavenumber showing the nature of the discontinuous transition from the single to the double island state.
- Fig.37 As per fig.36 (a) and (b) but as a function of wavelength instead.
- Fig.38 Contour plots of  $\psi$ ,  $J_z$ ,  $\phi$ , and  $V$  for a simulation made with  $K_p = 0.05$  showing an island state with four modulated islands per periodicity length.
- Fig.39 Schematic diagrams showing (a) the Petschek reconnection model and (b) the Sweet-Parker model where the shaded region represents the diffusion layer.
- Fig.40 Plots of (a) the measured local reconnection rate,  $M_{loc}$ , the local Sweet-Parker rate,  $M_{SP(loc)} = S_{loc}^{-0.5}$  and the local Petschek rate  $M_{P(loc)} = \pi(8 \ln S_{loc})^{-1}$  versus  $S_{loc}$ , (b) the same as in (a) but with  $S_{loc}$  replaced with  $S_{loc2} = B_{loc}S$  so that the diffusion length is kept constant and (c) the same as in (a) but with  $S_{loc}$  replaced with the asymptotic Lundquist number  $S$ .
- Fig.41 The measured local reconnection rate plotted against the different versions of the Sweet-Parker rate, i.e. (a)  $M_{loc}$  versus  $S^{-0.5}$ , (b)  $M_{loc}$  versus  $S_{loc}^{-0.5} = (B_{loc}S)^{-0.5}$  and (c)  $M_{loc}$  versus  $S_{loc}^{-0.5} = (B_{loc}S\Delta/\eta_{loc})^{-0.5}$  to show that good agreement can be obtained as long as the diffusion length is constant.
- Fig.42 The local inflow velocity incident to the current sheet,  $V_{loc}$ , plotted against the three versions of the Lundquist number showing that  $V_{loc} \sim S^{-0.73}$ ,  $V_{loc} \sim (B_{loc}S)^{-0.93}$  and  $V_{loc} \sim S_{loc}^{-1.63}$ .
- Fig.43 The local magnetic field,  $B_{loc}$ , (= local Alfvén velocity) at the edge of the current sheet plotted against the three versions of the Lundquist number showing that  $B_{loc} \sim S^{-0.21}$ ,  $B_{loc} \sim (B_{loc}S)^{-0.26}$  and  $B_{loc} \sim S_{loc}^{-0.46}$ .
- Fig.44 The linear growth rate of the reconnected flux as a function of  $K_p$  for  $X_w = 2.5, 4.0, 8.7$  and  $12.0$ .
- Fig.45 Plan view of the LT-4 tokamak, taken from reference [71], showing in particular the single armed iron core as well as the toroidal field coils, restraint frame and vacuum chamber.

- Fig.46 The maximum amplitude of the poloidal magnetic field oscillations versus  $q(a)$ , taken from ref. [18], showing four different regimes of MHD activity. The lower scale was calculated from  $B_{\theta}$  and  $B_{\phi}$  using the cylindrical approximation to the safety factor whereas the upper scale includes toroidal corrections to this.
- Fig.47 Schematic diagram, taken from reference [14], showing the two different routes to disruptions as observed on LT-4 : Type A is the  $B_{\theta}$ ' and soft x-ray signal for the regular activity and type B is the same for the irregular activity that occurs when the density falls during regime III.
- Fig.48 Examples of the regular and irregular MHD activity on the Mirnov coils not leading to disruption and a section of irregular activity which does, ref.[18].
- Fig.49 Magnetic and soft x-ray signals during the transition from regime II to III.<sup>[18]</sup>
- Fig.50 (a) Geometry for the description of a toroidal plasma configuration such as a tokamak. (b) Cylindrical geometry configuration used for approximating a toroidal plasma with a large aspect ratio. The helical ribbon defined by the magnetic axis and the helix of constant  $m\theta + kz$  and  $r$  is such that at the mode rational surface the magnetic field is tangent to the ribbon.
- Fig.51 The magnetic structure of an  $m=2/n=1$  resistive tearing mode.
- Fig.52 (a) Data points corresponding to the radial electron temperature profile obtained from Thompson scattering measurements on the LT-4 tokamak. Through them are drawn three fits : ————— fit(1), ..... fit(2), - - - - - fit(3) corresponding to the parameter values listed in table 4. (b) The toroidal current density profiles corresponding to the same three fits in (a) using  $J_z \propto T_e^{3/2}$ . Crosses mark the radial position of the  $m=2/n=1$  rational surface in each case.
- Fig.53 (a) The saturated island width versus  $q(a)$  for several different values of the parameter  $\lambda_0$  in the parameterization of the safety factor profile where  $\lambda_2=1.5$ ,  $q(0) = 0.9$  and  $\lambda_0 = 0.4, 0.6, 0.8, 1.0, 1.2, 1.4, 2.0, 2.5$  and  $4.0$ . (b) The same as in (a) but for different values of the parameter  $\lambda_2$  with  $\lambda_0 = 0.8$ ,  $q(a) = 0.9$  and  $\lambda_2 = 0.5, 1.0, 1.3, 1.5, 2.0, 4.0, 6.0, 8.0, 10.0$ . (c) The value of  $q(a)$  corresponding to the lower limit of the  $m=2/n=1$  mode activity plotted separately as a function of  $\lambda_0$  and  $\lambda_2$  showing that the peak of activity is shifted more effectively by changing  $\lambda_0$ .
- Fig.54 (a) The saturated magnetic island width versus  $q(a)$  for fit(2). The dotted line shows how mode locking for  $W_{sat}$  below  $1.05a$  would restrict the observable range of  $B_{\theta 1}/B_{\theta 0}$  oscillations to that shown in (b) between the vertical dotted lines - this being close to the experimentally observed range plotted in (c) which shows : —————  $B_{\theta 1}/B_{\theta 0}$  amplitude versus  $q(a)$  measured on LT-4, - - - - -  $B_{\theta 1}/B_{\theta 0}$  versus  $q(a)$  for fit(2) and .....  $B_{\theta 1}/B_{\theta 0}$  versus  $q(a)$  for fit(3).

- Fig.55 Schematic diagram of plasma slab model with corrugated perturbation of conducting walls.
- Fig.56 A series of contour plots of  $\psi$ ,  $J_z$  and  $\phi$  referred to a plot of the saturated reconnected flux versus  $V_{y0}/V_A$  showing the variation of the magnetic island state produced by a corrugated boundary perturbation of amplitude,  $\Delta W = 0.02$ , with  $S = 10^4$ ,  $\nu = 0.01$  as the zero order flow velocity,  $V_{y0}$ , is varied between 0 and  $V_a$ .
- Fig.57 A set of plots of (a) the saturated reconnected flux, (b) the saturated island width and (c) the phase shift ( in radians ) of the o-point of the islands produced by a corrugated boundary perturbation with  $\Delta W = 0.02$  as a function of  $V_{y0}/V_A$  for  $S = 10^3$  and  $10^4$  and  $\nu = 0.01$  and  $0.0001$ .
- Fig.58 Contour plots of  $\psi$ ,  $\phi$  and  $J_z$  for the case with  $S = 10^4$ ,  $\nu = 0.0001$ ,  $\Delta W = 0.02$  and  $V_{y0} = 0.01$  showing a forced magnetic reconnected island state in which the zero order flow is shown to be excluded from within the island region defined by the separatrix. This is more clearly shown in the four cross-section plots of the y-component of the fluid velocity taken at equal intervals along the island length.
- Fig.59 A set of 3-D perspective plots and contour plots of the z-current density for various force reconnected magnetic island states of interest showing the significant changes that can occur to the current as a function of  $\nu$ ,  $V_{y0}$  and  $S$ .
- Fig.60 Time evolution of (a) the positions of the x and o points ; (b) the variation in  $\psi - \psi_0$  at  $x=0, y=0$  and (c) the reconnected flux showing the mode locking of a tearing mode magnetic island by a corrugated boundary perturbation for the case with  $\Delta W = 0.05$ ,  $V_{y0} = 0.01$ ,  $S = 10^3$ ,  $\nu = 0.01$ ,  $K_p = 0.35$ ,  $X_w = 2.5$ .
- Fig.61 As per fig.60 but showing the partial modelocking of a tearing mode magnetic island for the case with perturbation amplitude reduced to  $\Delta W = 0.01$ .
- Fig.62 Contour plots of  $J_z$ ,  $\psi$ ,  $\phi$  and cross-section plots of  $V_y$  at two times during the partial mode locking process corresponding to (a) when the island is temporarily locked and (b) just after it has become unlocked.
- Fig.63 A series of weather maps showing a high pressure vortex (or anti-cyclone) getting temporarily locked in the Great Australian Bight for almost a week before squeezing out past the south eastern tip of the mainland to continue its journey eastwards.

### I-1.1 Introduction : Brief Review of the Resistive Tearing Mode

In order to achieve the high densities and temperatures required for a successful thermonuclear reactor, a plasma must be confined by a magnetic field for a sufficiently long time. In the attempts to achieve this confinement, the problem of stability has emerged as one of the most important. A plasma confined by a magnetic field is potentially able to break out of the confinement system by a large variety of instabilities, the most serious of which can be described by the magnetohydrodynamic (MHD) model<sup>[1]</sup> in which the plasma is assumed to behave as a conducting fluid.

In fact many of these instabilities can be adequately described by the more basic model of ideal MHD <sup>[2,3,4]</sup> which essentially describes how magnetic, inertial and pressure forces interact within a perfectly conducting plasma of arbitrary geometry. Because of the assumption of perfect conductivity it is possible to interpret the plasma motion as one in which both the plasma and magnetic flux move together. This has important implications for plasma stability, in that the magnetic field line topology is constrained to remain unchanged during any motion occurring on the hydromagnetic or Alfvén timescale. The success of ideal MHD in describing those instabilities that can grossly deform the plasma on the Alfvén timescale has made it the main consideration in the design of magnetic configurations for use in possible fusion reactors. But while favourable ideal MHD properties are necessary in a reactor, they may not be sufficient.

The inclusion of a finite but small amount of resistivity in the MHD equations relaxes the topological constraints imposed upon the plasma and allows the otherwise 'frozen in' magnetic field and fluid to decouple. This makes it possible, under certain circumstances which depend upon the initial configuration, for the plasma to relax to a state of lower magnetic energy. Such a state is topologically inaccessible in the ideal case.

The release of the free energy drives certain resistive instabilities <sup>[4,5,6,7]</sup> which can be classified into three main types : (1) the rippling mode, which is a short wavelength mode driven by a gradient in the resistivity, is usually not important except maybe in the

edge region of a plasma ; (2) the gravitational mode (or g-mode) which is the resistive analogue of the well known Rayleigh-Taylor interchange instability<sup>[4]</sup> also occurs at short wavelength and is stabilized by good field curvature and the effect of shear ; and (3) the tearing mode, which is the subject of this thesis, is the resistive equivalent of the ideal kink mode<sup>[4]</sup> and is driven essentially by gradients in the current density. It differs from the previous instabilities in that it is a long wavelength mode and causes a gross deformation of the magnetic field topology. It is this fact which makes it the most important in terms of its effect on the evolution of the plasma in magnetic devices such as the tokamak which rely on strong internal currents to achieve confinement.

Instabilities due to finite resistivity are also of considerable interest in astrophysics, where they find application, for example, in the study of solar flares, geomagnetic phenomena and in star formation theory. However it is the connection between these modes and the plasma processes leading to the disruption of tokamak plasma discharges which provides the main motivation for this study of the nonlinear behaviour of the resistive tearing mode. Nevertheless some of the bifurcation behaviour we have found may have astrophysical implications. Before discussing this further let us consider how the tearing mode arises.

Consider an ideal tokamak plasma equilibrium, in which the external current coils and transformer fields are so arranged as to produce a magnetic configuration in which the magnetic field lines are constrained to wind helically around the torus on nested toroidal flux surfaces with an average pitch or rotational transform varying from one surface to the next. A cross-section of the surfaces would thus appear as nested rings. Because of the localization of charged particles around magnetic field lines, the existence of such surfaces forms the basis of the confinement system - the sheared rotational transform being necessary to avoid certain ideal instabilities.

It is not immediately obvious how the inclusion of finite resistivity can change the topology of the configuration. One might expect that the only effect would be to cause the magnetic field to slowly decay away through the dissipation of the electrical currents.

However, it was shown <sup>[5]</sup> that though the field does diffuse across the entire plasma cross-section, the diffusion has a dominant effect at only a finite number of surfaces within the plasma where the pitch or helicity of the equilibrium field lines matches that of an instability. For there to exist a coherent wave structure such surfaces are such that the rotational transform is a rational fraction of the toroidal and poloidal winding numbers, i.e. where the field lines wind back upon themselves in a finite number of circuits of the torus. Such surfaces are therefore known as 'rational surfaces' or 'mode rational surfaces' when they are the source of an instability.

At these rational surfaces the plasma is locally able to move without causing the field lines to bend and the resistive diffusion changing the field is of a comparable magnitude to the changes caused by advection. This allows the fluid to decouple from the field so that they can diffuse with respect to each other to alter the topology of the field lines. To see this more clearly consider the induction equation :

$$\frac{\partial \mathbf{B}}{\partial t} = \nabla \times (\mathbf{V} \times \mathbf{B}) + \frac{\eta}{\mu_0} \nabla^2 \mathbf{B} \quad (1)$$

which can be derived from the resistive MHD equations listed in section I-2.1 by combining Ohm's law, (13), with the three pre-Maxwell equations : (14), (15) and (16) where  $\mathbf{B}$  is the magnetic field,  $\mathbf{V}$  is the fluid velocity and  $\eta$  is the resistivity. The first term on the right hand side of (1) represents the coupling of the field to the plasma while the second term gives the diffusion of the field.

Diffusion over a distance,  $a$ , has a characteristic timescale of  $\tau_R = \mu_0 a^2 / \eta$  while ideal MHD instabilities have a growth time characterized by the Alfvén velocity, i.e.  $\tau_A = a / V_A = a (\mu_0 \rho)^{1/2} / B$  where  $\rho$  is the mass density and  $B$  is the magnitude of the magnetic field. A comparison of the size of the terms in the induction equation can be made by normalizing with the characteristic quantities :  $a$ ,  $\tau_A$ ,  $\eta_0$ , and  $B_0$ . The dimensionless form of the induction equation becomes :

$$\frac{\partial \mathbf{B}}{\partial t} = \nabla \times (\mathbf{V} \times \mathbf{B}) + \frac{1}{S} \nabla^2 \mathbf{B} \quad (2)$$



where the ratio,  $S = \tau_R/\tau_A$ , is known as the Lundquist number. Inserting values of the parameters found in contemporary tokamaks gives  $S \sim 10^4$  to  $10^8$ , the latter figure being appropriate to a reactor plasma. Thus the timescale for diffusion in such devices is many orders of magnitude greater than that for the ideal hydromagnetic instabilities.

Consider a simple case in slab geometry of a plasma with a straight unidirectional field  $\mathbf{B}_0$  that varies across the slab like :  $\mathbf{B}_0 = B_0(x/a) \hat{e}_y$  so that it has a neutral line at  $x=0$ . Consider, also, perturbations to the magnetic field and velocity flow across the slab of the form :

$$B_x(x,y,z,t) = B_{x1}(x) \exp(ik_x x + ik_y y + \gamma t) \quad (3)$$

and insert this into the linearized form of the induction equation, (2), to give :

$$\gamma B_{x1} = i(\mathbf{k} \cdot \mathbf{B}_0) V_{x1} + \frac{1}{S} \left( \frac{\partial^2 B_{x1}}{\partial x^2} - k^2 B_{x1} \right) \quad (4)$$

$$\text{where } k^2 = k_x^2 + k_y^2 .$$

Since  $S$  is large, flux freezing characterized by  $\partial B_{x1}/\partial t \sim i(\mathbf{k} \cdot \mathbf{B}_0) V_{x1}$  will hold to a good approximation everywhere except in the neighborhood of the resonant ( or mode rational ) surface where  $\mathbf{k} \cdot \mathbf{B}_0 \sim 0$ . Near this surface the term  $i(\mathbf{k} \cdot \mathbf{B}_0) V_{x1}$  is small and all three terms in (4) will be comparable in magnitude. Since  $S \gg 1$ , this implies that  $\nabla^2 B_{x1}$  and hence  $\partial^2 B_{x1}/\partial x^2$  must become locally very large in a narrow resistive layer about the plane where  $\mathbf{k} \cdot \mathbf{B}_0 = 0$ . The problem is then a boundary layer type problem for which a solution away from where  $\mathbf{k} \cdot \mathbf{B}_0 = 0$  may be adequately described by the infinite conductivity limit with resistive effects being taken into consideration only in a narrow boundary or tearing layer about  $\mathbf{k} \cdot \mathbf{B}_0 = 0$ . Of course in order to obtain a solution another relationship between the linear variables  $B_x$  and  $V_x$  is required and this is obtained from the linearized version of the momentum equation, (10) of section I-2.1.

Without going into any detail the division of the problem into two parts defined by the regions inside and outside the boundary lends itself to the techniques of asymptotic

matching. For the exterior solution the scale is such that the perturbed field  $B_{x1}$  will appear to have a discontinuity in its first derivative across the surface at  $x=0$  given by :

$$\Delta' = \frac{B'_{x1}(0^+) - B'_{x1}(0^-)}{B_{x1}(0)} = \left[ \frac{\partial}{\partial x} \ln(B_{x1}) \right]_{0^-}^{0^+} \quad (5)$$

The linear growth rate of the resistive mode is then determined by requiring that the solution in the resistive layer around  $k \cdot B_0 = 0$  match the discontinuity,  $\Delta'_{ext}$ , in the outer solution, i.e. the growth rate,  $\gamma$ , is found from the eigenvalue equation :

$$\Delta'_{int}(\gamma) = \Delta'_{ext} \quad (6)$$

For the slab configuration discussed the eigenvalue equation has an analytical solution [5,6] of the form :

$$\gamma = (\Delta' a)^{4/5} \tau_R^{-3/5} \tau_A^{-2/5} \quad (7)$$

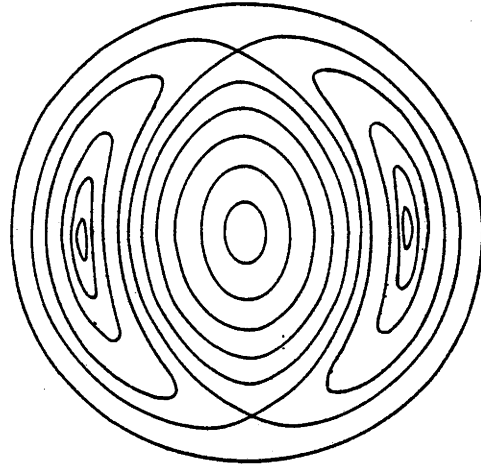
Using (7), an estimate [6] of the size of the tearing layer  $\delta$  over which the resistive diffusion term in (4) is comparable in magnitude to the ideal MHD term shows that  $\delta$  scales as  $\delta \sim S^{-2/5}$ . Using an energy principle analysis [6], it can also be shown that the tearing mode is unstable if  $\Delta' > 0$ .

Detailed simulations have been made [8] of the linear resistive tearing mode in a slab plasma showing the variation of the linear profile and growth rate with Lundquist number and periodicity length of the system. Despite the usefulness of such information, the linear stability theory of the tearing mode gives only an incomplete description of the behaviour of the mode, since in most laboratory plasmas nonlinear effects become important in the very early stages of development of the mode. Equation (7) shows that the linear growth rate lies between the resistive and the hydromagnetic timescales and in tokamak plasmas such as LT-4 the growth time would be typically of the order of a millisecond, which is a small fraction of the total discharge time of about 100 milliseconds. For this reason it is important to investigate the nonlinear behaviour of the tearing mode, especially since it is

after entering this stage that the topological changes to the magnetic field configuration, resulting from the reconnection in the diffusion layer, become evident.

The magnetic field tends to break up into a number of thin filaments which when viewed in cross section appear as magnetic islands joined end to end and separated by a separatrix, as shown in fig.(1). The x and o points of the island correspond to invariant rational field lines along which the island structure threads its way through the plasma.

Fig.1



As the islands grow, flux surfaces are pulled in from above and below to weld together at the x-points and then tear apart to form the closed surfaces within the island. Broadly speaking the process is driven by the need to reduce the magnetic energy in the regions away from the islands.

There are essentially two separate nonlinear stages. The first, investigated by Rutherford<sup>[9]</sup>, occurs when the magnetic island width exceeds the width of the tearing layer. At this point nonlinear eddy currents become large enough to significantly oppose the flow pattern so as to replace the inertia as the force opposing the growth of the mode. The result is a transition from an exponential to a slower algebraic growth with the island width,  $W$ , increasing linearly with time. More specifically the early nonlinear growth of an island in this 'Rutherford regime' is given approximately by<sup>[10]</sup> :

$$\frac{\partial W}{\partial t} = 1.66 \eta(r_s) \left[ \Delta'(W) - \alpha W \right] \quad (8)$$

where  $\eta(r_s)$  is the resistivity at the rational surface and  $\Delta'(W)$  is the logarithmic derivative across an island not much bigger than the diffusion layer. The second term on the right hand side of (8) was introduced by White et al.<sup>[10]</sup> by extending the work of Rutherford to include self-consistent changes in the resistivity due to the island. However the coefficient,  $\alpha$ , is practically negligible if the resistivity profile increases radially with the scale length of the minor radius.

The second stage occurs when the island size becomes comparable to the shear length associated with the initial field. During this stage, the behaviour of the mode is dominated by the gross geometry of the plasma, which may eventually lead to the saturation of the mode if a minimum magnetic energy state exists for a finite island width.

By extending the interpretation of (8) to include islands much greater than the diffusion layer and neglecting the term involving  $\alpha$ , an approximate condition for the saturation of the islands becomes :

$$\Delta'(W) = 0 \quad (9)$$

This criterion has been used in quasi-linear delta-prime calculations<sup>[10,11]</sup> to predict saturated magnetic island widths covering a sizeable fraction of the minor radius. Saturation of magnetic islands has also been demonstrated via fully nonlinear simulations in cylindrical geometry<sup>[12]</sup> as well as in slab geometry in this thesis. Given that the appropriate mode rational surfaces all lie within the plasma it is also possible for several island structures of different helicities to form simultaneously<sup>[13]</sup>. Such helical island structures represent a significant distortion to the original equilibrium and in fact it is generally believed that they are the cause of the periodic fluctuations in the poloidal magnetic field, known as Mirnov oscillations, which are detected on magnetic pickup coils at the edge of the plasma. The oscillation in the field apparently results from a toroidal rotation of the helical island structures around the torus.

Under conservative operating conditions the resonant tearing modes will saturate at a small enough amplitude not to seriously upset the evolution of the discharge, although,

because of the unconstrained motion of charged particles along magnetic field lines, the change in topology does increase the transport across the plasma and so degrades the particle and energy confinement. However usually as a consequence of trying to improve the performance of the tokamak discharge, by increasing the density, temperature or current in the plasma the MHD activity will behave more erratically perhaps stopping and restarting suddenly, disappearing altogether or undergoing sudden bursts of growth which can lead to a sudden termination of the discharge known as a major disruption<sup>[4,6]</sup>. Considerable damage to the device can occur during a disruption as the high energy plasma is quenched on the limiter or vessel wall. For this reason and because it is relatively unpredictable the disruptive instability is considered to be the most dangerous instability occurring in tokamak plasmas and presently represents, perhaps, the major obstacle for tokamaks to reach the conditions necessary for a fusion reactor.

Not much is known for certain about the dynamics of the major disruption but because it is nearly always preceded by certain MHD activity (usually by a fast growing  $m=2$  mode, although this is not as apparent in the LT-4 tokamak<sup>[14]</sup>) the inference is that it is closely tied up with the nonlinear behaviour of the saturated tearing mode magnetic islands. The imperative is therefore to understand the saturated behaviour of the tearing mode sufficiently to be able to explain the nature of the activity that precedes a disruption so that, hopefully, means can be developed to avoid such a destructive termination of the plasma discharge.

Several scenarios have been proposed for the plasma disruption, including ones involving the interaction of islands of different helicities<sup>[13,15,16]</sup>. The interaction of neighbouring island chains is believed to induce the disruption by causing ergodic wandering of the magnetic field lines<sup>[13]</sup>. The disruption could also be due to the interaction of magnetic islands with the limiter or wall or more simply just due to the current profile adiabatically changing to a form which causes an island to rapidly grow too large for the plasma to be sustained. None of the proposed models, however, gives a complete description of the final stages of the disruption so that it is uncertain how such

processes actually destroy the confinement. It is also difficult to see how they would account for the range of precursor MHD activity seen on the LT-4 tokamak [14,17,18,19,20] which is not always the same as elsewhere. The evidence so far suggests that there are many different forms of disruption, involving some combination of these or other processes.

Given the present uncertainty it is probably worthwhile to return to a more general investigation of the nonlinear resistive tearing mode as a means of uncovering further properties which may help in the resolution of the problem. It is this possibility which has provided the main motivation for the work in this thesis, especially in the first half which describes a detailed numerical study of the basic nonlinear evolution of the tearing mode on a current sheet. As well as tidying up some previous results, two new bifurcations have been found in addition to the standard one occurring at the minimum unstable tearing mode wavelength which are found to be approached via the processes of coalescence and secondary island generation, although it is not certain whether such behaviour would occur in tokamak plasmas. The second half represents a more direct attempt at using tearing mode theory to explain the varied MHD activity observed on the LT-4 tokamak. This includes using a quasi-linear delta-prime analysis to model the amplitude of MHD activity in the LT-4 tokamak on the basis of an  $m=2/n=1$  magnetic island. A mechanism of mode locking is invoked as a means of explaining the difference in the range of activity predicted by the theory as compared with experimental observation. This is followed by a numerical study of forced reconnection in a flowing plasma and finally a preliminary nonlinear numerical investigation of the dynamics of mode locking of tearing mode magnetic islands onto an external field perturbation.

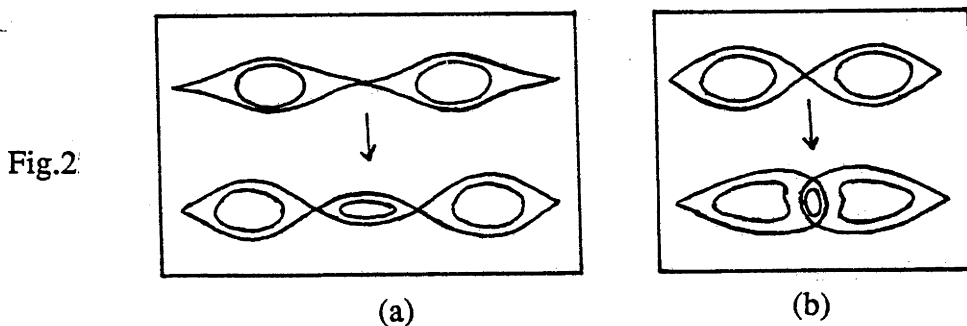
## I-1.2 Review of Nonlinear Behaviour.

Many investigations, usually numerical, have been made to establish the nonlinear behaviour of the tearing mode in various geometries but because of the complex nature of the problem, the results have fallen short of producing a systematic and conclusive picture. In particular many papers have been written on the tendency of magnetic islands to coalesce. The idea that this produces a state of lower energy was originally speculated by Furth, Rutherford and Selberg <sup>[21]</sup>. Following this, the existence of the linear ideal instability was proved by Finn and Kaw <sup>[22]</sup> by considering perturbations on a chain of magnetic islands in a 2-D plane slab plasma using the energy principle of ideal MHD while the linear dynamics of the instability and the nonlinear process of merging of two islands in the presence of resistivity was demonstrated by Pritchett and Wu <sup>[23]</sup>. Biskamp and Welter <sup>[24]</sup> then studied the process numerically over a wider range of values of the resistivity to determine scaling relations for various parameters including the reconnection rate during coalescence which, in general, favoured the Sweet-Parker model over that due to Petschek. The energy principle analysis was re-examined by Bondeson <sup>[25]</sup> to show that for small values of the island width,  $W$ , the growth rate scales as  $W^{3/2}$  and therefore that there is no threshold island size for the coalescence instability. Bhattacharjee, Brunel and Tajima <sup>[26]</sup> then made a more detailed numerical study of the coalescence process by including the effects of compressibility and the magnitude of the toroidal field on the rate of reconnection during coalescence.

The significance of these results is diminished somewhat by the fact that in all these papers the exact island equilibrium due to Fadeev, Kwartshava and Komorov <sup>[27]</sup> was used as the initial equilibrium. The advantages of starting with a ready made magnetic island configuration are obvious but unfortunately, as will be shown later, it is not a state accessible via the resistive tearing mode and hence it is less certain that a physical tearing mode will behave in the same way. The reality of this is made apparent by comparing the corresponding current distributions, The exact island equilibrium has a simple current

distribution peaked at each o-point to form a line of parallel current channels which allows the origin of the coalescence instability to be easily understood in terms of the tendency of parallel current filaments to attract each other. In contrast, for a magnetic island configuration generated by a tearing mode the current distribution is much more complex and as shown by Hayashi [28] it can have, at least temporarily, almost the opposite distribution with peaks at the x-points and troughs at the o-points during its evolution. Hayashi uses this observation to explain the absence of spontaneous coalescence in his simulation but incorrectly generalized this to conclude that the coalescence instability does not take place for magnetic islands generated by a tearing instability. It will be demonstrated here that for appropriate parameter values the tearing mode magnetic island will develop to a stage, much further on in the evolution than in Hayashi's simulations, where conditions are such that coalescence does indeed occur spontaneously.

It has generally been believed that a magnetic island chain will continue to coalesce until it reaches a state where further coalescence is restricted only by the finite plasma size or in the case of say a tokamak plasma, by the minimum mode numbers commensurate with the q-value on the particular rational surface on which it forms. In contrast nonlinear simulations of the tearing mode made by Steinolfson and Van Hoven [29] in slab geometry have shown the emergence of secondary magnetic islands between each of the primary magnetic islands, see fig.2(a), a process which would seem to be the opposite to coalescence.





To make the situation even more confusing Biskamp<sup>[30]</sup> has also shown the formation of a different kind of secondary island, see fig.2(b), in the neutral layer between two coalescing islands oriented perpendicular to the original neutral line, although their existence is questioned by Bhattacharjee, Brunel and Tajima<sup>[26]</sup> as being a consequence of the symmetry constraints imposed on his numerical scheme. Even so, the results of Steinolfson and Van Hoven and Hayashi certainly place a question mark over the actual tendencies of the nonlinear tearing mode magnetic islands and at least indicate that transformations of the magnetic islands other than coalescence can occur.

An alternative approach considered by Matthaeus and Lamkin<sup>[31,32]</sup> is to excite a broad band of fluctuations on a sheet pinch to investigate turbulent reconnection behaviour. This produces small and large scale magnetic islands which undergo a much more exotic variety of motions including internal pulsations of the larger islands and asymmetric coalescing of the small islands or bubbles. The motivation for this approach comes from the expectation that turbulent reconnection would occur in real plasmas because of their high Reynolds and Magnetic Reynolds numbers. High level turbulence would certainly be expected to dominate the ramp up phase of a plasma discharge but as it settles into a steady regime of operation the experimental evidence<sup>[33]</sup> is for a small number of tearing modes to rise above the noise and dominate the further evolution of the plasma. Studies of turbulence are notoriously demanding of computer time so rather than exciting a large number of modes and waiting for the dominant modes to emerge we shall content ourselves here with a smoother start up by initially exciting only the lowest order mode and allow higher order modes to be excited through the nonlinear coupling as required.

This first part of the thesis, comprising sections I-2.1 to I-3.7, is devoted to a systematic numerical study of the nonlinear behaviour of the resistive tearing mode on a linear current sheet in a plane slab plasma. In section I-2.1 is given a description of the equations and other details of the model including a discussion of the boundary conditions while section I-2.2 provides the details of the actual numerical scheme employed to solve

the equations. The limitations of the technique are made evident in section I-2.3 through a discussion of its convergence properties in various regimes of operation and in section I-2.4 which describes the numerical stability of the scheme. This includes a brief review of a novel alternative semi-implicit method <sup>[34]</sup> for temporally advancing the MHD equations which when applied to the reduced resistive MHD equations is shown to be equivalent to the addition of a viscous damping term. The results of the numerical simulations are given in section I-3, which begins in section I-3.1 with a description of the type of simple tearing mode evolution typically observed in previous numerical studies. All simulations are taken to saturation and in section I-3.2 an investigation is made of the variation of the saturated tearing mode states as a function of the various plasma parameters. This reveals evidence of a preferred island length,  $L_{\text{pref}}$ , which in section I-3.3 is shown to lead to the formation of unstable x point current sheets which result in the generation of secondary magnetic islands when the periodicity length,  $L_p$ , exceeds a critical length,  $L_{\text{crit}}$ . This is contrasted in section I-3.4 with a simulation of the coalescence of tearing mode magnetic islands for which a detailed description of the process clearly identifies three dynamical stages. In section I-3.5 it is shown how the competition between these two mechanisms, when  $L_p > L_{\text{crit}}$ , leads to a transition to more complex island structures with asymmetric current sheets and non-zero phase velocities. Two new bifurcations are distinguished as a function of  $L_p$ : a symmetry breaking bifurcation and a period doubling bifurcation. A study of the individual Fourier modes at saturation reveals a system to these transitions that indicates the likelihood of further such transitions at even higher values of the periodicity length. The steady state nature of the reconnection that persists after saturation, defines a reconnecting system suitable for comparison with the two steady state reconnection models due to Sweet-Parker <sup>[35,36]</sup> and Petschek <sup>[37]</sup>. This forms the topic of investigation in section I-3.6. Finally a summary of the results is given in section I-3.7 in which some conclusions and implications for further studies are made.

## I-2.1 Mathematical Model

The equations appropriate for the description of the low frequency long-wavelength phenomena, such as that produced by the resistive tearing mode, in a fluid of finite electrical conductivity and finite viscosity, are the visco-resistive magnetohydrodynamic (MHD) equations. These are given by:

$$\rho \frac{\partial \mathbf{V}}{\partial t} + \rho \mathbf{V} \cdot \nabla \mathbf{V} = \mathbf{J} \times \mathbf{B} - \nabla p + \nu \nabla^2 \mathbf{V} + \nu \frac{1}{3} \nabla (\nabla \cdot \mathbf{V}) \quad (10)$$

$$\frac{\partial \rho}{\partial t} + \nabla \cdot \rho \mathbf{V} = 0 \quad (11)$$

$$\frac{d}{dt} (p/\rho^\gamma) = S_E \quad (12)$$

$$\mathbf{E} + \mathbf{V} \times \mathbf{B} = \eta \mathbf{J} \quad (13)$$

$$\nabla \times \mathbf{E} = - \frac{\partial \mathbf{B}}{\partial t} \quad (14)$$

$$\nabla \times \mathbf{B} = \mu_0 \mathbf{J} \quad (15)$$

$$\nabla \cdot \mathbf{B} = 0 \quad (16)$$

and relate the electric and magnetic fields  $\mathbf{E}$  and  $\mathbf{B}$  to the fluid velocity  $\mathbf{V}$  and the thermodynamic variables of pressure  $p$  and mass density  $\rho$ . The transport coefficients of the dissipative terms in equations (10) and (13) are the bulk viscosity  $\nu$  and the electrical resistivity  $\eta$  while the source term on the right hand side of equation (12) corresponds to the energy dissipated by them. The equations are essentially the equations of fluid mechanics and electromagnetism (pre-Maxwell) joined together through Ohm's law. Equations (10) to (13), which are respectively : the equation of motion, the mass continuity equation, the adiabatic equation of state and the generalized Ohm's law, can be derived from the moments of the Boltzman equation <sup>[2,3]</sup> for each species of particles.

This is done by assuming the hydrodynamic or continuum approximation and combining them into a single fluid model in which ions and electrons are treated as a single electrically conducting fluid.

To study the nonlinear behaviour of the resistive tearing mode using these equations it is necessary to resort to numerical techniques as the complex reconnection activity described in the previous section makes it difficult to choose appropriate approximations to make the problem tractable analytically and still retain the essential properties. In fact even when using a numerical approach it is necessary to reduce the problem to its simplest possible form and operate close to numerical stability limits to bring the calculation within the range of available computational resources.

Since we are only interested in the qualitative behaviour of the tearing mode we will consider a 2-D plane slab plasma with  $\partial/\partial z = 0$ . Previous studies of the nonlinear tearing mode [26,38] have shown the effects of compressibility to be small in the limit of a large  $B_z$  field. In effect the large magnetic field strength makes the plasma behave incompressibly because of the increased tension it creates in the plasma. Tokamak plasmas tend to behave in a similar fashion because of their large toroidal field. We shall, therefore, also consider an incompressible plasma with uniform density especially since it allows greater simplification of the governing equations. Equation (11) then reduces to:

$$\nabla \cdot \mathbf{V} = 0 \quad . \quad (17)$$

so that the second viscosity term in equation (10) vanishes. Equations (16) and (17) now allow us to express the fluid velocity and magnetic field in terms of a velocity stream function  $\phi$  and a magnetic flux function  $\psi$  respectively by:

$$\mathbf{B} = \hat{\mathbf{e}}_z \times \nabla \psi + B_z \hat{\mathbf{e}}_z \quad (18)$$

$$\mathbf{V} = \hat{\mathbf{e}}_z \times \nabla \phi + V_z \hat{\mathbf{e}}_z \quad . \quad (19)$$

which makes it possible to reduce the visco-resistive MHD equations down to a set of coupled PDE's in terms of only two dependent variables,  $\psi$  and  $\phi$ , known as the reduced resistive MHD equations. We shall briefly show how they are derived.

Operating on eqn.(14) with  $\hat{e}_z \times$ , integrating and using eqn.(18) we obtain:

$$E_z = \frac{\partial \psi}{\partial t} + E_z^{\text{ext}} \quad (20)$$

where  $E_z^{\text{ext}}$  is an externally imposed constant electric field in the z-direction. Substituting this into the z-component of eqn.(13) ( Ohm's law ) we then get:

$$\frac{\partial \psi}{\partial t} + \mathbf{V} \cdot \nabla \psi = \eta J_z - E_z^{\text{ext}} \quad (21)$$

Substituting eqn.(18) into z-component of eqn.(15) we get:

$$J_z = \frac{1}{\mu_0} \nabla^2 \psi \quad (22)$$

Operating on eqn.(10) (the equation of motion) with  $\hat{e}_z \cdot \nabla \times$  and substituting in eqns.(18) and (19) we obtain an equation for  $\nabla^2 \phi$ :

$$\frac{\partial \zeta}{\partial t} + \mathbf{V} \cdot \nabla \zeta = \frac{1}{\rho} \hat{e}_z \cdot (\nabla \psi \times \nabla J_z) + \frac{\nu}{\rho} \nabla^2 \zeta \quad (23)$$

where

$$\zeta = \hat{e}_z \cdot \nabla \times \mathbf{V} = \nabla^2 \phi \quad (24)$$

is the z-component of the vorticity.

Equations (21) and (23) in conjunction with equations (22) and (24) are independent of  $p$ ,  $V_z$  and  $B_z$  and form a closed system which with boundary conditions and an equation for  $\eta$  constitute the reduced equations in slab geometry. They describe the field and flow behaviour in the x-y plane in terms of the two stream functions  $\phi$  and  $\psi$ , from which  $B_x$ ,  $B_y$ ,  $V_x$  and  $V_y$  can be obtained by substitution into eqns. (18) and (19).

Although the complete nonlinear dynamics is given by these equations it is also possible to derive the evolution equations for  $V_z$  and  $B_z$  which depend on  $\phi$  and  $\psi$ . But since these would add unnecessarily to the cpu time we will not do this here. It is however necessary to evolve the z-component if it is desired to know how the total energy is partitioned but it was considered better to sacrifice this information for the sake of greater computational speed.

In any case, a previous numerical investigation <sup>[29]</sup> that included the evolution of  $V_z$  and  $B_z$  showed that in most cases only a small fraction of the available energy appears as kinetic energy, with the majority being converted to either perturbed magnetic or thermal energy during the evolution of the tearing mode.

A dimensionless version of the reduced equations is obtained by normalizing: lengths with the current channel half width,  $a$ ; fields with  $B_0$ , the value of the initial equilibrium field at the plasma edge; times with the Alfvén or hydromagnetic time  $\tau_A = a(\mu_0\rho)^{1/2}/B_0$  and the remaining dimensional terms gathered to form the Lundquist number  $S = \tau_R/\tau_A$  where  $\tau_R = a^2\mu_0/\eta_0$  is the resistive diffusion time,  $\eta_0$  being the minimum value of  $\eta$ . These are:

$$\frac{\partial \hat{\psi}}{\partial \hat{t}} = [\hat{\psi}, \hat{\phi}] + \frac{1}{S} \left( \hat{\eta} \hat{J}_z - \hat{E}_z^{\text{ext}} \right) \quad (25)$$

$$\frac{\partial \hat{\xi}}{\partial \hat{t}} = [\hat{\xi}, \hat{\phi}] + [\hat{\psi}, \hat{J}_z] + \hat{\nabla} \hat{\nabla}^2 \hat{\xi} \quad (26)$$

$$\hat{J}_z = \hat{\nabla}^2 \hat{\psi} \quad (27)$$

$$\hat{\xi} = \hat{\nabla}^2 \hat{\phi} \quad (28)$$

where with further manipulation we have expressed some terms of the dimensionless equations in terms of a Poisson bracket defined by:

$$[f, g] = \frac{\partial f}{\partial x} \frac{\partial g}{\partial y} - \frac{\partial f}{\partial y} \frac{\partial g}{\partial x} \quad (29)$$

and where:

$$\begin{aligned}
\hat{\psi} &= \psi / (a B_0) & \hat{v} &= v / (\rho a^2 / \tau_A) & \hat{x} &= x / a \\
\hat{\phi} &= \phi / (a^2 / \tau_A) & \hat{\eta} &= \eta / \eta_0 & \hat{y} &= y / a \\
\hat{\zeta} &= \tau_A \zeta & \hat{E}_z^{\text{ext}} &= E_z^{\text{ext}} / (\eta_0 B_0 / (a \mu_0)) & \hat{t} &= t / \tau_A \\
\hat{J}_z &= J_z / (B_0 / (\mu_0 a)) & \hat{\nabla}^2 &= \frac{\partial^2}{\partial \hat{x}^2} + \frac{\partial^2}{\partial \hat{y}^2} & & 
\end{aligned} \tag{30}$$

Initial Conditions:

We consider an initial flowless equilibrium of the form:

$$\begin{aligned}
\mathbf{B}(t=0) &= B_0 \tanh(x/a) \hat{e}_y \\
V(t=0) &= 0
\end{aligned} \tag{31}$$

which has a line of field reversal at  $x = 0$  along which a tearing mode can generate a chain of magnetic islands.

The current channel associated with this equilibrium through  $\hat{J}_0 = \hat{\nabla} \times \hat{B}_0 = \text{sech}^2(\hat{x})$  is maintained by the uniform z-directed electric field  $\hat{E}_z^{\text{ext}}$  in conjunction with a non-uniform resistivity profile evaluated from Ohm's law to give:

$$\hat{\eta}(\hat{x}) = \hat{E}_z^{\text{ext}} / \hat{J}_{z0}(\hat{x}) = \cosh^2(\hat{x}) \tag{32}$$

This is a frequently used technique <sup>[16,39,40,41]</sup> to allow the tearing mode to proceed to saturation by preventing the resistive decay of the equilibrium on which it grows while still allowing for self-consistent nonlinear changes to the background field produced by the tearing mode itself. Note that  $\hat{\eta}$  has been normalized so that  $\hat{\eta}(0) = 1$ . Hence  $\hat{E}_z^{\text{ext}}$  is not a free parameter, but is in fact given by  $\hat{E}_z^{\text{ext}} = 1$ . The only explicit free dimensionless parameters are  $S$  and  $\hat{v}$ . Also note that we are assuming the applied electric field and resistivity to be constant in time, but not the total current. However by averaging equation (25) over the cross sectional area of the plasma it can be shown that  $\langle \eta J_z \rangle$  is conserved.





periodicity length  $L_p \equiv L_p/a$  makes the third and final free dimensionless parameter of the resistive slab equations. More precisely we have the following conditions on  $\phi$  and  $\psi$  :

$$\begin{aligned}
 \text{Impenetrability : } & V_x = 0 \quad \text{at } x = \pm X_w \\
 \Rightarrow & \left[ \frac{\partial \phi}{\partial y} \right]_{x=\pm X_w} = 0 \\
 \Rightarrow & \phi(x=\pm X_w) = \phi_w^\pm(t)
 \end{aligned} \tag{34}$$

$$\begin{aligned}
 \text{Perfect conductivity : } & B_x = 0 \quad \text{at } x = \pm X_w \\
 \Rightarrow & \left[ \frac{\partial \psi}{\partial y} \right]_{x=\pm X_w} = 0 \\
 \Rightarrow & \psi(x=\pm X_w) = \psi_w^\pm(t)
 \end{aligned}$$

We shall henceforth take  $\phi_w^\pm, \psi_w^\pm$  as constant with respect to  $t$ . In fact for simplicity we will set  $\phi_w^\pm = 0 = \psi_w^\pm$  for all cases in part I although a more complex set of conditions will be implemented in part II of this thesis.

Let us consider further the implications of these boundary conditions. First we note that the form invariance of the reduced equations under the following Galilean transformation:

$$\begin{aligned}
 \psi(x, y, t) & \rightarrow \psi(x, y - Vt, t) \\
 \phi(x, y, t) & \rightarrow \phi(x, y - Vt, t) + Vx
 \end{aligned} \tag{35}$$

shows that without loss of generality we can always choose a frame in which  $\phi_w^+ = \phi_w^-$  although the same is not true for  $\psi_w^+$  and  $\psi_w^-$ . No change of frame can make  $\psi_w^+$  and  $\psi_w^-$  equal if not originally so. The equations are also invariant under addition of arbitrary constants to  $\phi$  and  $\psi$  so we can also take  $\phi_w^+ = \phi_w^- = 0$ . We justify having  $\psi_w^+ = \psi_w^- = 0$  by ensuring that the initial equilibrium satisfies this condition.

It can also be shown that the value of  $\phi_w^+ - \phi_w^-$  is closely related to the electric potential.

From the x-component of equation (13) (ohm's law) we have

$$E_x = -(\mathbf{V} \times \mathbf{B})_x + \eta J_x . \quad (36)$$

From eqns.(18) and (19) we have

$$\mathbf{V} \times \mathbf{B} = \hat{e}_z \cdot \nabla \phi \times \nabla \psi \hat{e}_z + B_z \nabla \phi - V_z \nabla \psi \quad (37)$$

and from eqn.(15) we have

$$\mu_0 \mathbf{J} = \nabla^2 \psi \hat{e}_z - \hat{e}_z \times \nabla B_z . \quad (38)$$

Substituting the x-components of equations (37) and (38) into (36) yields

$$E_x = V_z \frac{\partial \psi}{\partial x} - B_z \frac{\partial \phi}{\partial x} + \frac{\eta}{\mu_0} \frac{\partial B_z}{\partial y} . \quad (39)$$

Thus if  $V_z$  and  $B_z$  are constant with respect to  $x$  and  $y$  then the potential difference between the walls is given by:

$$\Delta V = \int_{-X_w}^{X_w} E_x dx = V_z (\psi_w^+ - \psi_w^-) - B_z (\phi_w^+ - \phi_w^-) . \quad (40)$$

Taking the frame in which  $V_z = 0$  (assuming  $V_z$  is independent of  $t$ ) we then have

$$\Delta \phi_w = \phi_w^+ - \phi_w^- = \frac{1}{B_z} \int_{-X_w}^{X_w} E_x dx = \frac{1}{B_z} \Delta V \quad (41)$$

or

$$\Delta \phi_w = \frac{1}{B_z} \Delta V .$$

Thus the difference in wall values of the velocity stream function in this special case is proportional to the potential difference so the assumption that  $\phi_w^+ = \phi_w^- = 0$  corresponds to the short-circuiting of the walls. By the same token when the walls are held at different potentials, that is when  $\phi_w^+ \neq \phi_w^-$ , the resultant electric field  $E_x$  combined with the  $B_z$  field produces an  $\mathbf{E} \times \mathbf{B}$  drift in the  $y$ -direction.

By integrating the y-component of eqn.(19) across the plasma we find

$$\phi_w^+ - \phi_w^- = \int_{-X_w}^{X_w} V_y dx \quad (42)$$

so a uniform flow in the y-direction of magnitude V can be maintained by a difference in the velocity stream function of:

$$\phi_w^+ - \phi_w^- = 2 X_w V . \quad (43)$$

This technique is used in part II to study the effect of external perturbations on tearing modes in a flowing plasma.

The validity of the assumptions:  $V_z = 0$ ,  $B_z = \text{const.}$  for the above special case will now be given. Consider the conservation form of the equation of motion:

$$\frac{\partial}{\partial t} (\rho \mathbf{V}) + \nabla \cdot \left[ \rho \mathbf{V} \mathbf{V} + \left( p + \frac{B^2}{2\mu_0} \right) \mathbb{I} - \frac{1}{\mu_0} \mathbf{B} \mathbf{B} - \nu \nabla \nabla \right] = 0 . \quad (44)$$

By taking the z-component of this we obtain an equation for  $V_z$  :

$$\rho \left( \frac{\partial V_z}{\partial t} + \mathbf{V} \cdot \nabla V_z \right) - \nu \nabla^2 V_z = \frac{1}{\mu_0} \mathbf{B} \cdot \nabla B_z . \quad (45)$$

To obtain an equation for  $B_z$  we take the z-component of Faraday's law, equation (14), giving:

$$\frac{\partial B_z}{\partial t} + \nabla \cdot (\mathbf{E} \times \hat{\mathbf{e}}_z) = 0 \quad (46)$$

for which the right-hand term can be derived from Ohm's law, equation (13), to give:

$$\nabla \cdot (\mathbf{E} \times \hat{\mathbf{e}}_z) = \hat{\mathbf{e}}_z \cdot (\nabla \phi \times \nabla B_z) - \hat{\mathbf{e}}_z \cdot (\nabla \psi \times \nabla V_z) - \nabla \cdot \left( \frac{\eta}{\mu_0} \nabla B_z \right) . \quad (47)$$

Combining this with equation (46) we have

$$\frac{\partial B_z}{\partial t} = \hat{e}_z \cdot \nabla B_z \times \nabla \phi + \nabla \cdot \left( \frac{\eta}{\mu_0} \nabla B_z \right) - \hat{e}_z \cdot \nabla V_z \times \nabla \psi \quad (48)$$

$V_z = 0$ ,  $B_z = \text{const.}$  is a solution to equations (45) and (48) thus verifying the assumptions made in the special case.

The method used to solve the system of equations (25) to (28) requires a boundary condition to also be specified for the vorticity,  $\zeta$ . This is provided by the condition that no vorticity be generated at the wall, i.e.:

$$\hat{n} \times (\nabla \times \mathbf{V}) = 0 \quad \text{at the wall} \quad (49)$$

which for this set-up reduces to:

$$\zeta(x = \pm X_w) = 0 \quad (50)$$

Further insight into the significance of these conditions is gained from looking at momentum conservation. Integrating equation (44) over the plasma we have:

$$\frac{\partial}{\partial t} \int_V \rho \mathbf{V} \, d\tau + \int_S \hat{n} \cdot \left[ \rho \mathbf{V} \mathbf{V} + \left( p - \frac{B^2}{2\mu_0} \right) \mathbf{I} - \frac{1}{\mu_0} \mathbf{B} \mathbf{B} - \nu \nabla \mathbf{V} \right] ds = 0 \quad (51)$$

the y-component of which reduces to:

$$\frac{\partial}{\partial t} \left( \int_{-X_w}^{X_w} dx \int_0^{L_p} dy \rho V_y \right) = \nu \int_0^{L_p} dy \left( \left[ \frac{\partial V_y}{\partial x} \right]_{+X_w} - \left[ \frac{\partial V_y}{\partial x} \right]_{-X_w} \right) \quad (52)$$

Using equation (19) we have:

$$\frac{\partial}{\partial t} \left( \int_{-X_w}^{X_w} dx \int_0^{L_p} dy \rho \frac{\partial \phi}{\partial x} \right) = \nu \int_0^{L_p} dy \left[ \frac{\partial^2 \phi}{\partial x^2} \right]_{-X_w}^{X_w} \quad (53)$$

which reduces to:

$$\frac{\partial}{\partial t} \left( \rho L_p (\phi_w^+ - \phi_w^-) \right) = \nu \int_0^{L_p} dy \left[ \frac{\partial^2 \phi}{\partial x^2} \right]_{-X_w}^{X_w} \quad (54)$$

This implies that a boundary layer will form if the potential difference is varied in time.

Also the faster the changes are the steeper will be the flow gradients in the boundary layer.

Note that the impenetrability condition :

$$\left[ \frac{\partial \phi}{\partial y} \right]_{\pm X_w} = 0$$

means that

$$\zeta = \frac{\partial^2 \phi}{\partial x^2} \quad \text{at } x = \pm X_w$$

so equation (54) becomes

$$\frac{\partial}{\partial t} \left( \rho L_p \left( \phi_w^+ - \phi_w^- \right) \right) = \nu \int_0^{L_p} dy \left( \zeta_w^+ - \zeta_w^- \right) . \quad (55)$$

The boundary condition of vanishing vorticity at the walls is therefore consistent with the time independence of  $\phi_w^+$  and  $\phi_w^-$  for the purpose of conserving the momentum.

In summary the boundary conditions used in part I are :

$$\left. \begin{array}{l} \phi = 0 \\ \psi = 0 \\ \zeta = 0 \end{array} \right\} \text{ at } x = \pm X_w \quad (56)$$

Note that the method of solution does not require the specification of a boundary condition for the current.

## I-2.2 Numerical Scheme

The normalized equations, (25) to (28) are Fourier expanded in the  $y$ -direction and discretized in the  $x$ -direction to form the equations for a hybrid spectral/finite difference code which uses a two step semi-implicit timestepping scheme to evolve the four dependent variables  $\psi$ ,  $\phi$ ,  $J_z$  and  $\zeta$  in time. The approach is not new<sup>[42]</sup> and has been employed in 3-D calculations in cylindrical geometry<sup>[16,43-46]</sup>. Other techniques have been employed to solve these equations including an ADI (Alternating Direction Implicit) Scheme<sup>[47]</sup> for evolving the full set of resistive MHD equations. Such methods have good numerical stability properties but are usually considerably more expensive with cpu time.

The success of the semi-implicit method used here relies on two basic premises: firstly that the type of solutions expected are more naturally represented in a semi-spectral form and hence only require a small finite number of Fourier modes for convergence. And secondly, that the cpu intensive matrix inversions and iterations of fully implicit techniques are avoided by explicitly timestepping the nonlinear terms while maintaining numerical stability through the much simpler implicit timestepping of the linear dissipative terms. A discussion of how well these premises are upheld will be given in the next section.

In this section we shall, for completeness, describe how we have implemented the technique in slab geometry. Each of the field quantities in equations (25) to (28), ( ie.  $\psi$ ,  $\phi$ ,  $J_z$  and  $\zeta$ , the  $\wedge$  being implicit from here on ) is expanded using a truncated Fourier series given by:

$$\psi(x,y,t) = \frac{1}{2} \psi_o^c(x,t) + \sum_{m=1}^M \left[ \psi_m^c(x,t) \cos(k_m y) + \psi_m^s(x,t) \sin(k_m y) \right] \quad (57)$$

where  $M$  is the total number of modes,  $k_m = 2\pi m / L_p$  and  $L_p$  is the periodicity length in the  $y$ -direction.

The range of modes selected ( $0 < m < M$ ) is based on the expectation that the long wavelength nature of the tearing mode will cause the solution to be dominated by a low order Fourier mode such that the magnitudes of the amplitudes drop off rapidly with  $m$ .

Each equation is then multiplied by  $\cos(k_m y)$  or  $\sin(k_m y)$  and integrated with respect to  $y$  to project out the equations governing the evolution of each individual Fourier mode. For each mode number,  $p$ , there are four evolution equations: two corresponding to the cos and sin components of  $\psi$  and two corresponding to the cos and sin components of  $\zeta$ . These are:

$$\frac{\partial \psi_p^c}{\partial t} = S_{1p}^c + \frac{1}{S} \left( \eta J_{z p}^c - E_{z p}^{\text{ext}} \right) \quad (58)$$

$$\frac{\partial \psi_p^s}{\partial t} = S_{1p}^s + \frac{1}{S} \eta J_{z p}^s \quad (59)$$

$$\frac{\partial \zeta_p^c}{\partial t} = S_{2p}^c + v \nabla_p^2 \zeta_p^c \quad (60)$$

$$\frac{\partial \zeta_p^s}{\partial t} = S_{2p}^s + v \nabla_p^2 \zeta_p^s \quad (61)$$

where

$$E_{z p}^{\text{ext}} = \begin{cases} 2 & \text{when } p = 0 \\ 0 & \text{otherwise} \end{cases} , \quad (62)$$

$$\nabla_p^2 = \frac{\partial^2}{\partial x^2} - k_p^2 , \quad (63)$$

$$J_{z p}^{s,c} = \frac{\partial^2 \psi_p^{s,c}}{\partial x^2} - k_p^2 \psi_p^{s,c} , \quad (64)$$

$$\zeta_p^{s,c} = \frac{\partial^2 \phi_p^{s,c}}{\partial x^2} - k_p^2 \phi_p^{s,c} , \quad (65)$$

and  $S_{1p}^c$ ,  $S_{1p}^s$ ,  $S_{2p}^c$ ,  $S_{2p}^s$  are non-linear source terms given by :

$$S_{1p}^c = -\frac{1}{2} [\phi, \psi]_{0p}^{cs} - \sum_{n=1}^{\infty} \sum_{m=1}^{\infty} \frac{1}{2} A_{p,m,n} [\phi, \psi]_{nm}^{cs} + \sum_{n=1}^{\infty} \sum_{m=1}^{\infty} \frac{1}{2} B_{p,m,n} [\phi, \psi]_{nm}^{sc} \quad (66)$$

$$S_{1p}^s = \frac{1}{2} [\phi, \psi]_{0p}^{cc} + \sum_{n=1}^{\infty} \sum_{m=1}^{\infty} \frac{1}{2} C_{p,m,n} [\phi, \psi]_{nm}^{cc} - \sum_{n=1}^{\infty} \sum_{m=1}^{\infty} \frac{1}{2} D_{p,m,n} [\phi, \psi]_{nm}^{ss} \quad (67)$$

$$S_{2p}^c = -\frac{1}{2} \left( [\phi, \zeta]_{0p}^{cs} - [\psi, J_z]_{0p}^{cs} \right) - \sum_{n=1}^{\infty} \sum_{m=1}^{\infty} \frac{1}{2} A_{p,m,n} \left( [\phi, \zeta]_{nm}^{cs} - [\psi, J_z]_{nm}^{cs} \right) + \sum_{n=1}^{\infty} \sum_{m=1}^{\infty} \frac{1}{2} B_{p,m,n} \left( [\phi, \zeta]_{nm}^{sc} - [\psi, J_z]_{nm}^{sc} \right) \quad (68)$$

$$S_{2p}^s = \frac{1}{2} \left( [\phi, \zeta]_{0p}^{cc} - [\psi, J_z]_{0p}^{cc} \right) + \sum_{n=1}^{\infty} \sum_{m=1}^{\infty} \frac{1}{2} C_{p,m,n} \left( [\phi, \zeta]_{nm}^{cc} - [\psi, J_z]_{nm}^{cc} \right) - \sum_{n=1}^{\infty} \sum_{m=1}^{\infty} \frac{1}{2} D_{p,m,n} \left( [\phi, \zeta]_{nm}^{ss} - [\psi, J_z]_{nm}^{ss} \right) \quad (69)$$

where the scripted Poisson brackets are defined by :

$$[f, g]_{mn}^{cs} \equiv \frac{\partial f_m^c}{\partial x} k_n^s g_n^s - \frac{\partial g_m^c}{\partial x} k_n^s f_n^s \quad (70)$$



and where  $A_{p,m,n}$ ,  $B_{p,m,n}$ ,  $C_{p,m,n}$  and  $D_{p,m,n}$  are elements of sparse matrices defined by:

$$A_{p,m,n} = \delta_{p,m+n} + \delta_{p,m-n} + \delta_{p,n-m} \quad (71)$$

$$B_{p,m,n} = -\delta_{p,m+n} + \delta_{p,m-n} + \delta_{p,n-m} \quad (72)$$

$$C_{p,m,n} = \delta_{p,m+n} + \delta_{p,m-n} - \delta_{p,n-m} \quad (73)$$

$$D_{p,m,n} = \delta_{p,m+n} - \delta_{p,m-n} + \delta_{p,n-m} \quad (74)$$

for which the Kronecker deltas are defined by :

$$\delta_{ij} = \begin{cases} 1 & \text{when } i = j \\ 0 & \text{otherwise} \end{cases}$$

The evaluation of the convolutions in the source terms is the most time consuming part of the calculation and since they involve a double summation for each mode at each point on the grid one could naively consider the cpu time for each convolution to be proportional to  $M^3J$  where  $M$  is the number of modes and  $J$  is the number of grid points. However, by taking advantage of the sparse matrix nature of the coefficients defined by (71),(72),(73) and (74) this is reduced to proportional to  $LJ$  where :

$$L = (M-1)(M-2) + \sum_{m=1}^M m$$

by re-ordering the arrays so that operations are only performed on non-zero elements. Equations (58) to (65) are then temporally discretized using the following two step second order accurate scheme :

$$\psi_m^{t+\Delta t/2} = \psi_m^t + \frac{1}{2} \Delta t S_{1m}^t + \frac{1}{2} \Delta t \frac{1}{S} \left( \eta J_{zm}^{t+\Delta t/2} - E_{zm}^{\text{ext}} \right) \quad (75)$$

$$\zeta_m^{t+\Delta t/2} = \zeta_m^t + \frac{1}{2} \Delta t S_{2m}^t + \frac{1}{2} \Delta t v \left( \nabla^2 \zeta \right)_m^{t+\Delta t/2} \quad (76)$$

continued overleaf...

$$\Psi_m^{t+\Delta t} = \Psi_m^t + \Delta t S_{1m}^{t+\Delta t/2} + \Delta t \frac{1}{S} \left( \eta J_{zm}^{t+\Delta t/2} - E_{zm}^{\text{ext}} \right) \quad (77)$$

$$\zeta_m^{t+\Delta t} = \zeta_m^t + \Delta t S_{2m}^{t+\Delta t/2} + \Delta t v \left( \nabla^2 \zeta \right)_m^{t+\Delta t/2} \quad (78)$$

where each equation really represents  $2M$  equations corresponding to the cos and sin components of each Fourier mode. Equations (75) and (76) determine the semi-implicit advance of the cos and sin components of each Fourier mode of  $\psi$  and  $\zeta$  by half a timestep. From these are evaluated the new half timestep values of  $J_z$  and  $\phi$  using equations (64) and (65) and then all the nonlinear source functions using equations (66) to (69) which are then used in equations (77) and (78) to explicitly advance, to second order in  $\Delta t$ , the Fourier modes of  $\psi$  and  $\zeta$  over a full timestep. The timestep is completed by then reapplying equations (64) and (65) to evaluate the Fourier components of  $J_z$  and  $\zeta$  at the new timestep.

#### The Grid :

The spatial discretisation in the x-direction was performed using a non-uniform grid with the density of grid points increased around  $x=0$  to allow adequate resolution of the resistive diffusion layer. Two types of non-uniform grid were tried. The first, which is similar to that used by Steinolfson and Van Hoven<sup>[8]</sup> is given by :

$$\Delta X_j = X_j - X_{j-1} = \begin{cases} \Delta X_{\max} \left( \frac{\Delta X_{\min}}{\Delta X_{\max}} \right)^{\left( \frac{J_M - j}{J_M} \right)} & j < J_M \\ \Delta X_{\max} & j \geq J_M \end{cases} \quad (79)$$

with the constraint that :

$$X_w - \sum_{j=1}^J \Delta X_j = 0 \quad (80)$$

This was ensured by specifying  $X_w$ ,  $\Delta X_{\min}$ ,  $J$  and  $J_M$  and determining  $\Delta X_{\max}$  to a desired accuracy by finding the root of equation (80) using the Newton Raphson method<sup>[48]</sup>. This produced a grid with grid spacing increasing in size to a maximum at  $j = J_M$  and then maintained constant over the remaining grid points. It was noticed that the sharp transition between the two sections of grid caused a small spike to form in the mode profiles at this point due to the discontinuity in the derivative that this creates. Although this appeared to be mostly transitory a second smoother-joining grid was constructed with :

$$\Delta X_j = \begin{cases} \Delta X_{\min} + (\Delta X_{\max} - \Delta X_{\min}) \frac{1}{2} \left( 1 - \cos \left[ \left( \frac{j}{J_M} \right) \pi \right] \right) & \text{for } j < J_M \\ \Delta X_{\max} & \text{for } j > J_M \end{cases} \quad (81)$$

and with the constraint, equation (80), enforced by specifying  $X_w$ ,  $\Delta X_{\min}$ ,  $J_M$  and  $J$  and evaluating  $\Delta X_{\max}$  from :

$$\Delta X_{\max} = \frac{X_w - \frac{1}{2} (J_M + 1) \Delta X_{\min}}{J - \frac{1}{2} (J_M + 1)} \quad (82)$$

### Symmetry Conditions :

For the assumed geometry and initial equilibrium the equations are symmetric in  $x$  so the solution need only be computed for region  $0 \leq x \leq X_w$  . More precisely the symmetry properties are :  $\psi(x,y) = \psi(-x,y)$  and  $\phi(x,y) = -\phi(-x,y)$ . It is also common practice to reduce the size of the calculation further by assuming the same symmetry in the  $y$ -direction, ie.  $\psi(x,y) = \psi(x,-y)$ ,  $\phi(x,y) = -\phi(x,-y)$  but this is only true for stationary solutions. To implement this in a spectral code it is only necessary to suppress the evolution of the sin components of  $\psi$  and  $J_z$  and the cos components of  $\phi$  and  $\zeta$ . However with both the cos and sin components of the variables computed cases were found for

which the y-symmetry was not maintained even when started with a stationary initial equilibrium. These cases are illustrated in section I-3. They show that it is possible to simulate coalescence and secondary regeneration of magnetic islands separately, with both symmetry constraints imposed. When, however, as in the cases described in section I-3.5, coalescence follows regeneration in the same run, the position of the x-points after regeneration are such that the coalesced state must form a quarter of a wavelength further along, thus breaking the y-symmetry condition. Section I-3.5 also shows that this sequence of events often leads to a non-stationary state by the excitation of a travelling wave, which more clearly fails to satisfy the y-symmetry condition. No examples of x-symmetry breaking were observed when the grid was expanded to cover the full distance between the walls so this symmetry constraint was retained.

#### Difference Method :

Having defined the grid it is now possible to define the difference form of the differential operators, using a Taylor expansion truncated to first order in  $\Delta x$ , by :

$$\left(\frac{\partial \psi}{\partial x}\right)_j = \frac{\psi_{j+1} - \psi_{j-1}}{x_{j+1} - x_{j-1}} \quad \text{for } 1 \leq j \leq J-1 \quad (83)$$

$$\left(\frac{\partial^2 \psi}{\partial x^2}\right)_j = \frac{\frac{\psi_{j+1} - \psi_j}{x_{j+1} - x_j} - \frac{\psi_j - \psi_{j-1}}{x_j - x_{j-1}}}{\frac{1}{2}(x_{j+1} - x_{j-1})} \quad \text{for } 1 \leq j \leq J-1 \quad (84)$$

At  $x = 0$  (i.e.  $j = 0$ ):

$$\left(\frac{\partial \psi}{\partial x}\right)_0 = \begin{cases} 0 & \text{if } \psi \text{ is even} \\ \frac{\psi_1}{x_1} & \text{if } \psi \text{ is odd} \end{cases} \quad (85)$$

$$\left(\frac{\partial^2 \psi}{\partial x^2}\right)_0 = \begin{cases} \frac{2(\psi_1 - \psi_0)}{x_1^2} & \text{if } \psi \text{ is even} \\ 0 & \text{if } \psi \text{ is odd} \end{cases} \quad (86)$$

while at  $x = X_w$  (ie.  $j = J$ ):

$$\left(\frac{\partial \psi}{\partial x}\right)_J = \left(\frac{\partial \psi}{\partial x}\right)_{J-1} - \left(\frac{x_J - x_{J-1}}{x_{J-1} - x_{J-2}}\right) \left[ \left(\frac{\partial \psi}{\partial x}\right)_{J-2} - \left(\frac{\partial \psi}{\partial x}\right)_{J-1} \right] \quad (87)$$

and similarly for  $\left(\frac{\partial^2 \psi}{\partial x^2}\right)_J$

These finite difference forms of the differential operators are employed directly in equation (64) to solve for the current. This tends to be the least accurate part of the calculation and can cause rounding error problems when too small a precision is used. To solve equation (65) for  $\phi$  is obviously not as simple and at first glance appears to require an expensive matrix inversion. This is similarly the case for equations (75) and (76) which, because of the implicit nature of their dissipative terms, form simple elliptic differential equations for  $\psi^{t+\Delta t/2}$  and  $\zeta^{t+\Delta t/2}$  similar to  $\phi^t$  in equation (65). However because all three equations can be expressed in the form :

$$-A_j U_{j+1} + B_j U_j - C_j U_{j-1} = D_j \quad (88)$$

where for equation (65) :

$$U_j \rightarrow \phi_{jm}^{t+\Delta t} \quad (89)$$

$$A_j \rightarrow A_{\phi j} = \frac{1}{\frac{1}{2}(x_{j+1} - x_{j-1})(x_{j+1} - x_j)} \quad (90)$$

$$C_j \rightarrow C_{\phi j} = \frac{1}{\frac{1}{2}(x_{j+1} - x_{j-1})(x_j - x_{j-1})} \quad (91)$$

$$B_j \rightarrow B_{\phi jm} = A_{\phi j} + C_{\phi j} + k_m^2 \quad (92)$$

$$D_j \rightarrow \begin{cases} D_{\phi jm}^{c t} = -\zeta_{jm}^{c t} \\ D_{\phi jm}^{s t} = -\zeta_{jm}^{s t} \end{cases} \quad (93)$$

and for equation (75) :

$$U_j \rightarrow \psi_{j,m}^{t+\Delta t/2} \quad (94)$$

$$A_j \rightarrow A_{\psi j} = A_{\phi j} \eta_j \frac{1}{S} \quad (95)$$

$$C_j \rightarrow C_{\psi j} = C_{\phi j} v \quad (96)$$

$$B_j \rightarrow B_{\psi jm} = A_{\psi j} + C_{\psi j} + k_m^2 \eta_j \frac{1}{S} + \frac{2}{\Delta t} \quad (97)$$

$$D_j \rightarrow \begin{cases} D_{\psi jm}^{c t} = S_{1jm}^{c t} + \frac{2}{\Delta t} \psi_{jm}^{c t} - E_{z m}^{ext} \\ D_{\psi jm}^{s t} = S_{1jm}^{s t} + \frac{2}{\Delta t} \psi_{jm}^{s t} \end{cases} \quad (98)$$

and for equation (76) :

$$U_j \rightarrow \zeta_{j,m}^{t+\Delta t/2} \quad (99)$$

$$A_j \rightarrow A_{\zeta j} = v A_{\phi j} \quad (100)$$

$$C_j \rightarrow C_{\zeta j} = v C_{\phi j} \quad (101)$$

$$B_j \rightarrow B_{\zeta jm} = A_{\zeta j} + C_{\zeta j} + k_m^2 v + \frac{2}{\Delta t} \quad (102)$$

$$D_j \rightarrow \begin{cases} D_{\zeta jm}^{c t} = S_{2jm}^{c t} + \frac{2}{\Delta t} \zeta_{jm}^{c t} \\ D_{\zeta jm}^{s t} = S_{2jm}^{s t} + \frac{2}{\Delta t} \zeta_{jm}^{s t} \end{cases} \quad (103)$$

they can be solved numerically using the well known algorithm for tridiagonal systems<sup>[49,50,51]</sup>. Let :

$$U_j = E_j U_{j+1} + F_j \quad (104)$$

Substituting this algorithm evaluated for  $U_{j-1}$  into equation (88) yields :

$$U_j = \left[ \frac{A_j}{B_j - C_j E_{j-1}} \right] U_{j+1} + \left[ \frac{D_j + C_j F_{j-1}}{B_j - C_j E_{j-1}} \right] \quad (105)$$

and comparison with equation (104) shows that  $E_j$  and  $F_j$  are determined from the recurrence relations :

$$E_j = \frac{A_j}{B_j - C_j E_{j-1}} \quad (106)$$

$$F_j = \frac{D_j + C_j F_{j-1}}{B_j - C_j E_{j-1}} \quad (107)$$

The computational procedure involves two sweeps across the grid, sweeping first through the grid from  $x=0$  to  $x=X_w$  to calculate  $E_j$  and  $F_j$  using (106) and (107), then a sweep back through the grid from  $x=X_w$  to  $x=0$  to calculate  $U_j$  using equation (104).

#### Boundary Conditions :

This requires boundary conditions to be specified for  $E_0$  and  $F_0$  at  $x=0$  as well as those for  $U_j$  at  $x=X_w$ . To do this we make use of the symmetry conditions which apply at  $x=0$ . When  $U_j$  corresponds to an odd function, like  $\phi$  or  $\zeta$ , then the condition is simply  $U_0 = 0$  which from equation (104) implies that  $E_0 = 0$  and  $F_0 = 0$ . However, it is not so easy to determine an accurate boundary condition when  $U_j$  corresponds to an even function like  $\psi$  since  $U_0$  is then not necessarily a fixed value. We could use the condition on its derivative :

$$\text{ie.} \quad \left[ \frac{\partial U_j}{\partial x} \right]_{x=0} = 0$$

to provide the approximate condition :  $\psi_1 = \psi_2$  which from equation (104) implies  $E_0 = 1$  and  $F_0 = 0$ . However it is possible to avoid the error that this introduces by instead temporarily expanding the grid out to the second wall at  $x=-X_w$  just for the calculation of

$\psi$  so that the exact boundary condition  $\psi_{-J} = 0$  can be used to give  $E_{-J} = 0, F_{-J} = 0$ . This doubles the cpu time for calculating  $\psi_{jm}$  but because this method takes advantage of the tridiagonal nature of equation (75) to avoid expensive matrix inversions, it only varies as MJ, making it insignificant in comparison to the time required to calculate the convolutions in the source functions which vary roughly as  $M^2J$ . In summary the boundary conditions in difference form are :

$$\begin{aligned}\psi_J &= \psi_{-J} = F_{\psi_{-J}} = E_{\psi_{-J}} = 0 \\ \phi_J &= \phi_0 = F_{\phi_0} = E_{\phi_0} = 0 \\ \zeta_J &= \zeta_0 = F_{\zeta_0} = E_{\zeta_0} = 0\end{aligned}\tag{108}$$

#### The Initial Equilibrium :

The initial equilibrium given in equation (31) of the previous section becomes :

$$\begin{aligned}\psi_{jm}^c &= 2 \ln \left( \frac{\cosh(x_j)}{\cosh(X_w)} \right) \\ \psi_{jm}^s &= 0\end{aligned}\tag{109}$$

#### The Initial Perturbation :

To begin the calculation an initial perturbation must be applied to one of the dependent variables. The precise choice of perturbation should not be important in determining the final nonlinear state as long as the perturbation is small and all the Fourier modes are excited. For most runs this was achieved by triggering the fundamental sine Fourier mode of  $\phi$  with a profile closely approximating its linear shape given by :

$$\phi_{j1}^s = e^{-C_0} x_j \left( e^{-10|x_j|} - e^{-10X_w} \right)\tag{110}$$

The corresponding cosine Fourier mode,  $\phi_{j1}^c$ , was also initialized with a much smaller uniform amplitude in order to break the symmetry to allow for the possibility of asymmetric nonlinear behaviour.



### Diagnostics :

The progress of the instability was followed to saturation by monitoring the value of several diagnostic quantities. The reconnected flux across the tearing or neutral line defined by :

$$\Delta\Psi = \int_0^{L_p} | B_x(0,y,t) | dy \quad (111)$$

and its corresponding exponential growth rate :

$$\gamma = \frac{1}{\Delta\Psi} \frac{\partial(\Delta\Psi)}{\partial t} \quad (112)$$

were used to provide a measure of the overall nonlinear reconnective processes occurring during a simulation while the spatial behaviour of the resultant magnetic islands was determined through the evaluation of the position of the x and o-points along the tearing axis by :

$$\begin{aligned} Y_x &= Y\left( \psi_{\min}(x=0) \right) \\ Y_o &= Y\left( \psi_{\max}(x=0) \right) \end{aligned} \quad (113)$$

and the maximum island half-width by :

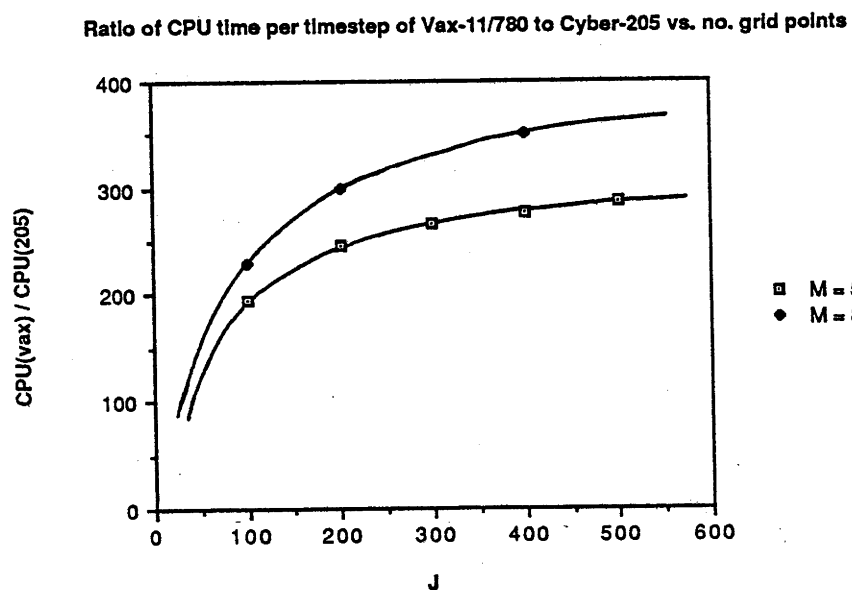
$$W = 2 x\left( \psi = \psi(0, Y_x), Y_o \right) \quad (114)$$

The spectral behaviour was also monitored by recording the amplitudes of the first four Fourier modes of  $\psi$  on the neutral line while a general data dump of all the Fourier modes of  $\psi$ ,  $\phi$ ,  $J_z$  and  $\zeta$  over the whole grid was made periodically throughout each run to provide a more detailed picture as well as for check pointing the calculation. The simulation could then be restarted near an interesting stage of development to obtain a more detailed description of the event.

### Performance :

The code was written on a Vax 11/780 and then adapted to run on a Cyber-205 super-computer where full use was made of its vector capability. The faster clock on the Cyber-205 already provided an increase in speed over the Vax 11/780 of roughly 20 times when operated in scalar mode. With most of the inner grid loops vectorized, and some of the Fourier mode loops vectorized, an increase in excess of 400 times the speed of a Vax 11/780 was achieved for runs with 100 grid points and 30 Fourier modes, corresponding to a 20 fold improvement due to vectorization. This was possible despite several loops being recursive, and hence unvectorizable, as most of the time is spent evaluating the convolutions, for which the large inner grid loop is vectorizable, although the higher level loops are not because of their sparse matrix nature. The plot below shows the ratio of the cpu time per timestep for the Vax-11/780 to that for the Cyber-205 versus the number of grid points, corresponding to some early runs made with only 5 and 8 Fourier modes. Automatic mode adjustment, see section I-2.3, was introduced to streamline the Fourier mode usage so that the number of modes varied considerably during each run depending on  $S$ ,  $v$ ,  $X_w$ , and  $L_p$ . The time taken to reach saturation also depended on these parameters, especially  $S$ , so that actual run times varied from 5 minutes to over an hour.

Fig.4



### I-2.3 Convergence

The x-dependence of the dependent variables  $\psi$ ,  $\phi$ ,  $J_z$  and  $\zeta$  is discretely sampled on a non-uniform grid using the linear profiles of  $\phi$  as a guide<sup>[8]</sup> to the optimal size to make the grid spacings, which must be small enough to resolve the resistive diffusion layer but large enough to avoid unnecessary CFL restrictions on the timestep (see sec.I-2.4). On the other hand, the y-dependence, which is parallel to the neutral line, is sampled through a finite number,  $M$ , of Fourier modes to take advantage of the assumption that only a few of them are necessary for the tearing mode solutions to be well approximated. This assumption was expected to make the calculation much cheaper than using a 2-D grid finitely differenced in both directions.

In practice the assumption holds very well for  $\psi$  as can be seen in fig.4(a) showing the relative amplitudes of the Fourier modes at saturation for a typical run. However, for the other three dependent variables :  $\phi$ ,  $J_z$  and  $\zeta$  many more modes are required with the vorticity always requiring the most for convergence, see figs.4(b),(c) and (d). The main problem, however, arises from the fact that, in the absence of significant dissipation, convergence of the vorticity is extremely slow, requiring an impractically large number of modes for convergence. This is particularly serious given that the cpu time increases roughly with the square of the total number of modes. By including significant viscous damping, however, convergence can be attained within a reasonable number of modes, see fig.5, and is the main reason for including the viscosity term in the equations.

The amount of viscosity required ( $\nu \sim 0.01$ ) is much larger than would exist in most magnetically confined plasmas of interest but this is justified by the observation that, even in the absence of the usual viscous forces, there appears to be a damping effect produced by a micro-turbulent viscosity mechanism associated with high order mode activity. In short it was found that in an unconverged simulation deficient of high order modes, with negligible viscosity ( $\nu = 0.0001$ ), anomalous secondary island activity was

Fig.5(a)

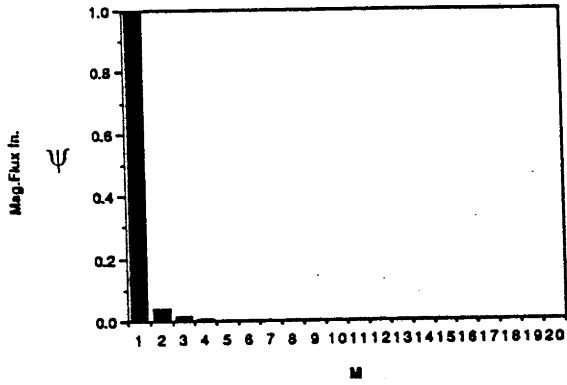


Fig.5(b)

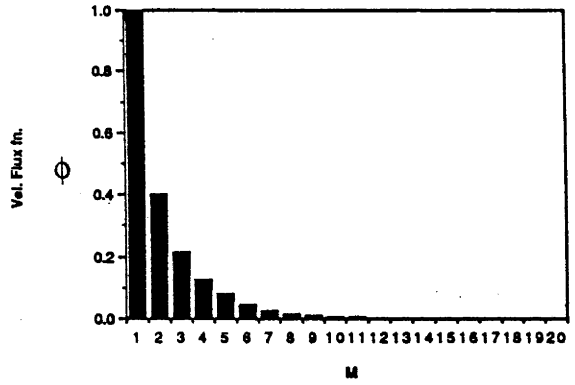


Fig.5(c)

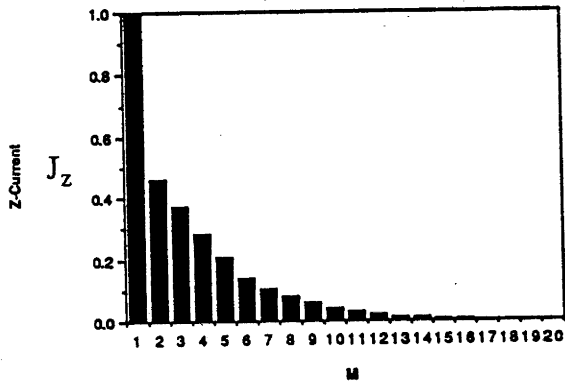


Fig.5(d)

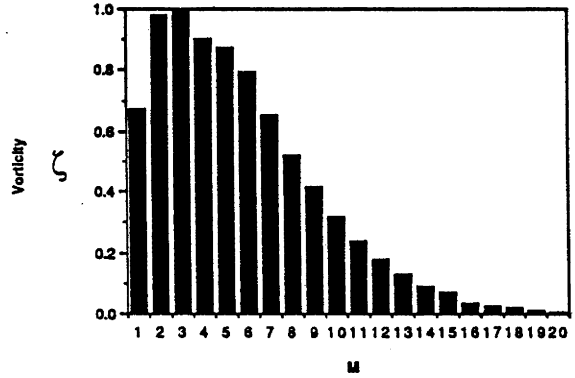
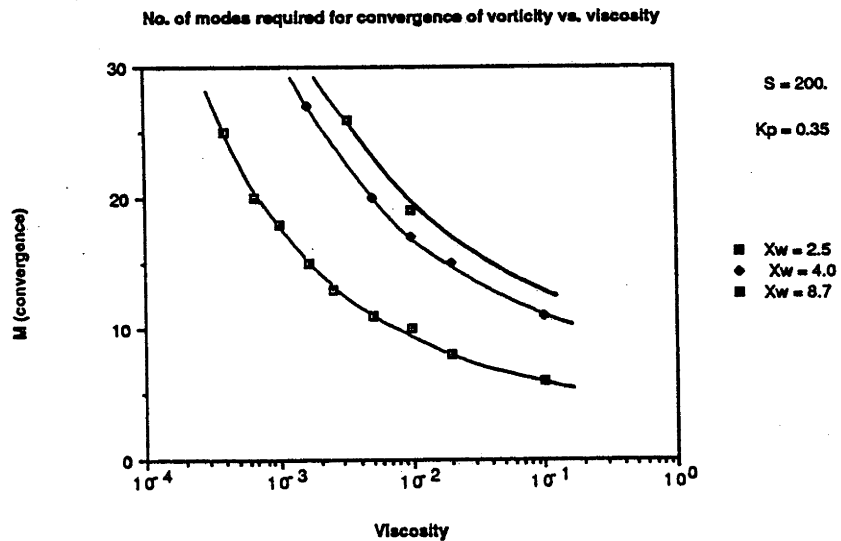


Fig.6



observed which did not occur when either the viscosity was increased (which reduced the number of modes required for convergence) or more interestingly when the number of Fourier modes was increased even though still not sufficient for convergence. The extra high order modes seem to damp out the anomalous behaviour, and the affect is probably related to the hyper-resistivity effect discussed by Strauss <sup>[52]</sup>. Fig.5 shows also that the required number of Fourier modes increases with the conducting wall separation indicating that the turbulent high order mode activity is also reduced by physically constraining the plasma.

During a simulation run the number of Fourier modes needed for convergence can vary quite a lot depending on what is happening and will obviously increase when spatially complex transformations are occurring. To minimize the mode usage during a run a routine was included in the code which dynamically adjusted the number of modes, up or down, to just maintain convergence of the vorticity - this being the slowest variable to converge. Convergence was tested by comparing the amplitudes of the Mth and (M-1)th Fourier modes with the dominant mode with  $m = L$  as follows :

$$\text{Let } \alpha_M = \frac{|\zeta_{jM}|_{\text{MAX}}}{|\zeta_{jL}|_{\text{MAX}}}$$

$$\text{and } \alpha_{M-1} = \frac{|\zeta_{jM-1}|_{\text{MAX}}}{|\zeta_{jL}|_{\text{MAX}}}$$

then the convergence is tested every couple of timesteps with the conditions for adjusting the number of modes defined as follows :

If  $\alpha_M > C_F$  then not converged so  $M_{\text{new}} = M + 1$

If  $\left\{ \begin{array}{l} \alpha_M < C_F \\ \alpha_{M-1} > C_F \end{array} \right\}$  then just converged so  $M_{\text{new}} = M$

continued overleaf...

$$\text{If } \left\{ \begin{array}{l} \alpha_M < C_F \\ \alpha_{M-1} < C_F \end{array} \right\} \text{ then over converged so } M_{\text{new}} = M - 1$$

where  $C_F$  is the convergence factor usually set as  $C_F = 0.01$ . This simple method for adjusting the timestep worked quite well when the dominant mode was  $L=1$  and still worked well even when  $L$  increased to a higher value later in the simulation. External adjustment was, however, required when the initial value of  $L$  was greater than 1 since then  $\alpha_M$  could be  $< C_F$  with  $\alpha_{M+1} > C_F$ . The situation was remedied by including more modes in the comparison. Using this technique the mode usage could be tracked throughout a simulation to expose the mode intensive stages. In general, with  $\nu = 0.01$ , as few as two modes were utilized during the linear stage while up to 30 modes were required during a particularly active nonlinear stage and often half this number at saturation.

The coalescence of magnetic islands is the most mode intensive part of the simulation for the obvious reason that many Fourier modes are required to resolve the temporary neutral layer that forms between the islands with an orientation perpendicular to the original neutral line. The non-uniform grid is of no help here since the high velocity gradients are now in the  $y$ -direction. The semi-spectral code is designed to be most effective for cases with boundary layers forming along the  $y$ -axis and so is clearly not suited to a study of coalescence, especially at high Lundquist numbers where the boundary layers are even narrower. For this reason we have restricted our study of coalescence to the case with  $S = 200$ , which is low enough to allow the coalescence-neutral layer to be resolved with an acceptable number of modes.

## I-2.4 Numerical Stability

For a completely explicit time advance the condition on numerical stability is given by the Courant-Friedrichs-Lewy (CFL) condition <sup>[50,51,53]</sup> which essentially requires the grid velocity, defined by  $\Delta x/\Delta t$ , to be greater than the fastest propagation velocity,  $V_{\max}$ , allowed by the equations.

$$\text{ie.} \quad \Delta t \leq \frac{\Delta x}{V_{\max}} \quad (115)$$

The problem with using an explicit technique for solving the resistive MHD equations arises from the presence of widely disparate time scales :

$$\text{i.e.} \quad V_{\text{Fast Magnetosonic}} \gg V_{\text{Shear Alfvén}} \gg V_{\text{Resistive}}$$

Our interest is in the evolution of disturbances occurring on the slow resistive time scale, but the size of the timestep in the full MHD equations would be determined through the CFL conditions by the fast compressional (magnetosonic) motion. The restriction is not as severe for the reduced equations since the incompressibility condition removes the fast compressional motion leaving the slower Shear Alfvén motion to determine the timestep. Fully implicit techniques which allow a disturbance to traverse the whole grid within one timestep do not suffer from the CFL constraint but are usually much more complicated to solve. The semi-implicit approach used here is a compromise designed to take advantage of the best attributes of both techniques. The explicit time advance of the nonlinear terms makes it as fast as completely explicit methods while the implicit time advance of the linear dissipative terms provides the expectation for improved numerical stability. The expectation is justified by the absence of any grid spacing dependence in the stability condition given by:

$$\Delta t \leq \frac{2}{\mathbf{k} \cdot \mathbf{B}_0} \leq \frac{2}{M k_1} \quad (116)$$

which was derived for the semi-implicit scheme of equations (75) to (78) using the standard von Neumann numerical stability analysis as in references [54] and [53].

This stability criterion really only applies to the linear part of the evolution and in practice the stability was found to vary as a function of the regime of operation. In the linear and weakly non-linear stages the numerical integrity was upheld for quite large timesteps ( $\Delta t \sim 2$ ) but during the fully non-linear stage the calculation was found to suffer from a weaker but temperamental form of the CFL condition. The dependence of numerical stability on the number of modes,  $M$ , was not observed, but instead, all instances of numerical instability were removed by either reducing the timestep or by increasing the size of the minimum grid spacing. The major consequence of this was that simulations were limited to cases with low Lundquist number. The reasons are twofold. Firstly, since the width of the resistive diffusion layer increases with resistivity, an increase in the Lundquist number will make it narrower and hence smaller grid spacings will be required in that section of the grid to resolve it. Because of the nonlinear CFL condition this also means using a smaller timestep to maintain stability. Secondly the growth rate of the tearing mode decreases with Lundquist number so that longer runs are needed to reach saturation. Since

$$N = \frac{T_{\text{sat}}}{\Delta t} \quad (117)$$

where  $N$  is the number of timesteps,  $\Delta t$  the timestep and  $T_{\text{sat}}$  the physical time required to reach saturation, the combined effect is to increase the total number of timesteps and hence the cpu time. This means there is an upper limit on the Lundquist number beyond which the calculation becomes prohibitively expensive and where a fully implicit approach would probably be more economical. Given this constraint, runs were made for values of the Lundquist number ranging from  $S = 10^2$  to  $S = 10^4$ .

Initially an attempt was made to include automatic timestep adjustment in order to work as closely as possible to the stability threshold and hence maximize the timestep. The timestep was adjusted up or down on the basis of keeping the incrementation of the highest Fourier mode of the current constant each timestep. This allowed larger timesteps to be used in the early stages but during active periods of the nonlinear stage the timestep



was forced down to unreasonably small values ( $\Delta t \leq 0.01$ ). It was found to be more efficient to operate further away from the stability threshold by using a constant, more conservative value for the timestep ( $\Delta t \sim 0.2$ ) and so the automatic timestep adjuster was scrapped.

Harned and Kerner<sup>[34]</sup> have since developed an alternative semi-implicit method for advancing the full set of MHD equations by adding a new term implicitly and then subtracting it explicitly from the equations to obtain numerical stability. Two semi-implicit terms of this type are included to remove both the fast magnetosonic and the shear Alfvén restrictions but since the first mode is already removed from the reduced equation we shall only consider the latter.

To derive the functional form of the semi-implicit term for the elimination of the Shear Alfvén timescale they linearize the incompressible MHD equations assuming uniform magnetic field, density and pressure to obtain :

$$\frac{\partial^2 \mathbf{V}}{\partial t^2} = \left[ \nabla \times \nabla \times (\mathbf{V} \times \mathbf{B}_0) \right] \times \mathbf{B}_0 \quad (118)$$

The term on the right hand side of the equation is then considered to be the appropriate form for the semi-implicit term with  $\mathbf{B}_0$  replaced by a vector quantity with constant coefficients :

$$\text{ie.} \quad \mathbf{C}_0 = C_x \hat{e}_x + C_y \hat{e}_y + C_z \hat{e}_z \quad (119)$$

to give:

$$\left[ \nabla \times \nabla \times (\mathbf{V} \times \mathbf{C}_0) \right] \times \mathbf{C}_0 \quad (120)$$

The term is then added implicitly and then subtracted explicitly from the equation for the velocity time advance. This was shown, using a stability analysis, to provide unconditional stability if  $C_x \geq B_x$ ,  $C_y \geq B_y$  and if terms of the form  $C_i C_j$  with  $i \neq j$  are eliminated. With appropriate values of  $C_x$  and  $C_y$  the numerical stability is maintained for timesteps as large as  $\Delta t = 200$  but, since the implicit and explicit parts of the new term

only exactly cancel in the limit that  $\Delta t \rightarrow 0$ , the accuracy becomes the limiting factor in the timestep. Unfortunately it was found that poor accuracy occurred for timesteps not much larger than that allowed by the Shear Alfvén CFL condition ( $\Delta t \sim 0.24$ ) although it was suggested that this could be remedied by using a 2nd or higher order accurate timestepping scheme. The technique also introduces damping of the fluid motion which increases with the value of the timestep. Despite this we shall consider how it could be implemented here. To apply this technique to the reduced equations the semi-implicit term must be modified to fit into the equation for the time advance of the vorticity of equation (26). To do this we operate on equation (118) with  $\hat{e}_z \cdot \nabla \times$  to obtain:

$$\frac{\partial^2 \zeta}{\partial t^2} = \hat{e}_z \cdot \nabla \times \left[ \nabla \times \nabla \times (\mathbf{V} \times \mathbf{B}_0) \right] \times \mathbf{B}_0 \quad (121)$$

So the new semi implicit term takes the form :

$$\hat{e}_z \cdot \nabla \times \left[ \nabla \times \nabla \times (\mathbf{V} \times \mathbf{C}_0) \right] \times \mathbf{C}_0 \quad (122)$$

To simplify this we substitute in the equation (19) for  $\mathbf{V}$  in terms of  $\phi$  and  $V_z$  and separate out there dependence into two separate terms given by :

$$\begin{aligned} & \hat{e}_z \cdot \nabla \times \left( \mathbf{C}_0 \times \left[ \nabla \times \nabla \times (\mathbf{C}_0 \times (\hat{e}_z \times \nabla \phi)) \right] \right) \\ & + \hat{e}_z \cdot \nabla \times \left( \mathbf{C}_0 \times \left[ \nabla \times \nabla \times (V_z (\mathbf{C}_0 \times \hat{e}_z)) \right] \right) \end{aligned} \quad (123)$$

After some algebra the term involving  $V_z$  vanishes while the other reduces to :

$$\mathbf{C}_0 \cdot \nabla \left( \nabla^2 (\mathbf{C}_0 \cdot \nabla \phi) \right) - C_z \hat{e}_z \cdot \nabla \left( \nabla^2 (\mathbf{C}_0 \cdot \nabla \phi) \right) \quad (124)$$

or more simply :

$$\begin{aligned} & C_x^2 \frac{\partial^2}{\partial x^2} \nabla^2 \phi + C_x C_y \frac{\partial^2}{\partial x \partial y} \nabla^2 \phi \\ & + C_y^2 \frac{\partial^2}{\partial x^2} \nabla^2 \phi + C_x C_y \frac{\partial^2}{\partial y \partial x} \nabla^2 \phi \end{aligned} \quad (125)$$

Removing terms of the form  $C_i C_j$  where  $i \neq j$  and noting that  $\zeta = \nabla^2 \phi$ , (125) becomes :

$$C_x^2 \frac{\partial^2 \zeta}{\partial x^2} + C_y^2 \frac{\partial^2 \zeta}{\partial y^2} \quad (126)$$

and if we then set

$$C_x = C_y = \sqrt{\nu}$$

this then becomes

$$\nu \nabla^2 \zeta \quad (127)$$

which means that the Harned-Kerner semi-implicit term for the reduced equations is essentially equivalent to the viscosity term of equation (26). This would perhaps explain the damping effect that they observed when the timestep was increased since at large timesteps the cancellation of the semi-implicit terms would be less complete, allowing their viscous nature to be felt more strongly. In any case, since a viscosity term was already included in our equations semi-implicitly, we considered it redundant to apply it again in the manner suggested by Harned and Kerner, especially since the accuracy of the method was still in question.

### I-3.1 Simple Nonlinear Tearing Mode Evolution

In this numerical investigation it will become apparent that the non-linear behaviour of the tearing mode on a current sheet can vary greatly from one region of parameter space to another. For the region of parameter space investigated, the most striking changes were observed to occur as a function of the periodicity length,  $L_p$ , while only relatively cosmetic changes were evident for variations in  $S$ ,  $\nu$ , and  $X_w$ . In this section we will briefly describe the simple or classical tearing mode evolution that occurs for small  $L_p$  and progress, in later sections, to the more complex behaviour that occurs for larger values.

A typical simple tearing mode evolution complete to saturation is recorded in fig.7 by the time evolution of the reconnected flux and its corresponding growth rate for the case with  $K_p = 0.35$  ( $L_p = 2\pi/0.35$ ),  $S = 200.0$ ,  $\nu = 0.01$  and  $X_w = 4.0$ . It shows : a distinct linear phase marked by a steady exponential growth rate; a relatively sharp transition to the slower algebraic growth of the non-linear phase and a rounding off with an overshoot of the reconnected flux as the mode saturates into the simple magnetic island state shown in fig.8(a).

The linear growth rate is slightly lower than that computed by Steinolfson and Van Hoven [8] because of the relatively large value of the viscosity and the closeness of the conducting walls which tend to reduce the rate of reconnection.

For much of the nonlinear phase the reconnected flux can be seen to increase almost linearly with time, although during the early nonlinear or weakly nonlinear stage the growth appears to have the  $t^2$  variation predicted by Rutherford [9]. Rutherford's analysis applies only to constant -  $\psi$  modes but the behaviour shown above was qualitatively the same in all simulations irrespective of what type of linear mode they arose from and includes simulations made with  $S$  and  $K_p$  in the ranges :  $10^2 < S < 10^4$  and  $0.75 < K_p < 0.1$ . In fact, despite the short wavelength, the low value of  $S$  in the above example makes it a nonconstant -  $\psi$  mode. It has been noted [8], however, that the effect of having the

Fig.7

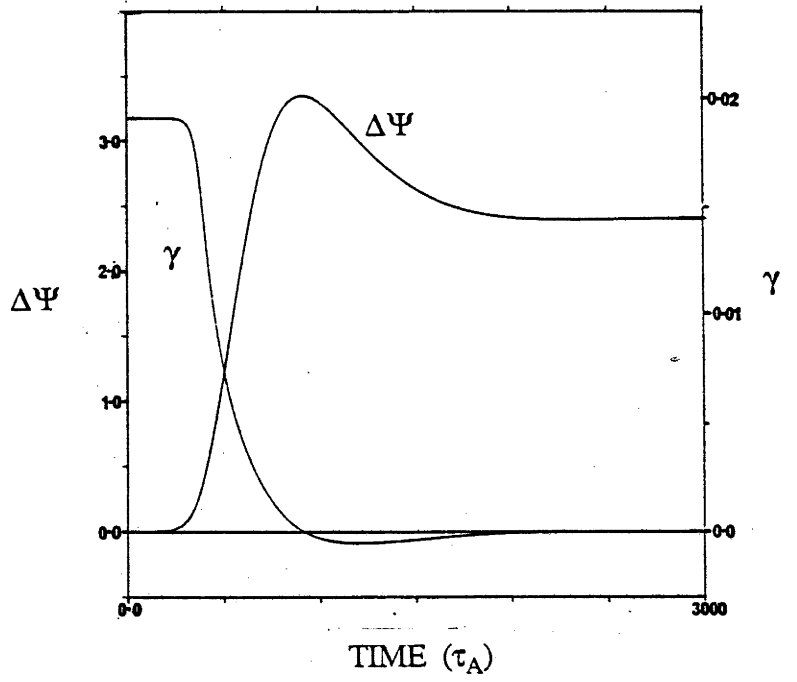
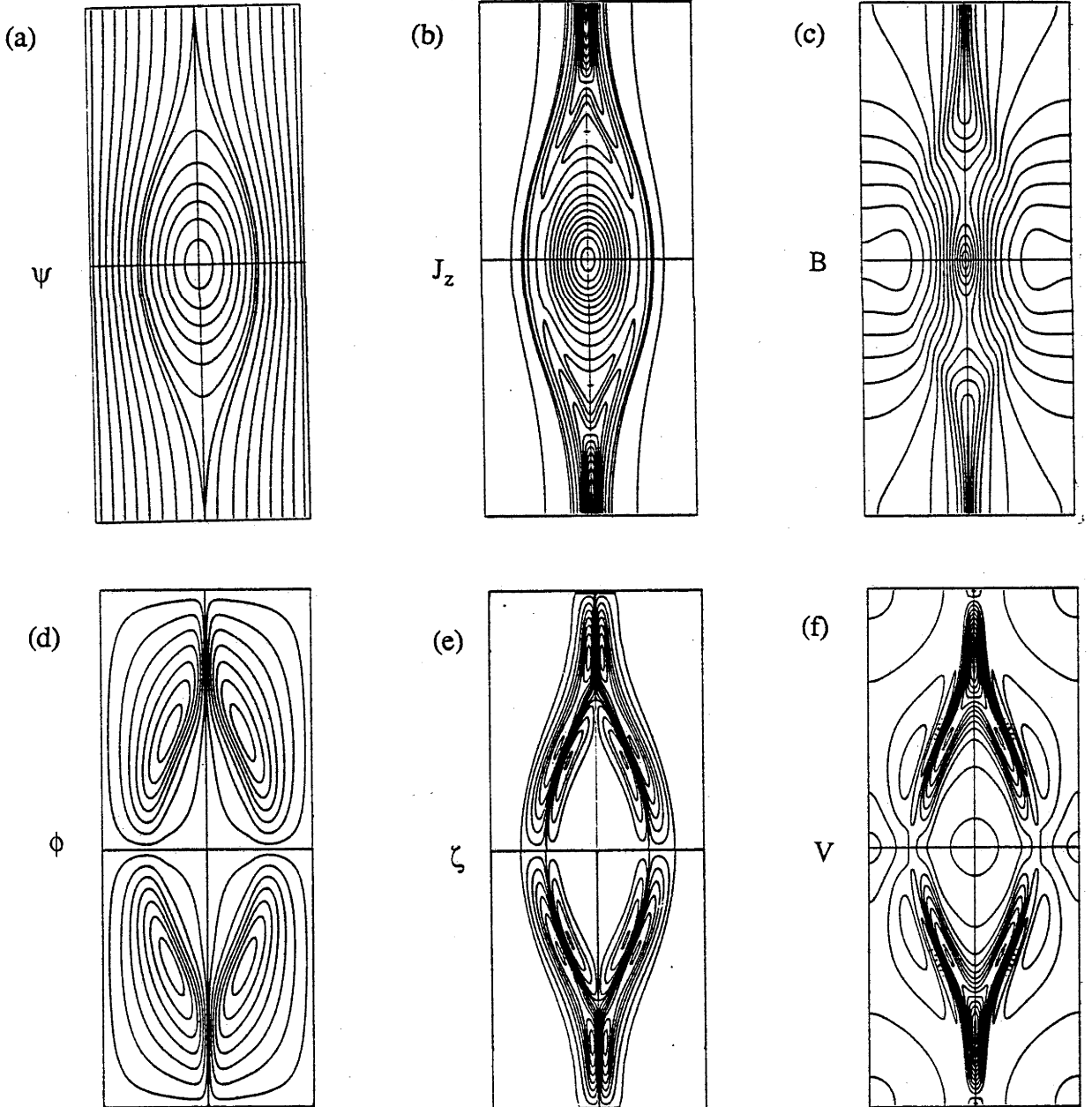


Fig.8



conducting walls close together is to make nonconstant -  $\psi$  modes look like constant -  $\psi$  modes so it could be argued that this is the case here since the half wall separation is only  $X_w = 2.5$ . Even so, simulations made with  $X_w = 12.0$  which, as shown in the next section, is large enough for wall effects to be negligible, only increases the magnitude of the growth rate and the amplitude reached at saturation without changing the qualitative variation of the reconnected flux with time.

In these simulations the initial equilibrium is maintained by an applied electric field and nonuniform resistivity whereas Steinolfson and Van Hoven <sup>[29]</sup> impose a constant background field and allow zero order variations around it. Although quite different, both schemes should allow saturation of the tearing mode and so the absence of saturation in their simulations is most likely due to not running them long enough. To see this, note that for a run made with  $S=200$  it took roughly  $t \approx 1000 \tau_A$  to reach saturation whereas their simulation, close to this value of  $S$ , was only run for  $t = 600 \tau_A$ . The reconnection rate is slower at higher  $S$  so that for  $S = 10^4$  it took  $t \approx 40,000 \tau_A$  whereas their run time at this higher value of  $S$  was only  $t = 3000 \tau_A$ . The difference cannot be accounted for by the smaller growth rate in our runs resulting from the finite values of  $\nu$  and  $X_w$ .

The size of the overshoot during the saturation phase of the evolution depends upon how constrained the plasma is, since it can be made smaller by decreasing the dimensions of the system through  $L_p$  and  $X_w$  or by increasing the viscous damping through  $\nu$ . A very similar evolution of the reconnected flux was calculated analytically by Kulsrud and Hahm <sup>[55,56]</sup> for a simple model of forced reconnection using a boundary layer analysis. The bulk of the variation was calculated using the constant -  $\psi$  approximation which predicts an overshoot and saturation remarkably similar to that shown here.

The other contour plots in fig.8 show the corresponding spatial variations of  $\phi$ ,  $J_z$ ,  $\zeta$ ,  $|B|$  and  $|V|$  at saturation. Fig.8(d) shows that the vortical flow associated with the reconnection process still persists after saturation, although with a smaller velocity

gradient near the x-points. This is, perhaps, not surprising given that the applied electric field and non-uniform resistivity were only set up to support the original current sheet. The difference between the magnetic island configuration and the original equilibrium therefore requires continued reconnection to balance the flux losses due to resistive decay. The process would be indirectly driven by the z-electric field through its maintenance of the bulk current channel. On the other hand one might ask whether the finite vortical flows at saturation could be avoided with a more judicious arrangement of the equilibrium quantities. For example since the resistivity is dependent only on the electron temperature, which tends to equilibrate on constant flux surfaces, it would be more realistic to set  $\eta = \eta(\psi)$  rather than  $\eta = \eta(x)$ . Both cases would be identical for the initial equilibrium but only for the former case is it possible to obtain a flowless equilibrium. To see this set  $\partial/\partial t = 0$ ,  $\phi = 0$  and  $\zeta = 0$  so that equation (23) reduces to :

$$\hat{e}_z \cdot (\nabla J_z \times \nabla \psi) = 0 \quad (128)$$

which implies that  $J_z = J_z(\psi)$ , while equation (21) becomes :

$$\eta = E_z^{\text{ext}} / J_z \quad (129)$$

Equations (128) and (129) can then only be satisfied if  $\eta = \eta(\psi)$  Therefore if we were only interested in flowless saturated island states we need only consider solutions of the equation :

$$\nabla^2 \psi = \frac{1}{\eta(\psi)} \quad (130)$$

and not trouble with the full set of reduced equations. If we then use the resistivity variation suggested in section I-2.1, equation (32), this reduces to a Liouville type equation <sup>[57]</sup> given by :

$$\nabla^2 \psi = e^{-2\psi} \quad (131)$$

which is similar to the equation satisfied by the flowless exact island equilibrium given by:

$$\nabla^2 \psi = (1 - \epsilon^2) e^{-2\psi} \quad (132)$$

where  $\epsilon$  is a dimensionless parameter related to the island width and defined by equation (133). Unfortunately, this class of island equilibria is restricted to a single periodicity length, i.e.  $K_p = 1$ , which, as shown in section I-3.4 is too large for the state to be reachable via the tearing mode and so is of less relevance here.

As a matter of interest it may be possible to solve equation (132) analytically with  $X_w = \infty$  using Backlund Transformations<sup>[57]</sup>, although ultimately it would be useful to redo the simulations using a more general form of  $\eta = \eta(\psi)$  with say an ADI type code<sup>[47]</sup> to determine the reality of the finite vortical flow. The numerical difficulties of setting  $\eta = \eta(\psi)$ , discussed in section I-2.1 prevent us from trying this here. It is, however, by no means certain that it would result in a flowless island equilibrium at saturation anyway. In fact Hesse and Schindler<sup>[58]</sup> found, using bifurcation theory techniques, that island solutions of (132) are unstable and therefore would not evolve from the time dependent equations.

Moving on to fig.8(b) we see that the saturated current distribution has sharp peaks over the x-points as well as the broader ones over the o-points. This can be seen more clearly in fig.9 which displays a 3-D perspective of the current distribution at several different times during the growth of the tearing mode for the case with  $K_p = 0.35$ ,  $S = 10,000$ ,  $X_w = 5.0$  and  $\nu = 0.01$ . These show that the shape of the current distribution is not always the same during the non-linear development of the tearing mode. Initially the current sheet peaks at the x-points and broadens around the o-points. During the early stages there is actually a trough in the current at the o-points which only develops into a broad peak as the tearing mode approaches saturation. The significance of these observations will be made apparent later, but it should be pointed out that since flowless island equilibria must have  $J_z = J_z(\psi)$  they would not have the x-point current spikes shown here.

This description of a tearing mode evolution is characteristic of all simulations made with a short periodicity length ( $K_p \geq 0.265$  for  $S = 200$ . ) so the changes in magnitude of



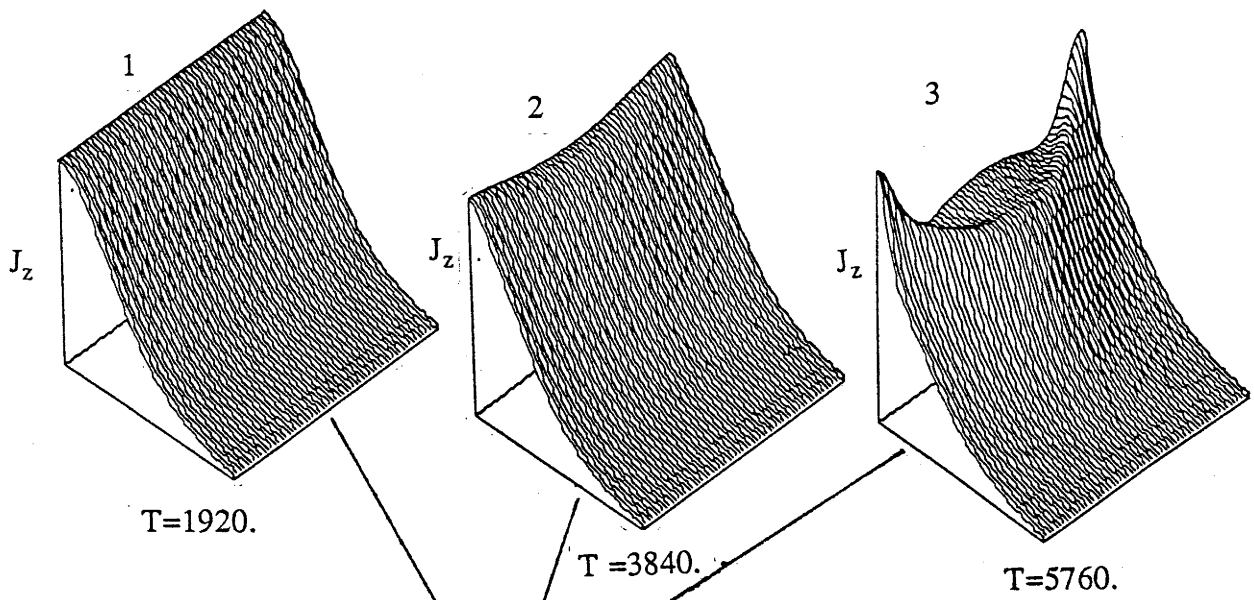
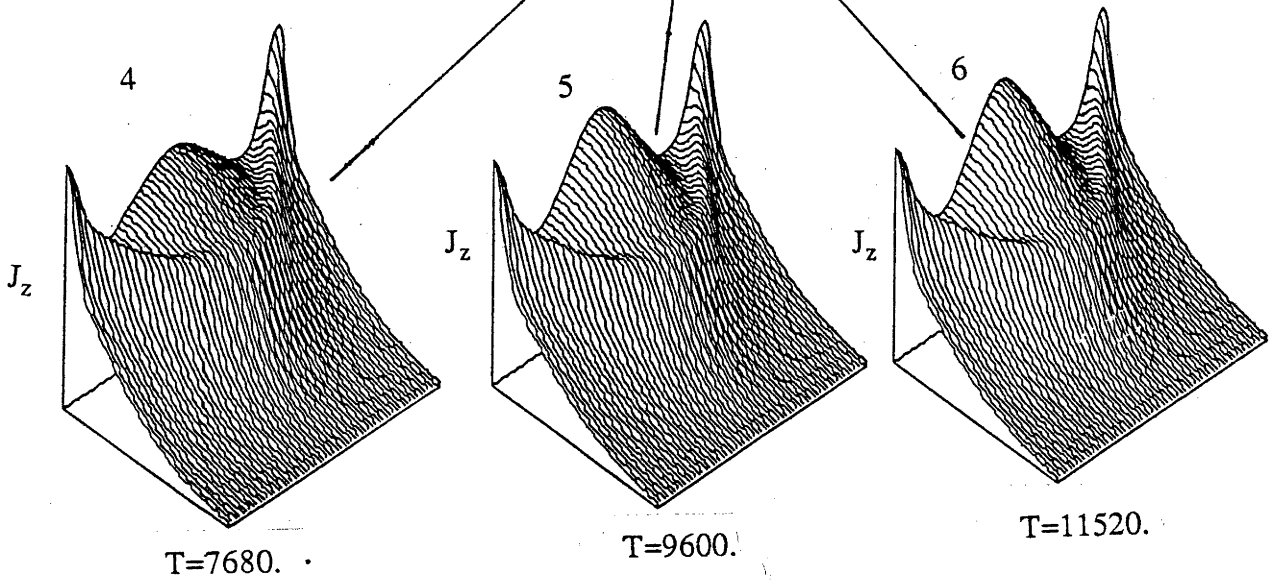
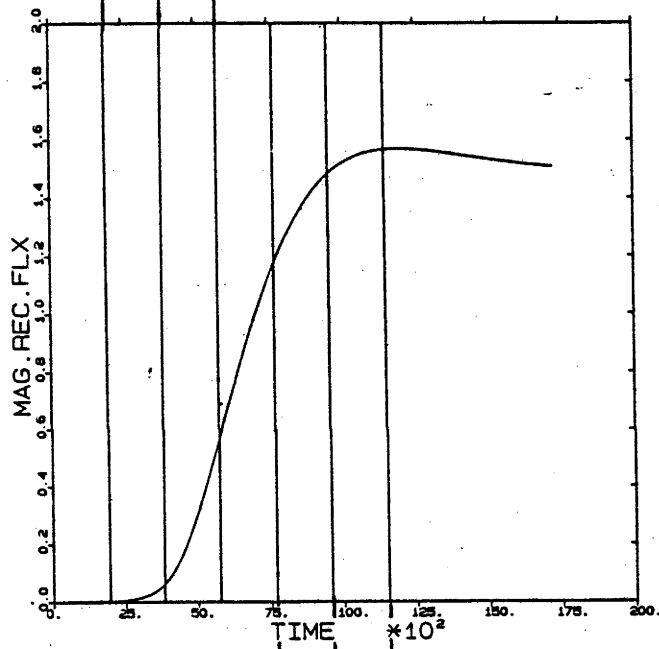


Fig.9



$\psi$ ,  $\phi$ ,  $J_z$  and  $\zeta$  due to variations in  $S$ ,  $X_w$ ,  $v$  and  $L_p$  are best discussed in terms of their value at saturation after all the transitory behaviour has disappeared. This will form the topic of the next section.

### I-3.2 Saturated Behaviour - Evidence of a Preferred Island Length.

Through a study of the tearing mode at saturation, evidence will be presented for the existence of a preferred island length. What is meant by 'preferred' will become obvious as we proceed. However before doing this we will first consider some ideas about the mechanism that drives the tearing mode, and how it saturates, in order to put the observations in some perspective. This will follow a line of reasoning given by E.N.Parker [59].

The resistive tearing mode involves the breakup of the field lines in the neighborhood of the neutral layer between two regions with oppositely directed field components. The original straight, parallel lines of opposite field reconnect into a number of neutral points ( x-points ) and magnetic islands in the manner illustrated in fig.8 of section I-3.1. The instability arises from the fact that the dissipation is very intense in the thin neutral layer where the field can decouple from the fluid. Suppose that the system is perturbed slightly so that the fields are pinched a little more closely at regular intervals along the neutral line, see fig.10(b). The diffusion and reconnection proceed more rapidly where the fields are pinched together, cutting the lines of force and rejoining them into localized elongated loops, see fig.10(c). Once an elongated loop is formed, the tension in the lines of force tends to pull the loop into a more nearly circular form, see fig.10(d,e). The affect then, is to pull the field and plasma away from the vicinity of each neutral point, sucking more field in from either side and further enhancing the reconnection there.

As the reconnected field loops expand out beyond the neutral layer into regions of greater field strength they find it increasingly more difficult to distort the unreconnected field lines which are maintained by the applied electric field and non-uniform resistivity. The tension in the unreconnected field lines opposes the distortion and hence provides a squeezing force on the reconnected field loops which eventually leads to the saturation of the tearing mode.

Fig.10

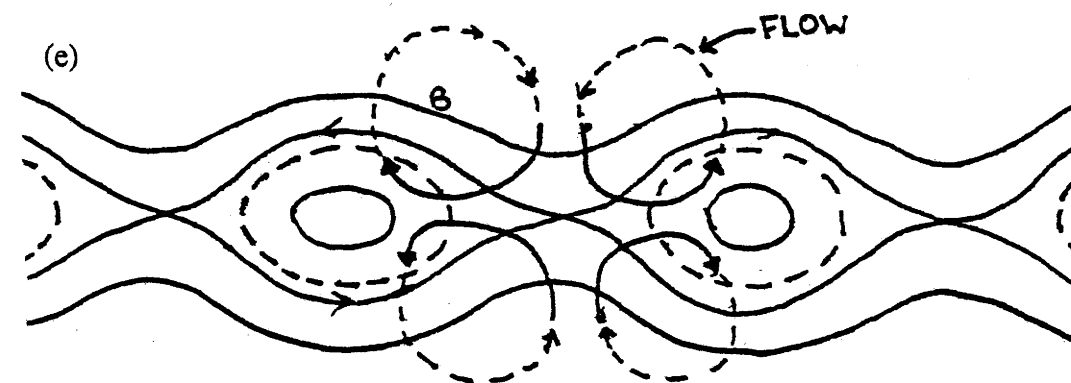
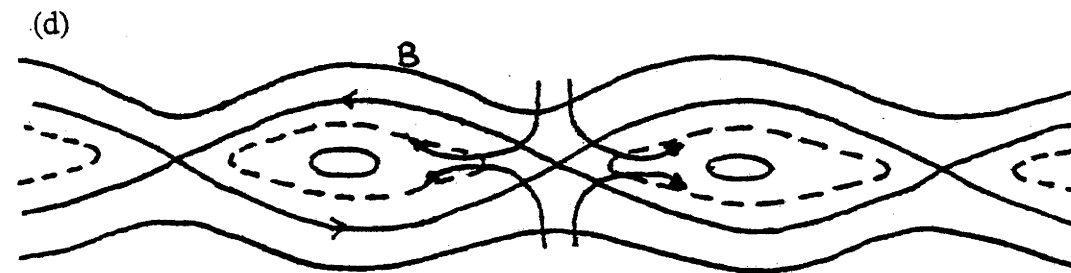
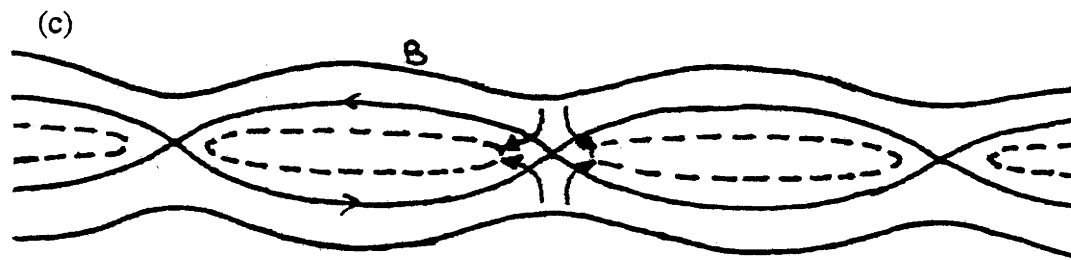
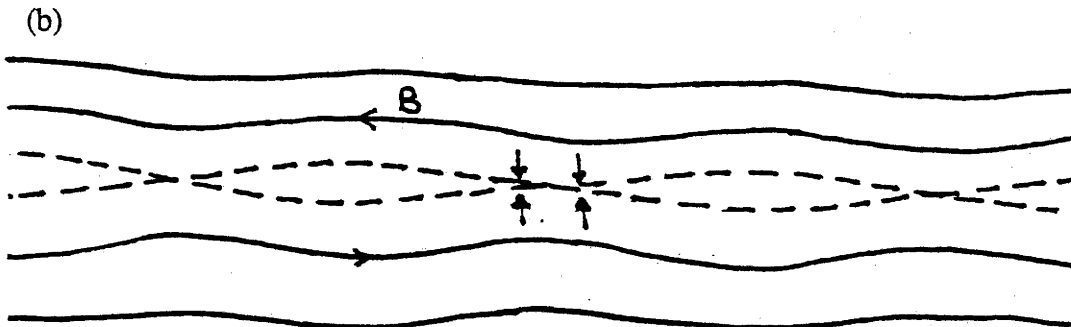
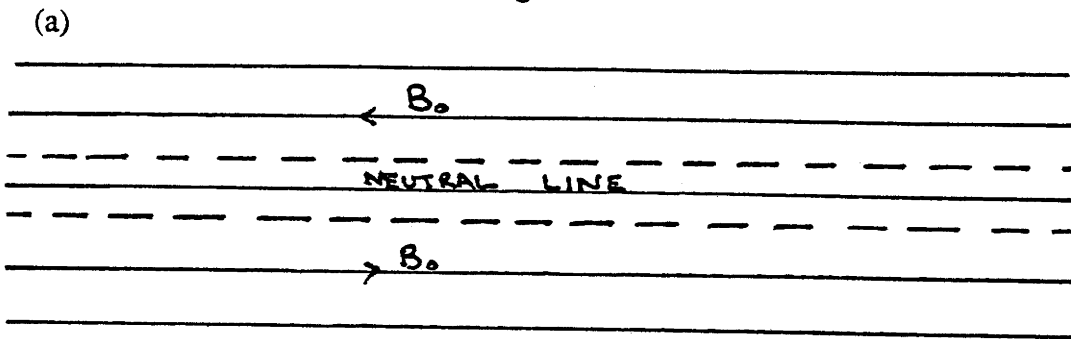
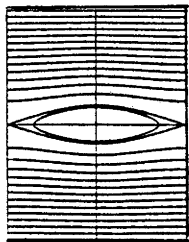
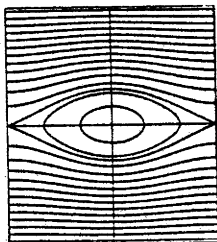


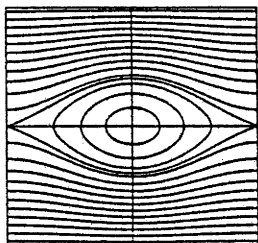
Fig.11(a)



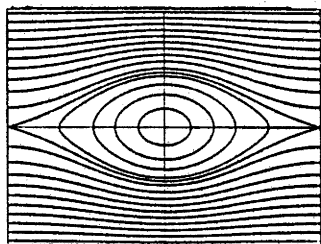
$K_p = 0.7$



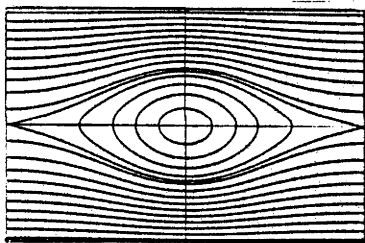
$K_p = 0.6$



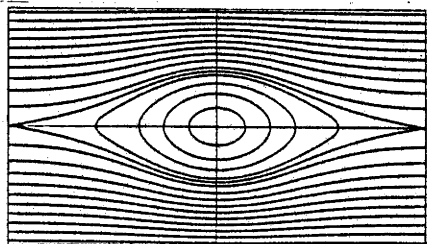
$K_p = 0.5$



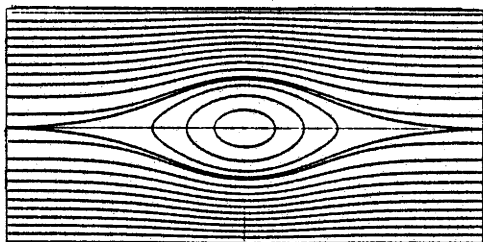
$K_p = 0.4$



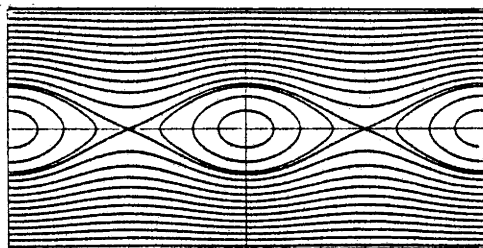
$K_p = 0.35$



$K_p = 0.3$

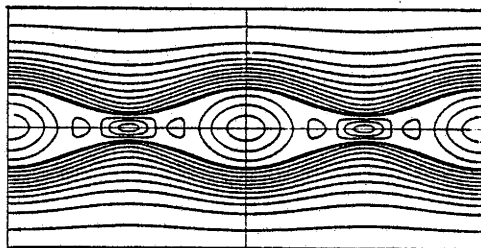
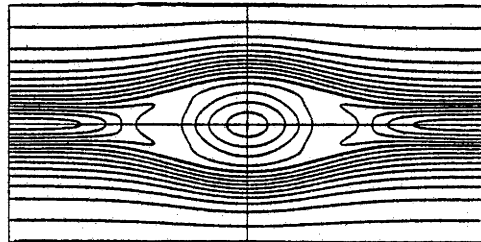
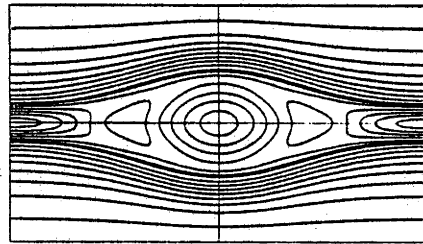
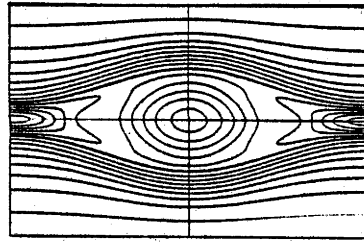
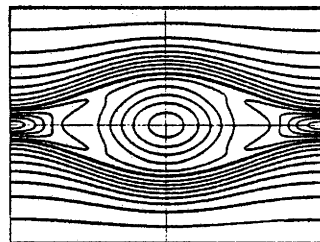
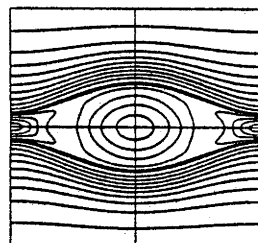
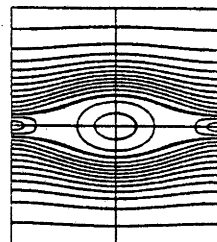
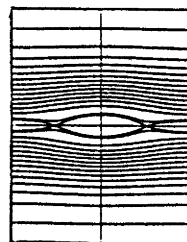


$K_p = 0.263$



$K_p = 0.263$

(b)



The series of contour plots of  $\psi$  in fig.11(a) show the cross-section of flux surfaces of the saturated magnetic island states for increasing values of the periodicity length,  $L_p$ . In the absence of a  $B_z$  component (which decouples from the evolution equations) these can be considered as magnetic field lines. The scale in the direction across the island has been expanded for clarity and is the same in each plot. By displaying them in this fashion it is clearly seen that the balance of forces at saturation results in the inner or central field loops having the same aspect ratio irrespective of the wavelength of the island. At small values of the periodicity length the invariance of this preferred aspect ratio means that the width of the island increases roughly in proportion to its length, with a corresponding steady increase in the amount of reconnected flux as shown in figs.12 and 13 respectively.

The threshold for tearing mode stabilization could thus be considered to occur when the wavelength of the initial perturbation is so small that the corresponding width of the field loop allowed by the preferred aspect ratio is too narrow to induce any further reconnection. For the cases shown in figs.12 and 13 the stability threshold occurs at  $K_p \approx 0.75$  when  $X_w = 2.5$  and  $K_p \approx 0.8$  when  $X_w = 4.0, 8.7$  and  $12.0$ .

The saturated island width does not continue to increase with  $L_p$  because eventually the compression of the field lines reaches a limit that prevents any further lateral extension of the island. This limit will, of course, depend on the wall separation but it will still occur even when the walls are infinitely far apart. The value of  $L_p$  at which this limit is just reached defines, in effect, a preferred island length,  $L_{p\text{ref}}$ , since, having reached the maximum island width, further increases in  $L_p$  would tend to induce the reconnected field loops to exceed their preferred aspect ratio. In practice, as  $L_p$  is increased, the inner reconnected field loops maintain a constant aspect ratio while those closer to the separatrix are forced to stretch out to form thin neck regions near the x-points with the length of these thin neck regions increasing with  $L_p$ , see fig.11(a). A similar sort of behaviour is shown by the corresponding contour plots of the current density in fig.11(b). Like the

Fig.12(a)

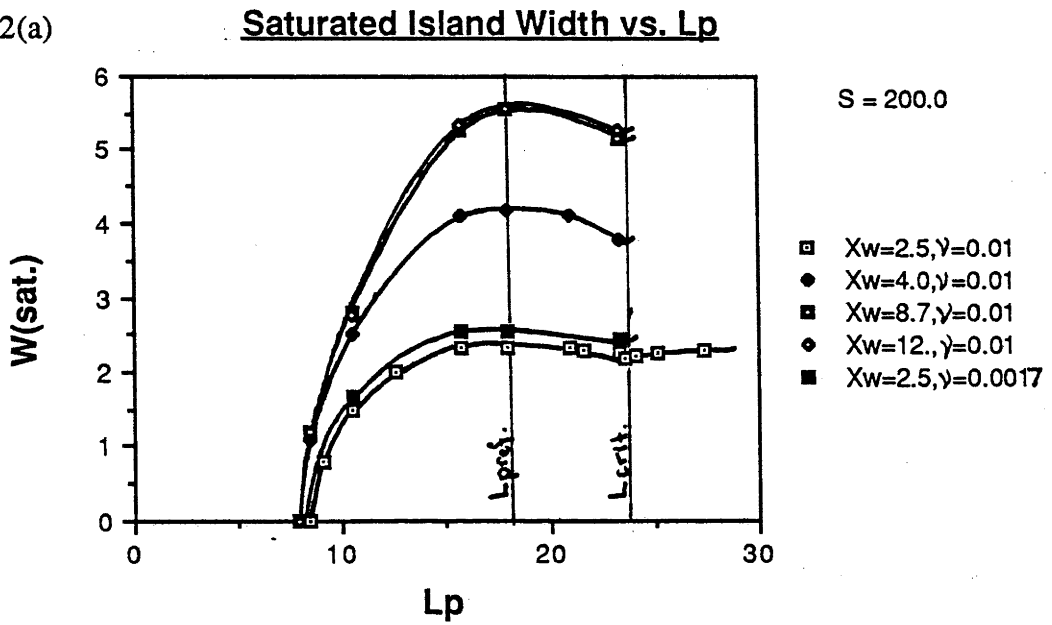


Fig.12(b)

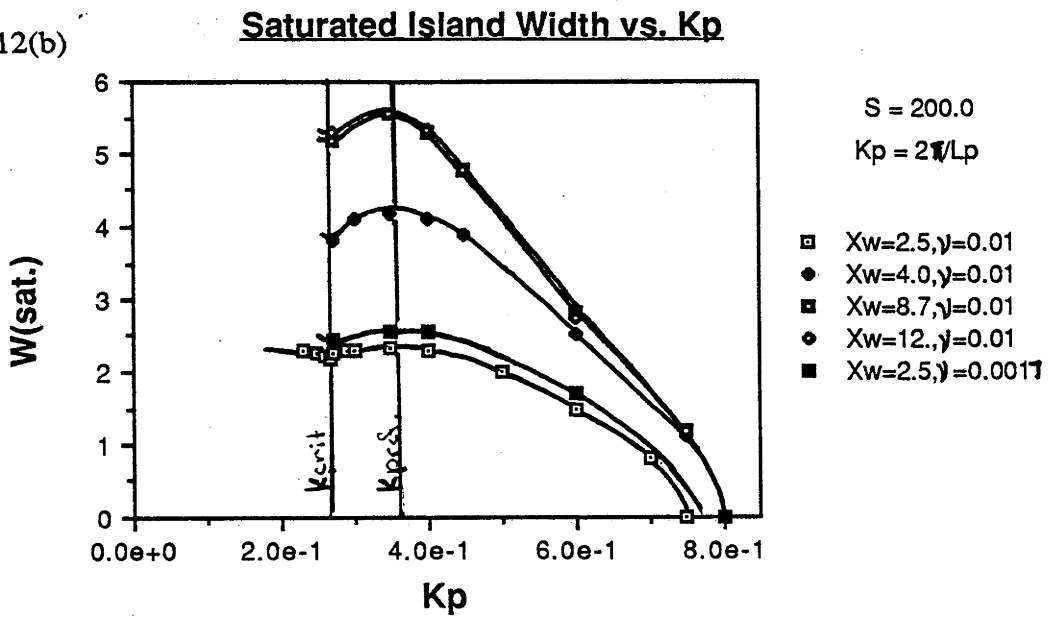
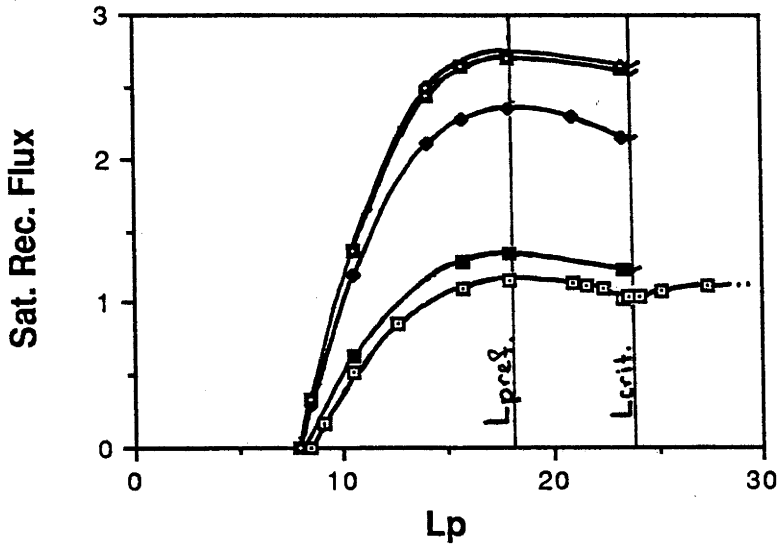


Fig.13(a)

Saturated Reconnected Flux vs.  $L_p$

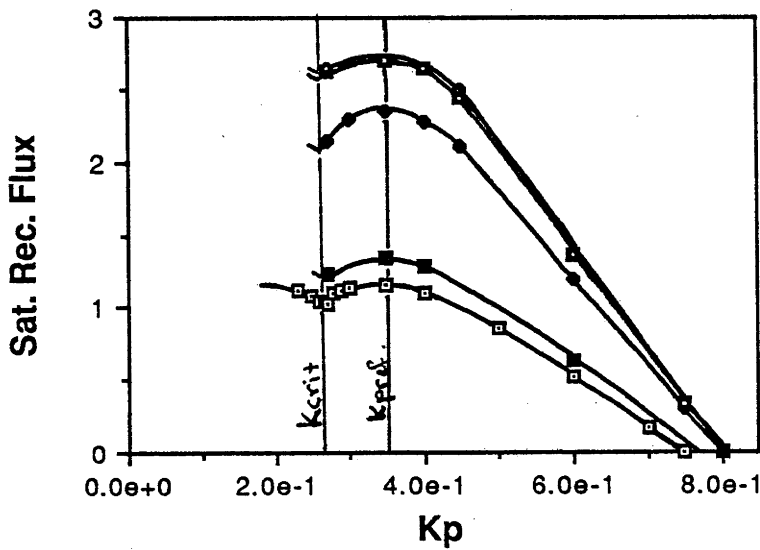


$S = 200.0$

- $X_w=2.5, \gamma=0.01$
- ◆  $X_w=4.0, \gamma=0.01$
- $X_w=8.7, \gamma=0.01$
- ◊  $X_w=12., \gamma=0.01$
- $X_w=2.5, \gamma=0.0017$

Fig.13(b)

Saturated Reconnected Flux vs.  $K_p$



$S = 200.0$

$K_p = 2\pi/L_p$

- $X_w=2.5, \gamma=0.01$
- ◆  $X_w=4.0, \gamma=0.01$
- $X_w=8.7, \gamma=0.01$
- ◊  $X_w=12., \gamma=0.01$
- $X_w=2.5, \gamma=0.0017$

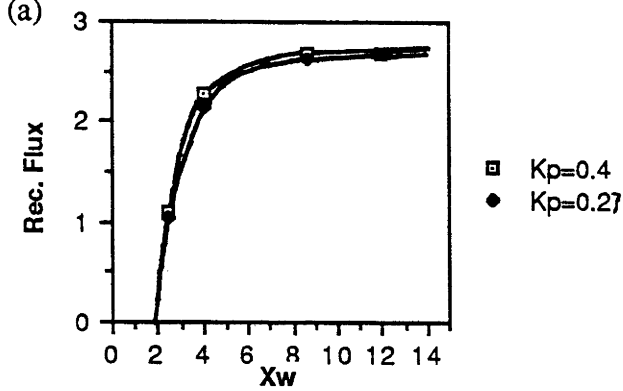


inner reconnected field loops the contours which form the o-point current peak maintain a constant aspect ratio independent of  $L_p$ . The size of the o-point current peak consequently increases with  $L_p$  up to  $L_{pref}$  and then stays reasonably constant thereafter. The x-point current peaks, on the other hand, stretch out to form current sheets to fill the remaining space, especially for  $L_p > L_{pref}$  where, like the thin neck regions of the  $\psi$  contours, they increase in length with  $L_p$ .

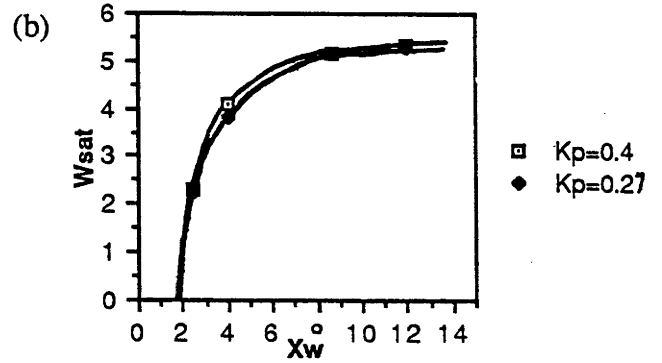
The plots in figs.12 and 13 show that  $L_{pref}$  corresponds to a peak value of both the reconnected flux,  $\Delta\Psi$ , and the island width,  $W$ , to provide an alternative more precise definition of the preferred island length. The fall in these quantities for  $L_p > L_{pref}$  could be due to the extra compressional force created by the stretching of the reconnected field loops close to the separatrix. Most of the other graphs in figs.12 and 13 correspond to simulations made with larger wall separations. When the walls are close together ( e.g. when  $X_w = 2.5$  ) the spatial restriction opposes the distortion of the field lines and consequently provides an extra stabilizing effect on the tearing mode. When the wall separation is increased, as shown for the cases with  $X_w = 4.0, 8.7$  and  $12.0$ , the effect is to reduce the compression on the reconnected field loops allowing them to expand out to a greater width. This occurs without any significant change in their length so that although their preferred aspect ratio is reduced, the value of  $L_{pref}$  remains practically unchanged. This is evident from the fact that the peaks in  $\Delta\Psi$  and  $W$  occur at the same value of  $L_p$  for each value of  $X_w$ . The plots in fig.14 of  $\Delta\Psi$ ,  $W$  and several other quantities at saturation versus  $X_w$  show that the effect of the walls is significant out to  $X_w \approx 9.0$ . Beyond this value the saturation is produced solely by the natural tension in the field lines which is also evident from figs.12 and 13 from the fact that the variations of the  $\Delta\Psi$  and  $W$  with  $L_p$  are almost identical for the cases with  $X_w = 8.7$  and  $X_w = 12.0$ .

The effect of including finite viscosity in the calculation is to damp down the fluid motion and reduce the high order mode activity during the evolution, making the simulations more efficient, see fig.6. However because of the vortical fluid motion that

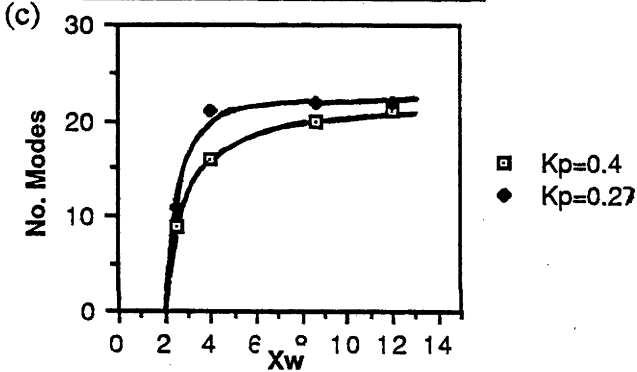
(a) Saturated Rec. Flux vs.  $X_w$



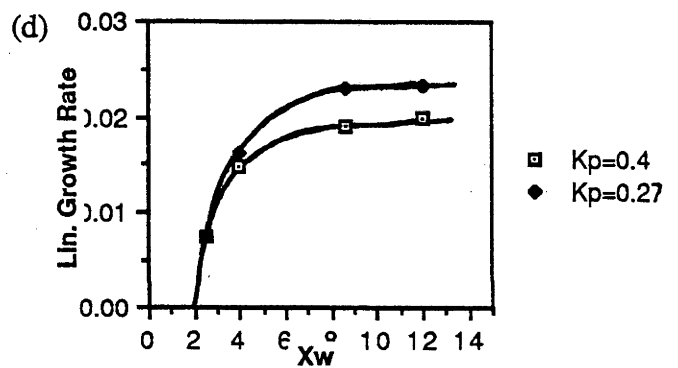
(b) Saturated Island Width vs.  $X_w$



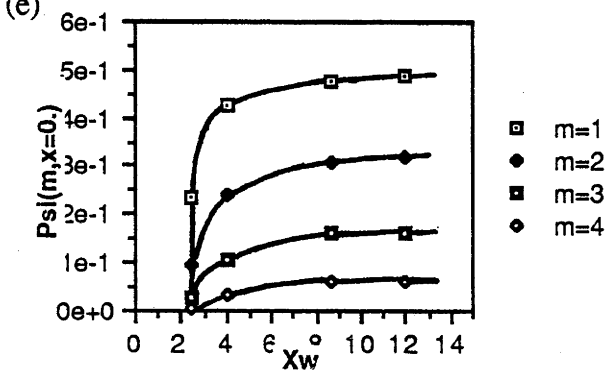
(c) No. Modes needed at sat. vs.  $X_w$



(d) Linear Growth Rate vs.  $X_w$



(e)  $\Psi(x=0.)$  vs.  $X_w$  ( $K_p = 0.27$ )



(f)  $\Psi(m=1,2,3)(x=0.)$  at Sat. vs.  $X_w$  ( $K_p = 0.4$ )

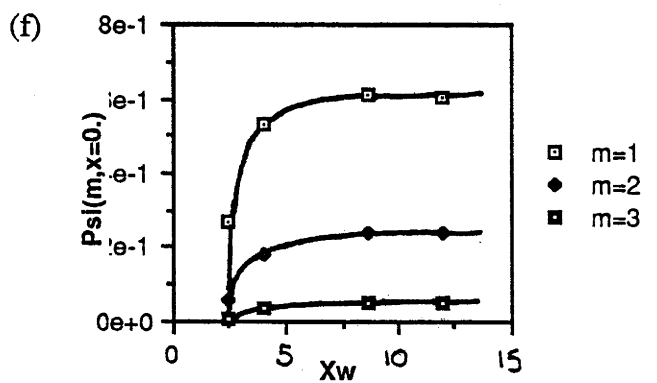


Fig.14

persists after saturation it also affects the properties of the final magnetic island equilibrium. The direct affect of the finite viscosity is to reduce the magnitude and gradient of the fluid velocity in the saturated island and, through the coupling of the field to the fluid, it also indirectly alters the field quantities as well. For instance figs.12 and 13 show from the variation of  $\Delta\Psi$  and  $W$  with  $L_p$  for  $\nu = 1/100$  and  $\nu = 1/600$ , that the viscosity reduces the reconnected flux and island width at saturation but does so without changing the value of  $L_p$  at which they peak. Therefore, although the size of the island is changed,  $L_{pref}$  is still preserved at least for  $\nu \leq 0.01$ . It will be shown later that other critical quantities also remain invariant to changes in the viscosity.

In contrast, a definite shift of the peak, and hence  $L_{pref}$ , towards larger  $L_p$  does occur when the the Lundquist number,  $S$ , is increased, see figs.15 and 16, and seems to correspond to an overall increase in physical size of the saturated island. Fig.17(a) shows this shift in  $L_{pref}$  with  $S$  ( and hence  $\eta^{-1}$  ) to be roughly linear in the range :  $100 < S < 2500$ . This variation with  $\eta$  shows that the reconnection region, where the effect of resistivity is dominant, still influences the properties of the magnetic islands after saturation, most likely through the mechanism of continued reconnection that persists to balance the diffusive decay.

Fig.15(a)

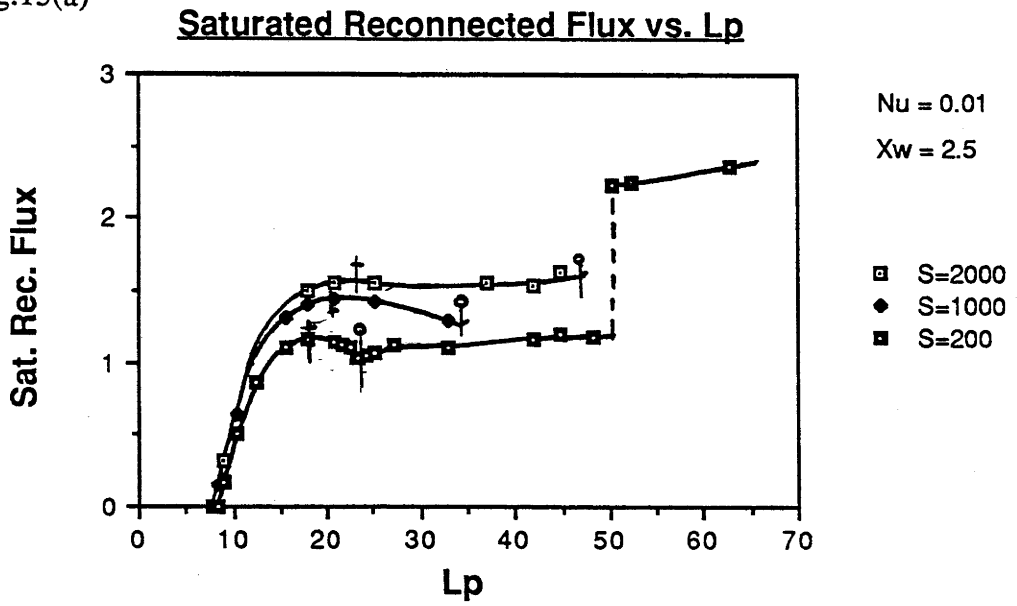


Fig.15(b)

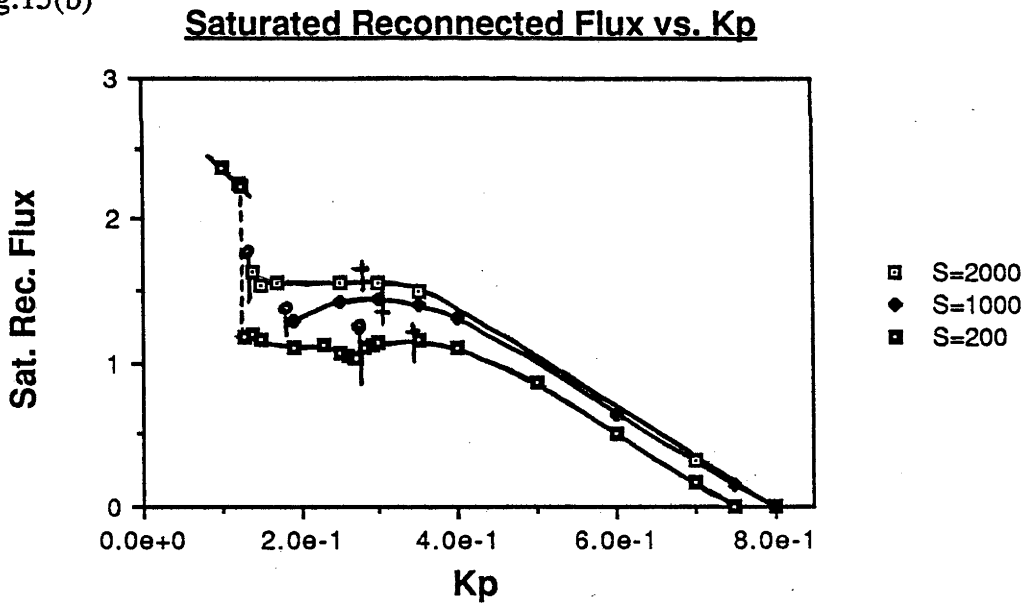


Fig.16(a)

**Max. Saturated Island Width vs Lp**

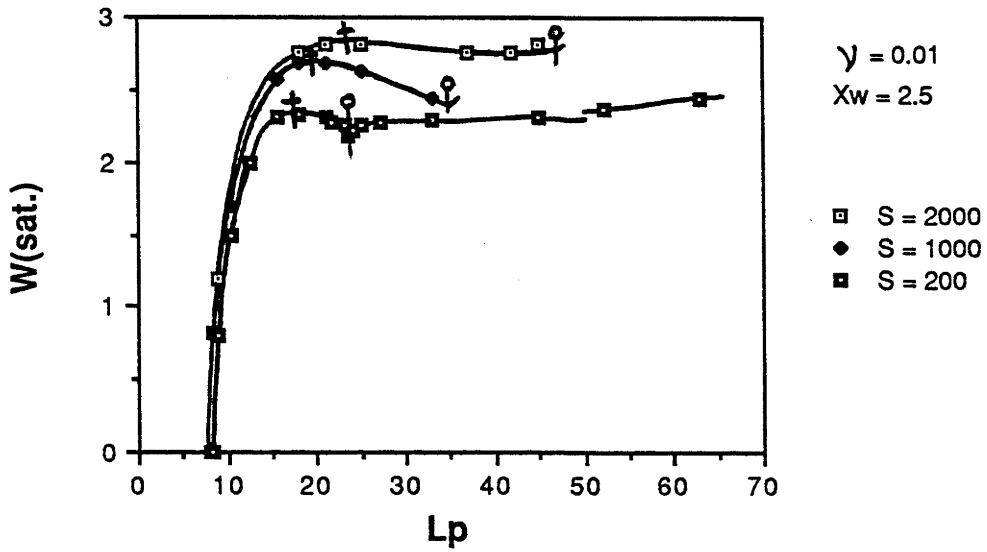


Fig.16(b)

**Max. Saturated Island Width vs. Kp**

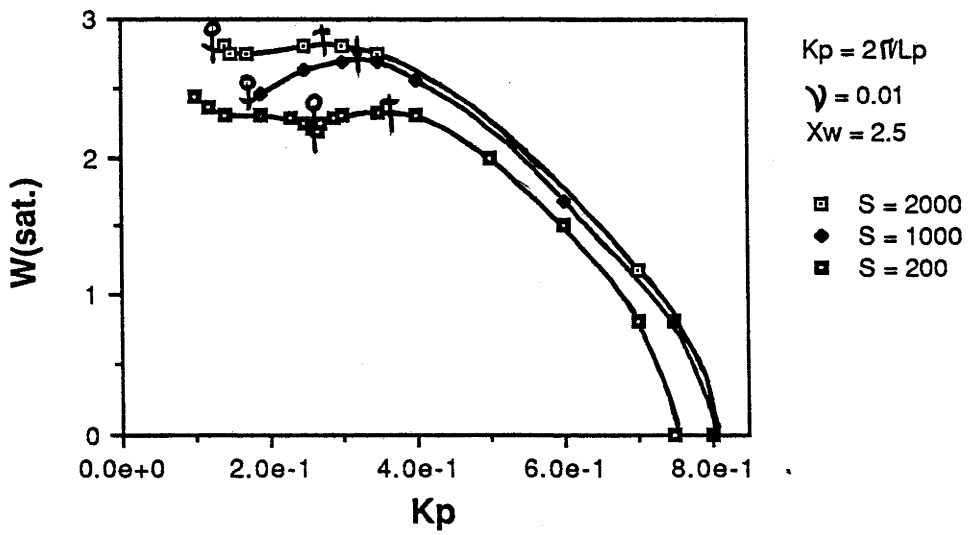


Fig.17(a)

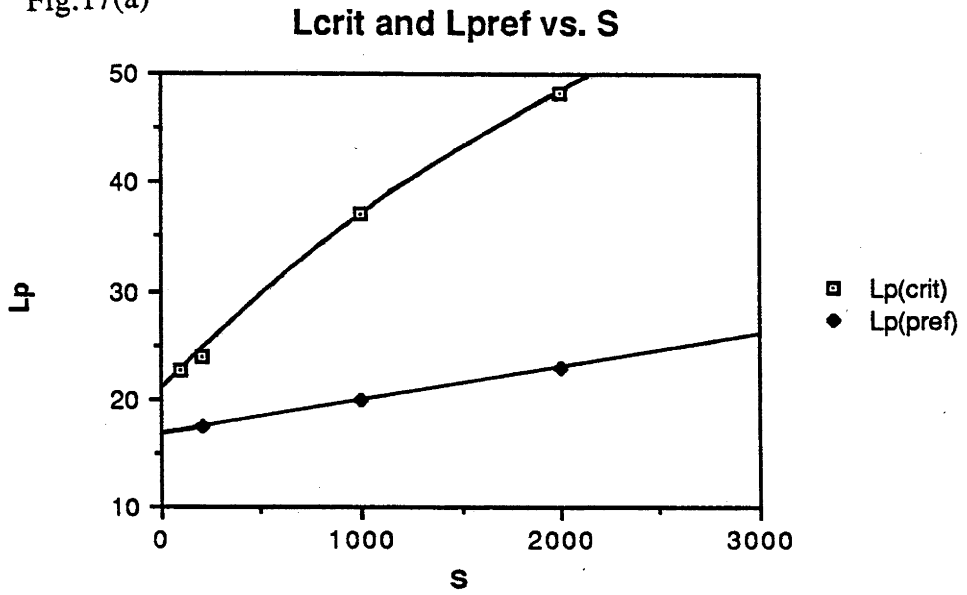
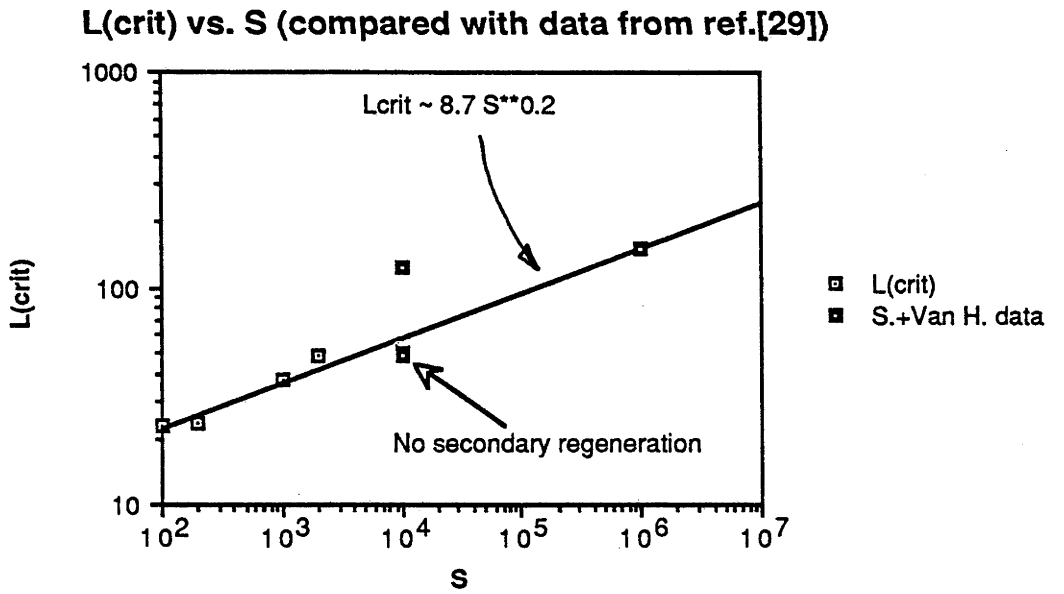


Fig.17(b)



### I-3.3 Secondary Island Generation

As the periodicity length is increased beyond  $L_{pref}$  a value,  $L_{crit}$ , is reached above which the plasma no longer saturates in the simple tearing mode island state with its wavelength equal to the periodicity length but instead undergoes a change in topology to a state with smaller islands.

To see this consider fig.18(a) showing the variation in the reconnected flux for part of the time evolution of a run made with periodicity length just greater than  $L_{crit}$  ( $K_{crit} \approx 0.263$ ). The first part of the run is just the same as for  $L_p < L_{crit}$  with the tearing mode almost saturating into a single island state, i.e. with one island per periodicity length. But instead of reaching steady state the reconnected flux suddenly increases again and begins to settle at a higher level. From frames 1, 2 and 3 in fig.20(a) of time lapsed contour plots of  $\psi$ , during the same phase for the case with  $K_p = 0.23$ , it can be seen that this corresponds to the emergence of a secondary island between each primary island just like in Steinolfson and Van Hoven's simulations <sup>[29]</sup> although here frames 4, 5 and 6 show that the secondary islands continue to grow and equalize with the primary ones. The spatial behaviour of this transformation is neatly summarized in fig.18(c) which shows the splitting of the x-point into two new x-points and an o-point. The evolution of the first four Fourier modes on the neutral line in fig.18(d) shows that this corresponds to a complete transfer of amplitude from the odd to the even modes, especially from  $\psi_1$  to  $\psi_2$ , while the almost doubling of the reconnected flux is consistent with doubling of the number of islands per periodicity length.

A more detailed study of the process in isolation was made for the case occurring during the evolution of a run made with  $K_p = 0.23$ , shown in figs.19,20 and 21 for which the behaviour of the magnetic flux function contours has already been discussed. The evolution of the current distribution provides the best insight into the origin of the transformation, which is most clearly illustrated in the 3-D perspective plots of fig.21.

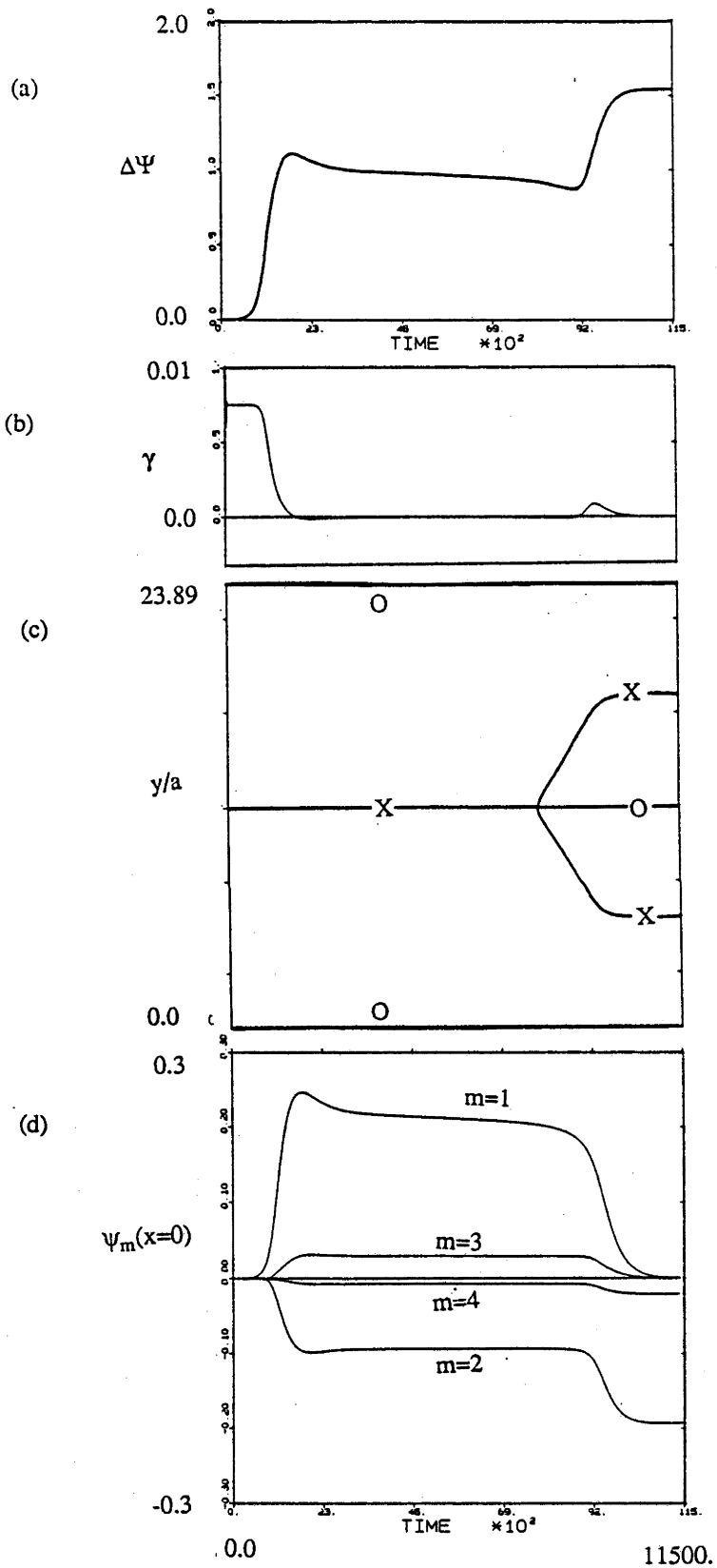


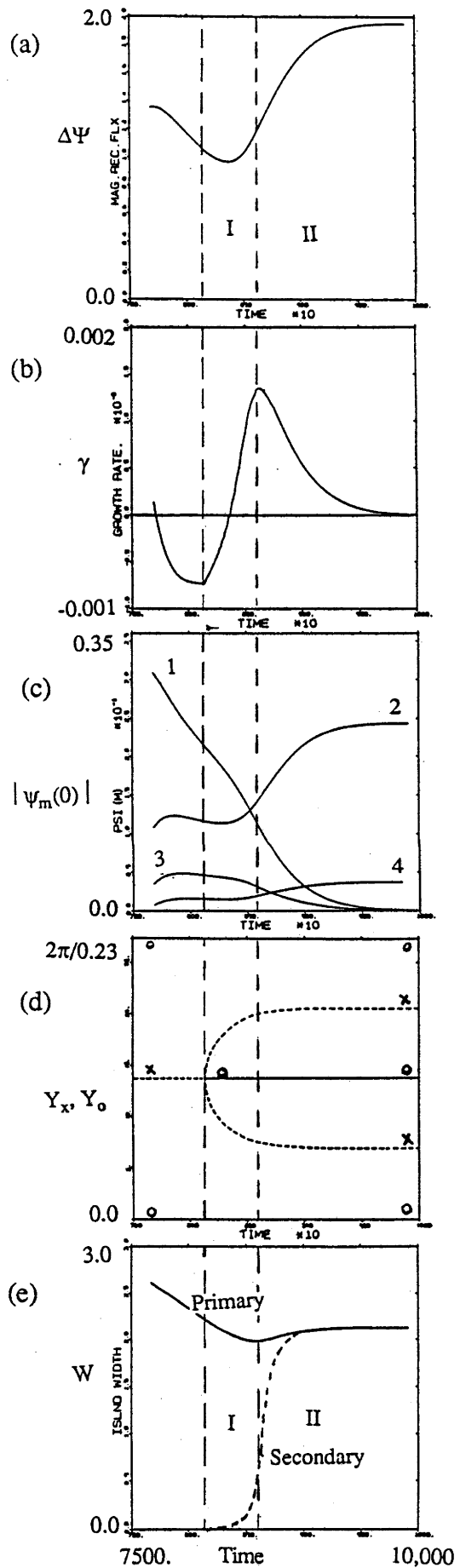
Fig.18



These show the current distribution at regular time intervals before and during the formation of a secondary island in reference to the variation in the reconnected flux. The first two frames show the relaxation towards the 'preferred' configuration with the contraction of the o-point current peaks and the consequent lengthening of the x-point current sheets that occurs because the wavelength of the island,  $\lambda = L_p$ , is greater than  $L_{pref}$ . If  $\lambda < L_{crit}$  the relaxation would eventually stop when the 'preferred' size was reached leaving a final equilibrium state with finite length x-point current sheets like those in fig.8(b). However because, in this case,  $\lambda > L_{crit}$ , the current sheets get so long they become unstable to a secondary resistive tearing mode. This is made most evident by comparing the break up of the x-point current sheet shown in the remaining frames of fig.21 with the similar behaviour produced by the tearing mode on the original current sheet in fig.9.

The onset of the secondary tearing instability is clearly marked by a sharp upturn in the growth rate, see fig.19(b), and also by the instant at which the x-points first split in two and separate to form the x-points of the new island, see fig.19(d). From these plots it is even possible to distinguish the usual stages of development of the tearing mode although the linear stage is more clearly shown in fig.18 for the case with  $K_p=0.263$ . This is because it is much closer to  $K_{crit}$  than the case with  $K_p = 0.23$  so that the primary tearing mode almost completely saturates before the x-point current sheets get long enough to go unstable. Consequently the variation in the diagnostic quantities in fig.18 is then almost totally derived from the activity of the secondary tearing mode. This makes the linear stage more easily discernible as the short period after the splitting of the x-points when the mode amplitudes remain constant and the secondary island width is still negligible. The longer wavelength of the primary island for the  $K_p = 0.23$  case means that the x-point current sheets go unstable well before the primary island gets close to its 'preferred' configuration. As a result the linear stage of the secondary tearing mode is

Fig.19  
PARAMETER VARIATION DURING  
SECONDARY ISLAND GENERATION.



SECONDARY ISLAND GENERATION.

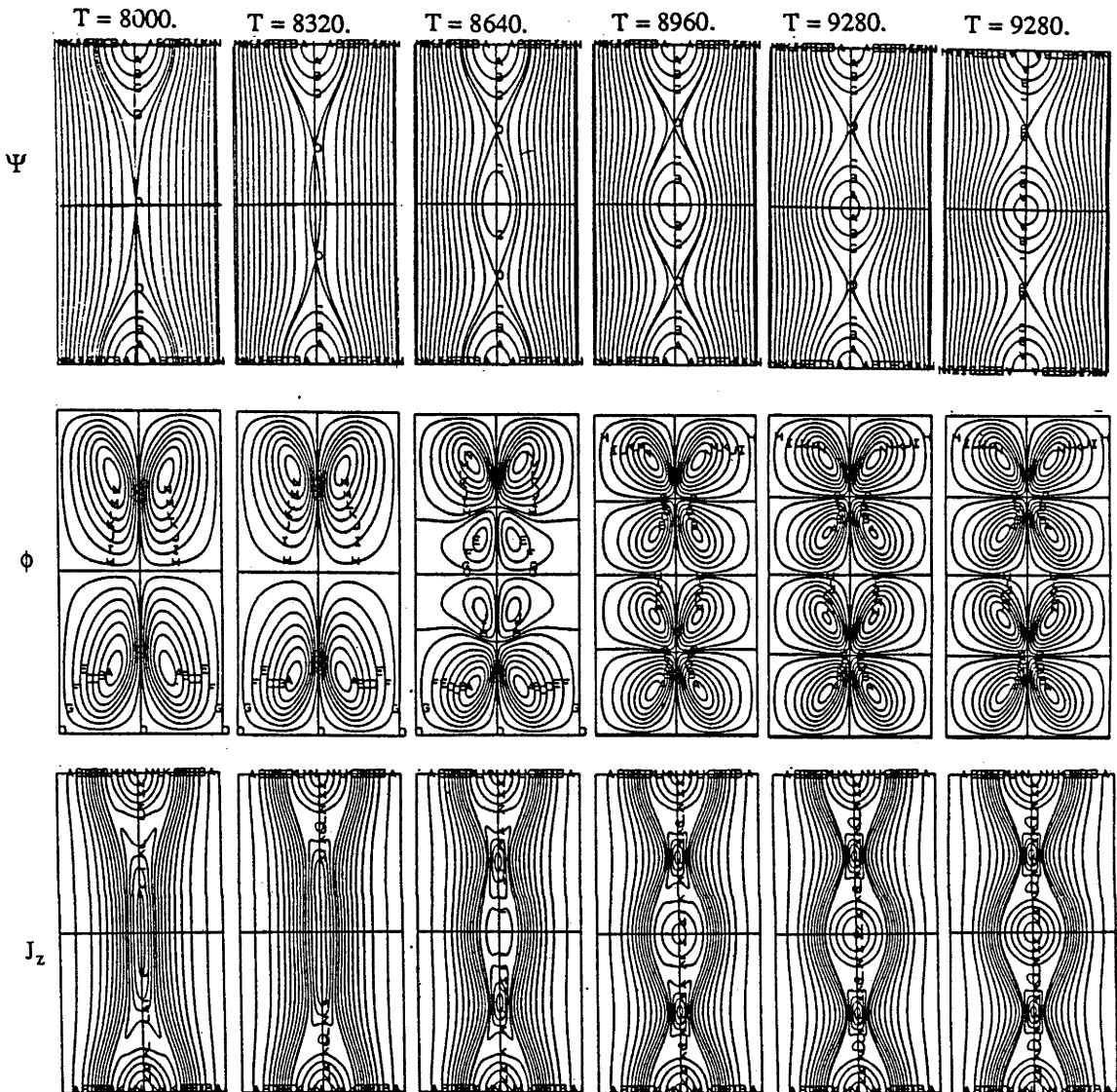
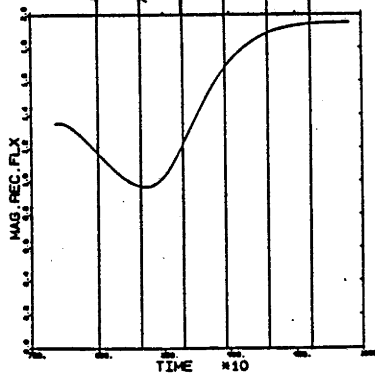


Fig.20



$S = 200.$

$\nu = 0.01$

$K_p = 0.23$

$X_w = 2.5$

3-D CURRENT DENSITY DURING  
SECONDARY ISLAND GENERATION

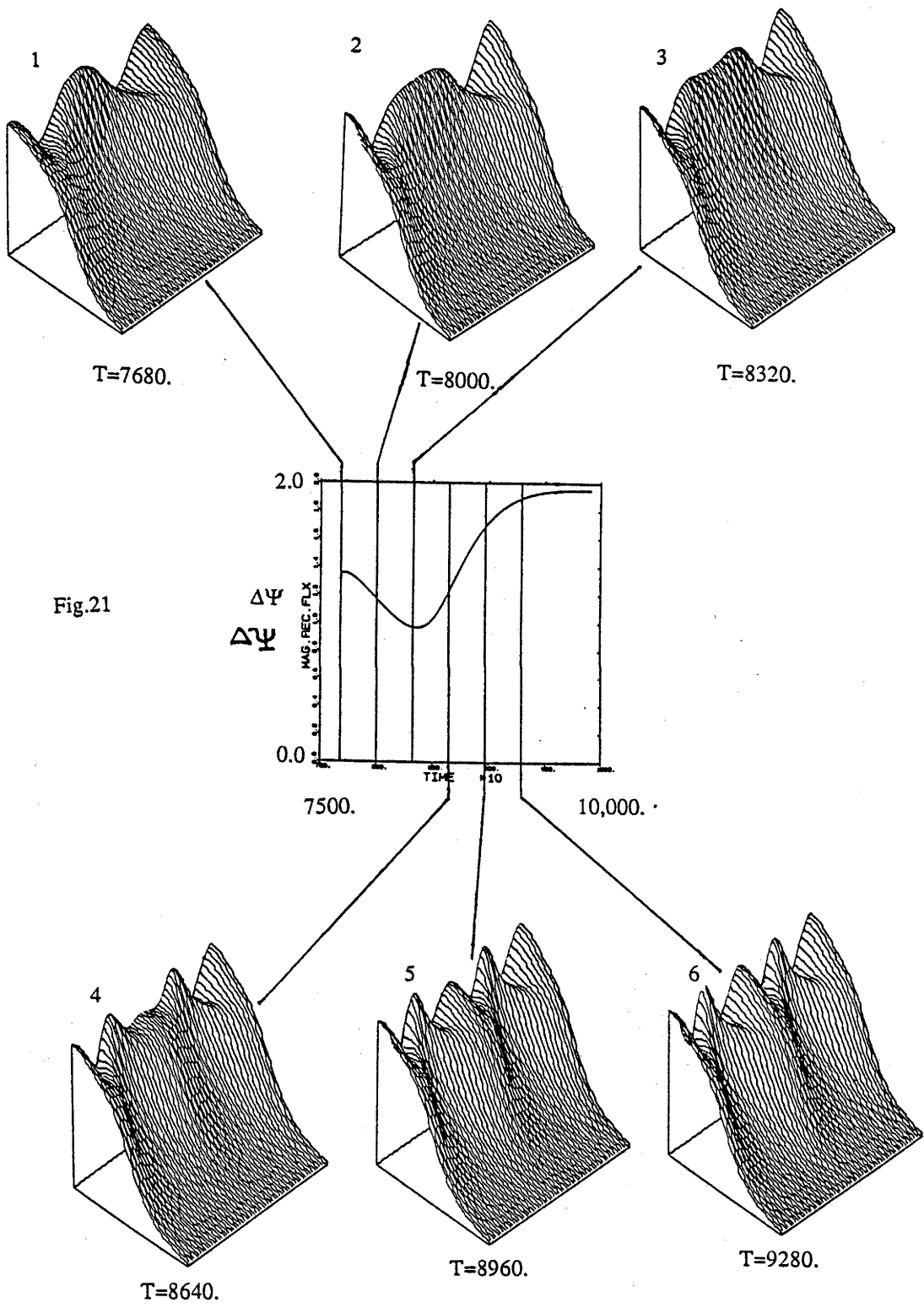


Fig.21

partially obscured by the continued variation in the mode amplitudes associated with the incomplete saturation of the primary tearing mode.

The linear stage merges into the weakly nonlinear stage as  $\psi_2$  (the double island mode) takes over from  $\psi_1$  (the single island mode) as the dominant Fourier mode. It is at this stage that a narrow island emerges and by the time the growth rate has reached a maximum the x-points of the new island have also reached their maximum separation. According to figs.20(a) and (b) the emergence of the secondary island appears to precede the emergence of the secondary flow vortices but the simulations made by Steinolfson and Van Hoven <sup>[29]</sup> indicate that the secondary flow vortices exist much earlier although too small to be seen other than on a log scale.

The point at which the exponential growth rate of the reconnected flux begins to fall signifies the transition to the algebraic growth of the nonlinear stage when most of the reconnection occurs. During this stage the secondary island width approaches that of the primary islands; the usual broad current peak forms over the new o-point and the set of secondary flow vortices clustered around the new o-point expand out to equalize with the contracting vortices of the primary islands. The result is a new island chain with half the wavelength of the original and with much shorter X-point current sheets, fig.20(c). This does not, however, represent the final equilibrium state of the system. Further transformations are to follow but these are best discussed in later sections.

So far it has been implicitly assumed that the length or aspect ratio of the current sheet is the critical factor in determining its stability to the tearing mode. The assumption seems reasonable given that the original current sheet, which can be considered as a finite aspect ratio current sheet minus end effects, is stable to the tearing mode when  $L_p < 2\pi/0.8$ . The periodicity length  $L_p$  is normalized with a length comparable with the half width of the original current sheet so the critical aspect ratio could be roughly given by :  $A_{crit} = L_p(\text{threshold})/2. \approx \pi/0.8 \approx 4.0$ . By this criterion, therefore, the x-point current sheet could be expected to become unstable to the tearing mode roughly when its aspect

ratio exceeded 4. To test this we need to obtain the aspect ratio of the x-point current sheet just before it goes unstable. Frame 1 of fig.20(c) shows a contour plot of  $J_z$  at a point in time close enough to the onset of the secondary tearing mode to obtain an estimate of  $A_{\text{crit}}$  from the contours that form the current sheet. Because the current sheet is tapered it is not immediately obvious which contour should be used but this turns out not to be so serious as the aspect ratio does not change much from contour to contour. The contour marked K near the base of the current sheet has a length,  $2\Delta \approx 13.24$  and a width,  $2\delta \approx 0.62$ , to give an aspect ratio,  $A_{\text{crit}} \approx 21$ . which is much larger than the value for  $A_{\text{crit}}$  calculated from the original current sheet. In other words the x-point current sheets are stable up to a larger aspect ratio than the original current sheet.

There is, however, a significant difference between these two types of current sheets which explains why. Along the x-point current sheet there is a stabilizing sheared flow, see fig.20(b), which is associated with the fluid dynamics of the primary island while the plasma in the original current sheet is completely stationary.

The stability of finite aspect ratio current sheets with sheared flow has previously been investigated by Biskamp<sup>[30,60]</sup> for the case of a different kind of secondary island formation in the neutral layer between two coalescing islands and in a study of forced reconnection via current sheets. In these he takes into account the stabilizing affect of this sheared flow to develop an approximate stability criterion for the current sheet in terms of its aspect ratio,  $A = \Delta / \delta$ . The stability criterion is obtained from the condition that during a growth time  $\gamma^{-1}$  ( $\gamma$  is the linear growth rate of the tearing mode) the distortion caused by the flow over a wavelength  $\lambda = 2\pi/k$  should exceed a characteristic fraction,  $k^{-1}$ , of the wavelength. More simply this is  $k \Delta v > \gamma$  where  $\Delta v = v(y + \lambda) - v(y)$  is the change in velocity over the wavelength. Since the flow speed increases along the edge of the sheet roughly linearly from zero near the x-point to the local Alfvén velocity  $V_{A(\text{loc})}$  at the end of the sheet then  $v \approx V_{A(\text{loc})} y / \Delta$  and so the stability condition becomes  $2\pi V_{A(\text{loc})} / \Delta > \gamma_m$  where  $\gamma_m$  is the maximum linear tearing mode growth rate in the static current sheet. This

is taken to be  $\gamma_m \approx 0.6 [V_{A(\text{loc})}/(S \delta^3)]^{1/2}$  in the limit that  $S V_{A(\text{loc})} \delta \gg 1$ , see ref. [5], hence the condition for stability is approximately :  $A < 4.8 (M_{\text{SP}(\text{loc})})^{-2/3}$  where  $M_{\text{SP}(\text{loc})} = (V_{A(\text{loc})} S \Delta)^{-1/2} = 1 / S_{\text{loc}}^{1/2}$  is the local Sweet-Parker Reconnection rate [60] and  $S_{\text{loc}}$  is the local value of the Lundquist number, for which the diffusion length is taken to be half the length of the current sheet. For the purposes of measurement this is taken to be the distance between the x-point and the point where the velocity along the sheet is maximal and corresponds well with the length of contour K which gave  $2\Delta \approx 13.2$ ,  $2\delta \approx 0.62$  and  $A_{\text{crit}} \approx 21$ . With the normalizing factors used here the local Alfvén velocity at the side edge of the current sheet is given by  $V_{A(\text{loc})} = |B_{\text{loc}}| \approx 0.2$  so that  $S_{\text{loc}} \approx 264$ ,  $M_{\text{SP}(\text{loc})} \approx 0.062$  and hence the condition for stability of the current sheet becomes  $A < 31$ . Given the coarseness of the approximation this is remarkably close the measured value of  $A_{\text{crit}} \approx 21$ . There are certain aspects of the approximation which could perhaps be improved upon but not enough to make the condition significantly more accurate. For our purposes it is sufficient that it provides a reasonable explanation of why the x-point current sheets are stable for a greater aspect ratio than the flowless original current sheet.

There is, however, the question of applicability, since the stability condition does not take into account the effects of viscosity and finite wall separation which are significant here. These tends to reduce the flow velocity and gradient in the current sheet so that, with  $\gamma = 0.01$  and  $X_w = 2.5$ , the plasma flow along the side edge of the current sheet is accelerated only up to about a tenth of the local Alfvén velocity, an order of magnitude less than that assumed in the stability condition.

Inspite of this, the critical periodicity length,  $L_{\text{crit}}$ , above which secondary island generation occurs, was found to be independent of the viscosity and the wall separation, at least for the values tested. This can be seen in fig.13 showing the reconnected flux at saturation versus  $L_p$  for  $X_w = 2.5, 4.0, 8.7$  and  $12.0$  and for  $\gamma = 0.01, 0.00167$  and similarly for the saturated island width, fig.12. For  $L_p > L_{\text{crit}}$  the values of the reconnected flux and magnetic island width shown in some of these plots do not actually

correspond to the double island states discussed in this section since, as has already been pointed out, these are a transient phase in the evolution. Nevertheless they do eventually reach a final equilibrium, to be discussed later, for which  $L_p = L_{crit}$  is marked by a kink in the variation at saturation of  $\Delta\Psi$  and  $W$  as shown.

To investigate this further, measurements were taken of the dimensions of the x-point current sheet from contour plots of the current density at saturation for simulations made with  $L_p < L_{crit}$ . In Table 1 are the results of these measurements for several values of  $\nu$  and  $X_w$  with  $K_p = 0.35$  and  $S = 200$ .

Table 1.

$\nu$	$X_w$	$\delta$	$\Delta$	$A$
0.02	2.5	0.62	6.75	10.88
0.005	2.5	0.47	4.61	9.81
0.00167	2.5	0.38	3.70	9.74
0.00067	2.5	0.36	3.53	9.81
0.005	2.5	0.47	4.61	9.81
0.005	4.0	0.58	5.59	9.64
0.005	8.7	0.73	7.05	9.66

These show that increasing the viscosity widens the current sheet but also lengthens it so that its aspect ratio remains reasonably constant. Similarly bringing the walls in closer together reduces the width of the current sheet but also reduces its length so that again the aspect ratio remains unchanged. The implication is therefore that  $A_{crit}$  will also be invariant and, on the assumption that the aspect ratio is the critical factor in determining



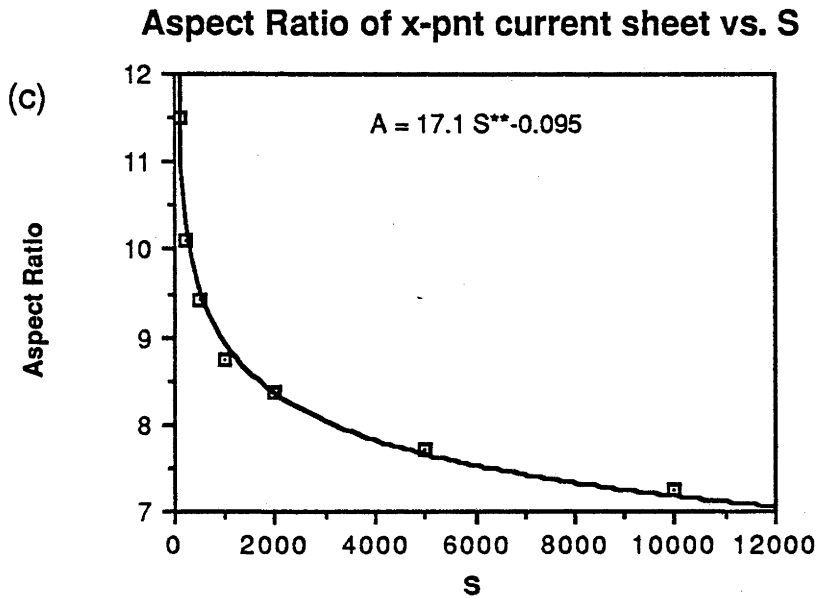
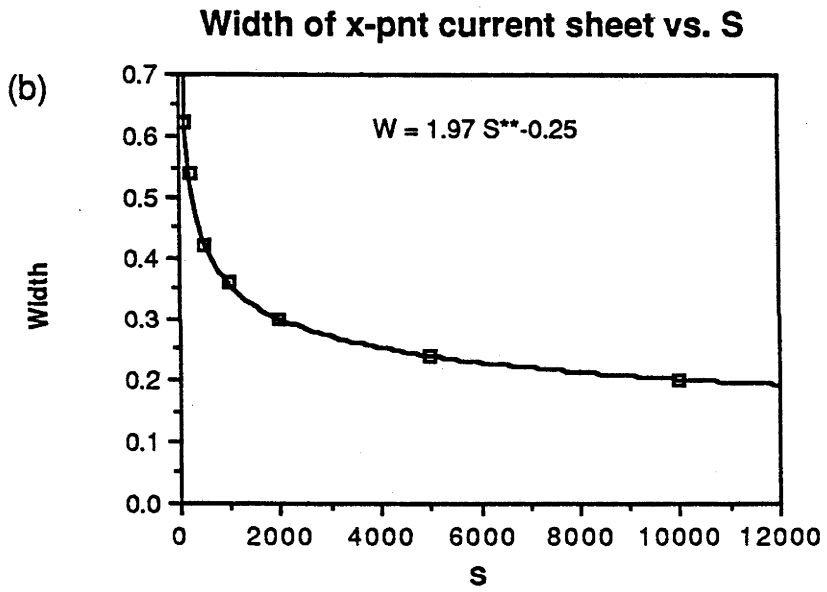
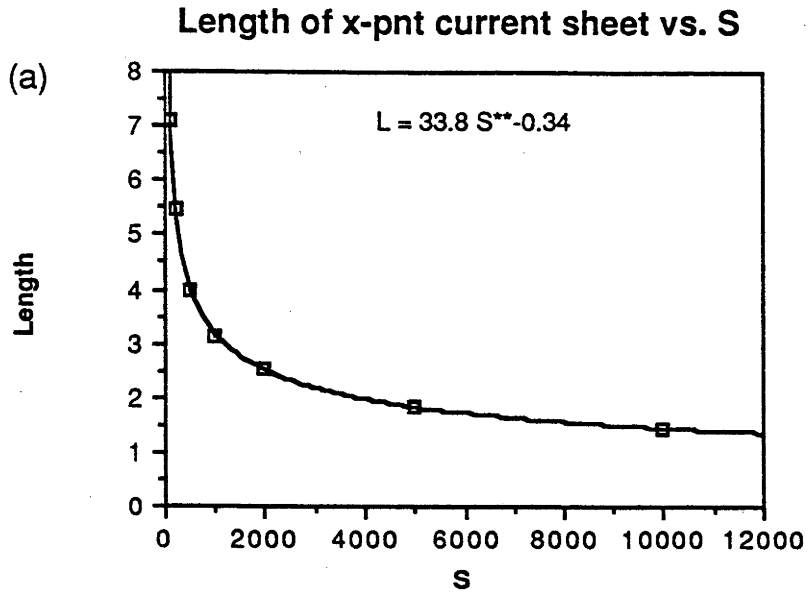
the stability of the current sheet, this would explain why  $L_{\text{crit}}$  is independent of the value of  $v$  and  $X_w$ . The fact that  $L_{\text{pref}}$  and  $L_{\text{crit}}$  are independent of  $v$  and  $X_w$  is important also because it means that by operating with a finite wall separation and significant viscosity we have been able to minimize the run time without altering the essential features of the tearing mode equilibrium.

From the plots of  $W_{\text{sat}}$  and  $\Delta\Psi_{\text{sat}}$  versus  $L_p$  for different values of the Lundquist number,  $S$ , in figs.15 and 16 it can be seen that, like  $L_{\text{pref}}$ ,  $L_{\text{crit}}$  also increases with  $S$ . The variation, shown in fig.17(a), appears to be almost linear for  $S < 2000$  although it shows signs of rounding off at large  $S$ , which it must, otherwise at much higher values of  $S$  ( $S = 10^4, 10^6$ ) it would be much larger than the value of  $L_p$  at which Steinolfson and Van Hoven [29] observed the emergence of secondary islands. The range of values of  $L_{\text{crit}}$  measured here is too small to determine the global variation of  $L_{\text{crit}}$  with  $S$ , however, in fig.17(b) the data is replotted on a log-log plot including values of  $L_p$  and  $S$  corresponding to three of the simulations made by Steinolfson and Van Hoven at high  $S$ , for which two underwent secondary island generation. Although the extra data does not necessarily correspond to values of  $L_p$  close to  $L_{\text{crit}}$  they do show that a variation of the form  $L_{\text{crit}} \propto S^{0.2}$  is reasonably consistent with both sets of data.

Increasing  $S$  seems to increase the overall size of the saturated island so that the 'preferred' island length is achieved at a larger value of  $L_p$  and appears to be why  $L_{\text{pref}}$  increases with  $S$ . It also means the O-point current peaks are broader, leaving less room for the x-point current sheets which are consequently shorter at higher  $S$ , as shown in figs.22(a). As a result a larger value of  $L_p$  is required for the x-point current sheet to reach the critical aspect ratio for tearing mode stability. Figs.22(a),(b) and (c) also show that  $\delta$ ,  $\Delta$  and  $A$  have a simple inverse power dependence on  $S$  of the form :  $\delta \propto S^{-0.25}$ ,  $\Delta \propto S^{-0.34}$  and  $A \propto S^{-0.095}$ .

Another way of looking at this is to note that because  $\eta \propto S^{-1}$  the width of the reconnection layer in which resistivity is important decreases with  $S$  like  $S^{-0.4}$ , see ref.

Fig.22

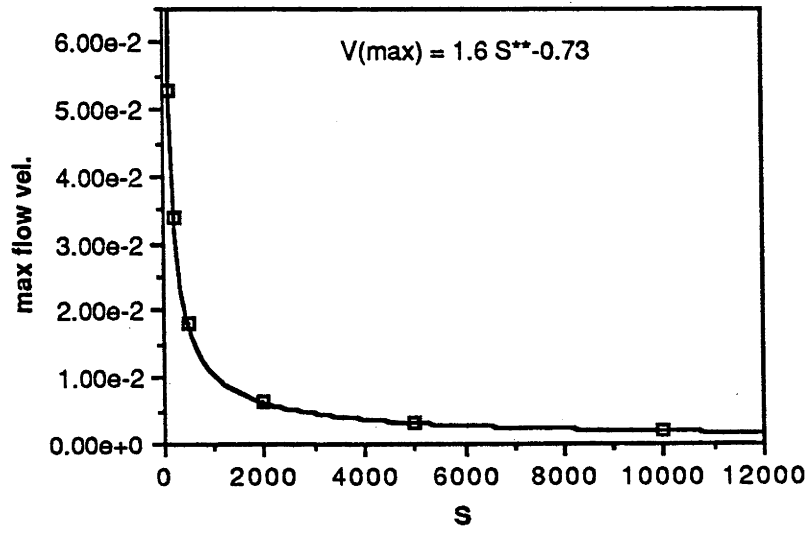


[6]. The width of the x-point current sheet which is related to the reconnection layer therefore also decreases with  $S$  albeit at a slower rate. The narrower reconnection layer also reduces the rate of reconnection (which persists at saturation to balance diffusion losses) so that the flow velocity reached at the end of the current sheet decreases with  $S$  like  $S^{-0.73}$ , as shown in fig.23, and perhaps causes the reduction in the length of the current sheet in the manner shown. This is in contrast with the changes in the flow velocity that occur when  $v$  or  $X_w$  are changed which alter the length and width of the current sheet without changing  $A$  and hence  $A_{crit}$ . The situation is still unclear and is an area marked for further investigation.

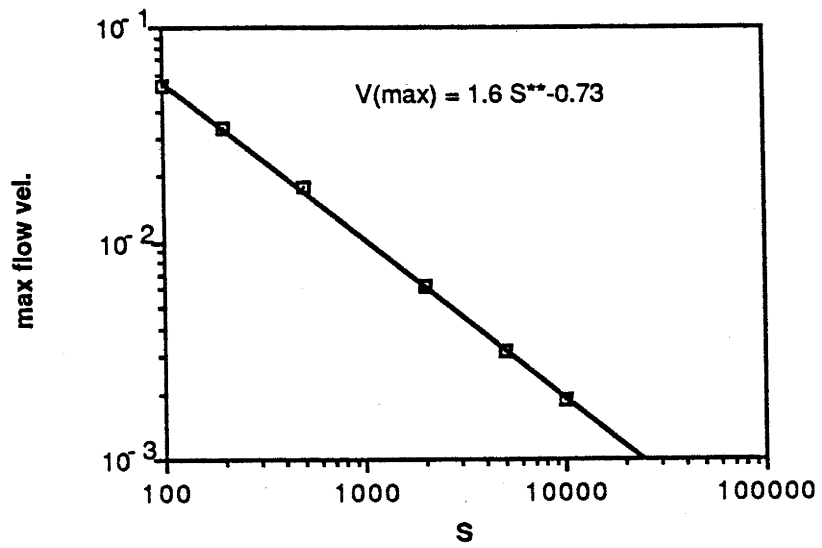
Measurements of the current sheet dimensions were also made as a function of the periodicity length right up to  $L_p = L_{crit}$  for several values of  $S$  as shown in figs.24(a),(b) and (c). These verify the observations made in the previous section that the length of the x-point current sheet does not change much for  $L_p < L_{pref}$  but starts increasing uniformly with  $L_p$  when  $L_p > L_{pref}$ . In contrast the width of the current sheet rounds off to a maximum value so that the aspect ratio also increases uniformly with  $L_p$ . The increase in the width and the small increase in the length with  $L_p$  that do occur for  $L_p < L_{pref}$  can be attributed to the general increase in size of the magnetic island that occurs in this range of  $L_p$ . These plots verify that at a higher value of  $S$  a larger value of  $L_p$  is required to obtain the same length current sheet as for a smaller value of  $S$ . They indicate, however, that this is not the only reason for  $L_{crit}$  increasing with  $S$  since they show  $A_{crit}$  also increasing with  $S$ . The increase of  $A_{crit}$  with  $S$  is not totally unexpected since it is predicted by Biskamp's approximate stability condition and hence is most likely due to the change in fluid flow along the current sheet that occurs when  $S$  is varied, as indicated in fig.23.

Fig.23

### Max. Flow Velocity on Current Sheet vs. S



### log-log plot



### Aspect Ratio of Current Sheet vs. $L_p$

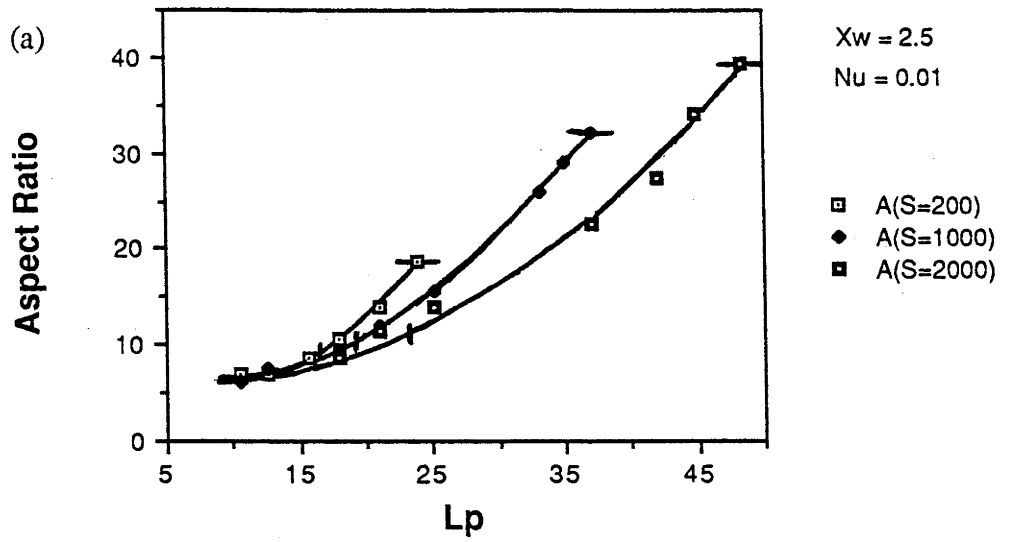
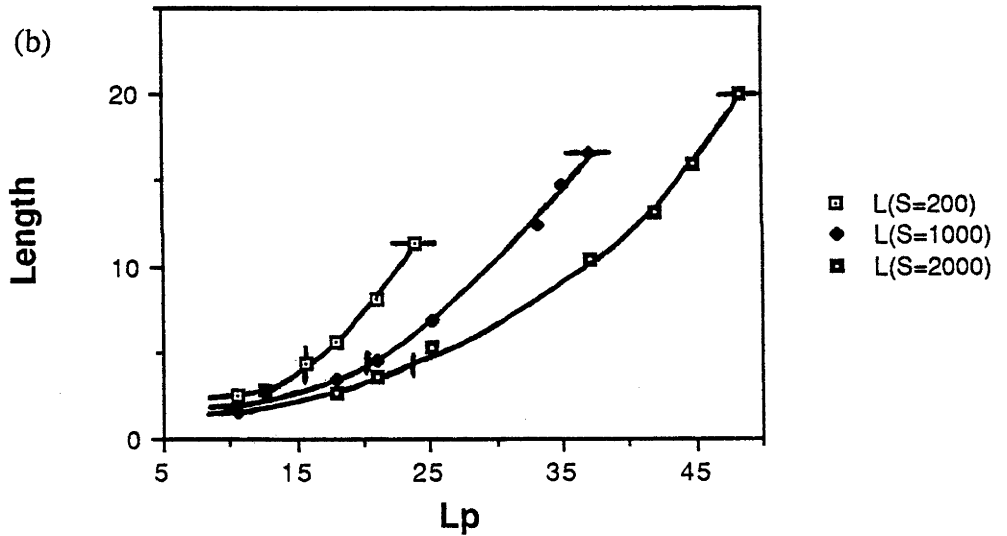
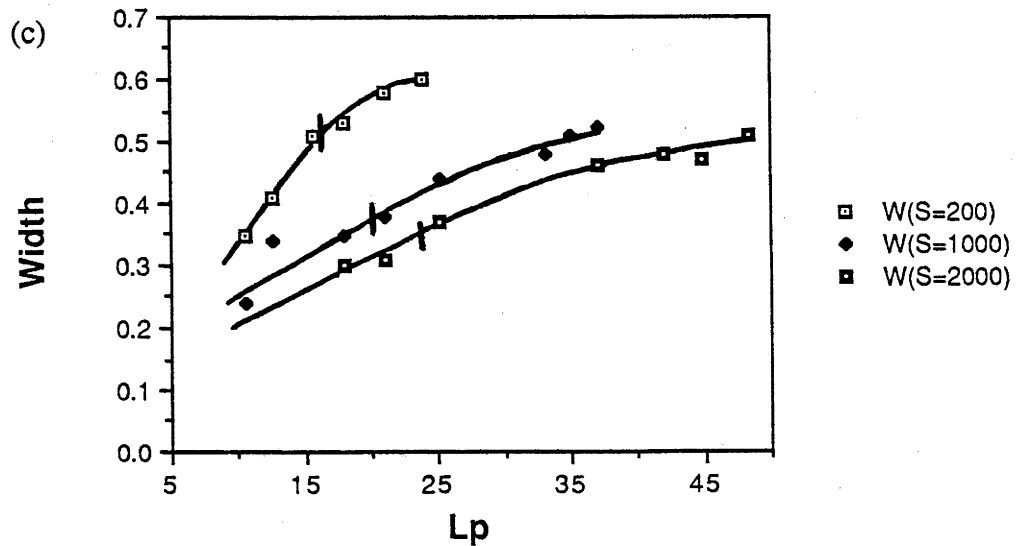


Fig.24

### Length of Current Sheet vs. $L_p$



### Width of Current Sheet vs. $L_p$



### I-3.4 Coalescence

In this section we shall consider the very different topological process known as coalescence which involves the merging of adjacent magnetic islands to form larger islands. As mentioned earlier, many studies have been made which simulate the coalescence instability but only successfully using the exact island equilibrium of Fadeev, Kwartshava and Komorov [27] given by :

$$\psi = \ln ( \cosh (k_p x) + \varepsilon \cos (k_p y) ) \quad (133)$$

When  $\varepsilon = 0$  and  $K_p = 1$ , it reduces to the well known  $B_y = \tanh(x)$  equilibrium used here as the initial state because of its well known instability to the tearing mode. Without loss of generalization we can set  $k_p = 1$  in equation (133) so that the asymptotic behaviour of  $J_z$  as  $|x| \rightarrow \infty$  is the same in both cases. For the case of infinite wall separation there is an analytical linear tearing mode solution [6], corresponding to the initial equilibrium of the form :

$$\psi_1(x) = e^{-k_p x} \left[ 1 \pm \tanh(x)/k_p \right] \quad (134)$$

valid for the region external to the tearing layer, which has a discontinuous derivative at  $x = 0$ , and hence a delta prime of the form:

$$\Delta' = \frac{\psi_1'(0^+) - \psi_1'(0^-)}{\psi_1(0)} = 2 \left[ \frac{1}{k_p} - k_p \right] \quad (135)$$

Evaluation of this by matching with an approximate solution for the inner tearing layer region gives the dependence of the linear growth rate in terms of  $\Delta'$  as :

$$\gamma \propto (\Delta')^{4/5} \quad (136)$$

which indicates that the  $\tanh(x)$  equilibrium is linearly stable to the tearing mode for  $k_p \geq 1.0$ . Furthermore our simulations show that the stability threshold actually occurs at a longer periodicity length, around  $k_p \approx 0.8$ , see fig.12 or 13, so the exact island

equilibrium which has  $k_p$  fixed at  $k_p = 1.0$  is clearly not accessible via a tearing mode since for this value of  $k_p$  the initial equilibrium is stable or at best neutrally stable to the tearing mode. The inaccessibility of the exact island equilibrium via a tearing mode means it is a less physical solution and so is of diminished significance to real plasma discharges. For instance, the traditional explanation for the onset of coalescence has been solely in terms of the attraction between parallel current channels that pass through the o-points of adjacent islands. This is fine for explaining coalescence in the exact island equilibrium since it has a simple current distribution given by

$$J_z = (1 - \epsilon^2) e^{-2\psi} \quad (137)$$

which forms a simple peak in the current over each o-point. This is evident from the fact that since  $J_z = J_z(\psi)$  it must have the same topology as  $\psi$ , which is only peaked over the o-points. But as was pointed out in the section I-3.1, see fig.9, the simulated tearing mode magnetic islands also have current peaks over the x-points which stretch into current sheets when  $\lambda > L_{\text{pref}}$ . In fact, in section I-3.3 we found that when  $\lambda > L_{\text{crit}}$ , far from coalescing to form larger islands, the island chain transformed via the breakup of the x-point current sheets to one with smaller islands. Therefore the idea that magnetic islands always tend to coalesce is clearly shown to be false, at least for finite S.

The existence of the 'preferred' island length discussed in section I-3.2 seems to play a major role in determining the evolution of the tearing mode. When the island wavelength,  $\lambda$ , is less than  $L_{\text{pref}}$  there is still a tendency for a larger island to form and so coalescence would be expected to occur. By the same token when  $\lambda > L_{\text{pref}}$  the tendency to coalesce could be diminished by the fact that the island is already longer than the 'preferred' island length.

Relating these considerations back to the current distribution it could be concluded that coalescence is certain to occur when the x-point current peaks are small (or non-existent as in the case of the exact island equilibrium); less likely when they lengthen into current sheets and absent when the sheets are long enough to be tearing mode unstable.

Note that the periodicity length must be at least double the island length to allow room for the coalescence to proceed.

Another consideration is at what stage during the growth of an island chain will the islands tend to coalesce. Fig.9 shows that although the x-point current peaks form almost immediately, the o-point current peaks do not form until much later and only reach full size as they approach saturation. Given the absence of a distinct current channel through the o-points of the islands during the early stage it is, perhaps, understandable that the short simulations of Hayashi [28] ( $t = 160 \tau_A$ ) failed to produce spontaneous coalescence. Had he run his simulation considerably longer to allow the o-point current peaks to form he would indeed have observed spontaneous coalescence like that shown in the contour plots of figs.26, 27 and 28, for the case with an initial island length of  $\lambda = 2\pi/0.43$  and periodicity length of  $L_p = 2\pi/0.23$ .

Coalescence of tearing mode magnetic islands is observed to occur in three distinct stages which appear to correspond to the three stages distinguished by Bhattacharjee, Brunel and Tajima [26] for coalescence of magnetic islands in the exact island equilibrium. It will be shown here, by relating the spatial behaviour of  $\psi$ ,  $\phi$  and  $J_z$  in figs.26 to 29 to the time dependence of  $\Delta\Psi$ ,  $v$ ,  $W$ ,  $|\psi_m(x=0)|$  and the x and o-point positions in fig.25, that the 3 stages can be characterized as : (I) a preparation phase, (II) a reconnection phase and (III) a relaxation phase.

#### Phase (I) Preparation :

Initially the merging of the magnetic islands is very slow as the sections of plasma within each island gradually gain momentum towards each other. In effect, the merging, which will involve considerable reconnection of the field lines, is delayed until the flow pattern is made more appropriate for the process. According to fig.26 showing contour plots of  $\psi$ ,  $\phi$  and  $J_z$  this means the shrinking and eventual removal of the vortical flow structure associated with the old x-points to allow the vortices of the permanent x-points to stretch out and fill the space. The resulting flow pattern between the merging islands



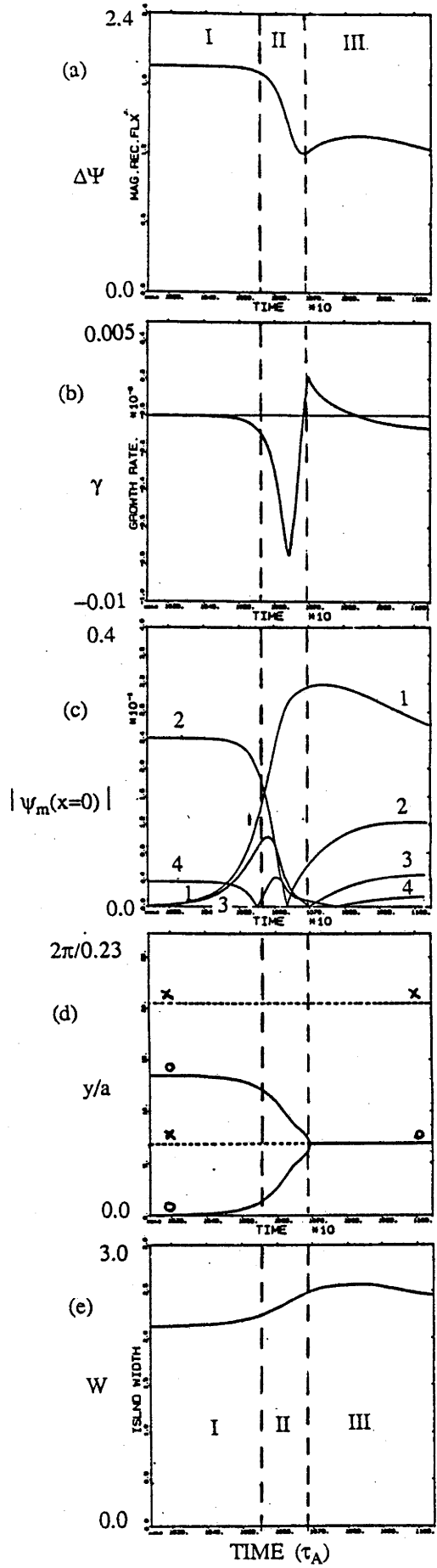
Fig.25  
PARAMETER VARIATION  
DURING COALESCENCE:

$S = 200.$

$\nu = 0.01$

$k_p = 0.23$

$X_w = 2.5$



COALESCENCE: PHASE I. - PREPARATION

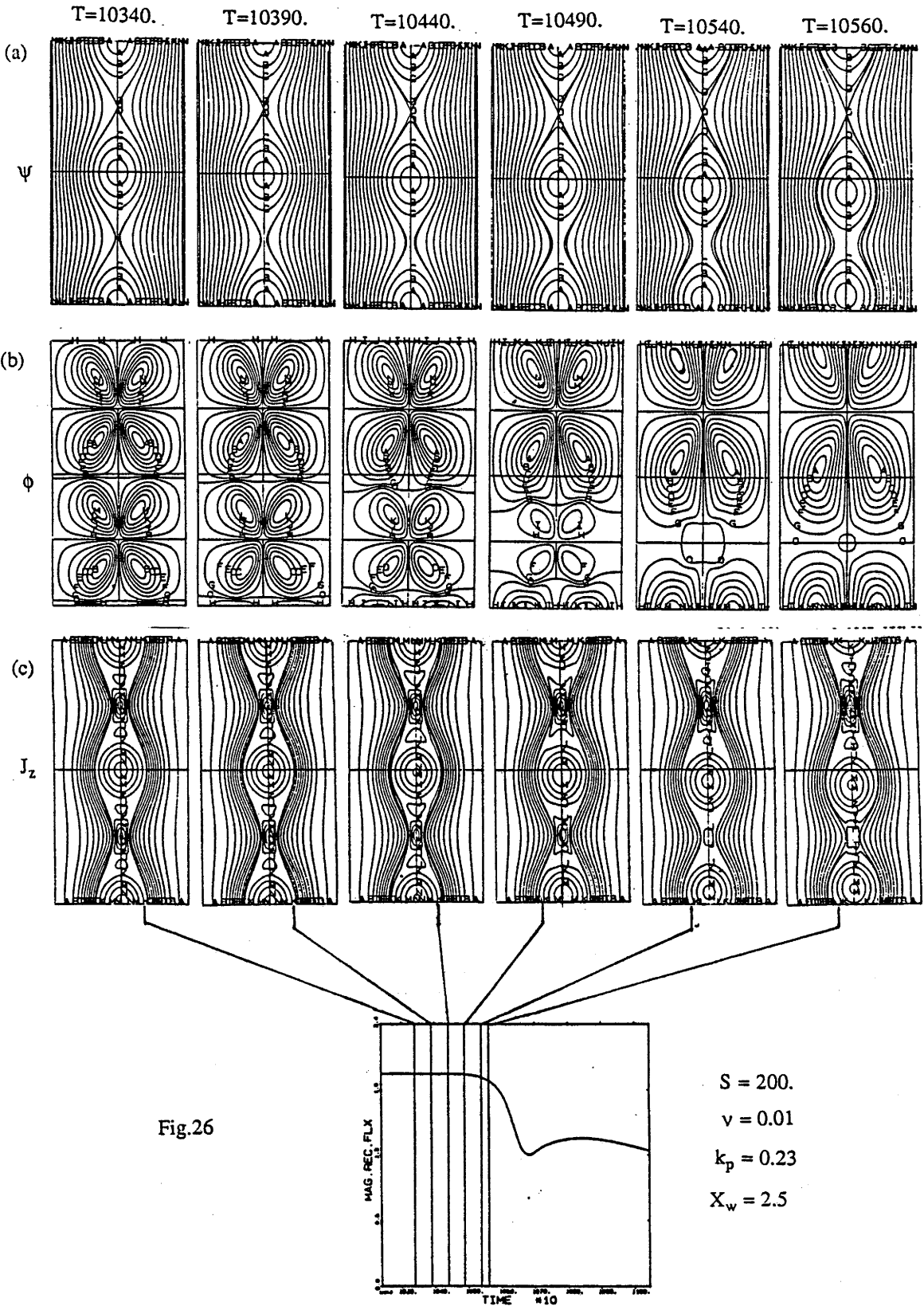


Fig.26

COALESCENCE : PHASE 2 - RECONNECTION

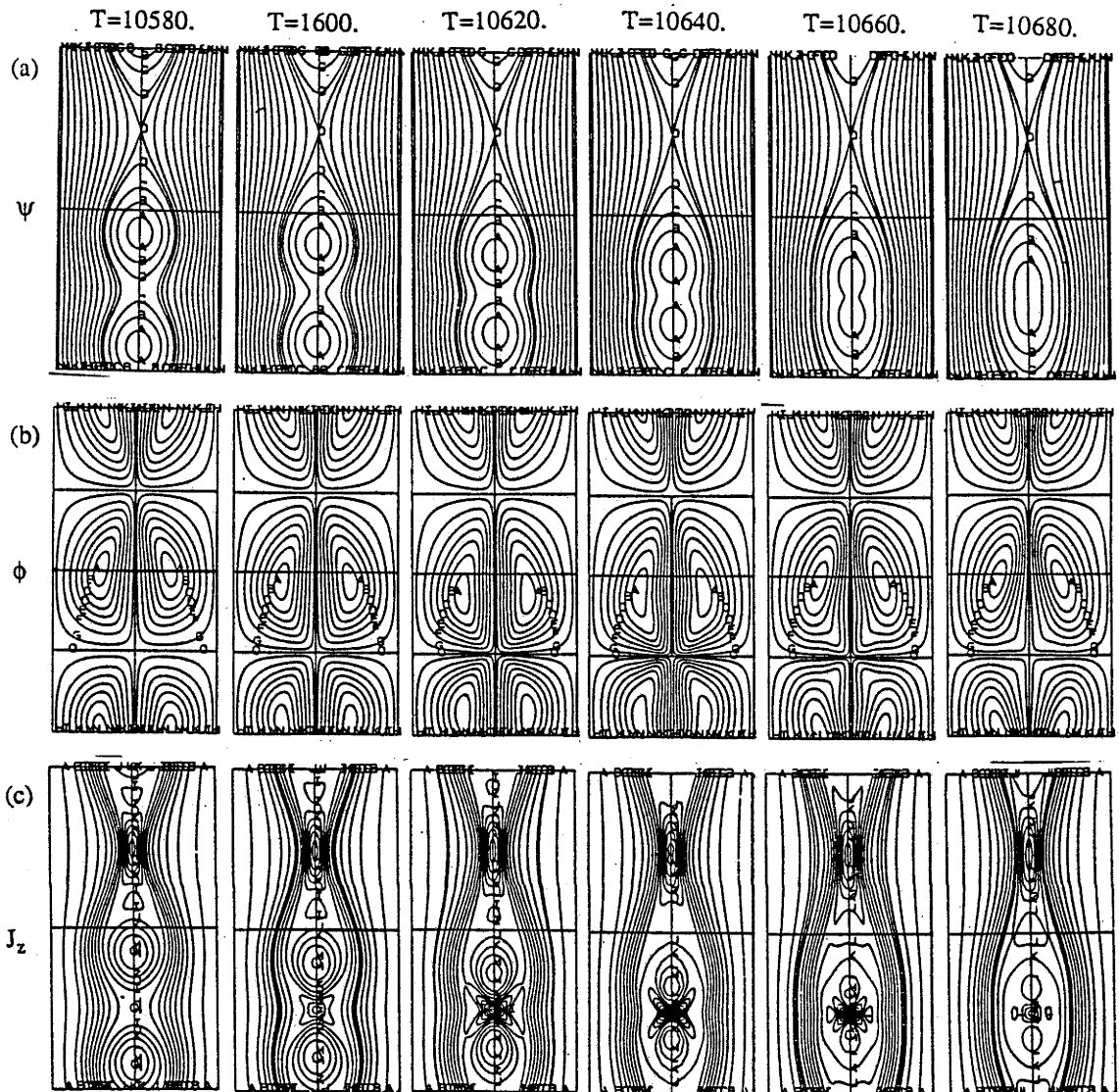
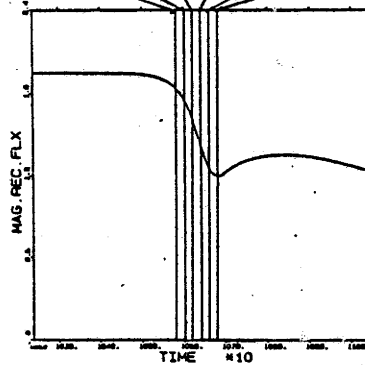


Fig.27



$S = 200.$   
 $\nu = 0.01$   
 $k_p = 0.23$   
 $X_w = 2.5$

COALESCENCE : PHASE 3 - RELAXATION

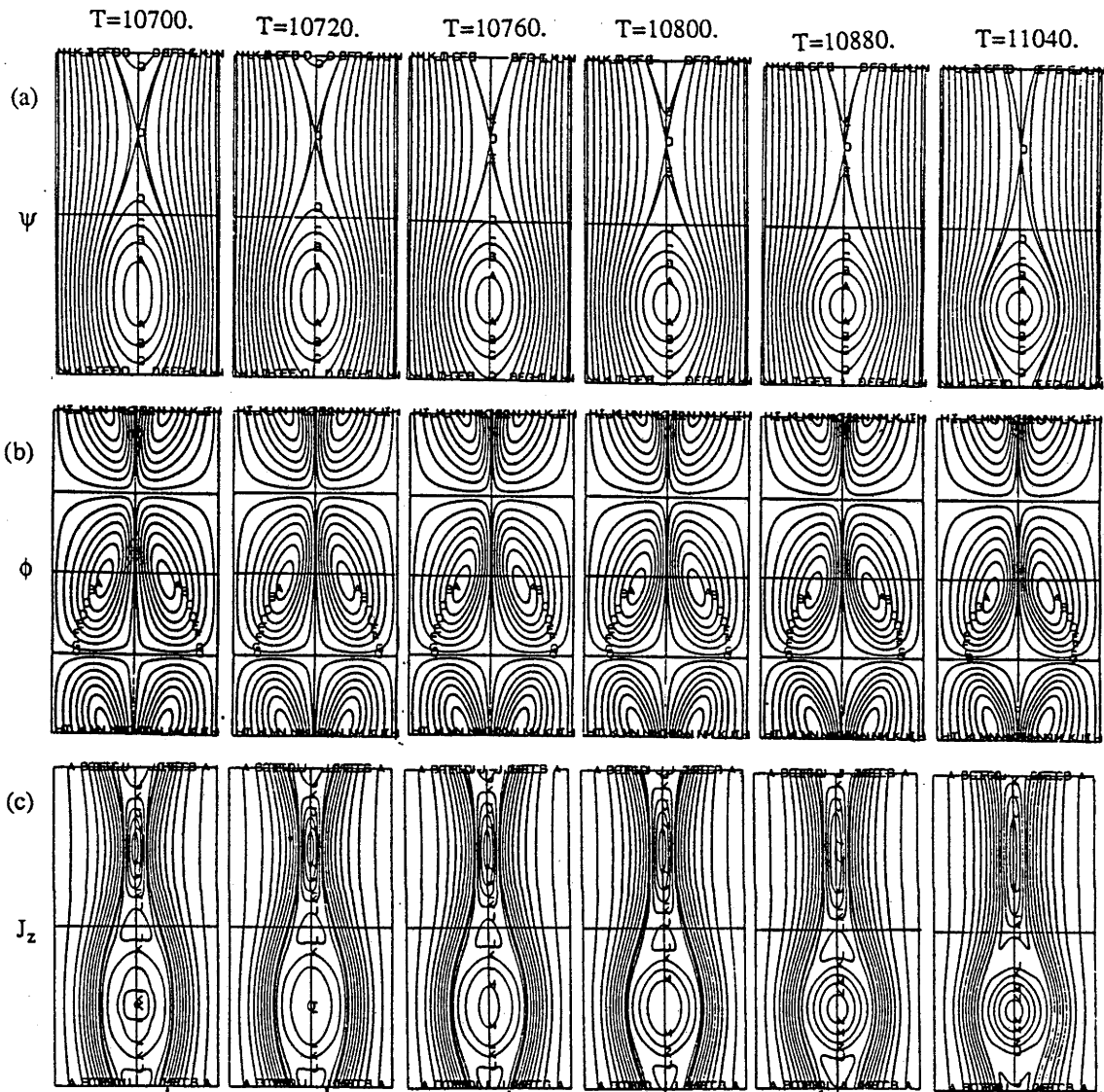
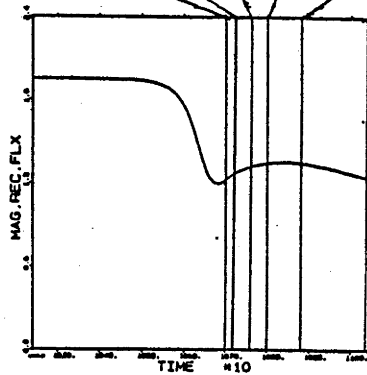


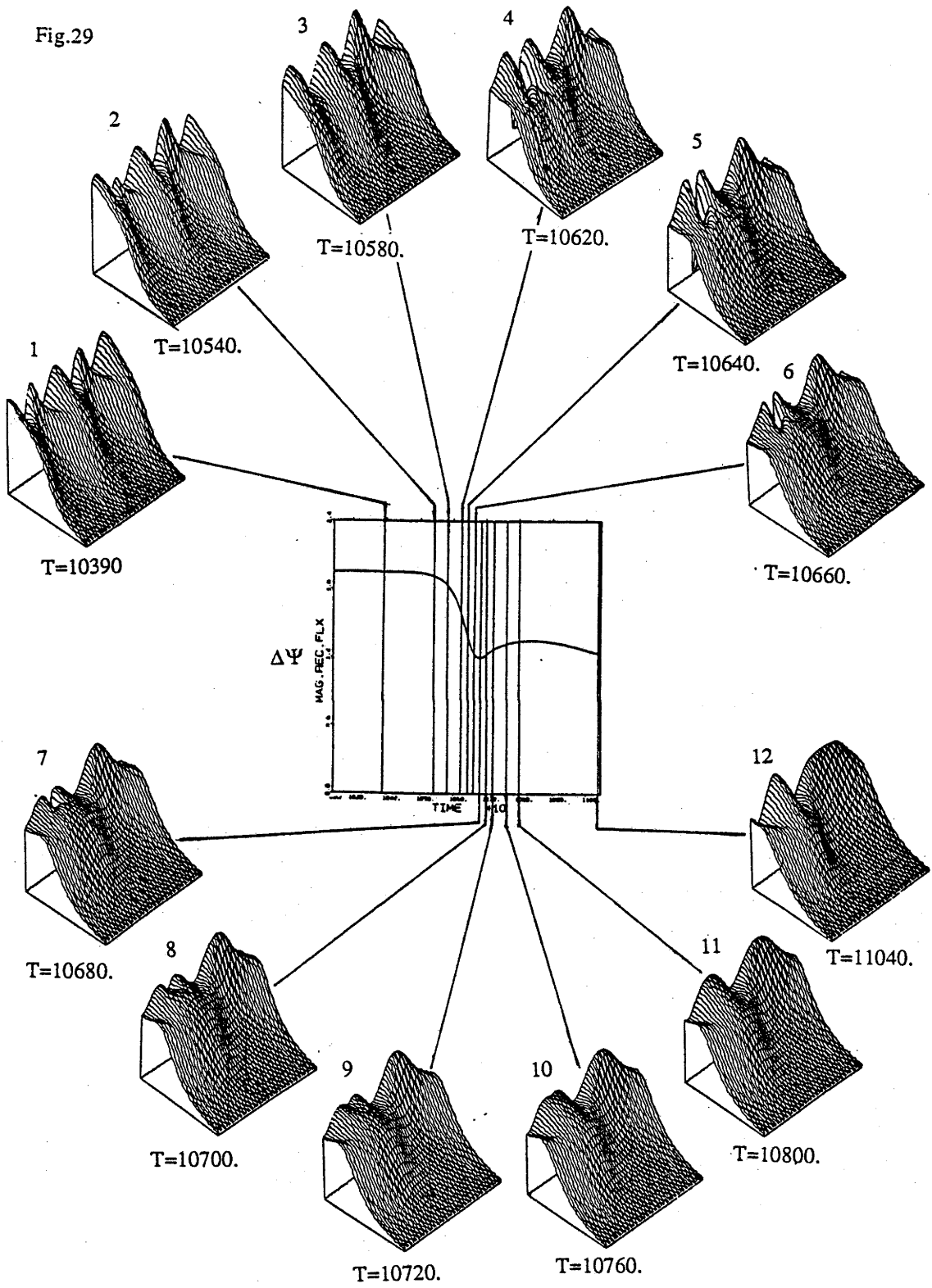
Fig.28



$S = 200.$   
 $\nu = 0.01$   
 $k_p = 0.23$   
 $X_w = 2.5$

3-D Z-CURRENT DENSITY DURING COALESCENCE.

Fig.29



then has plasma entering along the y-axis and exiting parallel to the x-axis, the opposite to that of the original x-point so that the reconnection during coalescence occurs in the same manner as for the initial tearing mode but orientated at right angles to it. The new flow pattern is also consistent with the new o-point that will exist there afterwards. The first 3 frames of fig.29 show, in 3-D perspective, that as the x-point changes its identity it also loses its current spike. In general the time dependent diagnostic parameters in fig.25 show little or no change during phase(I) except for the growth of the odd Fourier modes but the changes that have occurred, especially in the fluid motion, have prepared the way for the considerable reconnection that defines the next stage of the coalescence process.

### Phase II Reconnection :

With the appropriate flow structure now set up the two islands begin to approach each other at a faster rate, see fig.25(d) and 27(a), with a consequent steepening of the current and flow gradients and an increased compression of the field lines, see fig.27(b) and (c), so that a localized neutral layer is generated between them. From frames 4,5 and 6 of fig.29 it can be seen that this corresponds to the formation of a sharp current trough or reverse current sheet where once there was a peak and roughly defines the extent of the diffusion region within which the field lines of the two islands will reconnect to form a single island topology. Phase II is classified as the reconnection stage of the coalescence process because according to fig.25(a) and (b) it defines the stage during which the most flux is reconnected and at the fastest rate. Besides the sharp drop in the reconnected flux there is a small increase in the island width, see fig.25(e), as the pair of islands merge to form a single larger one. Fig.25(c) shows that the start of phase II occurs when the rising single island mode,  $\psi_1$ , begins to dominate over the falling double island Fourier mode,  $\psi_2$ . The end of phase II occurs when the flux destruction ends and is marked more precisely by the point at which the o-points come together as shown in fig.25(d).

### Phase III Relaxation :

After the majority of the reconnection is complete a relaxation phase follows during which the new composite island relaxes to a more preferable shape while removing

remnants of the reconnection process, see fig.28. The current trough is filled in to form the usual o-point current peak, see frames 7 to 12 of fig.29, and the velocity gradient around this new o-point is reduced, see fig.28(b). The wavelength of the new island that emerges from the reconnection phase is now longer than the preferred island length with  $\lambda = L_p = 2\pi/0.23 > L_{pref} \approx 0.35$ . As a consequence the central island region shrinks creating a steady decay of the reconnected flux during phase III although initially there is a rise as shown in fig.25(a) due to the increase in flux associated with the filling in of the current trough.

Biskamp and Welter <sup>[24]</sup>, in an earlier study of coalescence (using the exact island equilibrium), distinguish only two stages, the first of which corresponds to the Preparation phase described here plus the early part of Phase II describing the flux build up, which they, perhaps more appropriately describe as the 'MHD phase' since it represents that part of the process that occurs without any dissipation and hence resembles the evolution of the ideal MHD coalescence instability found by Finn and Kaw <sup>[22]</sup> and simulated by Pritchett and Wu <sup>[23]</sup>. They make no distinction between the Reconnection and the Relaxation phases but instead describe this part of the process simply as the Reconnection phase.

At no stage was there any evidence of secondary island formation in the neutral layer between the coalescing islands like those found by Biskamp <sup>[30]</sup>. According to Bhattacharjee, Brunel and Tajima <sup>[26]</sup> these secondary islands are always removed from the neutral layer by the flow and suggest that the results of Biskamp are a consequence of non-general symmetry constraints on the flow field employed to achieve higher numerical resolution.

### I-3.5 Long Time Behaviour with Symmetry Breaking and Period Doubling Bifurcations

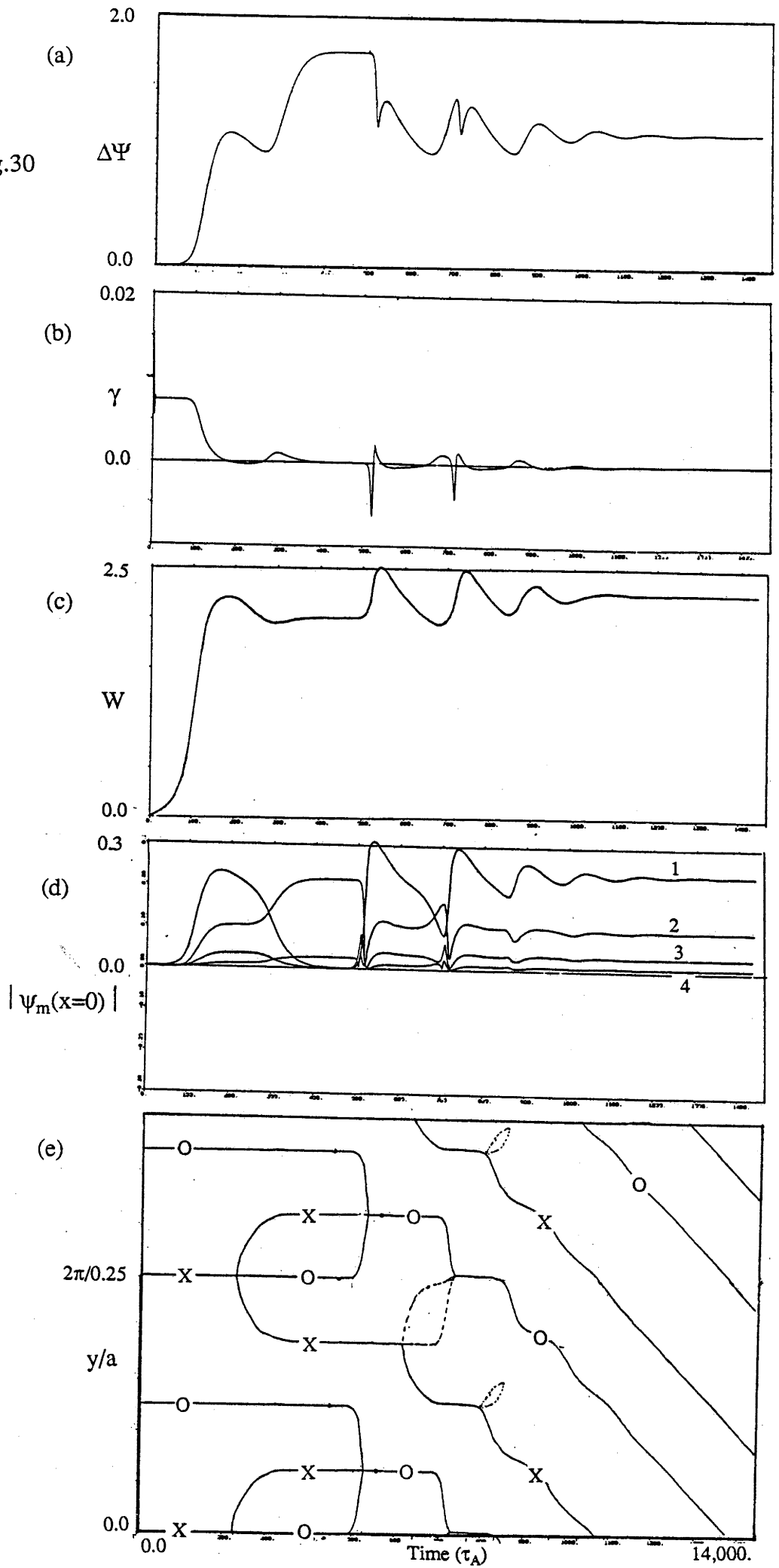
By this stage it should now be clear, especially from the forked behaviour of the  $x$  and  $o$ -point positions versus time, that coalescence and secondary island generation are essentially opposite topological transformations. Fig.25(d) shows that during coalescence two adjacent  $o$ -points merge together eliminating an  $x$ -point to remove an island while figs.18(c) and 19(d) show that during secondary island generation an  $x$ -point splits in two producing a new  $o$ -point between them to create a new island. In a sense secondary island generation and coalescence could be considered as creation and annihilation operations on the island chain.

It should also be apparent from the examples given in the previous two sections, fig.20 and figs.26 and 28, that the final state created after secondary island generation is similar to the state existing just before coalescence, and *vice versa*. In fact the two examples actually come from the same run with  $L_p = 2\pi/0.23$ . To see how this can occur we will now consider the full evolution of a similar run made with  $K_p = 0.25$ . This is shown in fig.30. By following the evolution of these diagnostic quantities, especially the reconnected flux and the positions of the  $x$  and  $o$ -points, it is possible to resolve the sequence of events by comparing them section by section with the plots of figs.25 and 19 corresponding to the instances of coalescence and secondary island generation.

The tearing mode is triggered with a wavelength  $\lambda = L_p = 2\pi/0.25$  and grows to form a chain of magnetic islands with that wavelength. However because  $L_p > L_{crit}$  the inner reconnected field loops contract to their 'preferred' aspect ratio, as do the  $o$ -point current peaks, causing the  $x$ -point current sheets to lengthen, so that they eventually become unstable to a secondary tearing mode. This results in the generation of secondary magnetic islands which equalize with the primary islands to form a new chain with half the original wavelength. The  $o$ -point current peaks, which have only been slightly decreased in size, take up a bigger fraction of the island length, leaving less room for the  $x$ -



Fig.30



point current sheets, which are consequently now short enough to be stable to further tearing modes. According to fig.30(a) the plasma appears to settle in this double island state, which is the same stage reached in the example shown in fig.18(a) of section I-3.3. However now that the wavelength,  $\lambda = L_p < L_{pref}$ , the o-points are close enough for the attraction of the parallel current channels to induce the islands to coalesce back to the single island state, i.e. back to a state with one island per periodicity length. This is marked by the sharp drop in reconnected flux that corresponds to the second phase of the coalescence process. Following this, the central island regions contract and the x-point current sheets lengthen, bringing the plasma back to the initial island state in which the x-point current sheets again become unstable to the secondary tearing mode so that the cycle can begin over again. However during the next secondary island generation the two processes begin to overlap, that is, the primary islands start coalescing with the secondary islands before the secondary islands have fully grown. The overlap increases with time so that the coalescence and regeneration reduce to a series of asymmetric peristaltic-like squashing and stretching motions in which a bulge forms to one side of the primary island, and in the process of being drawn back into the main body of the island induces a small shift in the island position, see fig.31. This is seen as a damped oscillation in all the diagnostic quantities of fig.30. As the competing mechanisms become more closely synchronised, the motion is damped down to a rigid drift of a chain of asymmetric islands with one island per periodicity length as shown in fig.32(b). It seems that the final state is reached when a perfect balance is achieved between the tendency to generate secondary magnetic islands and the tendency for them to coalesce.

In terms of the saturated behaviour as a function of  $L_p$  the asymmetric nature of the islands means that the critical point at  $L_p = L_{crit}$  is a parity breaking bifurcation. It represents the second such symmetry breaking transition as the first would be the onset of the tearing mode itself which breaks the translational symmetry, see fig.33(b).

Since the total momentum is conserved, the drift is actually a travelling wave motion of the magnetic island and its vortical flow structure through the stationary plasma. The

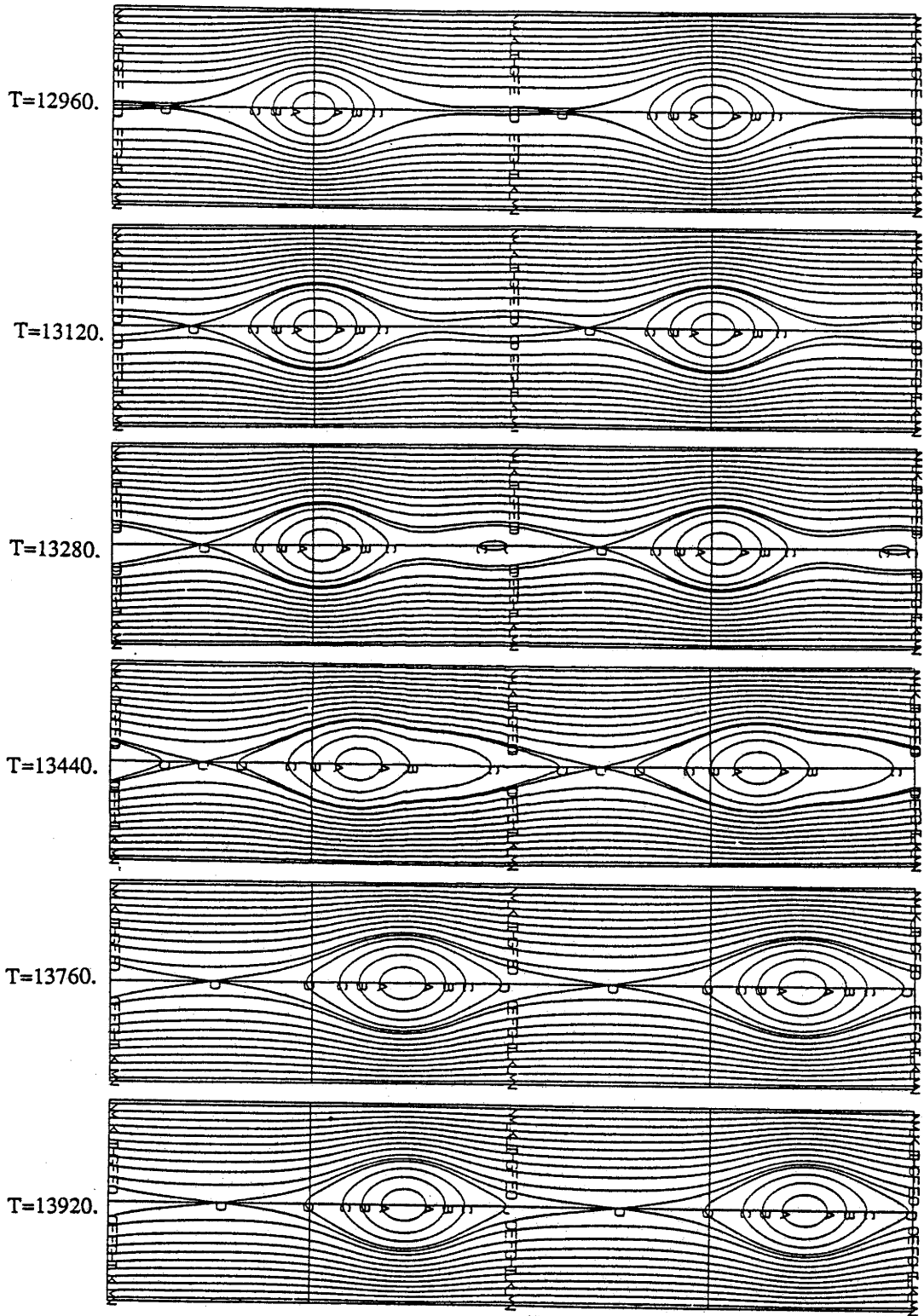


Fig.31

phase velocity of the travelling wave is given by the gradient of the  $x$  and  $o$ -point positions versus time, see fig.30(e), and shows it to be less than the resistive diffusion velocity, making it consistent with the degree of decoupling of the field from the fluid allowed by the finite resistivity. Again looking at fig.30(e) the motion can be seen to originate from the smoothing out of the  $1/4$  wavelength phase shift that is produced after the island chain has undergone both secondary island generation and coalescence.

This type of evolution also occurred in essentially the same manner for simulations made with  $K_p = 0.26, 0.25, 0.23, 0.19, 0.15, 0.14$  and  $0.13$ . In each case the final saturated state was a chain of drifting asymmetric islands as shown in fig.32(b),(c),(d) and (e). These contour plots of  $\psi$  have been cut and pasted in order to show a full island length which, because of the drift, is usually out of phase with the simulation region. They have also been orientated with their long neck sections pointing in the same direction so that the drift in all cases depicted is from left to right.

The direction of the travelling wave, positive or negative, depends on which side the primary island moves in when it first coalesces with a secondary island, and, since there does not appear to be any reason for a preferred direction to exist, the choice should be random, perhaps depending on the rounding error in the calculation. This seems to be backed up by the fact that three of the cases ( $K_p = 0.26, 0.25$  and  $0.14$ ) had phase velocities in the opposite direction to the others. This means that the parity breaking transition at  $L_p = L_{crit}$  also represents a bifurcation of the phase velocity and from fig.33(a) it appears to be a typical parabolic bifurcation. The plot shows the zero phase velocity symmetric island solution becoming unstable for  $L_p > L_{crit}$  and being replaced by two finite phase velocity solutions corresponding to the right and left going asymmetric island states.

The onset of the first secondary island generation occurs earlier in the evolution the longer is the periodicity length. For the case with  $L_p$  very close to  $L_{crit}$ , i.e.  $K_p = 0.263$  shown in fig.18(a), the initial tearing mode has almost saturated before the  $x$ -point current

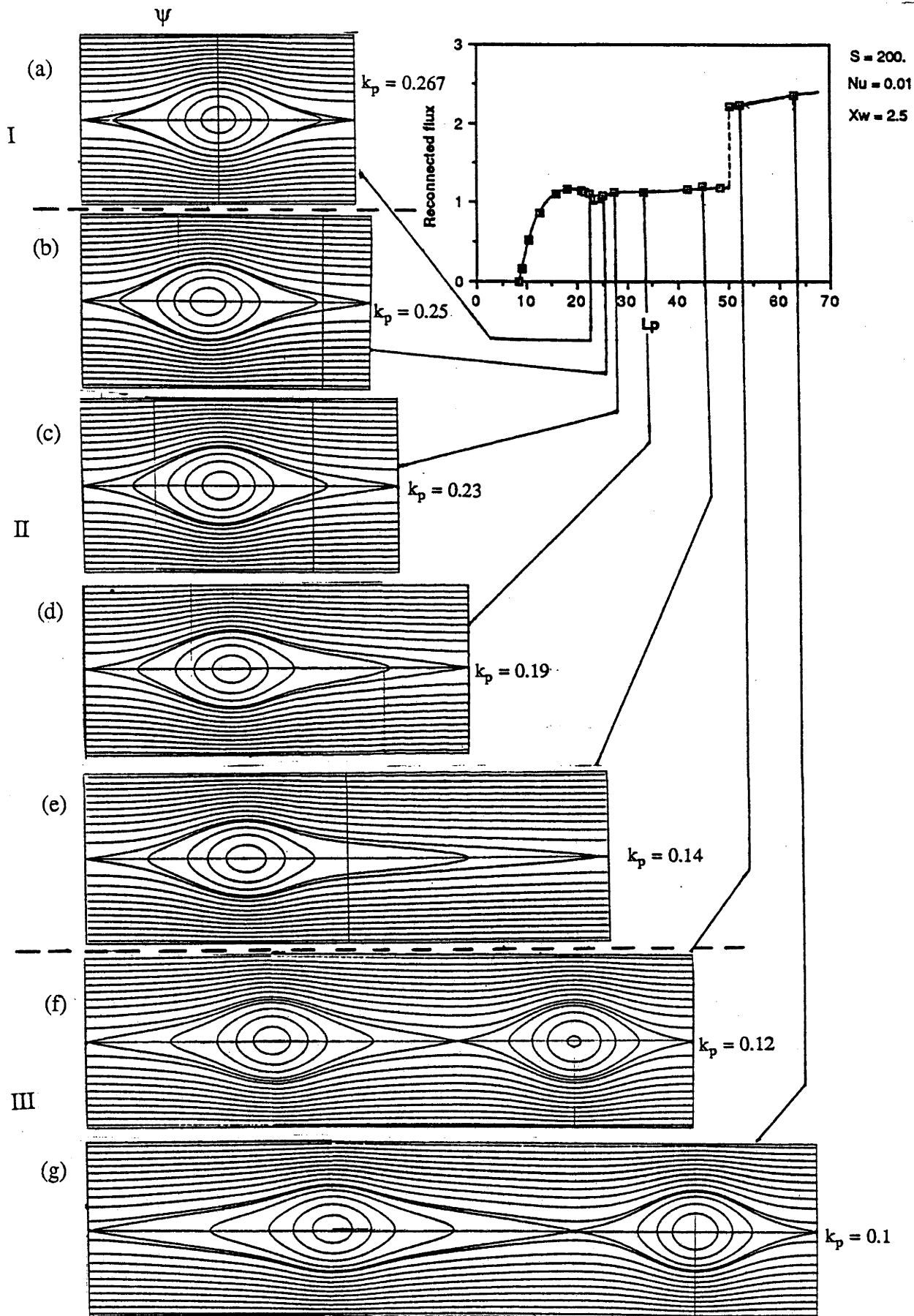


Fig.32

Fig.33(a)

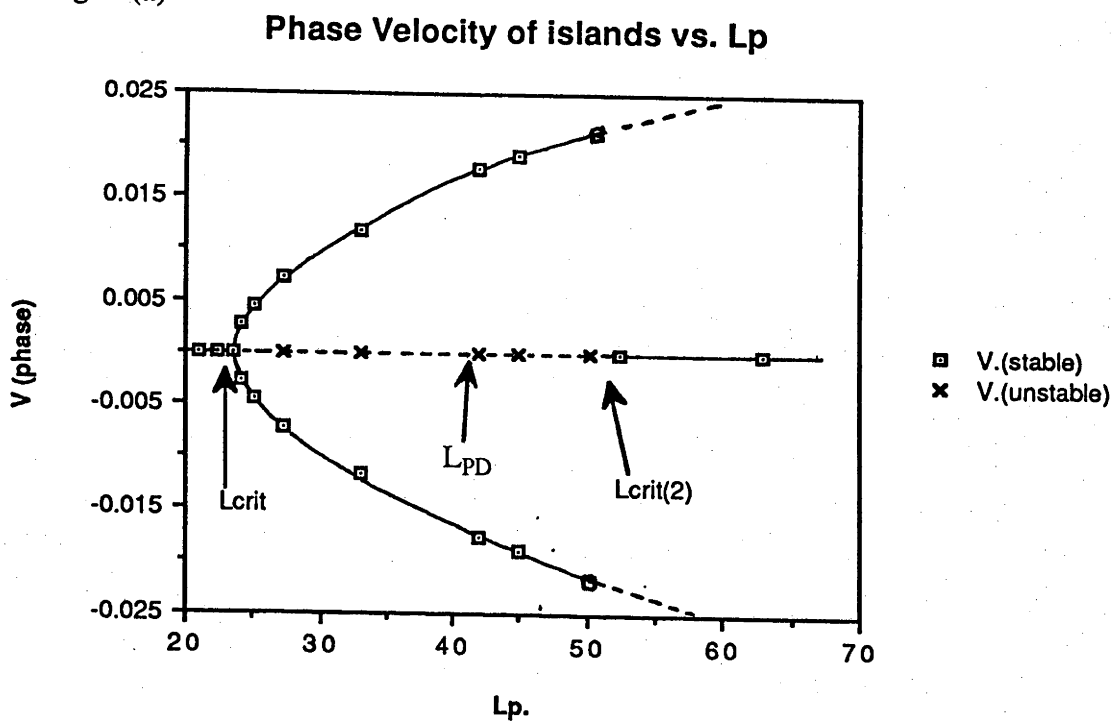
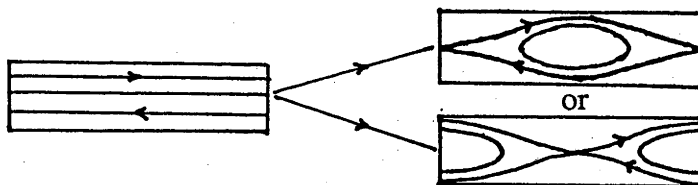
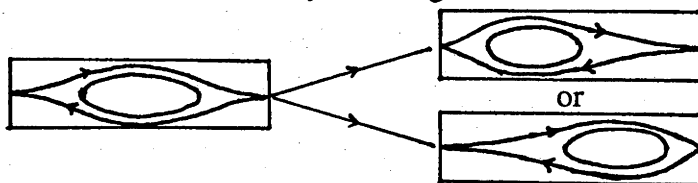


Fig.33(b)

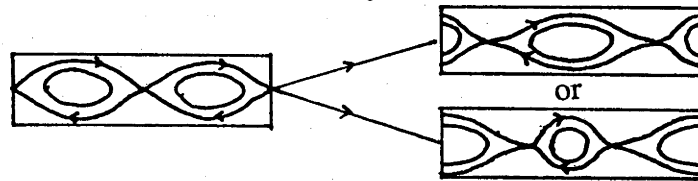
Tearing Mode Bifurcation (breaks translational symmetry)



Parity Symmetry Breaking Bifurcation



Period Doubling Bifurcation



sheets have got long enough to go unstable to the secondary tearing mode. With  $L_p$  increased to  $L_p = 2\pi/0.25$ , see fig.30(a), the x-point current sheets reach the critical length soon after the overshoot of the saturating primary tearing mode while for  $L_p$  increased to  $L_p = 2\pi/0.14$  the periodicity length is so much greater than the 'preferred' island length that the current sheets become unstable before the primary tearing mode has finished growing. The time between the first regeneration and coalescence also decreases with  $L_p$  so that although they are well separated for  $K_p = 0.25$  they overlap straight away for  $K_p = 0.14$  .

From fig.32, showing the flux contours of several saturated states for increasing values of  $L_p$ , it can be seen that the size and aspect ratio of the inner reconnected field loops are still reasonably well preserved despite the increased length of the islands and the growing asymmetry. From the corresponding contour plots of the current density in fig.34 it can be seen that the asymmetry is mostly in the x-point current sheets (see also the 3-D perspective plots in fig.35) which increase in length with  $L_p$  while the o-point current peaks remain much the same size. The asymmetry of the x-point current sheets must be the feature which provides stabilization against secondary island generation since symmetric current sheets of these lengths have proven to be unstable. Since they represent stable equilibria the asymmetry must somehow also stabilize the tendency to coalesce.

Consider now the unstable zero phase solutions for  $L_p > L_{crit}$ . If a parity symmetry constraint (i.e.  $\psi(x,y) = \psi(x,-y)$ ,  $\phi(x,y) = -\phi(x,-y)$  ) is enforced in the simulation by only exciting the cos components of  $\phi$  in the initial perturbation, then the symmetry breaking bifurcation is prevented from occurring. The secondary island still forms, but, because it produces a quarter wavelength shift of the x-points, the islands are prevented from coalescing since this would require coupling to the cos modes of  $\psi$ . As a result the plasma is forced to saturate into a symmetric double island state (i.e. with two islands per periodicity length). Of course, as soon as the symmetry constraint is relaxed the islands are able to coalesce and so forth until the asymmetric travelling island solution is attained.

$J_z$

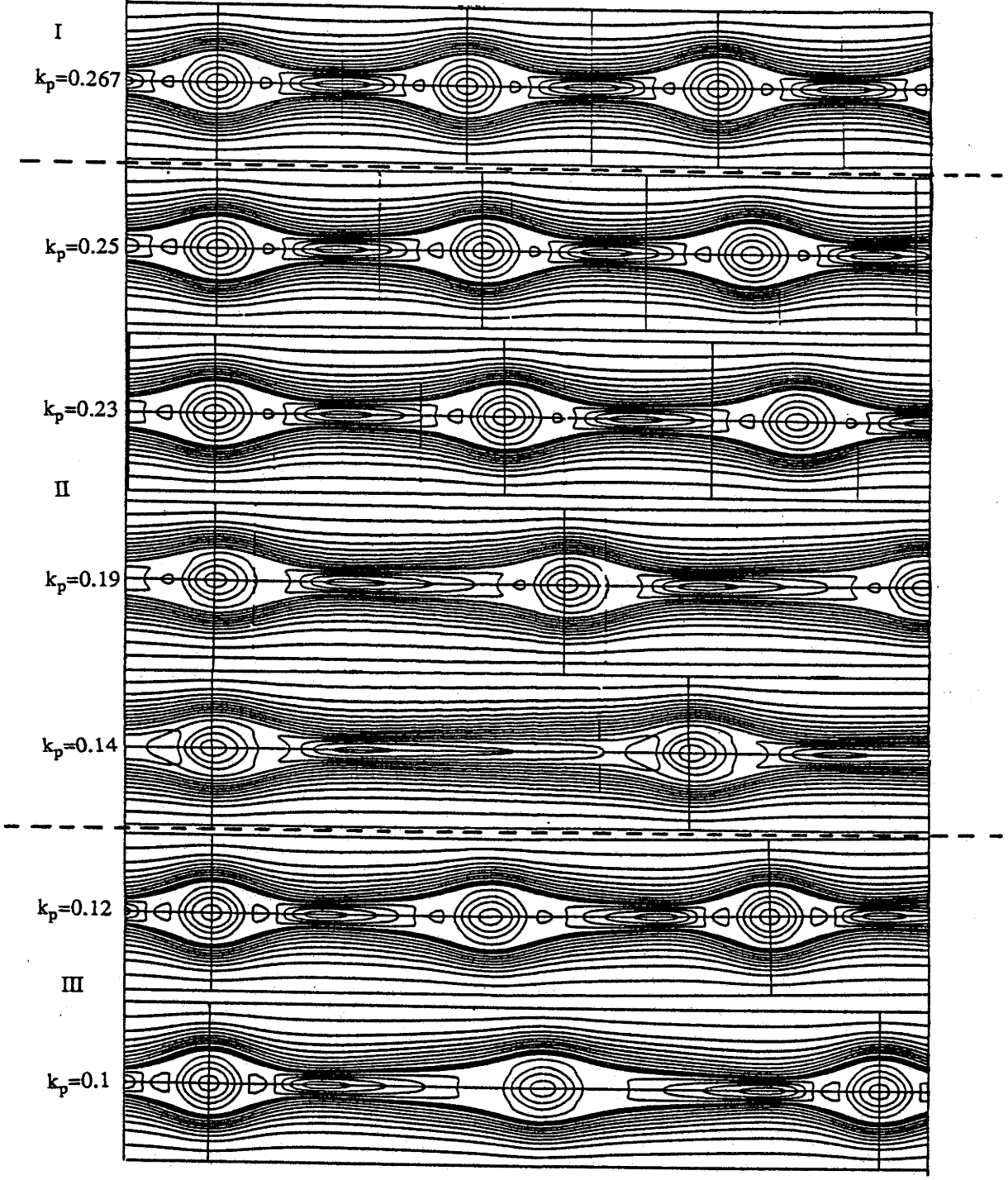


Fig.34



However it is instructive to consider further these symmetric solutions as will become apparent from the set of simulations, made in this way, with  $k_p = 0.23, 0.19, 0.15, 0.14, 0.125, 0.12$  and  $0.1$ .

The first three of these developed into double island states with equal sized islands at saturation, identical to each other as well as identical to islands produced in simulations with half the periodicity length so that the effective periodicity length was reduced to  $L_p/2$ . Thus with the symmetry constraint imposed the symmetry breaking bifurcation at  $L_p = L_{crit}$  reduces to a period halving transition. The amplitudes of the odd Fourier modes in this case are all vanishingly small, as shown in fig.18(d). The cases with  $L_p > 2\pi/0.15$ , on the other hand, developed into modulated double island states with one long island and one short island per periodicity length as shown in fig.32 for the cases with  $k_p = 0.12$  and  $0.1$ . Note that, because of the symmetry constraint, they actually form with a long/short island in the middle of the simulation region and half a short/long island on either side, whereas the plots in fig.32 have been cut and pasted to show the complete island lengths. With these cases the odd Fourier modes have finite amplitude, especially  $\psi_1$ , which is the mode that produces the modulation of the islands. The disparity in the island size increases with periodicity length along with the amplitude of the  $\psi_1$  mode as shown in figs.36 and 37 by the series of crosses. By ruling a line through these points and extrapolating back to the axis to where  $\psi_1$  vanishes, we can determine the value of  $L_p$  corresponding to the onset of this change in island configuration to be  $L_p \approx 41.8$ , i.e.  $k_p \approx 0.15$ . The transition to the modulated island state above this value of  $L_p$  destroys the sub-periodicity length of  $L_p/2$  and therefore represents what is known as a period doubling bifurcation. We shall denote it by  $L_{pD}$ . In other words, when  $L_p > L_{pD}$  the identical double island solution becomes unstable and the system ( which still has the symmetry constraint imposed) bifurcates to either a modulated island state with the short island in the middle or one with the long island in the middle as shown in fig.33(b). The difference in the two states is just a half wavelength phase shift of the island chain.

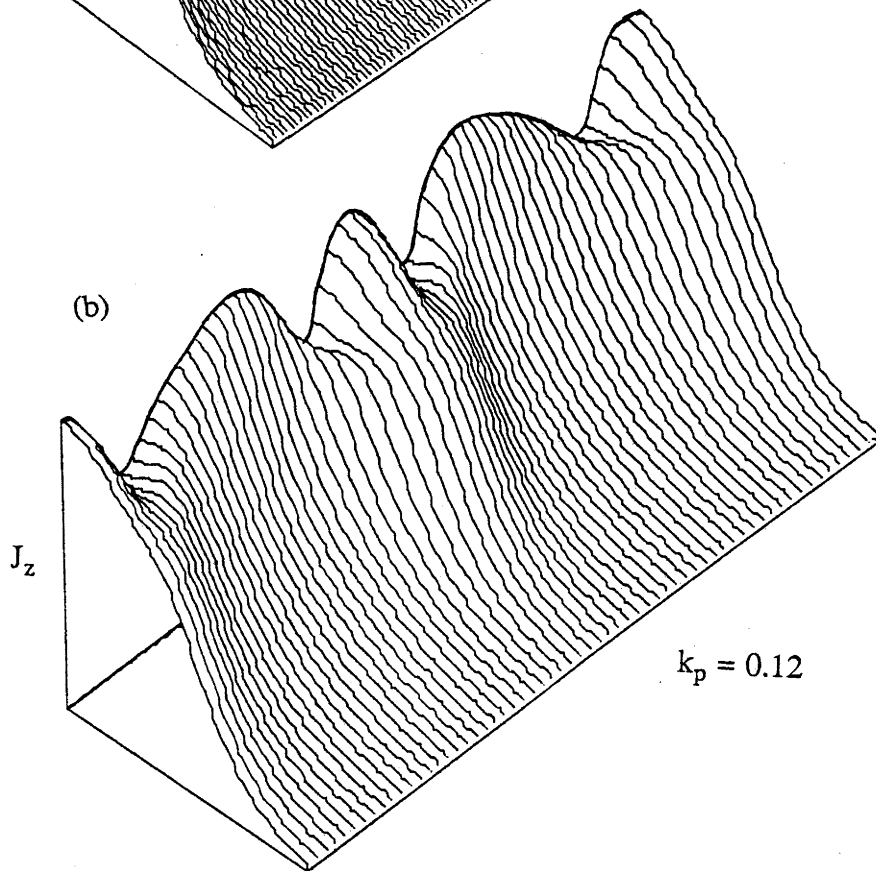
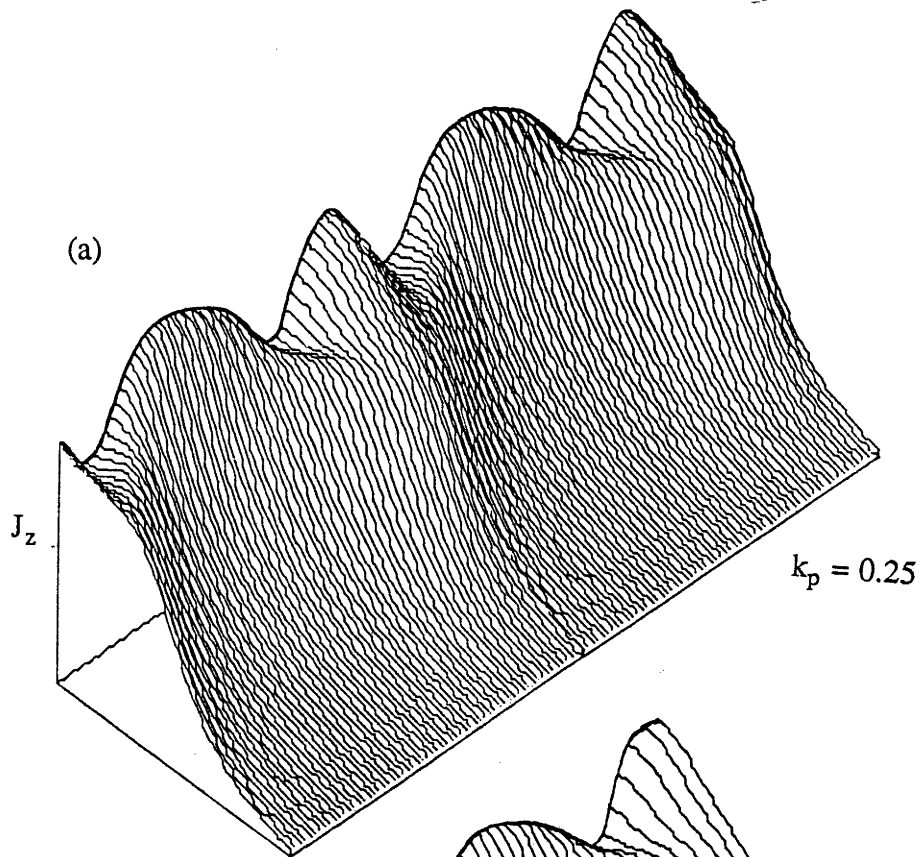


Fig.35

Looking now at fig.34 showing the corresponding contour plots of the z-current density we see that the x-point current sheets of the modulated island states are asymmetric just like those for the asymmetric travelling island solutions with half the periodicity length, although in this case they are arranged symmetrically about each o-point. The similarity of the x-point current sheets in these two types of solution is more clearly shown in the 3-D perspective plots of  $J_z$  in fig.35.

Having identified the period doubling bifurcation for the symmetric solution branch it is now worth considering the stability of these new modulated island states with the parity symmetry constraint removed. This is easily done by restarting the simulation with a small symmetry breaking perturbation of the cos component of  $\phi_1$ . When this was done for the cases with  $L_p < L_{PD}$  the perturbation immediately developed an exponential growth rate eventually leading to the usual sequence of coalescence and secondary island generation back to the asymmetric single island travelling island solution. For the modulated island states with  $k_p = 0.15, 0.14$  and  $0.125$ , i.e. with  $L_p$  just greater than  $L_{PD}$ , the perturbation amplitude was much more docile and tended to oscillate although with an ever increasing amplitude indicating that these solutions are also unstable, but more weakly. However, for the last two modulated island states with  $k_p = 0.12$  and  $0.1$  the perturbation exponentially decayed away showing that they are, in fact, stable solutions even with the symmetry constraint removed.

Thus we now have another critical transition point at  $L_p = L_{crit(2)}$ , located between  $L_p = 2\pi/0.12$  and  $2\pi/0.125$ , which appears to correspond to the interchange of stability from the asymmetric travelling island state to the symmetric modulated double island state, as indicated in fig.33(a). The stability of these solutions again seems to be related to asymmetric property of the x-point current sheets. As  $L_p$  is increased above  $L_{PD}$ , the x-point current sheets become more asymmetric until finally at  $L_p = L_{crit(2)}$  the asymmetry is sufficiently developed to stabilize the tendency of the islands to coalesce and regenerate so

that, with or without the symmetry constraint in place, the modulated double island state becomes the stable solution.

The double island state was attained with only one secondary island generation, and not the repetitive action of coalescence and regeneration, so the islands do not develop any drift. That is, their phase velocity is zero. It would seem therefore that the parabolic variation in the phase velocity of the asymmetric travelling island solution, shown in fig.33(a), discontinuously terminates at this second transition point although it is possible that this may just be a consequence of the initial conditions used - the plasma may have been started in the basin of attraction of the zero phase velocity state.

To see this more clearly, consider the following analogy of a potential surface with a saddle point, corresponding to the unstable symmetric solution, and two wells on either side, the bottom points of which correspond to the two stable asymmetric travelling island states. This effectively describes the situation for  $L_p < L_{crit(2)}$ . The saddle point defines a stable solution only when the system is constrained to the ridge passing through the saddle point in analogy to the way that the symmetric island solution is stable only when the symmetry constraint is enforced. Once this constraint is relaxed the trajectory would fall away from the saddle into one of the wells corresponding to the transition to the asymmetric travelling island state.

As  $L_p$  is increased towards  $L_{crit(2)}$  one can imagine the potential surface changing so that the saddle point gets lower and lower until for  $L_p > L_{crit(2)}$  it becomes lower than the wells and hence takes over as the most stable state of the system. This could happen in at least 3 ways. As the saddle point moves below the wells either: (1) the wells cease to exist in which case the asymmetric travelling island solutions no longer exist and the parabolic branches in the phase velocity plot would simply terminate, or (2) The wells become points of inflection so that the symmetric travelling island solution exists but is no longer stable producing an interchange of stability to the symmetric modulated island solution which would then be represented by a well on the potential surface or (3) The wells remain locally as wells so that several basins of attraction exist with the final solution

depending on which basin the initial conditions are closest to. The wells of the asymmetric travelling island solution may eventually disappear at a higher value of  $L_p$  so that a hysteresis type bifurcation is formed; an occurrence common in bifurcation theory<sup>[61]</sup>. This would mean that close to  $L_{crit(2)}$  both the symmetric, modulated double and the asymmetric, travelling single island states would be stable with the transition point occurring at a different value of  $L_p$  depending on which state we force the state into to begin with. With the simulations made so far, the possible extent of the overlap, if it exists, is limited to between  $k_p = 0.125$  and  $0.12$ . Further runs made between these limits would be required to resolve the question of hysteresis but this will be left for a later investigation.

The flux contour plots in fig.32 and the current contour plots in fig.34 are divided by dotted lines into the three types of saturated states determined so far as a function of  $L_p$ . The first plot is an example of the symmetric stationary single island state that exists for  $L_p < L_{crit}$ . The next four are examples of the asymmetric, single island, travelling wave solutions that occur for  $L_{crit} < L_p < L_{crit(2)}$  and the last two are examples of the stationary modulated double island solutions that exist for  $L_p > L_{crit(2)}$ . These are all referred to a plot of the saturated reconnected flux as a function of  $L_p$  which highlights the difference in the nature of the transitions at  $L_{crit}$  and  $L_{crit(2)}$ . The symmetry breaking transition at  $L_p = L_{crit}$  is marked by a sharp dip in  $\Delta\Psi$  while the transition at  $L_p = L_{crit(2)}$ , which appears to occur because of the need to keep the density of islands within a certain range, is marked by a discontinuous jump in  $\Delta\Psi$  corresponding to the extra reconnection produced by the introduction of a second island. Note that  $\Delta\Psi$  is the total reconnected flux over one periodicity length. If this was changed to the average reconnected flux per unit length the second transition would still be discontinuous but the variation would look more like a saw tooth with  $\Delta\Psi$  decreasing steadily before the transition, then jumping up and decreasing again after the transition. The transition thus also serves to bring the average reconnected flux per unit length back close to the value it has at  $L_{pref}$  and

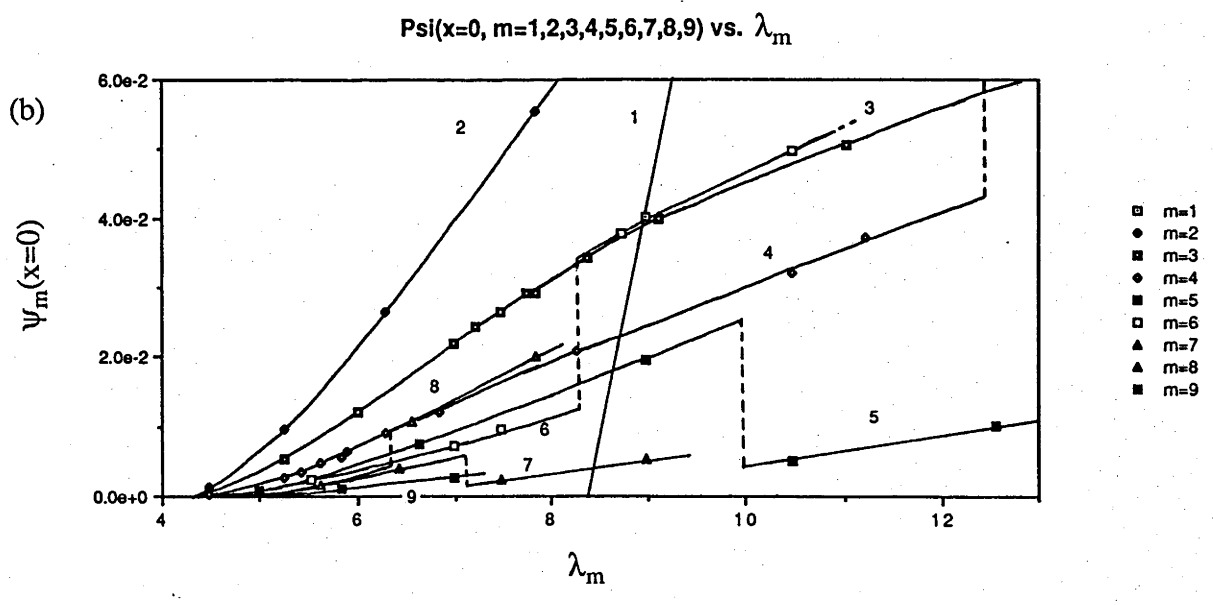
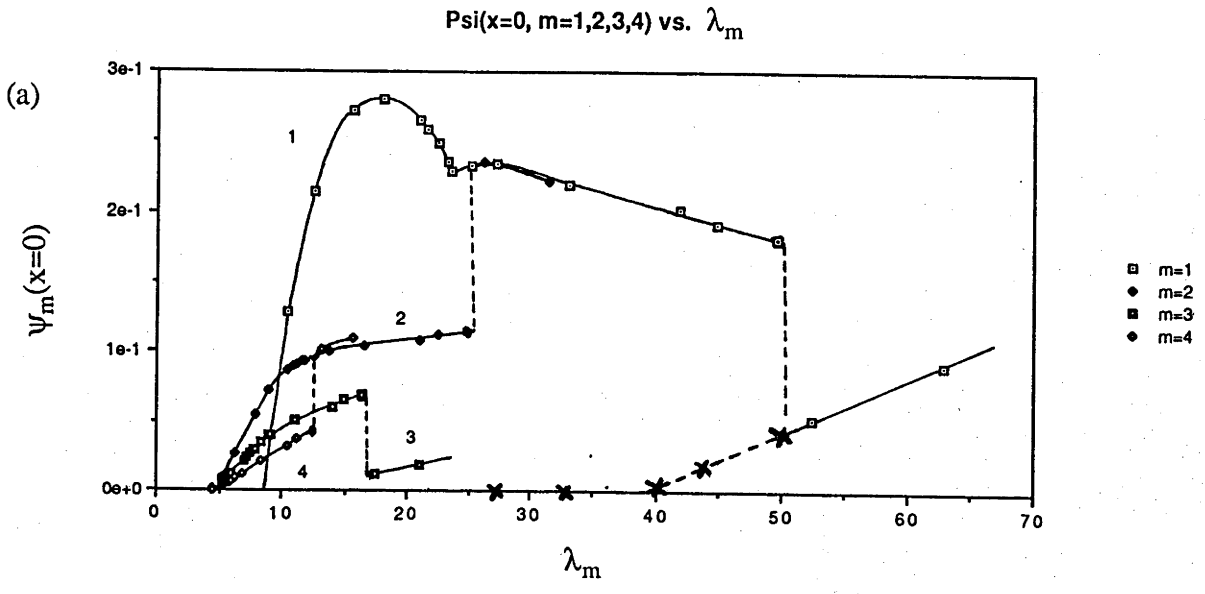


Fig.36

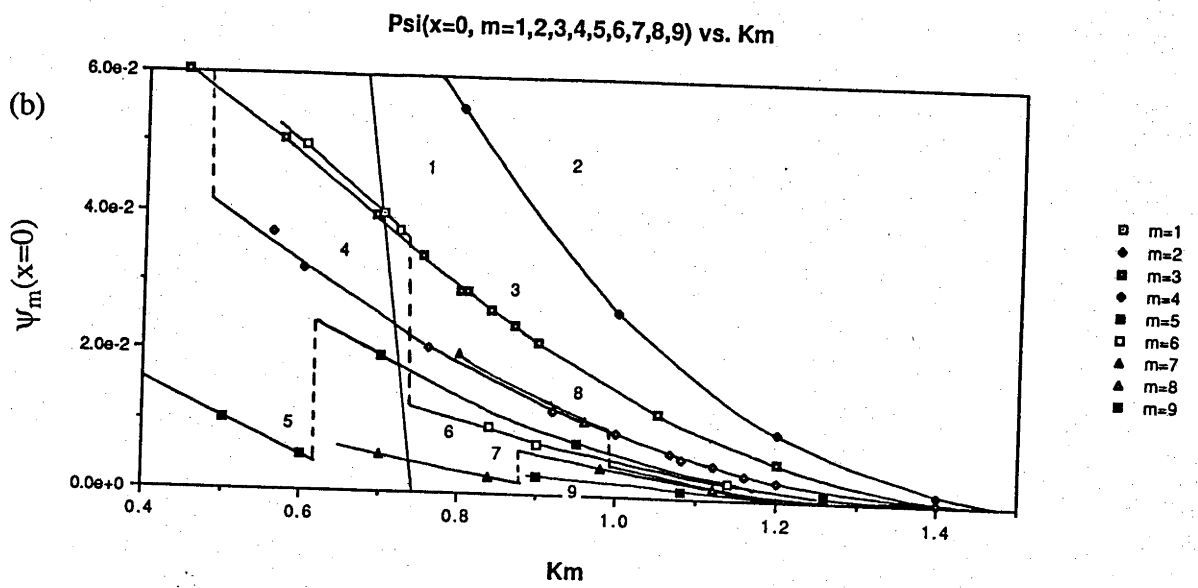
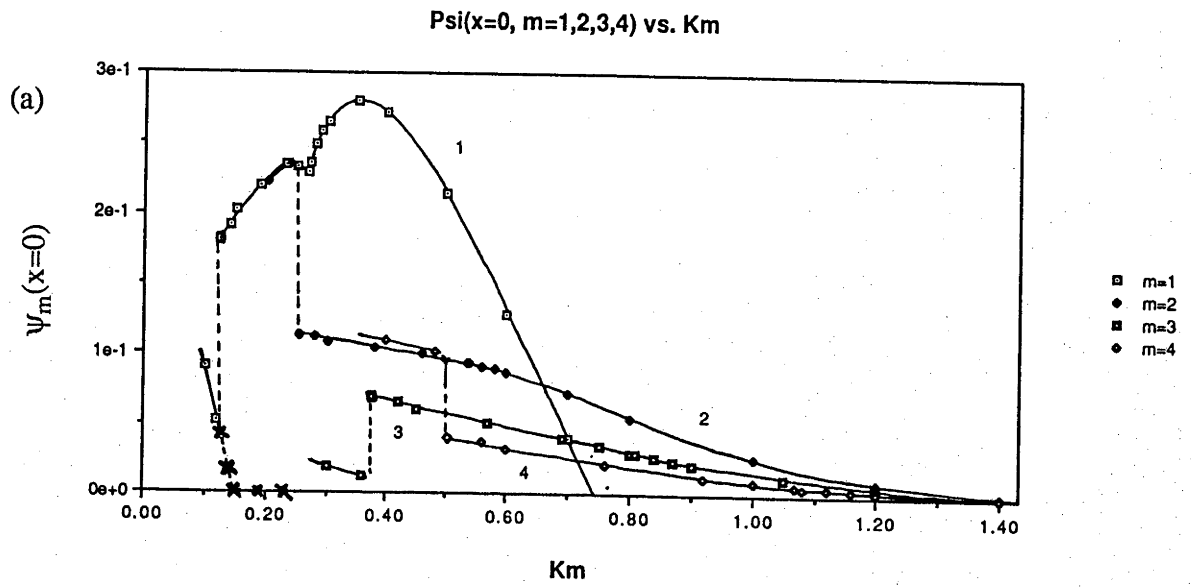


Fig.37

indicates that, if this behaviour is to be maintained, further such transitions will occur at larger values of  $L_p$

To see how this may happen it is instructive to consider the behaviour of each individual Fourier mode as a function of wavenumber,  $k_m \equiv mk_p$ , or wavelength,  $\lambda_m \equiv 2\pi/k_m$ , not to be confused with periodicity length  $L_p \equiv \lambda_1$ . Plots of the first four Fourier modes of  $\psi$  on the neutral line,  $|\psi_m(x=0)|$ , are shown in fig.36(a) as a function of  $k_m$  and in fig.37(a) as a function of  $\lambda_m$ . The variations of the higher order modes tend to clutter together at the short wavelength end of these plots, so to see them more clearly, higher resolution plots covering only the short wavelength range of  $k_m$  and  $\lambda_m$  are also given in figs.36(b) and 37(b) for  $m = 1, 2, \dots, 9$ .

The  $m = 1$  mode has a wavelength equal to the periodicity length and since it represents the single island component of  $\psi$  its variation as a function of  $\lambda$  is very similar to the variation of  $\Delta\Psi$  as a function of  $L_p$  up to  $\lambda = L_p = L_{\text{crit}(2)}$ . At  $\lambda = L_{\text{crit}(2)}$ , which corresponds to the transition to the double island state,  $|\psi_1|$  discontinuously drops down to a lower amplitude while at the same time the  $m = 2$  amplitude,  $|\psi_2|$ , jumps up at  $\lambda = L_{\text{crit}(2)}/2$  to take over as the dominant Fourier mode. What's more, it does so by taking on almost exactly the same amplitude as  $|\psi_1|$  did in the range of  $\lambda$  between  $L_{\text{crit}(2)}/2$  and  $L_{\text{crit}(2)}$ . This behaviour is repeated by all the even modes with the  $m = 4$  mode,  $|\psi_4|$ , jumping up at  $\lambda = L_{\text{crit}(2)}/4$  to follow the same amplitude as  $|\psi_2|$ , the  $m = 8$  mode,  $|\psi_8|$ , jumping up to the value of  $|\psi_4|$  at  $\lambda = L_{\text{crit}(2)}/8$  and the  $m = 6$  mode,  $|\psi_6|$ , jumping up to the value of  $|\psi_3|$  at  $\lambda = L_{\text{crit}(2)}/6$ . The transitions of the odd Fourier modes, on the other hand, are always just to a smaller amplitude. From this it is clear that after the transition each even mode takes on the same amplitude as the mode with half its wavenumber to form the following sequences of mode amplitude transitions, one for each odd Fourier mode like so :



$$\begin{aligned}
& \dots \rightarrow \psi_{16} \rightarrow \psi_8 \rightarrow \psi_4 \rightarrow \psi_2 \rightarrow \psi_1 \quad \Leftarrow \text{Dominant Sequence} \\
& \dots \rightarrow \psi_{48} \rightarrow \psi_{24} \rightarrow \psi_{12} \rightarrow \psi_6 \rightarrow \psi_3 \\
& \dots \rightarrow \psi_{80} \rightarrow \psi_{40} \rightarrow \psi_{20} \rightarrow \psi_{10} \rightarrow \psi_5 \\
& \dots \rightarrow \psi_{112} \rightarrow \psi_{56} \rightarrow \psi_{28} \rightarrow \psi_{14} \rightarrow \psi_7 \\
& \dots \quad \dots \quad \dots \quad \dots \quad \dots \quad \dots
\end{aligned}$$

The implication from this is that, as  $L_p$  is increased above  $L_{\text{crit}(2)}$ , we can expect more such transitions to states with larger numbers of islands per periodicity length which are dominated consecutively by the amplitudes of the modes in the lowest order sequence, shown above, as they move into the optimal range  $L_{\text{crit}(2)}/2 < \lambda < L_{\text{crit}(2)}$ . This has already been shown to be the case for  $\psi_1$  and  $\psi_2$ ;  $\psi_3$  would be expected to remain subdominant while  $\psi_4$ , which follows the amplitude of  $\psi_2$ , would be expected to jump up to the amplitude of  $\psi_1$  at  $L_p \approx 2 L_{\text{crit}(2)}$  to take over from  $\psi_2$  as the dominant mode, creating a quadruple island state. Similarly as  $L_p$  is increased further so that  $\psi_4$  moves out of the optimal range,  $\psi_8$  should take over as the dominant mode to create an octuple island state and so on.

This optimal range would therefore represent the range of wavelengths which islands in an island chain will transform towards via the mechanisms of coalescence and secondary island generation, irrespective of the initial wavelength or periodicity length, except when  $L_p < L_{\text{crit}}$  where it is constrained not to.

Note that the islands in the double island state, which is dominated by  $\psi_2$ , are of different sizes, i.e. big, small, big, small, ....etc. This is because they are modulated by the finite, although subdominant, amplitude of the longer wavelength  $\psi_1$  mode. As  $L_p$  is increased to much higher values, more of the low order modes will have longer wavelengths than the reigning dominant mode, including those which were never dominant at smaller values of  $L_p$ . This will tend to increase the complexity of the modulation so that islands with many different sizes, shapes and orientations should be

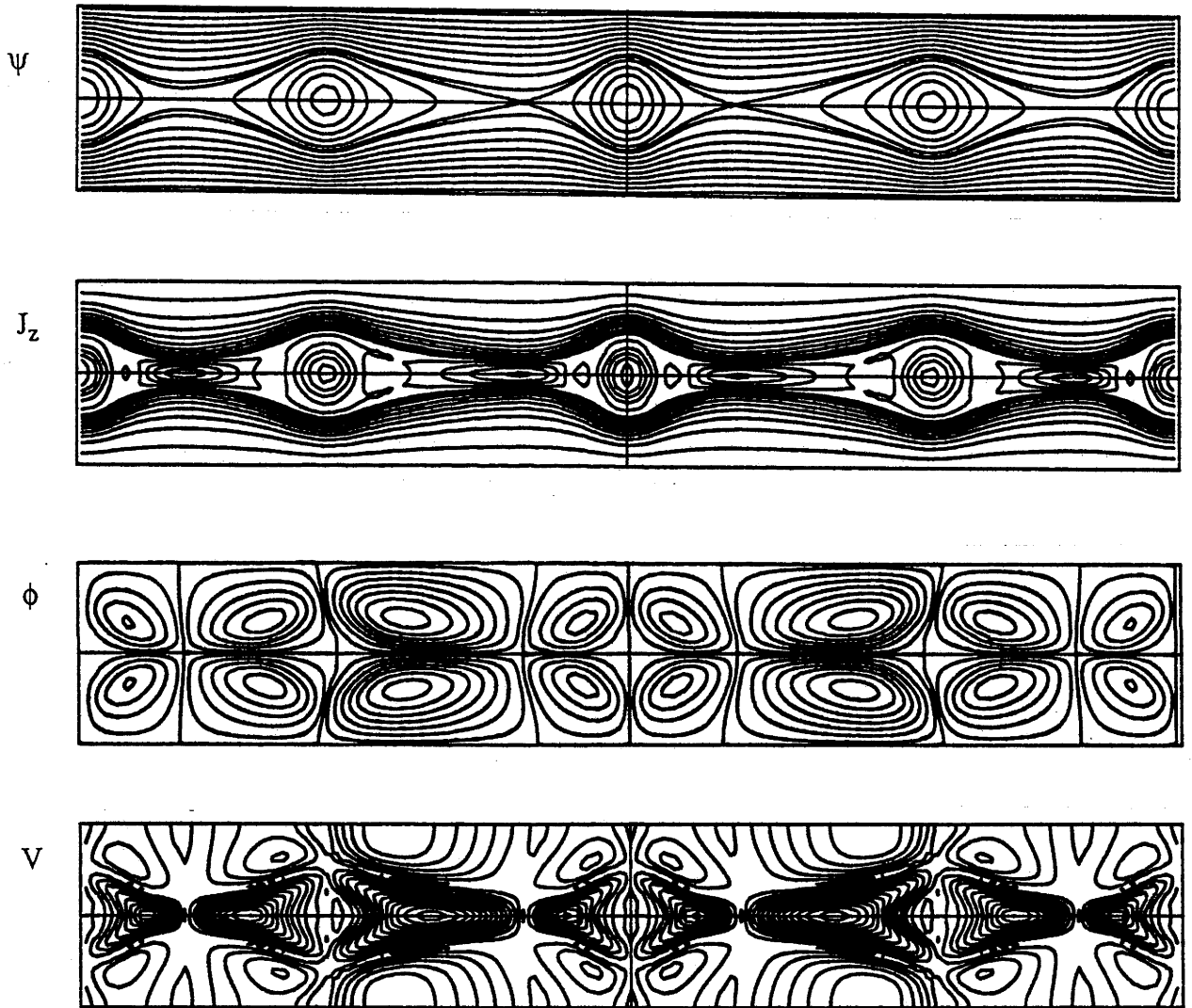


Fig.38

produced. In fact a run was made with  $K_p = 0.05$  which by this scenario puts it in the range of  $\psi_4$  dominance so that it should have four islands per periodicity length. Although the run was not quite completed to saturation it was run long enough to show the transformation via two regenerations into a quadruple island state as shown in fig.38. Besides further verifying the predicted hierarchy of dominance as a function of  $L_p$ , it also shows the more exotic modulation due to the effect of the  $\psi_1, \psi_2$  and  $\psi_3$  modes; producing a state with two asymmetric islands orientated in opposite directions, which are separated by two smaller symmetric islands.

As  $L_p$  is increased we might therefore expect the saturated island chain to change, through a series of island doubling transitions at  $L_p \approx L_{crit(n)} = 2^{n-2} L_{crit(2)}$  where  $n = 2, 3, 4, \dots$ , to more complex arrangements of the islands which in the limit that  $L_p \rightarrow \infty$  would be quite chaotic. The number of islands per periodicity length would increase but the density of islands would remain reasonably constant while the shape and size of the islands would vary from island to island. In a sense  $L_p$  could be considered as an order parameter like those in transitions to chaos that occur in bifurcation theory. It is, however, not clear what type of transition will occur at higher values of  $L_p$ , that is, whether a series of symmetry breaking and period doubling bifurcations will generate these more complex island states or whether some other type and/or combination will occur. Simulating this would be expensive since the characteristic scale length of the islands is expected to remain in the range of the dominant wavelength between  $1/2 L_{crit(2)}$  and  $L_{crit(2)}$  so that the number of Fourier modes needed would increase with  $L_p$ .

### I-3.6 Reconnection Rates

Two types of magnetic configurations giving rise to enhanced reconnection have been discussed in the literature, a 'diffusion' model proposed by Sweet<sup>[35]</sup> and Parker<sup>[36]</sup> and a 'wave' model first discussed by Petschek<sup>[37,62,63]</sup>. In this section we shall briefly discuss how the reconnection occurring in our simulations compares with these two models.

The Sweet-Parker model assumes that the reconnection mechanism is confined to the diffusion region around the x-point where the frozen-in condition is violated and over which the x-point current sheet forms. In this region the magnetic diffusion is balanced by the inward flux transport, while the incoming plasma is accelerated along the sheet mainly by the pressure force. In contrast, Petschek proposed that the diffusion region is relatively small and that the reconnection process is dominated by two pairs of MHD mode shocks placed back to back bounding the field reversal region, see fig.39(a). The propagation of the waves away from the field reversal region is balanced exactly by the plasma flow into it so that the shocks remain stationary. As the plasma flows through the shock wave front, the magnetic fields are refracted toward the normal which reduces the magnitude of the magnetic field and accelerates the plasma flow along the fronts to the upstream Alfvén speed.

The incompressibility constraint used here eliminates the fast compressional or magnetosonic mode while leaving essentially unchanged the shear Alfvén mode and the slow mode. But since the slow mode may give rise to shocks travelling at an arbitrarily slow speed, stationary shocks can still be generated in systems, as here, with slow plasma flows so that the Petschek configuration is still possible. The incompressibility constraint does however eliminate the possibility of fast reconnection<sup>[64]</sup>.

In previous studies of reconnection, the process has been simulated either by externally driven reconnection<sup>[60]</sup> or reconnection driven by instabilities which are self-consistently realized in a plasma<sup>[26,30,41]</sup>. According to Biskamp<sup>[60]</sup> the distinction is

Fig.39(a)

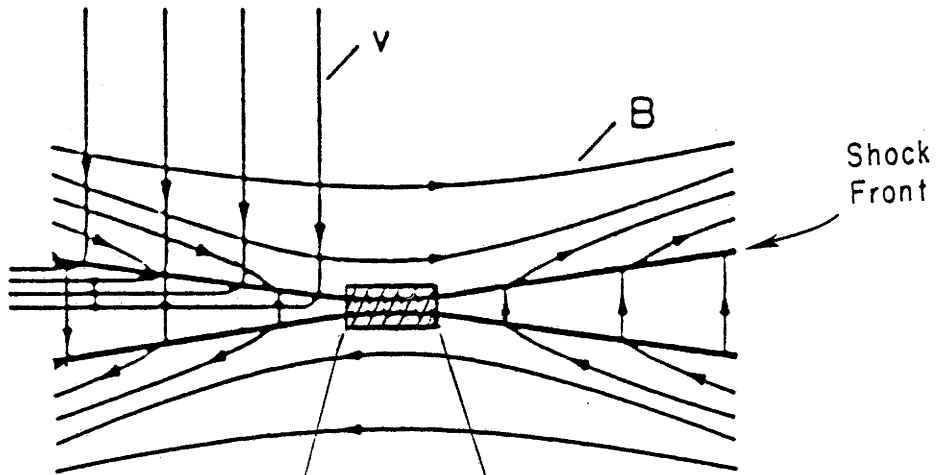
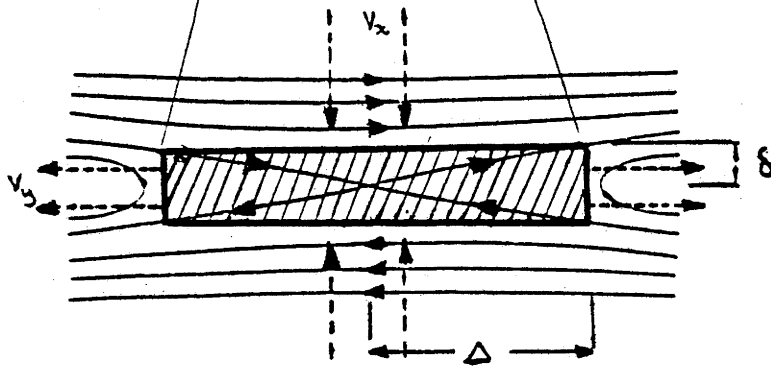


Fig.39(b)



largely overemphasized, the basic reconnection process being the same, at least within the same model equations. A driven system may be regarded as a small section of some spontaneously reconnecting one, whose global geometry and available energy are simulated by suitably chosen boundary conditions. The problem is then to create inflow and outflow conditions which are consistent with the reconnection process. Biskamp achieved this by using an iterative method to remove the spurious boundary current layers that form when the outflow is inconsistent with the inflow, to obtain reconnection rates in good agreement with the Sweet-Parker scaling.

On the other hand, reconnection via an instability has the advantage of avoiding the messy adjustment of boundary conditions but usually requires a much larger grid to fully contain all the flows and field structure associated with the self-consistent evolution of the instability, which usually extend well beyond the reconnection region. The main problem, however, is that once perturbed from equilibrium, a plasma driven by an instability is in a state of dynamical non-equilibrium until it saturates and so the assumption of steady state, crucial to the Sweet-Parker and Petschek models is not strictly valid. Thus although it would be interesting to compare the rates of reconnection during a tearing instability, or coalescence, or secondary island generation with the reconnection models, the constantly changing rates of reconnection occurring during these processes, as indicated by the varying growth rates, make this hard to justify. In spite of this, Bhattacharjee, Brunel and Tajima <sup>[26]</sup> attempted a comparison with that part of the evolution during their simulations of coalescence where the rate was momentarily constant (presumably when the growth rate was at a maximum) and claimed to have obtained a variation conforming with the Sweet-Parker Scaling. Unfortunately, in the present study, because the outputs from each run were mostly only made at regular intervals, data corresponding to the point of maximum growth during each of the reconnection processes was not always available, so a comparison could not be made without considerable extra effort. That is, except to point out that the much higher growth rate during coalescence as compared with secondary island generation indicates a much higher rate of reconnection during coalescence.

Nevertheless, since each simulation was evolved completely to saturation, where reconnection persists to balance the diffusion losses, the final states obtained do indeed represent systems of truly steady state, selfconsistent reconnection which can therefore be compared with the two steady state reconnection models. But first, as a means of introducing the relevant parameters, a brief derivation of the Sweet-Parker scaling law will be given. A more thorough review of the various reconnection models is given by Vasyliunas [63].

The diffusion region is represented by a rectangular box in fig.39(b) with half length  $\Delta$ , and half-width  $\delta$  and where  $V_x$  is the speed of the plasma flow into the diffusion region and  $V_y$  the flow out. Given that the system is in steady state, the magnetic Mach number,  $M = V_x/V_A$ , is a measure of the magnetic flux reconnected per unit time and is therefore, also called the reconnection rate. The aim is to employ this model to determine the rate of reconnection in terms of the resistivity, or more appropriately the Lundquist number  $S$ . In this simple model all quantities are treated as constant over the face of the box. We begin by integrating the z-component of Ohm's law over one quarter of the box to give:

$$E_z \delta \Delta = \eta \int_0^{\delta} \int_0^{\Delta} J_z dx dy \quad (138)$$

where  $E_z$  is considered constant and where the diffusion region around the neutral line is sufficiently small that the  $\mathbf{V} \times \mathbf{B}$  term can be neglected. The right hand side is evaluated by integrating Ampere's law around the box to give:

$$\int_0^{\delta} \int_0^{\Delta} J_z dx dy \approx \eta B_y \Delta / \mu_0 \quad (139)$$

where  $B_x \ll B_y$  just above and below the diffusion region. Outside the diffusion region Ohm's law reduces to  $\mathbf{E} + \mathbf{V} \times \mathbf{B} \approx 0$ . so that :

$$E_z \approx V_x B_y \quad (140)$$

and from conservation of mass, with the assumption of incompressible flow we have :

$$V_x \Delta = V_y \delta \quad (141)$$

Combining equations (138) to (141) and eliminating  $\delta$  gives :

$$V_x^2 \approx \frac{\eta V_y}{\mu_o \Delta} \quad (142)$$

By taking the characteristic diffusion length to be equal to the length of the diffusion region,  $\Delta$ , equation (142) reduces to :

$$V_x^2 \approx V_{R(\text{loc})} V_y \quad (143)$$

where  $V_{R(\text{loc})} = \eta/(\mu_o \Delta)$  is the local resistive diffusion velocity at the edge of the diffusion region. The plasma flow is considered to be accelerated up to the local Alfvén velocity at the end of the diffusion region, which fixes  $V_y = V_{A(\text{loc})} = B_{\text{loc}}/(\mu_o \rho)^{1/2}$ . The local Sweet-Parker reconnection rate is thus given by :

$$M_{\text{SP}} = \frac{V_x}{V_{A(\text{loc})}} \approx S_{\text{loc}}^{-1/2} \quad (144)$$

where  $S_{\text{loc}}(\Delta) = V_{A(\text{loc})}/V_{R(\text{loc})}$  is the local value of the Lundquist number just in front of the diffusion region. In terms of dimensionless variables defined in section I-2.1 this becomes  $S_{\text{loc}}(\Delta) = B_{\text{loc}} \Delta S / \eta_{\text{loc}}$  where  $V_{A(\text{loc})} = B_{\text{loc}}$ ,  $V_{R(\text{loc})} = \eta_{\text{loc}}/(S\Delta)$ ,  $\eta_{\text{loc}} = \cosh^2(\delta)$  and  $S$  is the asymptotic Lundquist number. This is not quite true since even though the wall value of the magnetic field is used in  $S$ , it includes the axial value of the resistivity, which is much smaller than the wall value because of the  $\cosh^2 x$  dependence. Nevertheless  $S$  still turns out to be an important scaling parameter. A derivation of the Petschek Scaling law <sup>[63]</sup> gives a different reconnection rate which takes the form :

$$M_p = \pi / ( 8 \ln( S_{\text{loc}} ) ) \quad (145)$$

With the dimensionless terms used here the local reconnection rate is given by  $M_{\text{loc}} = V_{\text{loc}}/B_{\text{loc}}$ , the ratio of the inflow velocity to the magnetic field just in front of the diffusion region. The dimensions of the diffusion region correspond roughly to those of



the current sheet so that as in section I-3.3 we will equate  $\delta$  with the half width of the current sheet and  $\Delta$  with the half length, the values of which are measured from contour plots of  $J_z$ . The value of  $\delta$  is then used in contour plots of  $V$  and  $B$  to determine the values of  $V_{loc} = |V_x(x=\delta, y=0)|$  and  $B_{loc} = |B(x=\delta, y=0)|$ .

As was shown in section I-3.2 the significant viscosity and finite wall separation used in these simulations alters the size of the current sheet and the rate of reconnection, so that it is not possible to make a direct comparison with the reconnection rates predicted by the two models. It is, however, possible to compare the scaling with the Lundquist number and that is what is done here. The Sweet-Parker and Petschek reconnection scalings have, however, been modified by Park, Monticello and White <sup>[41]</sup> to include the effect of viscosity, for which simulations done in cylindrical geometry asymptotically approach the modified Sweet-Parker scaling. But because of the conducting wall stabilization it is still not possible to make a direct comparison, so for the present, a comparison will only be made with the unmodified scalings.

In fig.40(a) are plotted the measured reconnection rate,  $M_{loc}$ , the local Sweet-Parker rate,  $M_{SP(loc)}$ , and the local Petschek rate,  $M_{P(loc)}$  as a function of  $S_{loc}(\Delta)$ . The variation of  $M_{loc}$ , which varies as  $S_{loc}^{-1.12}$ , shows poor agreement with both models although it is clearly closer to  $M_{SP(loc)}$ . If, as shown in fig.40(b), the diffusion length is fixed at a constant value (in this case set equal to the half width of the original current channel so that  $S_{loc} = B_{loc} S / \eta_{loc}$ ) instead of using the half length of the x-point current sheet, which decreases with  $S$ , the agreement of  $M_{loc}$  with the new local Sweet-Parker rate is greatly improved, that is  $M_{loc} \propto S_{loc}^{-0.66}$ . But, as shown in fig.40(c), the best agreement is achieved if the asymptotic value of the Lundquist number,  $S$ , is used giving  $M_{loc} \propto S^{-0.52}$ . In all cases there is very poor agreement with the Petschek rate. In fig.41(a),(b) and (c)  $M_{loc}$  is plotted against  $S_{loc}(\Delta)^{-0.5}$ ,  $S_{loc}^{-0.5}$  and  $S^{-0.5}$  to show that good linear fits can be obtained with the two versions of the Sweet-Parker scaling which have a constant characteristic diffusion length.

Fig.40

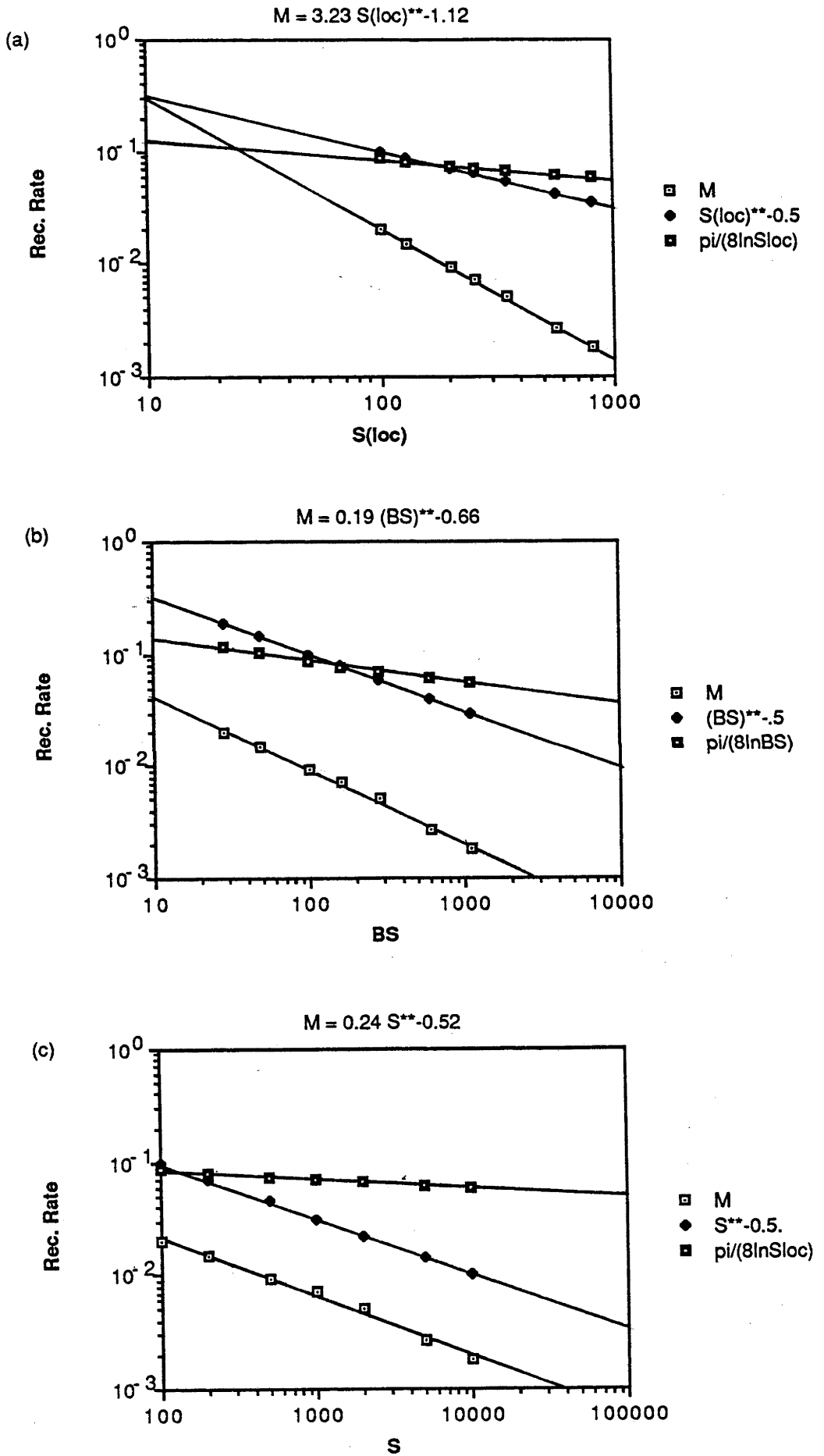
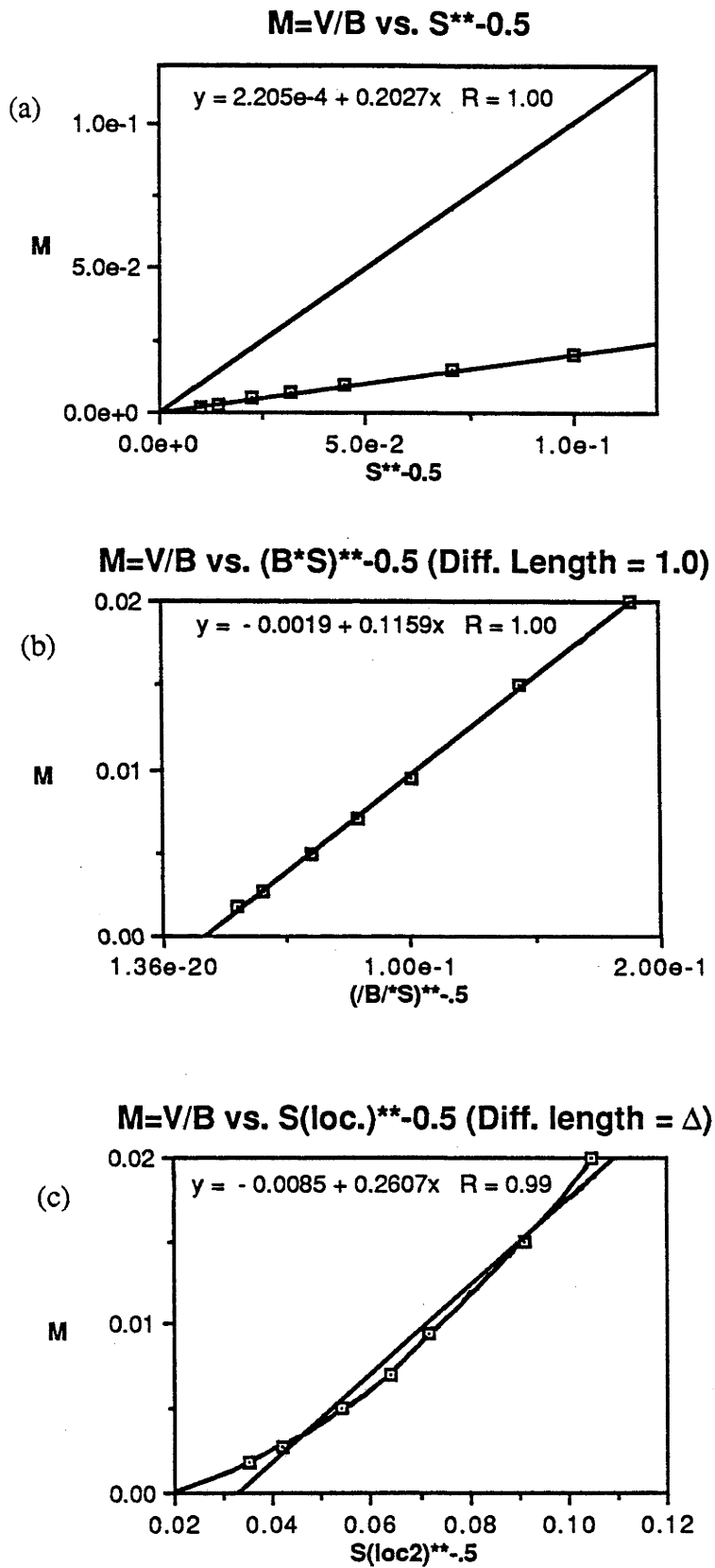
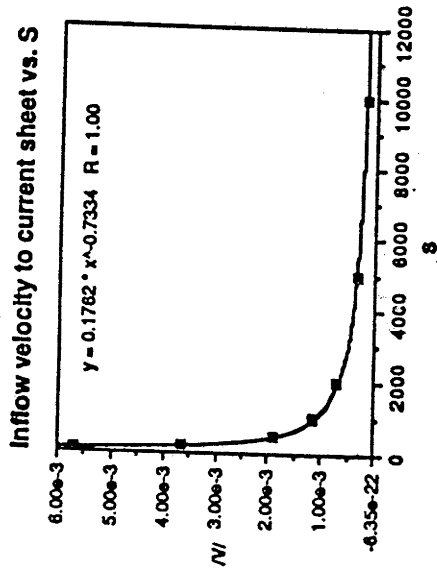
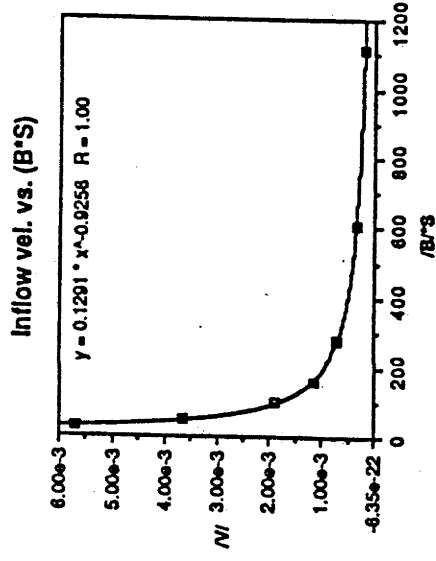
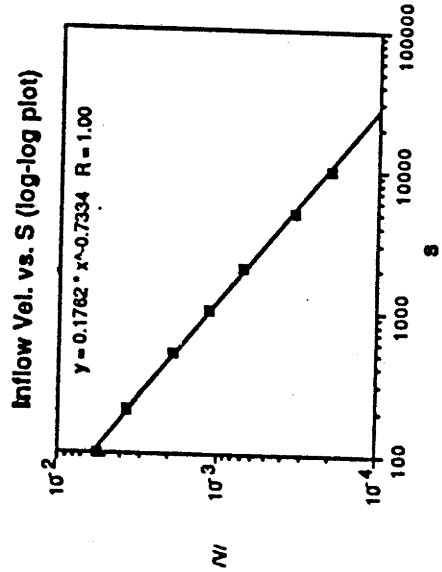


Fig.41

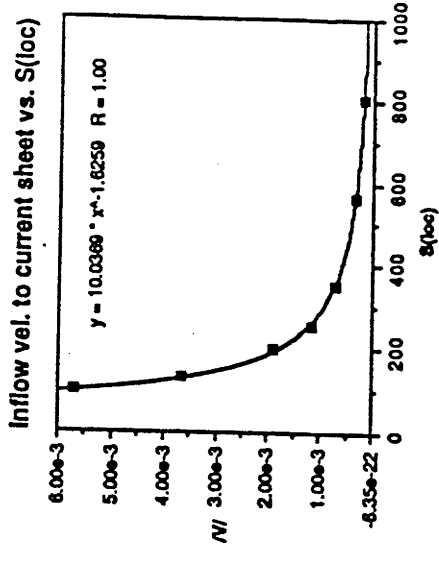
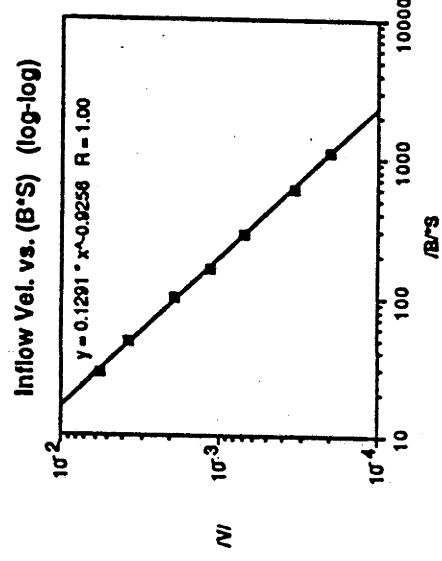




(a)



(b)



(c)

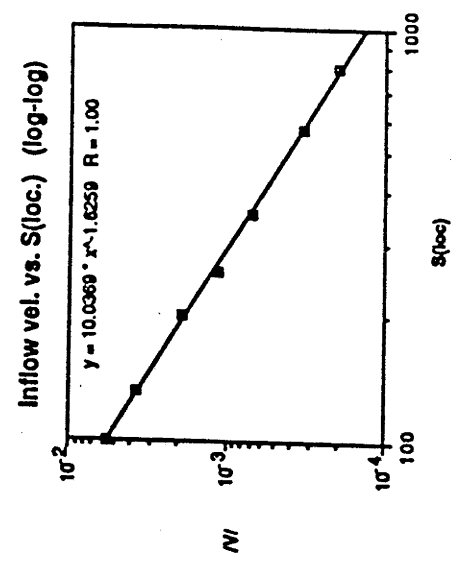
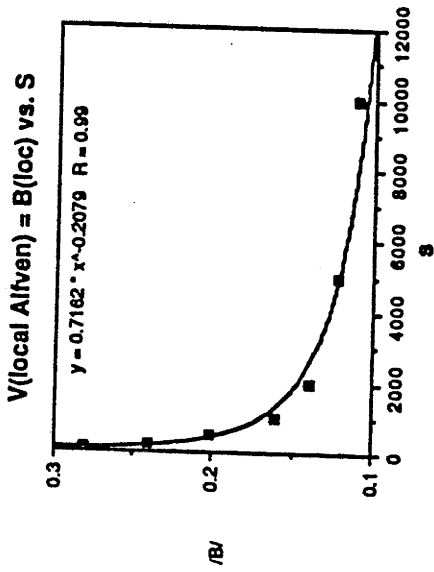
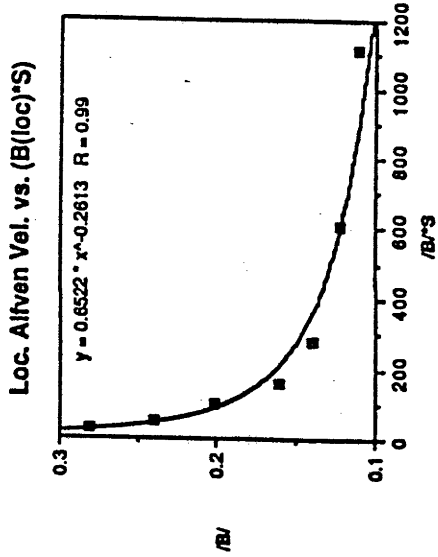
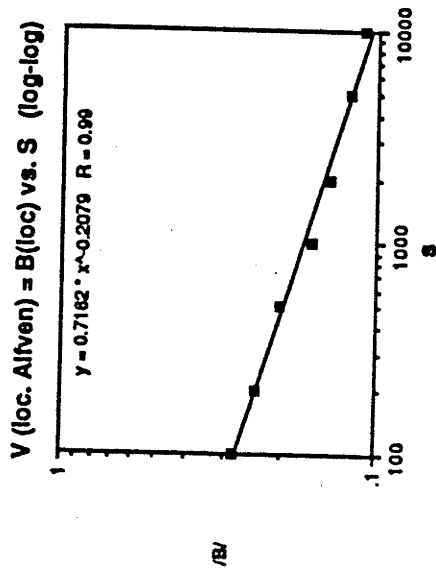


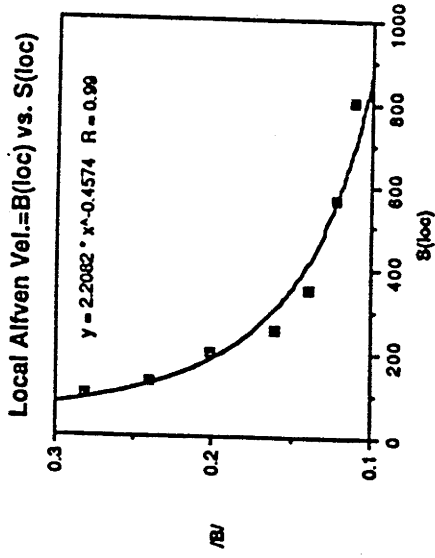
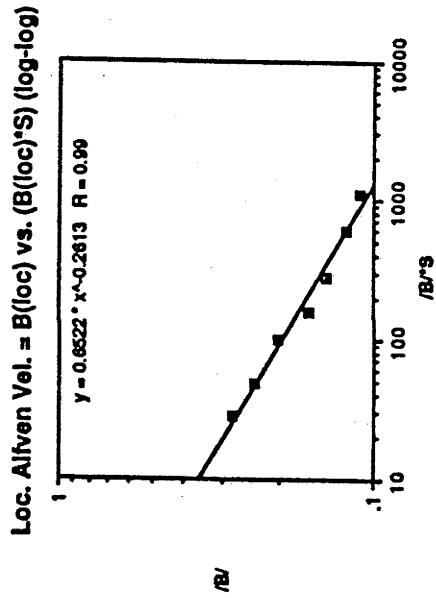
Fig.42



(a)



(b)



(c)

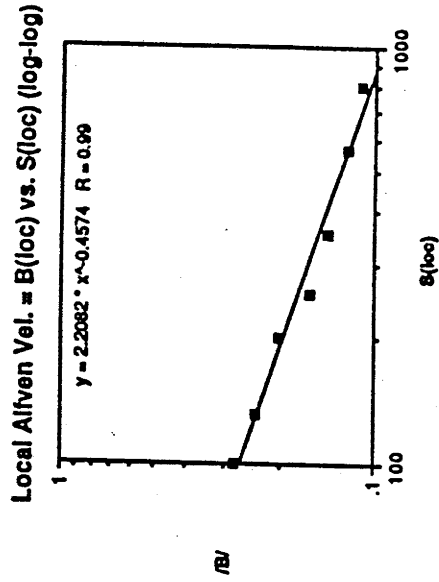


Fig.43

The inflow velocity  $V_{loc}$  and the local Alfvén velocity ( $= B_{loc}$ ) are also plotted as a function of  $S$ ,  $S_{loc}$  and  $S_{loc}(\Delta)$  in figs.42(a), (b), (c) and 43(a), (b), (c). Since the measurements are taken from the steady state configuration where inflow matches outflow it is perhaps not surprising that the inflow velocity,  $V_{loc}$ , has the same dependence on  $S$  as the maximum outflow velocity given fig.23 of section I-3.3, i.e.  $V_{loc}, V_{max} \propto S^{-0.73}$ . The measurements of  $B_{loc}$ , the field strength just in front of the current sheet, are a little less accurate but they too show a definite inverse power variation with  $S$ ,  $S_{loc}$  and  $S_{loc}(\Delta)$  which is due, at least partly, to the decrease in the width,  $\delta$ , of the current sheet with  $S$  because of the decreasing field strength towards the neutral line.

In review, the results, although not absolutely conclusive, clearly favour the Sweet-Parker scaling above the Petschek in line with the findings obtained in several other studies [26,30,41,60] although there do exist studies of reconnection which have found Petschek scaling [65,66]. Note also that the Petschek model has  $\Delta \sim \delta \sim S^{-1}$  while the Sweet-Parker model has  $\delta \sim S^{-1}$  but  $\Delta \sim 1$ . The observations here are that although both  $\Delta$  and  $\delta$  decrease with increasing  $S$ , see fig.22,  $\Delta$  can be made larger by increasing  $L_p$ , see fig.24, so that even if  $S$  is large,  $\Delta$  can still be of order 1 providing a further evidence against the Petschek model.

### I-3.7 Summary and Conclusion

In summary it has been shown by systematic numerical computation :

(1) That the magnetic islands produced by a tearing mode on a current sheet develop narrow x-point current peaks in addition to the usual, broad o-point current peaks which persist after saturation, see fig.9 of section I-3.1.

(ii) The existence of  $L_{\text{pref}}$  : a periodicity length,  $L_p$ , beyond which the magnetic islands cease to become larger, and instead the x-point current peaks stretch into current sheets, see fig.11 of section I-3.2.

(iii) The existence of  $L_{\text{crit}}$  : the periodicity length ( $> L_{\text{pref}}$ ) at which the x-point current sheets become tearing unstable and consequently generate secondary magnetic islands, see figs.19, 20 and 21.

(iv) Coalescence can occur if the wavelength,  $\lambda$ , is around  $L_{\text{pref}}$  or less ( and the periodicity length,  $L_p$ , is long enough to allow it ), see figs.25, 26, 27, 28 and 29.

(v) The dynamical competition between secondary island generation and coalescence is the factor determining the form of the final saturated state for  $L_p > L_{\text{crit}}$ , see fig.31.

(vi) The conflict between current sheet instability (secondary island generation) and coalescence is finally resolved in the long time limit by the formation of travelling islands with stable asymmetric current sheets, see figs.32 and 34.

(vii) Thus  $L_{\text{crit}}$  corresponds to a new, symmetry-breaking bifurcation point (c.f. the well known bifurcation at the value of  $L_p$  at which the linear tearing instability occurs when the original current sheet bifurcates to a static island chain ), see fig.33.

(viii) That the values of  $L_{\text{crit}}$  and  $L_{\text{pref}}$  and the qualitative nature of the transition is independent of both wall separation and viscosity but does depend on the resistivity ( i.e. the Lundquist number  $S$ ), see figs.12,13,15,16 and 17.

(ix) If a parity symmetry constraint is imposed in the y-direction, then, when  $L_p > L_{crit}$ , the symmetry breaking bifurcation is prevented and instead a period halving transition occurs at  $L_{crit}$  to a state with two equal sized symmetric islands per periodicity length, see fig.11.

(x) As  $L_p$  is increased beyond  $L_{crit}$  another transition point,  $L_{pD}$ , has been found, where the symmetric double island state changes in form to a modulated double island state (with locally asymmetric x-point current sheets arranged symmetrically about each island), see figs.32 and 34.

(xi)  $L_{pD}$  therefore corresponds to a new period doubling bifurcation of the symmetric solution branch, see fig.33.

(xii) With the symmetry constraint relaxed a further transition at  $L_p = L_{crit(2)} > L_{pD}$  has been found, corresponding to an interchange of stability from the asymmetric travelling single island state to the stationary symmetric modulated double island state, see fig.33.

(xiii) A simulation done at even higher periodicity length has shown the existence of a static quadruple modulated island state with both symmetric and asymmetric islands.

The nature of the discontinuous transitions of the individual Fourier modes on the neutral line as a function of  $L_p$  indicate a likelihood for further transitions, at higher  $L_p$ , which double the number of islands per periodicity length each time, ie from  $m=1$  mode dominance to  $m=2$  mode dominance to  $m=4$  mode dominance and so on, as the wavelength of these particular Fourier modes move into the optimal range of wavelengths between  $L_{crit(2)}/2$  and  $L_{crit(2)}$ . Although this appears to be reasonably evident from the results obtained, it is still rather speculative and so it would be worthwhile to obtain further confirmation by computing one or more of the higher order transitions, say from the the double to the quadruple and/or from the quadruple to the octuple island states; also verifying the complete absence of a triple, pentuple, hextuple, heptuple and other non mode number doubling states.



The possibility that magnetic islands would break up into smaller ones as well as coalesce to form larger ones depending on the wavelength of the original islands was previously conjectured by Biskamp and Welter<sup>[24]</sup>. However the 'breakup' of islands is not technically correct since, although the final result is essentially equivalent to each island having split into two smaller ones, the actual transformation, as shown in fig.20, involves the birth of new secondary islands between each of the original islands which consequently shrink to make room. They also suggest that coalescence would be more frequent on the basis that short wavelength tearing modes usually have larger growth rates leading to islands that subsequently tend to coalesce. Fig.44 indicates that this is essentially correct, as it shows the linear growth rate peaking pretty well at the same low wavelength as the saturated reconnected flux and island width, i.e. close to  $\lambda \approx L_{pref}$ . The actual wavelength of the dominant linear mode will not necessarily be able to take on this particular value since it must divide a whole number of times into the periodicity length,  $L_p$ , but it could be expected to be close to  $L_{pref}$ . If  $\lambda = L_p \approx L_{pref}$  then the island will just saturate with this wavelength but if  $L_p > \lambda$  then because the optimal range of wavelengths lies to the higher side of  $L_{pref}$  the islands will coalesce but, as we have found here, this can still involve one or more secondary island generations between each coalescence as the system undergoes a damped oscillation around the final configuration.

There is, however, the question of whether this behaviour would be reproduced in a geometry and conditions more closely resembling those of laboratory plasmas or whether it is just a consequence or artifact of the specific numerical setup. For instance, it was shown that if we had chosen a slightly more realistic saturation mechanism with  $\eta = \eta(\psi)$  instead of  $\eta = \eta(x)$  there would have been the possibility of obtaining saturated magnetic island states without any fluid motion and hence none of the steady state reconnection that seemed to govern the properties of the equilibria simulated here. The results of Hesse and Schindler<sup>[58]</sup> indicate that such states don't exist but this should still be checked, as well as the effect of the geometry. Although the plane slab configuration used here is

### Linear Growth Rate vs. Lp

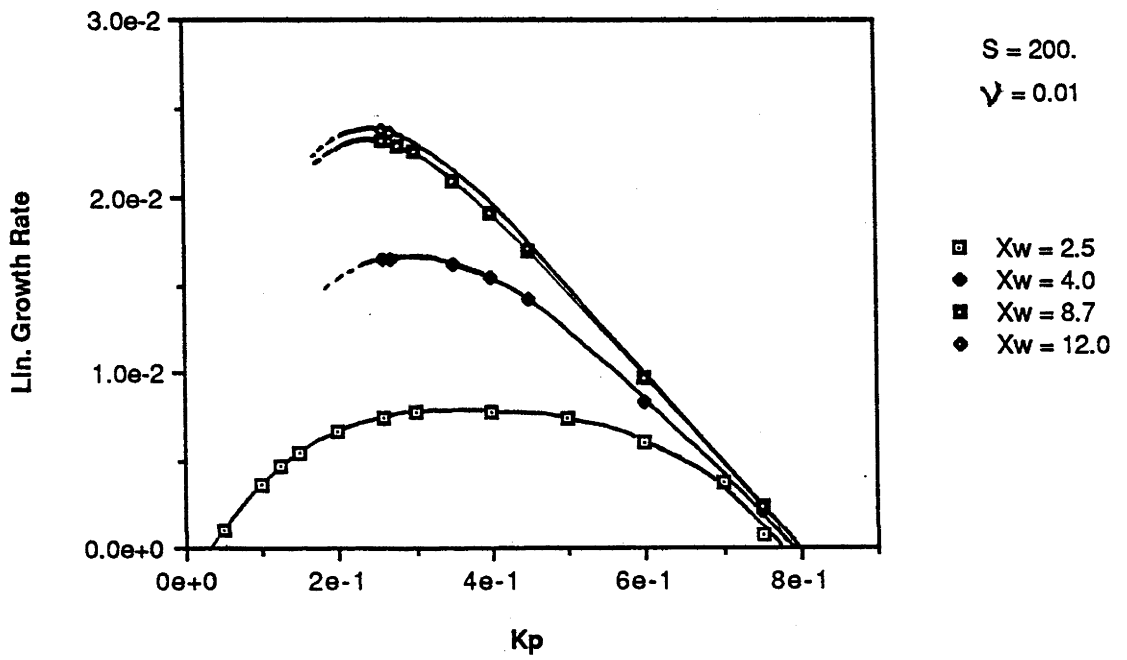


Fig.44

topologically different from most experimental setups it is considered to be a reasonable approximation to the region around a single mode rational surface that is sufficiently far from the edge of the plasma for geometrical effects to be relatively unimportant. The closeness of the conducting walls in these simulations, which are set this way for the purpose of improving numerical efficiency, is justified by the fact that the essential aspects of the complex phenomena demonstrated here were found to be independent of the wall separation with the major effects being simply to reduce the growth rate, see fig.44, and the the size of the saturated islands. Even so there are other aspects of the configuration which do not transfer easily to the toroidal plasma configuration of tokamaks, such as the symmetric nature of the initial equilibrium around the neutral line. In contrast, the variation of the field quantities around a proper mode rational surface corresponding to a particular helicity are quite asymmetric, with the instability to the tearing mode being more critically dependent upon the field gradients on either side. It would therefore probably be useful to redo all these simulations for the case of say a single helical mode in cylindrical geometry to see if the various transitions via coalescence and secondary island generation will occur as a function of the helical periodicity length, which would depend on the major diameter (i.e. periodicity length of the cylinder) and the radius of the mode rational surface. Many simulations have already been made in 2 and 3-D cylindrical configurations but so far there has been little clear evidence of the behaviour shown here in slab geometry. Nevertheless Park, Monticello, and White <sup>[41]</sup> have shown, in their simulations of helical tearing modes in a cylindrical plasma, the formation of localized current sheets at the x-points between the evolving magnetic islands. What is more, they found that, when the viscosity was made negligibly small compared with the resistivity, i.e.  $\nu \ll \eta$ , the long current sheet that formed at the x-point of an  $m=1$  resistive internal kink magnetic island became unstable to  $m>1$  tearing modes, but, because of the considerable increase in the mode usage that this entailed, they could not afford to investigate the evolution very far. Even so, there are aspects which are already different from what was observed here. For instance the observation that the instability of the current sheet depended on there

being negligible viscosity conflicts with the fact that, in all our simulations of secondary island generation, not only was the normalized viscosity ( $\nu = 0.01$ ) larger than the resistivity ( $\eta = S^{-1} \leq 0.005$ ), it showed no influence over the critical periodicity length,  $L_{\text{crit}}$ , that marks the threshold tearing mode stability of the x-point current sheets. They also observed a transition to higher and higher  $m$  components indicative of a transition to turbulence around the reconnection layer. On the other hand, Biskamp [60], who performed a similar simulation, found that a small secondary tearing mode magnetic island, or bubble, was convected along the x-point current sheet to merge with the main body of the  $m=1$  kink magnetic island before it could grow to a significant size. Another island would then emerge which would also be convected along the sheet so that the process was repeated over again. This could, perhaps, be related to the repetitive coalescence and regeneration of magnetic islands described in section I-3.5, although there are many differences. It is possible that the curvature of the cylindrical configuration prevents the secondary magnetic islands from being able to maintain position long enough to develop into a sustained secondary island structure as in the slab case although this idea is negated to some extent by the fact that he also demonstrated a similar sort of behaviour in a simulation of forced reconnection in slab geometry. In any case, on the basis that the slab behaviour does transfer directly to the cylindrical case, the evidence here implies that sustained higher order island structures should be generated as long as the helical periodicity length is made large enough. To show this will be the task for a future investigation. For realistic values of  $S$  ( $\sim 10^6$ ), however,  $L_{\text{crit}} \geq 100$ , see fig.17(b), so the scale length for a current sheet would have to be roughly less than 1/16 of the minor radius in order reach the new symmetry breaking regime. Consequently applications in space and astrophysical plasmas sound more likely.

In line with most recent studies of reconnection [26,41,60] we find our simulations to be reasonably consistent with the Sweet-Parker scaling for the reconnection rate. The scaling of the diffusion region as defined by the current sheets is different from that

determined by Biskamp, although it is not inconsistent with the Sweet-Parker model. The evidence here is that the length of the x-point current sheet is determined, not so much by the properties of the reconnection process occurring within the diffusion layer but more by external influences which allow it to extend to fill the available space. In particular, because of the invariance in size of the o-point current peaks for  $L_p > L_{pref}$ , it tends to increase in direct proportion with the periodicity length, ie  $\Delta \sim L_p S^{-0.34}$ . The decrease of  $\Delta$  with increasing  $S$  also appears to be more a consequence of the decrease in space left as a result of the increase in size of the central island region and hence the o-point current peak with  $S$ . In the simulations of forced reconnection made by Biskamp, in which there are no magnetic islands to influence the length of the current sheet, he found that  $\Delta$  was completely independent of  $S$  but was so highly sensitive to the driven asymptotic inflow velocity,  $M$ , i.e.  $\Delta \sim M^4$ , that within a short range of values of  $M$ ,  $\Delta$  reached the global system size. This is perhaps analogous to the direct dependence of  $\Delta$  on  $L_p$  shown here. However, in contrast to Biskamp it was also found that the width,  $\delta$ , of the current sheet shrinks with decreasing  $\eta$ , ie  $\delta \sim S^{-0.24}$  in line with elementary boundary layer theory.

Besides the bifurcation behaviour found in this study it is possible that further investigations will uncover more exotic phenomena similar to that already found for a model of an interchange-unstable plasma in a shearless field using the 'Navier-Stokes approximation'. In this study Maschke and Saramito<sup>[67]</sup> identified successive bifurcations leading to turbulence including regimes involving period doubling and strange attractors. They also showed that this system of equations was formally similar to that for a tearing mode unstable layer. To avoid the computational expense of simulating the full evolution they later applied bifurcation theory for compact operators to calculate solution branches for the time asymptotic states of nonlinear tearing modes<sup>[68,69,70]</sup>, but except for the bifurcation of the tearing mode itself as a function of  $S$ , they did not appear to have computed anything resembling any of the symmetric or asymmetric solutions found here.

## II-1.1 Introduction : Tearing Modes, MHD Activity and Mode Locking

So far the study has been mainly exploratory, guided loosely if at all by experimental observations. In this second part of the thesis a more concerted effort is made to try to understand the specific nature of the MHD activity observed on the LT-4 tokamak.

Such large scale fluctuations are detected on LT-4<sup>[71]</sup> by means of several detection systems including : banks of external magnetic pickup coils (often called Mirnov coils) which detect fluctuations in the poloidal magnetic field; the monitoring of the soft X-ray continuum emissions from the hot centre of the plasma which show fluctuations in the plasma temperature and/or density; and phase scintillation interferometry techniques which detect local density fluctuations. The main concern here is with the poloidal magnetic field fluctuations which can be classified into several types or regimes, as in fig.45, according to their amplitude as a function of the safety factor,  $q(a)$ , (or inverse rotational transform) at the limiter radius,  $r=a$ , which defines the edge of the plasma.

The appearance of such fluctuations is a common occurrence in tokamak discharges, and in LT-4<sup>[17,18]</sup> they generally have a frequency of around 12 kHz in regime III and 20 kHz elsewhere. Spatial analysis of the signals shows that they result from the rotation of helical magnetic structures within the plasma. Because of this and the fact that the plasma is assumed to be ideally stable it is generally believed that such oscillations are the result of nonlinearly saturated magnetic islands produced by resistive tearing modes. These would arise from perturbations of the form:  $\xi = \xi_0 \exp\{i(m\theta - n\phi) + \gamma t\}$  around a rational surface with minor radius  $r=r_s$ , defined by  $q(r_s) = m/n$  where  $m$  and  $n$  are the poloidal and toroidal mode numbers, to eventually form a helical magnetic island structure like that drawn schematically in fig.51 for the case with  $m=2/n=1$ . Note that with  $m=2$  and  $n=1$  a double island structure is generated in which the field lines forming the x and o points travel twice the long way around the torus for each circuit around the short way before coming back upon themselves.

The helical magnetic island topology also affects the density and temperature distribution as well as the magnetic field within the plasma so that periodic signals in the various detectors are produced because of the motion of the islands around the torus. Many theories have been proposed to explain the cause of the mode rotation, which is either due to the islands having a finite phase velocity through the plasma or more simply a convection of the islands along with the bulk fluid motion of the plasma, or even a combination of both.

Tearing mode simulations by Monticello and White<sup>[12]</sup> have shown that the inclusion of diamagnetic effects cause a mode rotation at the diamagnetic frequency without affecting the nonlinear growth or saturation of the islands. The rotation is shown to correspond to a drift through the plasma because of the constancy of the angular momentum. However, the possibility of this being the source of mode rotation was confounded by a similar simulation made by Scott, Hassam and Drake<sup>[72]</sup> which included compressibility in the calculation to show that the diamagnetic drift of the islands is damped out by sound waves the along field lines as the tearing mode becomes nonlinear. The rotation of the saturated tearing mode magnetic islands therefore cannot be due to a diamagnetic drift.

On the other hand Sigmar et al.<sup>[73]</sup> observed experimentally that the rotation of the islands is altered by the toroidal rotation of the plasma as a whole, while Stringer<sup>[74]</sup> showed that when inertial, resistive and parallel viscosity are included in the equilibrium equations radial electric fields build up in order to equalize the ion and electron diffusion rates. The  $\mathbf{E} \times \mathbf{B}$  drift that results from this ambipolar diffusion produces the rotation of the plasma. The stability of such a radial electric field in non-axisymmetric tori is also discussed from a thermodynamic point of view by Shaing<sup>[75]</sup>.

The resulting fluid motion may have poloidal and toroidal components, although a study of the time evolution of mass flows in a collisional tokamak by Hassam and Kulsrud<sup>[76]</sup> indicates that the poloidal rotation is strongly damped by magnetic pumping. Magnetic pumping occurs as plasma rotates through the inhomogeneous toroidal magnetic

field. This heats up the plasma and leads to a transformation of the kinetic energy of rotation into thermal energy which damps the poloidal rotation.

It is also possible that the remaining toroidal plasma rotation is sheared. However the experimental evidence shows that the  $m/n = 1/1, 2/1$  and  $3/1$  signals are often phase locked <sup>[17,18]</sup> when they are present simultaneously in the plasma. Assuming that these signals are actually due to separate modes occurring on different rational surfaces and not Fourier components of a single mode then this observation would seem to be consistent only with a rigid uniform rotation of the plasma.

Assuming therefore that the MHD activity is due to saturated tearing mode magnetic islands convecting along in a rigid toroidally rotating plasma it is then necessary to determine more specifically how this scenario would account for the range and variability in amplitude and frequency of the MHD activity that is observed. This is particularly important if we are to understand the dynamical behaviour of the magnetic islands that leads to the onset of a major disruption.

LT-4 exhibits a variety of activity as shown in figs.47, 48 and 49 which is not always the same as in other tokamaks. Fig.47 shows that instead of a growing oscillatory  $m=2$  signal as seen in TFR <sup>[77]</sup>, the conditions preceding a disruption in LT-4 are reasonably quiescent before being punctuated by a series of fast transients which are referred to as minor disruptions. Considering the overwhelming evidence for the existence of an  $m=2$  island preceding the disruption in other tokamaks it is hard to reconcile its apparent absence at this stage in LT-4. An alternative possibility is that, preceding the disruption, an  $m=2$  mode does exist but is mode locked so that no oscillatory signal is generated on the pickup coils. This seems likely to be the case in the type B discharge shown in fig.47 where the termination of the MHD oscillations in regime III occurs within one cycle. In fact during this irregular phase, which occurs when the density drops in regime III, the MHD activity is observed to stop within a cycle and restart several cycles later with otherwise no change in amplitude or frequency. Given that saturated tearing modes tend to change adiabatically on a resistive timescale the rapid disappearance and re-



Fig.45

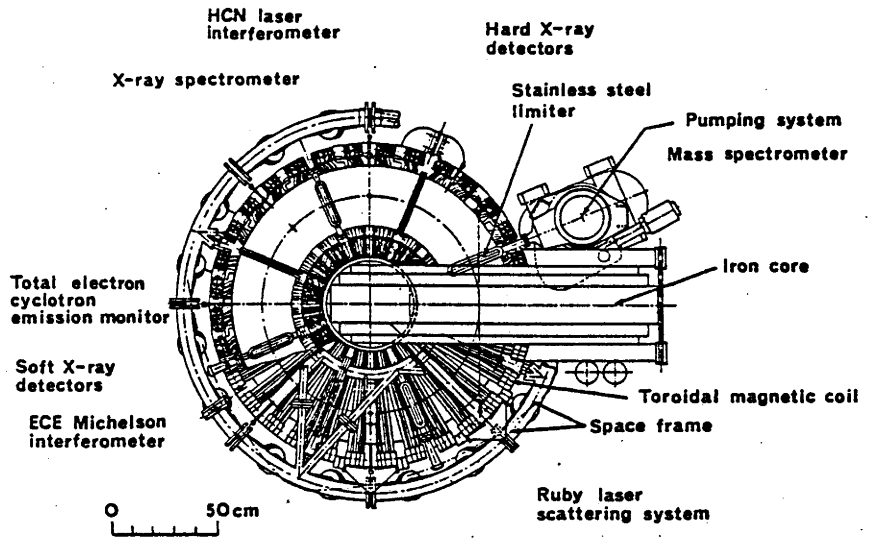


Fig.46

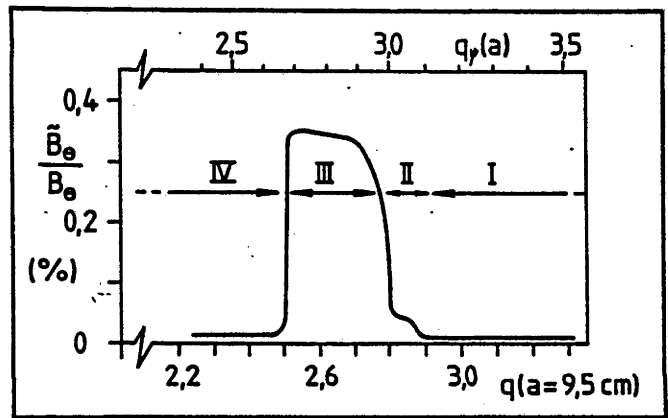
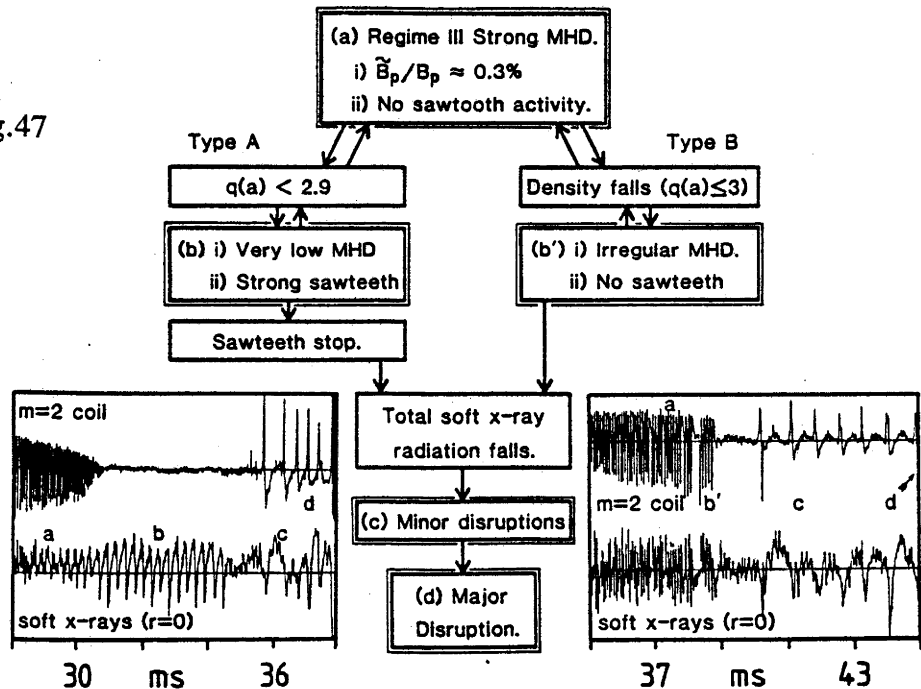


Fig.47



Schematic diagram showing the two different routes to disruptions as observed on LT-4.

Fig.48

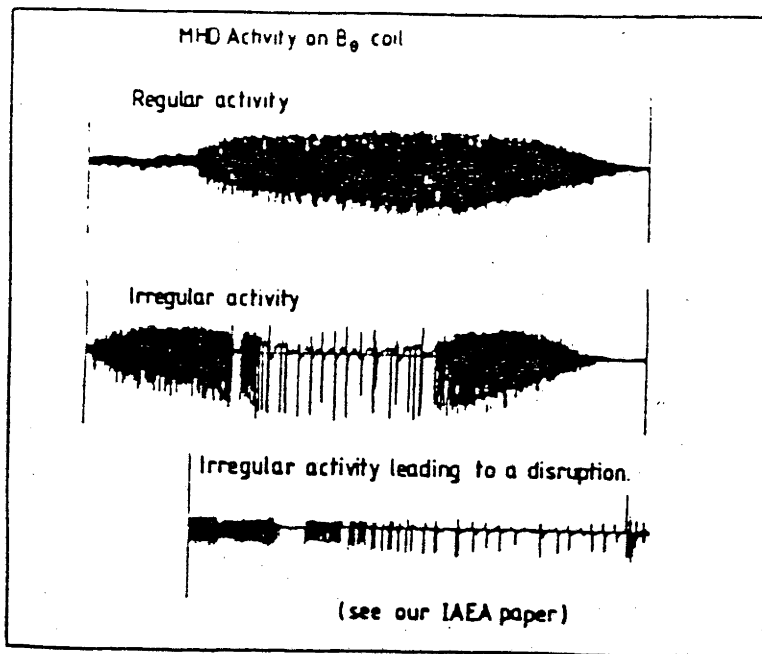


Fig.49

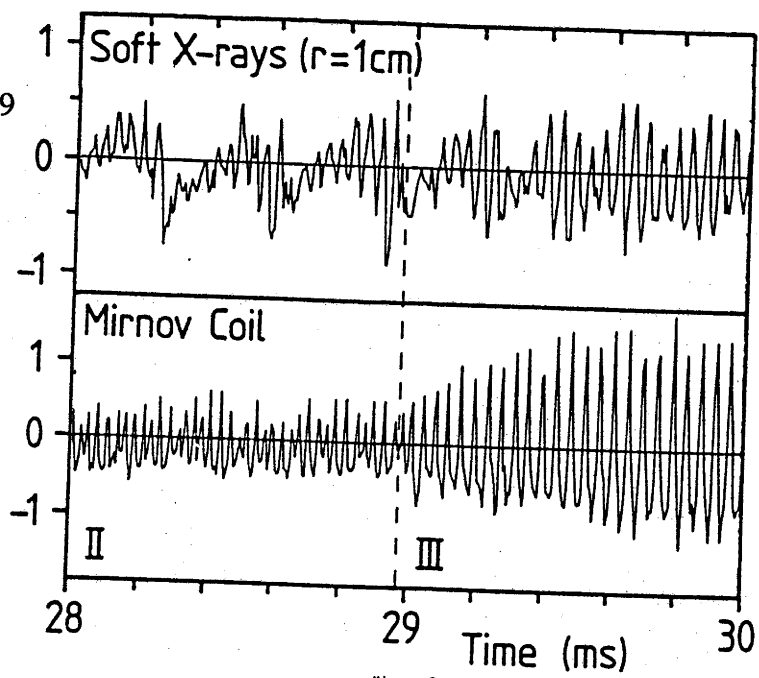


Figure 7

Fig.50(a)

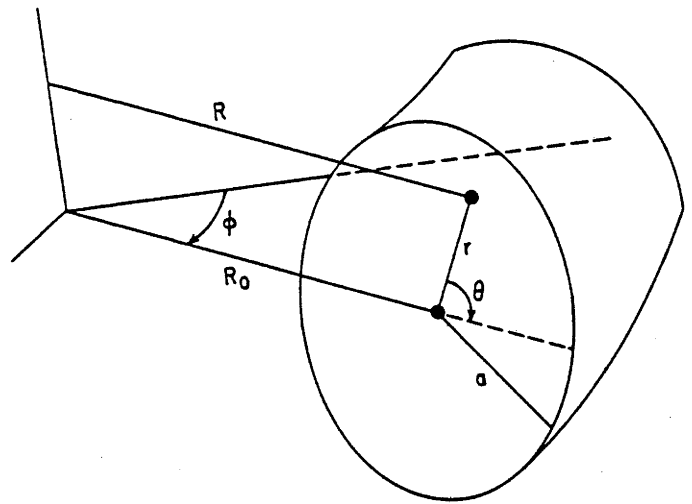


Fig.50(b)

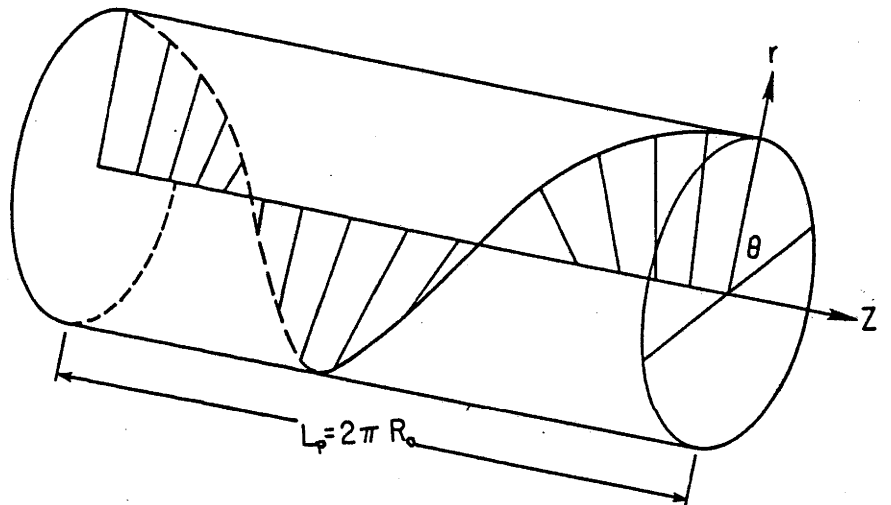
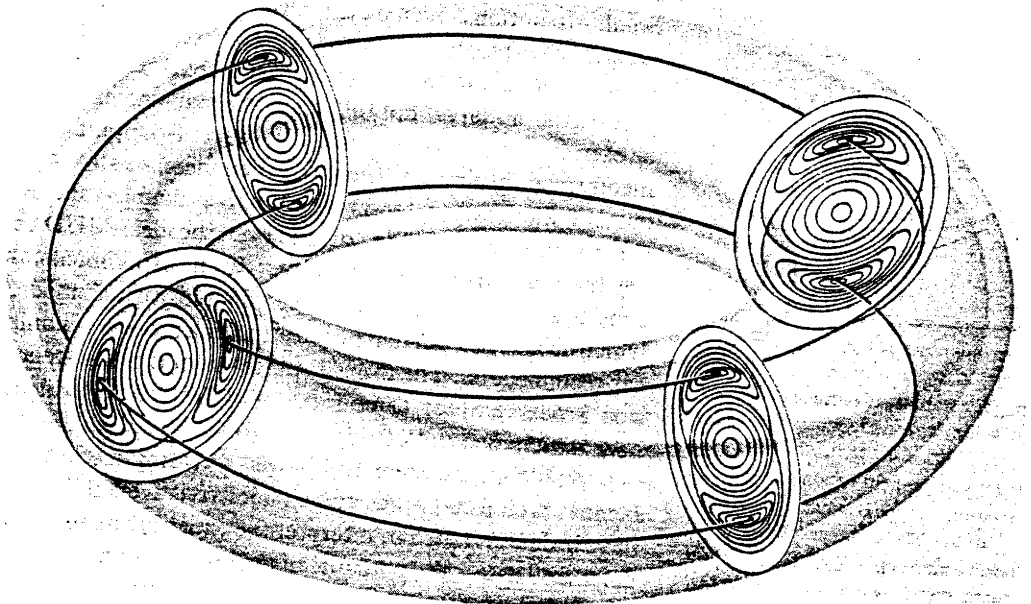


Fig.51



emergence of the signal is unlikely to be due to changes in the size of the islands but more simply due to a temporary cessation in their rotation. This irregular phase does not always lead to a disruption but may return to normal cyclic activity as shown in fig.48, if the density or  $q(a)$  becomes higher.

As mentioned earlier magnetic islands may lock in phase with other islands of different helicities but for a mode to stop rotating it must interact with something external to the plasma so it can be locked into the laboratory frame. Such an external field perturbation could be produced by the limiter or in the case of LT-4 through the periodic vertical field perturbation produced by its single armed iron core, see fig.45.

In the absence of tearing modes the externally imposed perturbations may interact resonantly with the rational surfaces to create magnetic islands by means of forced reconnection<sup>[55,56]</sup>. In fact a calculation of the vacuum magnetic surfaces for a tokamak configuration in the presence of a periodic vertical field perturbation to model the affect of the iron core<sup>[78]</sup> showed the formation of several stationary magnetic island chains including an  $m=2/n=1$  island with a width approx. 10.% of the minor radius. Whether these static force reconnected islands will be reproduced in a rotating plasma is considered in section II-3.2. Assuming that they do then it is relevent to ask how they would affect the evolution of tearing mode magnetic islands which normally tend to convect along with the plasma. This would result in a competition between the two conflicting island states, the resolution of which should shed light on the mechanism of mode locking. This forms the subject of investigation in section II-3.3. In any case the size of these static islands could at least be considered as a measure of the influence or coupling that the external perturbation has at the rational surfaces within the plasma and is used in section II-2.1 as a rough criterion for predicting when mode locking might occur.

An alternative mechanism of mode locking involving the effect of a resistive wall is described by Nave and Wesson<sup>[79]</sup>. A perfectly conducting wall responds to fluctuations in the magnetic field immediately, so that no persistent currents can be supported in it, whereas in a finitely conducting wall eddy currents can be induced because of the reduced

response time. The induced currents give rise to  $\mathbf{J} \times \mathbf{B}$  forces which interact back on the plasma resulting in a transfer of momentum from the plasma to the wall. This causes a slowing down of the plasma which, as discussed in section II-2.3, allows increased penetration of the fields into the wall so that the interaction is strengthened. The consequence is an increasingly rapid transfer of momentum from the plasma, which finally brings the magnetic islands to rest. This was shown to occur over many cycles with an initially  $t^5$  dependence of the frequency followed by exponential decay. It does not however represent a viable modelocking mechanism for explaining the stop/start MHD activity shown in figs.47 and 48 where the  $B_\theta'$  fluctuations stop within a cycle and return again several cycles later with no change in frequency or amplitude.

Persson and Bondeson<sup>[80]</sup> have demonstrated a similar sort of resistive wall modelocking for the case when the rational surface of an  $m=2/n=1$  mode moves outside the plasma. Once outside, the mode is no longer forced to rotate with the plasma and is dragged to a halt by its interaction with the finitely conducting wall. The reduced stabilization that results then allows the mode to grow as an external kink on the timescale of the resistive wall. This scenario is considered to be a likely process leading to the onset of a major disruption as the current increases so that  $q(a)$  falls below 2.

In LT-4 the apparent mode locking and onset of disruptions occur when  $2 < q(a) < 3$ . That is, when there are no rational surfaces near the edge of the plasma to allow mode locking in this way. An alternative scenario is therefore required, although it is possible that it could be applied to the  $m=3/n=1$  mode to explain the drop in signal for  $q(a) > 3$ . In this study consideration has been restricted to mode locking due to the interaction of the mode with an external asymmetric field perturbation.

One way to verify mode locking experimentally would be to apply a controllable external field perturbation to the outside of the plasma which could be tuned to lock and unlock the modes at will. This has, in fact, already been done on several tokamaks<sup>[81,82,83]</sup>, including the Pulsator tokamak in Garching which was equipped with a set of  $m=2/n=1$  helical coils around the plasma. As the current in these coils was

increased a point was reached where the Mirnov oscillations would stop, and when the helical current was turned off they would resume again with the same amplitude and frequency. Such observations are remarkably similar to the irregular MHD activity observed on LT-4, see fig.47 and 48, reinforcing the belief that they are due to this form of mode locking.

The importance of these experiments, however, is brought out by the fact that the mode locking tends to delay the onset of a disruption, although it doesn't prevent it. This may be because the helical currents lock the phase of the tearing mode island without preventing further growth. In the Pulsator experiment it was also found that if the current was increased further a disruption could be triggered even in a discharge that is not otherwise disruptive; thus providing a clear indication of the connection between the  $m=2/n=1$  island and the major disruption.

The problem with mode locking as a means of stabilizing a tearing mode magnetic island is that the island is locked out of phase with the external helical perturbation so that increasing the size of the perturbation just makes the island bigger while decreasing it just allows it to become unlocked. To suppress the growth of the island the external perturbation must be in phase with the mode so that the island has a squeezing force on it to retard its growth. This was made apparent in a quasi-linear numerical study of feedback stabilization <sup>[12,84]</sup> which showed that, while a feedback signal with the proper phase relation can successfully stabilize magnetic island growth, a phase independent or dynamical stabilization scheme does not exist. Without feedback, phase information island growth is only momentarily reversed when the feedback phase opposes growth, but overall stabilization is not achieved. A full non-linear simulation of feedback stabilization showed <sup>[85]</sup> that even when there is no mode rotation the tearing modes tend to flip out of phase with the feedback signal applied at the boundary so that growth is enhanced instead of retarded. Only by pulsing the feedback signal was it possible to limit the growth of the tearing mode islands and prevent a disruption, although this method was not successful when mode rotation was included.

Another way, considered by Holmes et al.<sup>[85]</sup>, to control the amplitude of the tearing mode is to modify the current profile near the rational surface by raising the temperature outside it. This would reduce the current gradient that drives the tearing mode and so stabilize the mode. Reiman<sup>[86]</sup> showed numerically that this method of island suppression could be achieved by locally heating the plasma with rf driven currents without the use of feedback control. The calculation was performed self consistently with specialization to currents driven by lower hybrid waves, although similar calculations<sup>[87]</sup> have been used to explore the feasibility of using electron cyclotron heating (ECH) for the purpose.

The techniques of tearing mode stabilization through a feedback signal or current profile modification are based essentially on the idea of reducing the available free energy. Chu et al.<sup>[88]</sup> consider an alternative method based on increasing the effective singular current layer width in order to artificially induce the Rutherford regime in which the growth of the mode is slowed down to the flux diffusion time across the layer. This happens normally as an island becomes nonlinear but can be induced by externally imposed magnetic islands. The difference between this and the feedback stabilization scheme is that the harmonic number of the externally imposed islands is required to be much higher than that of the tearing mode for the scheme to be effective.

The use of externally applied resonant perturbations for stabilizing tearing modes is obviously important for avoiding disruptions. However, here we are more concerned with how such effects can be tied in with the behaviour of the tearing mode in order to explain the observed MHD activity. This may ultimately prove to be more important by contributing to the understanding of how the disruption can occur in the first place.

The work in part II is organised into two parts. In the first, a quasi-linear delta-prime analysis is used to calculate the amplitude of the poloidal magnetic field oscillations that would be produced by an  $m=2/n=1$  saturated tearing mode magnetic island. The theory, including a derivation of the expression for  $B_{\theta 1}/B_{\theta 0}$  is given in section II-2.1, while in section II-2.2, the results of the calculation based on electron temperature data

from LT-4 are used to predict the variation of  $B_{\theta 1}/B_{\theta 0}$  as a function of the value of the safety factor,  $q(a)$ , at the edge of the plasma. This is compared with the corresponding experimentally observed variation and a mode locking scenario is invoked as a possible explanation for the narrow range of  $q(a)$  covered by the experimental results as compared with theory. A discussion of the results is then presented in section II-2.3.

In the second half of part II are presented some preliminary nonlinear simulations of the effect of a corrugated boundary perturbation on the evolution of the tearing mode magnetic islands in a flowing plasma to qualitatively model the effect of the limiter or iron core. A derivation of the corrugated wall boundary condition is given in section II-3.1 which is first used in section II-3.2 to study the effect of the flow velocity on the magnetic islands produced via forced reconnection by the corrugated boundary. In these simulations the walls are brought in close, so that the tearing mode is completely stabilized. In section II-3.3 the corrugated walls are separated again to demonstrate mode locking and partial mode locking of tearing mode magnetic islands, which is shown to occur with a dynamical response very similar to that observed experimentally. At this stage my grant for using the Cyber 205 supercomputer ran out so that many obvious questions about this work were regrettably left unanswered, although it is hoped to continue the investigation at a later date.



## II-2.1 A Quasi-Linear Delta-Prime Model for Poloidal Magnetic Field Fluctuations

The MHD activity observed in LT-4 <sup>[17,18]</sup>, as with other tokamaks, is found to have a direct correlation with the value of the safety factor at the edge of the plasma,  $q(a)$ . This is summarized graphically in fig.46, which shows a significant peak in the amplitude of the poloidal magnetic field fluctuations over the range :  $2.5 \leq q(a) \leq 2.9$ , referred to as regime III. If, as is generally believed, this activity is a consequence of rotating tearing mode magnetic islands then it should be possible to reproduce the same range of activity using numerical modelling techniques. Ideally this could be done with a fully nonlinear code, however, as an initial step, a far simpler quasi-linear delta-prime analysis <sup>[11]</sup> is used here. The calculation is based on the radial safety factor profiles inferred from experimental electron temperature data and on the assumption that the poloidal magnetic field oscillations are due to a saturated  $m/n = 2/1$  tearing mode. Using this technique Carreras et al.<sup>[11]</sup> were able to calculate amplitudes as a function of  $q(a)$  in good agreement with results from the Ormak and T-4 tokamaks.

Given the success of the approach it is the aim here to perform a similar calculation using temperature profile data from the LT-4 tokamak to verify that the variation of the amplitude of poloidal field fluctuations as a function of  $q(a)$  in fig.46 can also be explained in terms of the saturated tearing mode activity. In the rest of this section is provided the details of the model equations used .

Now that we are trying to obtain quantitative results to compare with experimental data it is necessary to employ a more realistic geometry. Consider a tokamak of circular cross-section with the usual ordering  $B_\phi \gg B_\theta$  where  $B_\phi$  and  $B_\theta$  are the toroidal and poloidal components of the magnetic field. To model this we use a cylindrical approximation to the torus ( $B_\phi \rightarrow B_z$ ) and limit our interest to a single helical mode of the form :  $f(r,t) \exp[ i ( m\theta + kz ) ]$  where  $k = n/R_0$ ,  $m$  and  $n$  are the poloidal and toroidal mode numbers of the perturbation and  $r$ ,  $\theta$ ,  $z$ ,  $R_0$  are as defined in figs.50(a) and

(b). The helical symmetry implies that all quantities are a function of  $\tau$ ,  $r$  and  $t$  only, where  $\tau = m\theta + kz$  so that the problem reduces to a two dimensional one with  $\partial/\partial z = (k/m)\partial/\partial\theta$ . This symmetry together with  $\nabla \cdot \mathbf{B} = 0$  also allows the magnetic field to be specified in terms of a helical flux function,  $\psi_h$  similar to the flux function in equation (18) defined for the slab case :

$$\mathbf{B} = \hat{e}_z \times \nabla \psi_h - \frac{kr}{m} B_z \hat{e}_\theta + B_z \hat{e}_z \quad (146)$$

and is related to the vector potential,  $A$ , by  $\psi_h = (kr/m) A_\theta - A_z$ .  $\psi_h$  is called a helical flux function because it is proportional to the flux through a helical ribbon defined by the magnetic axis and a helix of constant  $\tau$  at a minor radius of  $r$  as in fig.50(b).

The specific aim here is to evaluate the relative amplitude of the poloidal magnetic field oscillations,  $B_{\theta 1}/B_{\theta 0}$ , at the edge of the plasma,  $r=a$ , due to a helical tearing mode magnetic island located at the rational surface,  $r=r_s$ , where the safety factor,  $q$ , defined in cylindrical geometry by :

$$q = - \frac{r B_{z0}}{R B_{\theta 0}} \quad (147)$$

is equal to the rational fraction  $m/n$ . The subscript '1' denotes the perturbed quantity while the subscript '0' denotes the zero order background field. Until otherwise stated, the helical flux function will be referred to as just  $\psi$ , leaving off the subscript 'h' for convenience. From (146) the zero order poloidal magnetic field is given by :

$$B_{\theta 0} = \frac{\partial \psi_0}{\partial r} - \frac{kr}{m} B_{z0} \quad (148)$$

and substituting this into (147) gives :

$$q(r) = \frac{-r B_{z0}}{R \left[ \psi'_0 - (kr/m) B_{z0} \right]} \quad (149)$$

The shear in  $q$  is then given by :

$$q'(r) = \frac{q}{r} \left[ \frac{\Psi_0' + r \Psi_0''}{\Psi_0' - (kr/m) B_{z0}} \right] \quad (150)$$

At the mode rational surface,  $r_s$ , where  $\Psi_0'(r_s) = 0$  and  $q(r_s) = m/n$  this becomes :

$$q'(r_s) = - \left( \frac{m}{n} \right)^2 \frac{R}{r_s} \frac{\Psi_0''(r_s)}{B_{z0}} \quad (151)$$

where  $B_{z0}$  is taken to be constant with respect to  $r$ . The width,  $W$ , of the island in the narrow island approximation<sup>[4]</sup> in terms of the amplitude of perturbed helical flux function,  $\psi_1$ , is given by :

$$W = 4 \left( - \frac{\Psi_1(r_s)}{\Psi_0''(r_s)} \right)^{1/2} \quad (152)$$

which when combined with (151) gives :

$$B_{z0} = 16 \left( \frac{m}{n} \right)^2 \frac{R}{r_s} \frac{\Psi_1(r_s)}{q'(r_s) W^2} \quad (153)$$

By substituting this back into (147) an expression for the zero order poloidal field at  $r=a$  is obtained in terms of the safety factor and the perturbed helical flux function at the mode rational surface as follows :

$$B_{\theta 0} \Big|_{r=a} = - 16 \left( \frac{m}{n} \right)^2 \frac{a}{r_s} \frac{\Psi_1(r_s)}{q(a) q'(r_s) W^2} \quad (154)$$

Using the standard tokamak orderings<sup>[89]</sup> in terms of the small inverse aspect ratio,  $\epsilon = a/R$ , where  $B_{z1} \sim O(\epsilon^2)$ ,  $kr/m \sim O(\epsilon)$ ,  $\Psi_1' \sim O(\epsilon^2)$ , the perturbed poloidal magnetic field is given approximately by :

$$B_{\theta 1} \Big|_{r=a} \approx \frac{\partial \Psi_1}{\partial r} \Big|_{r=a} \quad (155)$$

Combining this with (154) then gives the desired expression for the relative amplitude of the poloidal magnetic field fluctuations at the edge of the plasma :

$$\frac{B_{\theta 1}}{B_{\theta 0}} \Big|_{r=a} = -q(a) \frac{W^2}{16 (m/n)^2} \left( \frac{r_s}{a} \right) q'(r_s) \left[ \frac{1}{\psi_1(r_s)} \frac{\partial \psi_1}{\partial r} \Big|_{r=a} \right] \quad (156)$$

The task is now to calculate the perturbed flux function,  $\psi_1$ , and island width,  $W$ , for the saturated tearing mode. To do this a set of reduced resistive MHD equations for the helical flux function and velocity stream function in cylindrical geometry are derived<sup>[6]</sup> in a similar manner to those for the slab case in section I-2.1 by using equation (146), assuming incompressibility and only keeping terms of lowest order in  $\varepsilon$ <sup>[89]</sup>. They are :

$$\frac{\partial \psi}{\partial t} + \mathbf{V} \cdot \nabla \psi = \eta J_z - E_z^{\text{ext}} \quad (157)$$

$$\frac{d}{dt} (\nabla \cdot \rho \nabla \phi) = -\hat{e}_z \cdot [\nabla \psi \times \nabla J_z] \quad (158)$$

$$\mu_0 J_z = \nabla^2 \psi - \frac{2k B_z}{m} \quad (159)$$

where  $\phi$  is defined the same as in the slab case by  $\mathbf{V} = \hat{e}_z \times \nabla \phi + V_z \hat{e}_z$ . Except for the 2nd. term in (159) and the neglect of viscosity these equations have the same general form as equations (25), (26) and (27) in part I-2.1. They form the basic set of equations for studying the evolution of an  $m \geq 2$  tearing mode magnetic island in a tokamak type plasma.

While the sizes of the magnetic islands are still small compared to the width of the diffusion layer their behaviour is adequately described by the linear form of these equations, which predicts an exponential growth rate on a hybrid hydromagnetic-resistive time scale. However, when the magnetic island exceeds the width of the diffusion layer, higher order eddy currents, which oppose the zero order current near the rational surface, become dominant and produce a force which replaces the inertia as the force which impedes the growth of the mode<sup>[9]</sup>. From this point onwards the inertial term in (158) can be neglected so that :

$$\hat{e}_z \cdot [\nabla \psi \times \nabla J_z] = 0 \quad (160)$$

which was used by Rutherford<sup>[9]</sup> to show how, at this stage, the growth slows to an algebraic rate.

At saturation the  $\psi_1$  mode has essentially the same shape as the linear eigenmode, so the factor in the square brackets of equation (156) is estimated using the linear form of  $\psi$  through :

$$\psi(r,\theta,z,t) = \psi_0(r) + \psi_1(r,t) \cos(m\theta + kz) \quad (161)$$

Substituting this into (160) we find to first order in  $\epsilon$  :

$$\frac{1}{r} \frac{\partial}{\partial r} \left( r \frac{\partial \psi_1}{\partial r} \right) - \frac{m^2}{r^2} \psi_1 = - \frac{\partial J_{z0}}{\partial \psi_0} \psi_1 \quad (162)$$

which, given the equilibrium toroidal current,  $J_{z0}$ , and the equilibrium flux function,  $\psi_0$ , is suitable for calculating the linear eigenfunction,  $\psi_1$ , valid for the region outside the diffusion layer. Equation (162) is integrated numerically in cylindrical geometry using a 1-D shooting code written by R.B. White.

With the boundary conditions for  $\psi_1$  and  $\psi'_1$  specified by :

$$\begin{aligned} \psi_1 &= r^m, & \psi'_1 &= m r^{m-1} & \text{near } r &= 0 \\ \psi_1 &= 0, & \psi'_1 &= -1 & \text{at } r &= a. \end{aligned} \quad (163)$$

the code integrates in from the plasma edge and out from the axis toward the rational surface at  $r = r_s$  and then normalizes the results so that  $\psi_1$  is continuous there.

Since the equations are only valid for the region exterior to the diffusion layer,  $\psi'_1$  is discontinuous at  $r = r_s$  corresponding to the finite linear  $\Delta'$  mentioned in section I-1.1. To calculate the saturated island width of the tearing mode magnetic island we employ the concept of a nonlinear  $\Delta'$ , that was also discussed in section I-1.1 and is defined by :

$$\Delta'(W) \equiv \frac{1}{\psi_1(r_s)} \left[ \frac{\partial \psi_1}{\partial r} \Big|_{r_s+W/2} - \frac{\partial \psi_1}{\partial r} \Big|_{r_s-W/2} \right] \quad (164)$$

where  $W$  is the full island width across the separatrix at its widest point. The saturated island width,  $W_{\text{sat}}$ , is then simply obtained from the condition given in section I-1.1 that  $\Delta'(W_{\text{sat}}) = 0$ .  $\Delta'$  is effectively proportional to the free magnetic energy of the initial equilibrium that can be released through reconnection of the field lines. The saturation condition therefore simply means that the island stops growing when there is no free energy left to drive it.

Having specified the initial equilibrium and from it evaluated the linear profile of the perturbed flux function and then the corresponding saturated island width, equation (156) can finally be used to calculate the amplitude of the  $B_\theta$  fluctuations at  $r = a$  corresponding to a particular helical magnetic island at  $r = r_s$  with poloidal and toroidal mode numbers  $m$  and  $n$ .

## II-2.2 Results - Comparison with LT-4 MHD Activity

The equilibrium is specified through the following parametrization of the safety factor<sup>[11]</sup> :

$$q(r) = q(0) \left( 1 + (r/r_0)^{2\lambda(r)} \right)^{1/\lambda(r)} \quad (165)$$

$$\text{where } \lambda(r) = \lambda_0 + \frac{1}{2} \lambda_2 (r/a)^2$$

Values of the parameters  $q(0)$ ,  $\lambda_0$ ,  $\lambda_2$ , and  $r_0$  are determined by fitting with experimental electron temperature,  $T_e$ , profile data obtained from Thompson scattering measurements on LT-4. According to Spitzer<sup>[90]</sup> :  $\eta \propto T_e^{-3/2}$ , so assuming a static equilibrium and uniform electric field in Ohm's law the current density varies approximately as  $J_z \propto T_e^{3/2}$ . This establishes the connection between the electron temperature data and the current density. From Ampere's law and equation (147) the expression :

$$J_z = \frac{B_z}{\mu_0 R} \frac{1}{q(r)} \left[ 2 - \frac{r}{q(r)} \frac{\partial q}{\partial r} \right] \quad (166)$$

can then be used to relate the current density to the safety factor. This is done by inserting the parametrization of  $q$ , (165), into (166) to give a corresponding parametrization for  $J_z$

$$J_z(r) = J_z(0) f^{-1/\lambda} \left( 1 - \frac{f-1}{f} \left[ 1 + \frac{\lambda_2}{\lambda} \left( \frac{r}{a} \right)^2 \ln \left( \frac{r}{r_0} \right) \right] - \frac{\lambda_2}{2\lambda^2} \left( \frac{r}{a} \right)^2 \ln(f) \right)$$

$$\text{where } f = 1 + \left( \frac{r}{r_0} \right)^{2\lambda} \quad (167)$$

and where  $J_z(0)$  is related to  $q(0)$  through :

$$q(0) = \frac{2 B_z}{\mu_0 R J_z(0)} \quad (168)$$

This was derived from Ampere's Law by assuming that, in the limit  $r \rightarrow 0$ ,  $B_\theta \propto r$ .

The fitting parameters are then obtained by fitting the parametrization (167) to the LT-4 electron temperature data taken to the  $3/2$  power while the value of  $q(0)$  is evaluated using (168) after adjusting  $J_z(0)$  so that the total current is equal to that measured directly on LT-4.

Ideally, all the Thompson scattering measurements for profile determination should be made simultaneously with measurements of the amplitude of the poloidal magnetic field oscillations at the edge of the plasma, as was the case on Ormak<sup>[11]</sup>. This would allow a point for point comparison of experimental  $B_{\theta 1}/B_{\theta 0}$  measurements with theoretical values calculated from each  $q$ -profile. Thompson scattering measurements on LT-4, however, were limited to one per discharge making it necessary to run a series of similar discharges to build up a single temperature profile<sup>[91]</sup>. The difficulties in reproducing the exact same conditions in each discharge puts obvious limitations on the accuracy, making it unrealistic to attempt more than one profile determination, see fig.52(a).

However if we assume that the basic shape of the  $q$ -profile remains approximately the same, then the parameter  $r_0$ , in the parametrization for  $q$  in equation (165), can be varied, keeping  $q(0)$  fixed, to obtain different  $q$ -profiles for a range of  $q(a)$  corresponding to a variation in the total current. In this way a plot of  $B_{\theta 1}/B_{\theta 0}$  versus  $q(a)$  can still be generated.

Even with this approach a further problem arises because of the scarcity of experimental data points, see fig.52(a). With only four data points, accurate to within  $\pm 70$  eV, it was not possible to obtain a unique fit, so a rough hand fit was made from which a parametrization was obtained using a least squares fitting code. The data points are most scarce towards the outside region of the plasma where the  $m \geq 2$  rational surfaces tend to be and hence where the current density gradients would most sensitively affect the size of the magnetic islands. Probably as a consequence of this, the initial fit (fit(1) in table 2.), when used in the calculation, predicted negligible  $B_{\theta}$  amplitudes for all except



Fig.52(a)

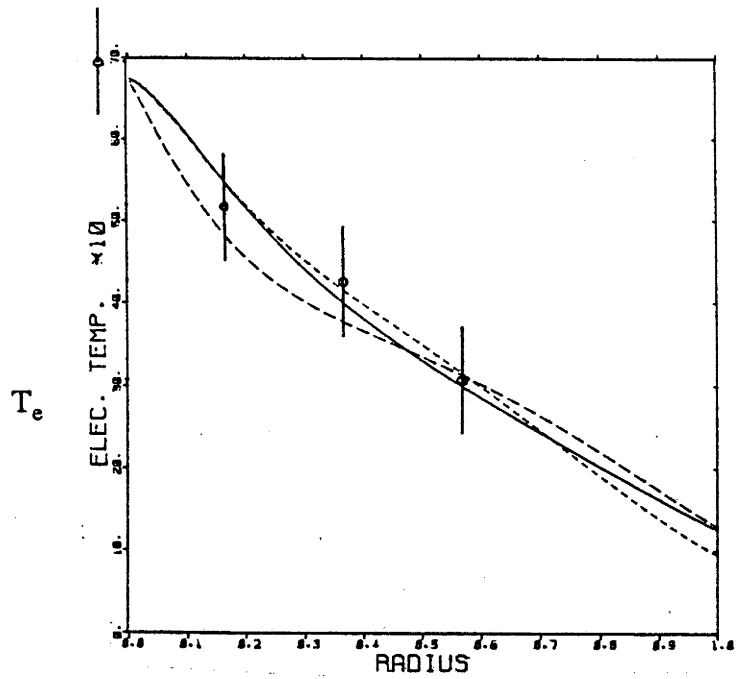


Fig.52(b)

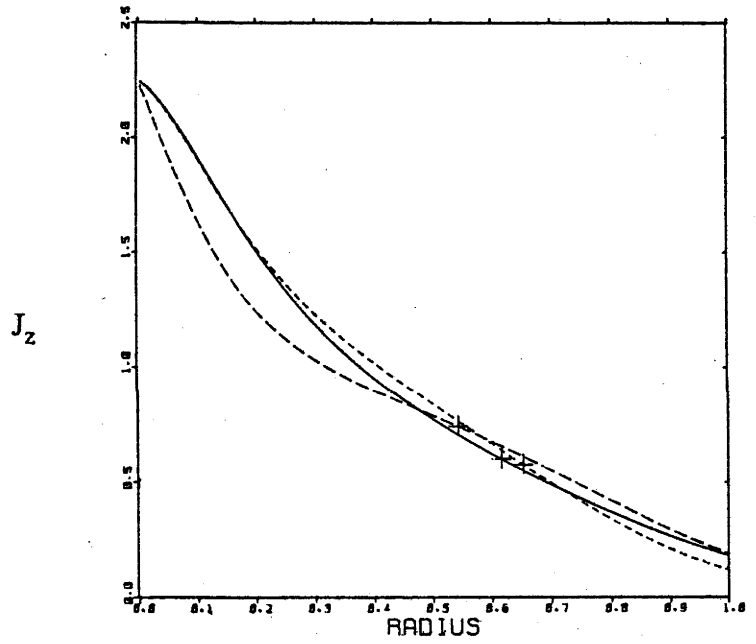


Table 2

Profile	$\lambda_0$	$\lambda_2$	$r_z$	$q(0)$	$q(a)$
Fit (1)	0.7715	1.2147	0.5502	0.888	3.3333
Fit(2)	0.77	2.0	0.5311	0.888	3.3333
Fit(3)	0.6	1.7	0.5452	0.888	3.3333

the  $m=2/n=1$  mode which peaked around the same range of  $q(a)$  as in LT-4 but was an order of magnitude too small with  $B_{\theta 1}/B_{\theta 0} \sim 0.02\%$  instead of  $0.3\%$ .

The saturated island width, which is the dominant factor determining the size of the MHD activity, was found by Carreras et al. <sup>[11]</sup> to be very sensitive to small changes in the shape of the profile. With this in mind, a parameter study was made of the behaviour of  $W_{\text{sat}}$  versus  $q(a)$  as a function of  $\lambda_0$  and  $\lambda_2$ , the aim being to determine values of these parameters which give  $W_{\text{sat}}$  and  $B_{\theta 1}/B_{\theta 0}$  for an  $m=2$  island more closely resembling the experimental results in fig.46. The results of this study are recorded in figs.53(a),(b) and (c) and show that in most cases the saturated island width peaks within a finite range of  $q(a)$ . In particular fig.53(a) shows that increasing  $\lambda_0$  : broadens the range of the peak, shifts the peak towards larger  $q(a)$  and, except for  $\lambda_0 < 0.7$ , only mildly affects the size of the peak. On the other hand fig.53(b) shows that the main effect of increasing  $\lambda_2$  is to increase the size of the peak with less change in position as is made clearer in fig.53(c).

Given this information a second fit ( fit(2) in table 2.) was produced by increasing  $\lambda_2$  from 1.2 to 2.0 so as to bring the peak amplitude roughly up to that observed experimentally, see fig.54(c). However, now the problem is that the peak is too broad. A third fit ( fit(3) in table 2. ) was therefore made by decreasing  $\lambda_0$  from 0.77 to 0.6 so as to make the peak narrower, then readjusting  $\lambda_2$  to get back to the correct peak amplitude. Unfortunately, as noted in the parameter study, decreasing  $\lambda_0$  also shifts the peak to a lower  $q(a)$ , so that, although the peak in  $B_{\theta 1}/B_{\theta 0}$  vs.  $q(a)$  now has roughly the same height and width as the experimental results, see fig.54(c), it is centred on a significantly lower  $q(a)$ . This discrepancy is accentuated by the fact that correcting the calculated values of the safety factor of the experimental results for toroidal effects indicates that the range of MHD activity occurs at a slightly higher range of  $q(a)$ , as shown on the upper scale of fig.46.

The current and electron temperature profiles corresponding to these fits are plotted in fig.53(a) and (b) and show that fit(2) is actually a better fit to the data while fit(3) is

Fig.53(a)

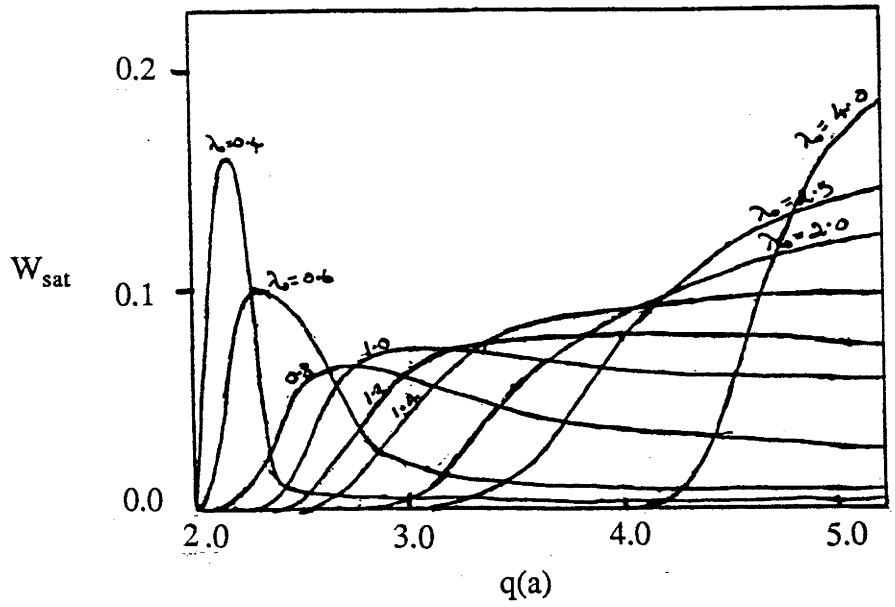


Fig.53(b)

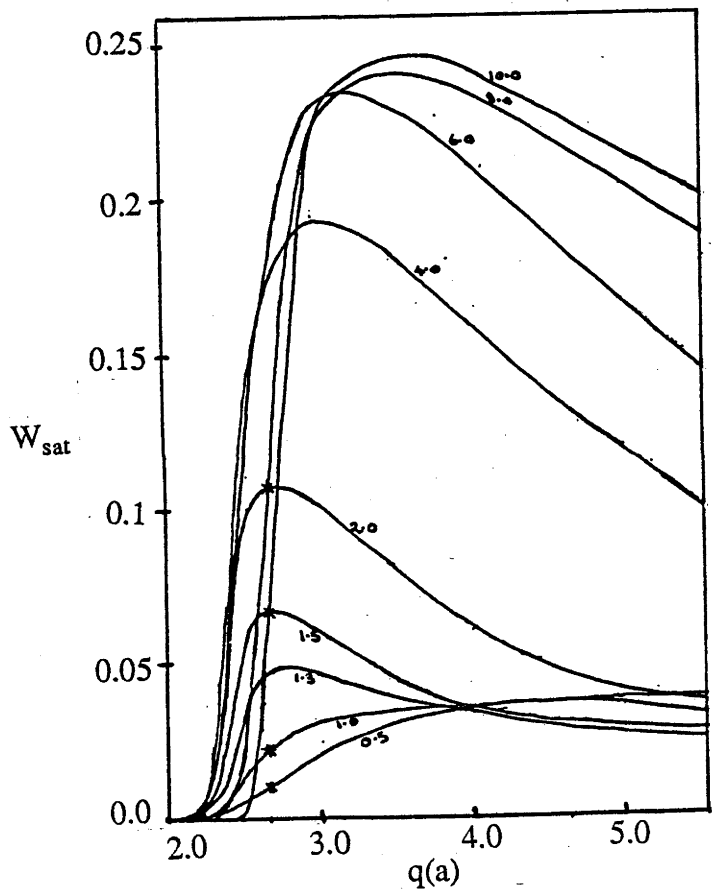


Fig.53(c)

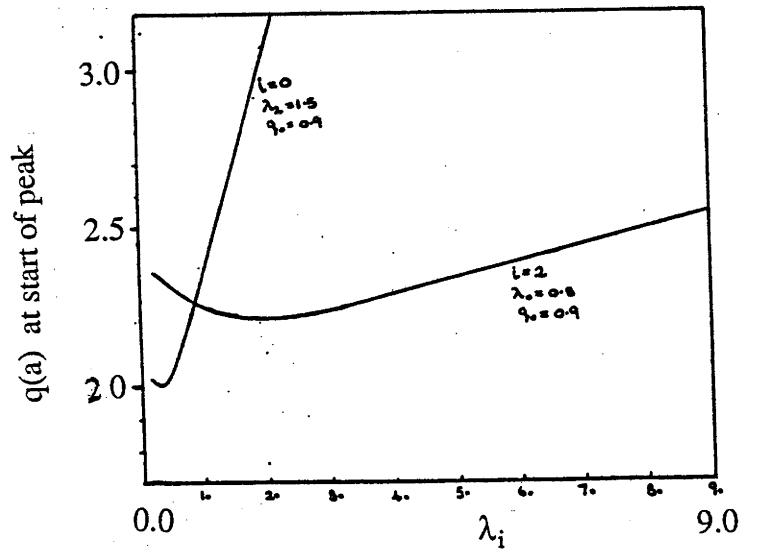


Fig.54(a)

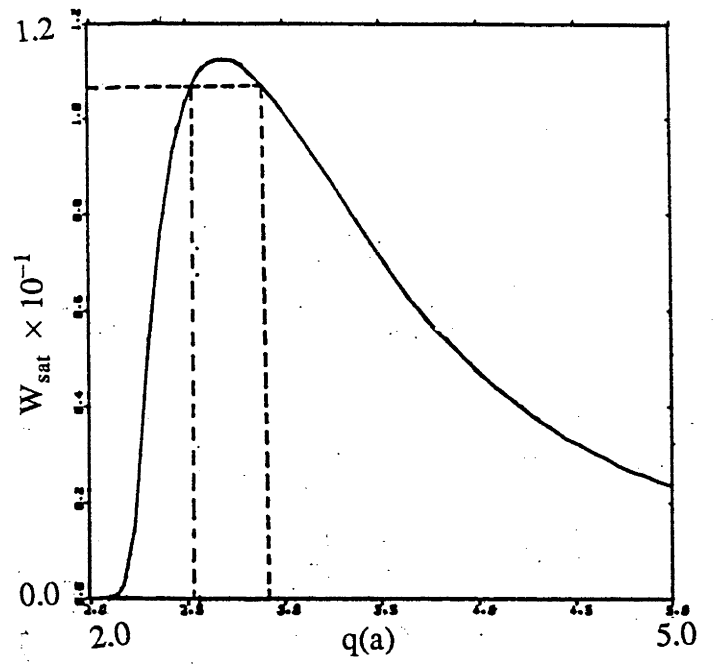


Fig.54(b)

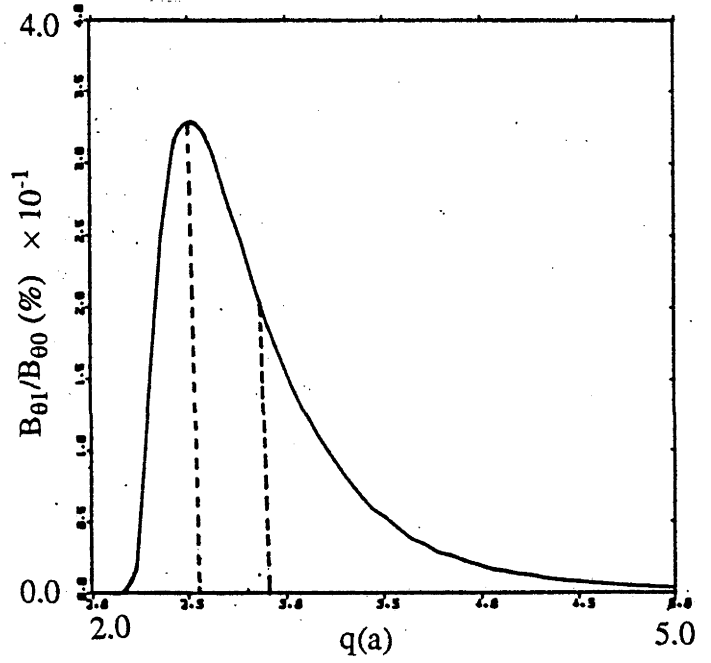
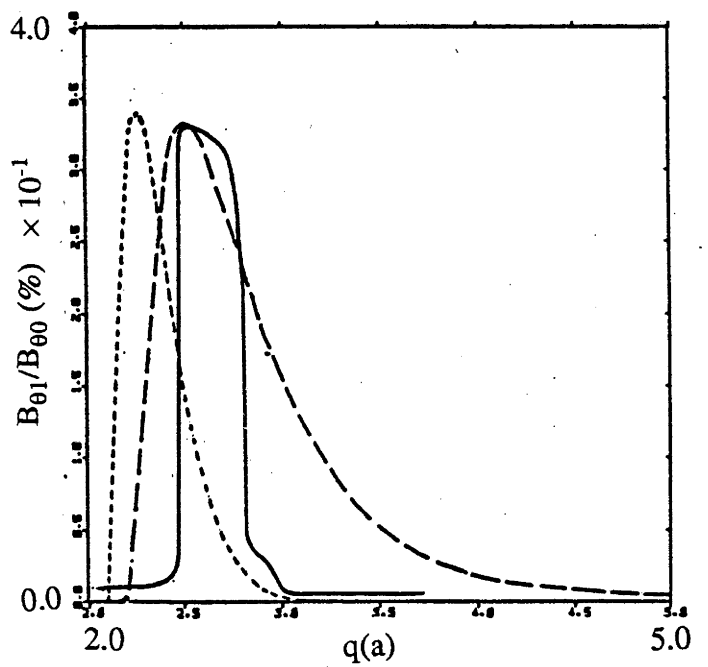


Fig.54(c)



worse, although all are within experimental error. Further adjustment of  $\lambda_0$  and  $\lambda_2$  could not be made to produce a better fit to the experimentally observed MHD activity. Therefore either the theoretical model is not sophisticated enough to predict the correct range, which is likely, or the magnetic islands are still there but for some reason the field perturbation is not detected outside the narrow range of  $q(a)$  shown in fig.46 and 52(c).

It was noted in section II-1.1 that there are several possible sources of asymmetric external field perturbations, such as would be produced by the limiter or the single armed iron core and according to the vacuum calculation by Dewar<sup>[78]</sup> these can interact resonantly with the rational surfaces to produce stationary magnetic islands with widths a significant fraction of the minor radius. Such islands would, through the coupling of the field to the fluid, create a drag effect on the rotating plasma in the vicinity of the rational surfaces and would clearly conflict with the tearing mode magnetic islands which normally convect along with the plasma. A possible scenario is that when the tearing mode islands are small, the external perturbation forces the mode to be stationary with respect to the laboratory frame but as the island grows larger, so that a larger region of the plasma is prevented from rotating, a point must come where the drag forces on the plasma within the island are sufficient to overcome the influence of the external perturbation causing the island to get dragged around the torus with the rest of the plasma.

The significance of this scenario here is in the fact that it is only when the magnetic islands are unlocked and rotating past the Mirnov coils that the temporal fluctuations in the poloidal magnetic field are produced. Therefore mode-locking of the islands to an external field perturbation could explain the absence of a signal even when the magnetic islands are still large enough to significantly perturb the poloidal magnetic field.

A rough criterion for estimating the point of transition to the unlocked state could be when the tearing mode island width exceeds that calculated for the static, forced reconnected islands which were found to be roughly 10 % of the minor radius, i.e.  $r \approx 0.1a$ <sup>[78]</sup>. By invoking mode-locking below an island width of  $W = 0.105$ , as in fig.54(a), the detectable  $B_\theta$  signal is then restricted to the range :  $2.6 \leq q(a) \leq 2.9$ , which

brings the theoretical prediction of fit(2), shown in figs.54(b), into good agreement with the experimentally observed range of MHD activity as function of  $q(a)$ , see fig.54(c).

The plausibility of this argument is diminished somewhat when considering how the transition to the mode-locked state would occur as function of time. Arguably this could occur suddenly with the signal disappearing within one cycle as is observed during the irregular MHD activity, see fig.48, or gradually over several cycles with a slowing down in frequency. However the regular MHD activity, see fig.48, appears to decay over a number of cycles with a steadily decreasing amplitude and with no change in frequency. Note that the decrease in amplitude of  $B_{\theta}'$  ( $\sim \omega B_{\theta}$ ) cannot be due to a decrease in frequency,  $\omega$ , since the period of the signal does not get longer. This amplitude decrease would perhaps be more consistent with a decrease in island size rather than a locking of the mode and since the range of MHD activity shown in fig.46 applies to both the regular and irregular activity the above mode-locking scenario appears less convincing.

But despite its shortcomings as an explanation for the  $B_{\theta}'$  versus  $q(a)$  diagram, evidence of mode-locking during the irregular MHD activity is overwhelming and in section II-3.3 a numerical investigation is made of the way this might occur.

## II-2.3 Discussion of Results and Conclusions

Even without mode locking there are several discrepancies in the calculation which require further qualification. For instance there is the question of the validity of using perfectly conducting wall boundary conditions in modelling the LT-4 plasma. In reality, the vacuum vessel wall is not perfectly conducting but has a finite resistive skin time and, because of the presence of a limiter, it is also separated from the edge of the plasma by several centimetres, not right up against the plasma as was assumed in the calculation.

The finite resistivity allows flux penetration of the wall so that it no longer acts as a rigid flux surface and therefore no longer provides the stabilization produced by a perfectly conducting wall. This, however, is not necessarily the case if the plasma is rotating. According to a calculation done by Jensen and Chu <sup>[92]</sup> a resistive wall will stabilize modes just like a perfectly conducting wall if the plasma rotates past it with a period,  $\omega^{-1}$ , much shorter than the resistive skin time of the wall,  $\tau_{R(\text{wall})} = \mu_0 \delta a / \eta_w$ , i.e. when  $\omega \tau_{R(\text{wall})} \gg 1$  where  $\eta_w$  is the resistivity, and  $\delta$  is the thickness of the wall. If the flow is sheared, however, the effect is destabilizing but only very weakly for the parameters of most tokamak plasmas. A report by Rutherford and Furth <sup>[93]</sup> also indicated the same sort of resistive wall stabilization for ideal kink instabilities at the edge of a rotating plasma provided the oscillation frequency of the stabilized kinks exceeded the rotation frequency of the plasma.

Even assuming that the plasma rotation is fast enough for the resistive wall to be treated as if perfectly conducting, the wall is still separated from the edge of the plasma by the limiter and therefore its stabilizing effect will be somewhat reduced.

To investigate the effect of moving the conducting wall further out, the calculation was extended beyond the limiter radius at  $r = a$ , by adding a smoothly joining exponentially decaying tail to the current profile, with the conducting wall boundary condition applied at a larger radius at  $r = b$ . This is based on the assumption that a diffuse plasma, which supports a weak current, exists between the limiter and the wall.

The destabilizing effect is quite dramatic even when  $b$  is only a little greater than  $a$ . When  $b = 1.5a$  the peak saturated island width is almost doubled, producing an almost sixfold increase in the  $B_\theta$  amplitude. Even the original equilibrium current profile, fit(1), resulted in a peak amplitude many times greater than for the experimentally observed signal when the wall radius was increased. In fact it was difficult to find a set of parameters for the current profile which would not produce such large amplitudes for the  $m=2/n=1$  mode. It would therefore seem almost necessary to have full perfectly conducting wall stabilization to account for the smallness of the experimentally observed signal.

The reason for this may involve the limiter. One proposition put forward by Freidberg, Goedbloed and Rohatgi<sup>[94]</sup> to explain the absence of experimentally observed external ideal MHD kinks is that the limiter would stabilize such modes by forcing them to assume the form of a standing wave with a node occurring at the limiter. The constraint can be thought of as a coupling of plus and minus  $n$  numbers for each  $m$  so that the net effect is one of stabilization. Alternatively, it is conceivable that the rotation of the plasma past the limiter might have a stabilizing affect by preventing such nonaxisymmetric field perturbations from penetrating out beyond the limiter. If the rotation is fast enough the limiter may possibly act on the plasma like a conducting wall even though it forms a ring at only one point around the torus. It is in the light of such considerations that we justify the use of perfectly conducting wall boundary conditions adjacent to the plasma.

The results of the quasi-linear delta-prime calculations, described in the previous section, have been based solely on the  $m=2/n=1$  saturated tearing mode magnetic island, however a spatial analysis of the signal shows the experimentally observed MHD activity to have a large, often dominant  $m=3$  component. It has therefore been suggested that the MHD activity is actually due to an  $m=3$  tearing or kink mode, since it begins near where the  $q = 3$  rational surface enters the plasma. This is especially evident when toroidal corrections are made to the  $q$ -values, see upper scale in fig.46.



It is however unlikely that an  $m=3/n=1$  mode forms the dominant magnetic island in the plasma since no spontaneous  $m=3/n=1$  amplitude was produced in the calculation even with the conducting walls pulled further out, although this may be due to poor fitting of the electron temperature profile in the outer region of the plasma. By the same token it would be hard to explain the absence in the plasma of a dominant  $m=2/n=1$  island given the apparent easily destabilized nature of the  $m=2$  mode shown by the calculation. A possible scenario is that there is a small  $m=3$  island which is driven by the  $m=2$  mode through the coupling created by the poloidal variation of the toroidal field in the manner demonstrated by Finn<sup>[15]</sup>. On this basis it would contribute to the signal but only over the range of  $q(a)$  for which the  $m=2$  mode is unstable. In fact since the  $q=3$  rational surface is closer to the the edge of the plasma than the  $q=2$  surface the Mirnov coils would probably tend to pick up a larger proportion of  $m=3$  signal even if the  $m=3$  island is much smaller.

A significant  $m=2$  component of the signal is observed on the Mirnov coils but its dominance should be more evident with an internal detection system. The soft X-ray emissions clearly show fluctuations in the temperature and density but since most of the flux comes mainly from the hot centre of the plasma they are only suitable in LT-4 for distinguishing sawteeth oscillations and  $m=1$  modes. Phase scintillation interferometry on the other hand detects only density fluctuations and is therefore more suitable for picking up signals from the region between those covered by soft X-rays and Mirnov coils. Results from this technique seem to indicate a large  $m=2/n=1$  mode<sup>[95]</sup> but this is not yet conclusive because the method involves a line integral through a volume of plasma which makes it difficult to determine the mode structure of the signal.

Spatial analysis of the magnetic coil signals in the small tail of activity of regime II in fig.46 reveals it to be almost a pure  $m=3/n=1$  mode. It is therefore likely that this activity does correspond to a spontaneous  $m=3$  kink or tearing mode. If we assume, as proposed earlier, that the absence of an  $m=2$  signal in regime II is because it is mode locked then the fact that the  $m=3$  mode is not implies a weaker coupling of the external perturbation to the  $m=3$  island. This seems unlikely given that the  $m=3/n=1$  rational

surface is closer to the edge of the plasma and this therefore represents another drawback to the mode locking scenario as a means of explaining the narrow range of MHD activity of regime III.

In conclusion, although the mode locking scenario provides a neat way to clip the unexplainably broad range of activity predicted by the quasi-linear delta prime calculation as a function of  $q(a)$ , it is more likely that its failure to predict the narrow range observed experimentally is an artifact of the way in which a single temperature profile was, with minimal justification, adjusted to represent the profiles corresponding to a range of  $q(a)$ . More accurate representations of the temperature profile for several values of  $q(a)$  would probably allow the same calculation to predict a range of activity closer to that observed.

The validity of the calculation is backed up by its successful application to results from Ormak and T-4 [11]. These devices exhibit broader ranges of MHD activity as a function of  $q(a)$  than LT-4 which agree more closely with the theoretical predictions without invoking mode locking. This could just mean that they do not have sufficient asymmetry to induce locking of their islands. In any case the quasi-linear delta prime theory has been successfully applied to many situations including a calculation of plasma disruptions by Turner and Wesson [96] in which the self consistent interaction of the tearing mode evolution with transport processes is investigated.

The major limitation of the analysis, as used here, is the scarcity and poor quality of the electron temperature data. The few Thompson scattering measurements are clearly insufficient to distinguish the subtle changes in the current profile for which the saturated island width is so sensitive. Conversely it is because of this great sensitivity that a reasonable fit to the temperature data could be found which was also reasonably consistent with the observed amplitudes of the poloidal magnetic field fluctuations.

If mode locking is dependent upon the size of the islands, as suggested, then the sensitivity to the current profile could mean that the general transport related fluctuations in the current during the discharge may produce changes in the island size sufficient to induce a switching back and forth between the locked and unlocked states similar to that

indicated by the irregular MHD activity. Fig.54(a) indicates that a fluctuation in island width of only  $\sim 3\%$  of the minor radius would be required. In any case the overwhelming evidence for mode locking during this irregular MHD activity provides the main motivation for investigating the process further.

### II-3.1 Corrugated Wall Boundary Conditions.

In the calculations of the previous section a mode locking scenario involving the effect of an external field perturbation in the LT-4 tokamak was invoked without actually demonstrating how it would occur or whether it can occur. These questions are, perhaps, best tackled using numerical modelling techniques for which the nonlinear 2-D plane-slab visco resistive code used in Part I is suitable for doing a qualitative study of the process. To simulate the relative motion of the plasma past the walls, a uniform  $E \times B$  drift in the  $y$ -direction,  $V_y$ , is set up as described in section I-2.1 by introducing a potential difference between them. This is implemented in the code by setting the initial zero order velocity stream function as :

$$\phi_0^c(x) = V_y x \quad (169)$$

which is maintained by fixing the wall values at :

$$\phi_0^c(\pm X_w) = \pm V_y X_w \quad (170)$$

To simulate the periodic field perturbation of the limiter or iron core a sinusoidal magnetic field variation can be imposed at the boundary, although to avoid the generation of artificial viscous boundary layers it is also necessary to perturb the fluid in the same way. This can be achieved by adjusting the boundary conditions to model a corrugated perfectly conducting wall as schematically shown in fig.55.

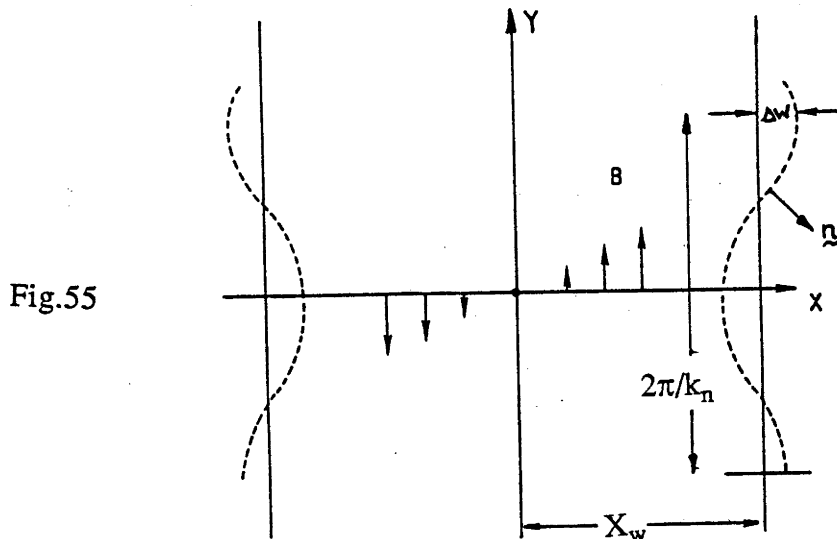


Fig.55

The boundary conditions that are required to be satisfied at this corrugated wall are :

$$\mathbf{n} \cdot \mathbf{B} \Big|_{\text{wall}} = 0 \quad \rightarrow \quad \text{perfectly conducting wall} \quad (171)$$

$$\mathbf{n} \cdot \mathbf{V} \Big|_{\text{wall}} = 0 \quad \rightarrow \quad \text{Impenetrable wall} \quad (172)$$

$$\mathbf{n} \times (\nabla \times \mathbf{V}) \Big|_{\text{wall}} = 0 \quad \rightarrow \quad \text{No generation of vorticity at wall} \quad (173)$$

The equation of the corrugated wall is :

$$x = X_w + \Delta W \cos(k_n y) \quad (174)$$

for which a (non-unit) vector normal to the surface of the wall is :

$$\mathbf{n} = \hat{\mathbf{e}}_x + k_n \Delta W \sin(k_n y) \hat{\mathbf{e}}_y \quad (175)$$

Consider first the boundary condition on the magnetic field in equation (171) which becomes :

$$B_x + B_y k_n \Delta W \sin(k_n y) \Big|_{X_w + \Delta W \cos(k_n y)} = 0 \quad (176)$$

The grid in the code is fixed between  $x = \pm X_w$  and cannot be made to follow the corrugation without altering the geometry of the grid and hence the entire structure of the code. Alternatively the values of  $\psi$ ,  $\phi$  and  $\zeta$  can be specified at  $x = \pm X_w$  but so as to be consistent with a corrugated perfectly conducting wall. To do this we can take advantage of the fact that  $\Delta W \ll X_w$  and expand the boundary condition, (176), in a Taylor series to first order in  $\Delta W$  around  $x = X_w$  like :

$$B_x(X_w) + \left[ \frac{\partial B_x}{\partial x} \right]_{X_w} \Delta W \cos(k_n y) + B_y(X_w) k_n \Delta W \sin(k_n y) = 0 \quad (177)$$

then substituting in equation (18) of part I-2.1 for  $\mathbf{B}$  in terms of  $\psi$  this becomes :

$$-\left[ \frac{\partial \psi}{\partial y} \right]_{X_w} - \left[ \frac{\partial^2 \psi}{\partial x \partial y} \right]_{X_w} \Delta W \cos(k_n y) + \left[ \frac{\partial \psi}{\partial x} \right]_{X_w} k_n \Delta W \sin(k_n y) = 0 \quad (178)$$

The spectral nature of the code means that it is also necessary to express  $\psi$  in equation (178) in a Fourier expansion in order to extract out the boundary conditions for each Fourier component. To be consistent the largest period allowed for the boundary perturbation must equal the periodicity length of the plasma so that  $k_n = 2\pi n/L_p$ . The condition then becomes :

$$\begin{aligned}
\sum_{m=1}^{\infty} \left\{ - \psi_m^s(X_w) m \cos(k_m y) + \psi_m^c(X_w) m \sin(k_m y) \right. \\
- \frac{1}{2} \Delta W \left[ \frac{\partial \psi_m^s}{\partial x} \right]_{X_w} \left( (m+n) \cos(k_{m+n} y) + (m-n) \cos(k_{m-n} y) \right) \\
+ \frac{1}{2} \Delta W \left[ \frac{\partial \psi_m^c}{\partial x} \right]_{X_w} \left( (m+n) \sin(k_{m+n} y) + (m-n) \sin(k_{m-n} y) \right) \left. \right\} \\
+ \frac{1}{2} \Delta W \left[ \frac{\partial \psi_0^c}{\partial x} \right]_{X_w} n \sin(k_n y) = 0 \tag{179}
\end{aligned}$$

where  $k_m = m k_1$  and where we have divided through by  $k_1$ . In general to satisfy this condition the coefficients of each Fourier component must vanish so that the following individual boundary conditions for each  $\psi_m^c$  and  $\psi_m^s$  are obtained by gathering terms with the same arguments :

$$\begin{aligned}
\psi_m^c(X_w) &= \frac{1}{2} \Delta W \left( \left[ \frac{\partial \psi_{|m-n|}^c}{\partial x} \right]_{X_w} + \left[ \frac{\partial \psi_{m+n}^c}{\partial x} \right]_{X_w} \right) \\
\psi_m^s(X_w) &= \frac{1}{2} \Delta W \left( \frac{m-n}{|m-n|} \left[ \frac{\partial \psi_{|m-n|}^s}{\partial x} \right]_{X_w} + \left[ \frac{\partial \psi_{m+n}^s}{\partial x} \right]_{X_w} \right) \tag{180} \\
m &= 1, 2, 3, \dots
\end{aligned}$$

As with the straight conducting wall, the corrugated conducting wall imposes no constraint on the  $\psi^c_0$  component, so it is arbitrarily set to zero to be consistent with the prepared form of the initial conditions.

The boundary condition (172) generates an identical set of conditions for the Fourier components of  $\phi$  :

$$\begin{aligned}\phi_m^c(X_w) &= \frac{1}{2} \Delta W \left( \left[ \frac{\partial \phi_{|m-n|}^c}{\partial x} \right]_{X_w} + \left[ \frac{\partial \phi_{m+n}^c}{\partial x} \right]_{X_w} \right) \\ \phi_m^s(X_w) &= \frac{1}{2} \Delta W \left( \frac{m-n}{|m-n|} \left[ \frac{\partial \phi_{|m-n|}^s}{\partial x} \right]_{X_w} + \left[ \frac{\partial \phi_{m+n}^s}{\partial x} \right]_{X_w} \right)\end{aligned}\quad (181)$$

The condition (173) on the vorticity reduces to :

$$[\zeta]_{\text{wall}} = 0 \quad (182)$$

which, although quite different from the boundary conditions for  $\psi$  and  $\phi$ , also generates an identical set of mode conditions to them except for the zero order mode which does have a definite vanishing constraint imposed upon it as follows :

$$\begin{aligned}\zeta_0^c(X_w) &= 0 \\ \zeta_m^c(X_w) &= \frac{1}{2} \Delta W \left( \left[ \frac{\partial \zeta_{|m-n|}^c}{\partial x} \right]_{X_w} + \left[ \frac{\partial \zeta_{m+n}^c}{\partial x} \right]_{X_w} \right) \\ \zeta_m^s(X_w) &= \frac{1}{2} \Delta W \left( \frac{m-n}{|m-n|} \left[ \frac{\partial \zeta_{|m-n|}^s}{\partial x} \right]_{X_w} + \left[ \frac{\partial \zeta_{m+n}^s}{\partial x} \right]_{X_w} \right)\end{aligned}\quad (183)$$

The boundary conditions (180), (181) and (183) can be greatly simplified by noting that, close to the corrugated wall, the plasma will be dominated by the zero'th and the resonant or n'th Fourier modes. If we, therefore, neglect the contributions to all but these modes then the corrugation boundary conditions at  $x = \pm X_w$  reduce to :

$$\psi_m^c(X_w) = \begin{cases} \frac{1}{2} \Delta W \left[ \frac{\partial \psi_0^c}{\partial x} \right]_{X_w} & \text{when } m=n \\ 0 & \text{otherwise} \end{cases}$$

$$\psi_m^s(X_w) = 0 \quad \text{for all } m, \quad (184)$$

and similarly for  $\phi$  and  $\zeta$ . This is further justified because we are really only interested in what is going on well within the plasma, so that the purpose of the corrugation is just to create some sort of periodic external field perturbation which will interact with the plasma at the neutral line in a similar way to that produced by the limiter or iron core. It is therefore not important that the disturbance at the wall have a perfectly sinusoidal variation as long as the conditions are sufficiently well behaved not to produce any significant boundary layer effects. The corrugated boundary conditions were implemented in this simplified form and were found to be quite satisfactory for the purpose, with no significant velocity shear being produced at the boundary as was the case when only the magnetic field was perturbed. At  $t = 0$  we have :

$$\psi_0^c(x) = 2 \ln \left( \frac{\cosh(x)}{\cosh(X_w)} \right)$$

$$\phi_0^c(x) = 2 \times V_y$$

$$\zeta_0^c(x) = 0$$

so the boundary conditions should then take the form :

$$\psi_n^c(X_w, t=0) = -\Delta W \tanh(X_w)$$

$$\phi_n^c(X_w, t=0) = -\Delta W V_y$$

$$\zeta_n^c(X_w, t=0) = 0$$



However, so as to avoid generating any unwanted Alfvén waves the corrugation was turned on adiabatically, with the amplitude,  $\Delta W$ , increasing (half) sinusoidally from zero over a period of time (usually  $t = 3,000 \tau_A$ ) up to the desired value for the run.

In all the simulations made so far, only the  $n=1$  mode of corrugation with period equal to  $L_p$  has been used, although the conditions obviously do allow for studies requiring finer corrugations.

### II-3.2 Forced Reconnection in a Flowing Plasma

Before employing the corrugated boundary condition in a calculation involving tearing mode magnetic islands it is first worthwhile to investigate what its effect will be in a plasma without tearing modes. Fig.14 shows that conducting wall stabilization can be used to completely stabilize the tearing instability by having the wall separation less than the current channel width. In this section we make use of this fact to study forced reconnection in isolation by setting  $X_w = 1.0$  and begin by considering the effect of a corrugation with amplitude  $\Delta W = 0.02$  in an initially stationary plasma, i.e. with  $V_{y0} = 0$ .

As also demonstrated previously [55,56,78] the effect of such a perturbation is for it to interact resonantly with the plasma at the neutral line to produce a magnetic island considerably larger than the perturbation at the boundary, see fig.56, with the x-point of the island forming directly opposite the point of maximum inward amplitude of the corrugation.

The original current channel is maintained by a z-directed electric field and non-uniform resistivity in the same manner as for the tearing mode simulations of Part I, so that the plasma can reach a steady or saturated state. The time taken to reach this saturated state after introducing the boundary perturbation is, as with the tearing mode, governed by the reconnection rate, except of course, when the amplitude of the corrugation is increased more slowly than the reconnection process. This was found to be the case here with simulations done with  $S = 10^4$  taking much longer to reach saturation than when  $S = 10^3$ , consistent, perhaps, with the Sweet-Parker scaling. This aspect of forced reconnection has been thoroughly investigated by Biskamp [60] so will not be gone into any further here.

The general properties of the final saturated state are also similar to those of the tearing mode. The current distribution, see fig.56, has a peak at the o-point and a narrower peak at the x-point although both are much less prominent than for the tearing mode, see fig.8(b). The usual vortical flows associated with the continued reconnection

after saturation also form with the plasma incident at the x-point being accelerated along the current sheet towards the o-point.

The reconnection process produced by perturbing the boundary conditions has been studied analytically by Kulsrud and Hahm [55,56] and later by Hu [97]. In these a simple analytical island solution is derived in the limit of perfect conductivity for a plane slab configuration similar to that in fig.55 and the resistive evolution to this state is examined using various asymptotic techniques. The island width predicted by the analytical solution is much smaller than that determined here but this is presumably because they use a simpler initial equilibrium of the form  $\mathbf{B}_0 = x/a \hat{e}_y$  in which the magnetic field increases uniformly instead of rounding off to a limit as with the  $\mathbf{B}_0 = \tanh(x/a) \hat{e}_y$  equilibrium used here. The stronger field away from the neutral line in the former case creates a greater tension in the field lines which prevents the island from pushing out as far as in the latter case.

The formation of magnetic islands through forced reconnection induced by a resonant boundary perturbation is clearly not new and has even been demonstrated experimentally by inducing an island large enough to trigger a disruption of a tokamak plasma [81]. However the mechanism becomes more interesting when the plasma is given a uniform bulk flow in the y-direction (parallel to the neutral line) . Then the situation is not so trivial and should provide some insight into whether the influence of a boundary perturbation such as would be produced by the limiter is diminished at all by the rotation of the plasma.

In the simulations performed here an initially uniform zero order flow,  $V_{y0}$ , is driven by an electric field,  $E_x$  , in the form of an  $\mathbf{E} \times \mathbf{B}$  drift maintained by a potential difference between the walls as described in section I-2.2 and II-3.1.

The interesting aspect of this arrangement comes from the basic conflict that exists between the zero order flow and the static island produced by the corrugated boundary perturbation. To see this note that the magnetic island induced by the boundary

perturbation divides the plasma into two distinct topological regions of (1) inside and (2) outside the separatrix of the island. Because of the highly conducting nature of the plasma the magnetic field is coupled to the fluid through the so called 'flux freezing' condition. The Lundquist number, which is the ratio of the Alfvén to the resistive velocity, defines how fast the plasma may diffuse relative to the field lines due to the finite resistivity and so provides a measure of the strength of this fluid-field coupling. In many situations of interest the resistivity is so small that the resistive diffusion can be neglected, so that the approximation of  $S = \infty$  can be employed. In this case the fluid can be considered to be exactly coupled to the field so that no relative motion is possible, at least across the field lines.

The  $\mathbf{E} \times \mathbf{B}$  drift generated by the applied electric field forces the plasma to flow in the  $y$ -direction. This is all right for the plasma outside the separatrix where the topology of the field lines does not inhibit such a motion, but, because of the locally closed nature of the field lines within the island region, the flux freezing constraint prevents the plasma within the separatrix from doing the same. In fact, except for flows of the magnitude of the weak vortical flows associated with the continued reconnection after saturation, the zero order flow must be completely excluded from the island region.

The simulation also includes a finite scalar viscosity, which provides a coupling between adjacent fluid elements, tending to retard their relative motion. If the viscosity is weak then we could expect an island to form in which the zero order flow is totally excluded from the island region with a velocity gradient created just outside the separatrix depending on the size of the zero order flow,  $V_{y0}$ . However if the viscosity is large the drag force exerted by the fluid outside the separatrix on the fluid inside it will tend to transfer momentum to the plasma within the island so that it is also dragged downstream. But if  $S$  is very large then this penetration of the zero order flow would violate the flux freezing constraint. To avoid this the island must either be removed, or at least reduce in size to where the local value of  $S$  is small enough for the flow through the island to be consistent with the degree of decoupling allowed by the finite resistivity. This is possible

since the Lundquist number decreases towards the neutral line due to the decrease in magnitude of the magnetic field, which vanishes on the neutral line. The size of this decoupling region will decrease with increasing  $S$  and in the limit that  $S \rightarrow \infty$  the plasma has only two options: (1) to either form an island with the zero order flow totally excluded or (2) not form an island at all and allow the zero order flow to extend across the whole plasma.

For a finitely conducting plasma, what happens will depend basically on four parameters : (1) the amplitude of the boundary perturbation,  $\Delta W$ ; the size of the zero order flow,  $V_{y0}$ , produced by the applied electric field; and the two coupling constants,  $\nu$ , the viscosity and  $S$  the Lundquist number. Since it is reasonably clear that increasing  $\Delta W$  will tend to increase the size of the island, we will only consider, in this initial study, the dependence of the forced-reconnected magnetic island on  $V_{y0}$  in the range between 0 and  $V_A$  for several values of  $\nu$  and  $S$ . Note also that we will only ever consider one periodicity length with  $K_p = 0.35$ .

It was shown earlier that lower numbers of Fourier modes are needed in simulations with reasonably high viscosity so most of the simulations of forced reconnection were done with  $\nu = 0.01$  with fewer, but more expensive, simulations run with  $\nu = 0.0001$ .

In fig.56 are arranged a set of contour plots of  $\psi$ ,  $J_z$  and  $\phi$  for  $S = 10^4$ ,  $\nu = 0.01$ , which show the changes to the forced reconnected island that occur with increasing values of the zero order flow velocity. They are all referred to a plot of the corresponding saturated reconnected flux versus  $V_{y0}$  which provides a more quantitative measure of the changes occurring to the island. Note that with the normalizing factors used here  $V_{y0}$  is actually a dimensionless ratio of the flow velocity to the Alfvén velocity, as written explicitly on the plot, and hence really represents a magnetic Mach number. The plots show that, while  $V_{y0}$  is around the magnitude of the vortical reconnection flows (approx.  $5 \times 10^{-4}$ ), the zero order flow is mostly diverted around the island. But because of the relatively high viscosity it penetrates the island region when  $V_{y0}$  is not much higher than

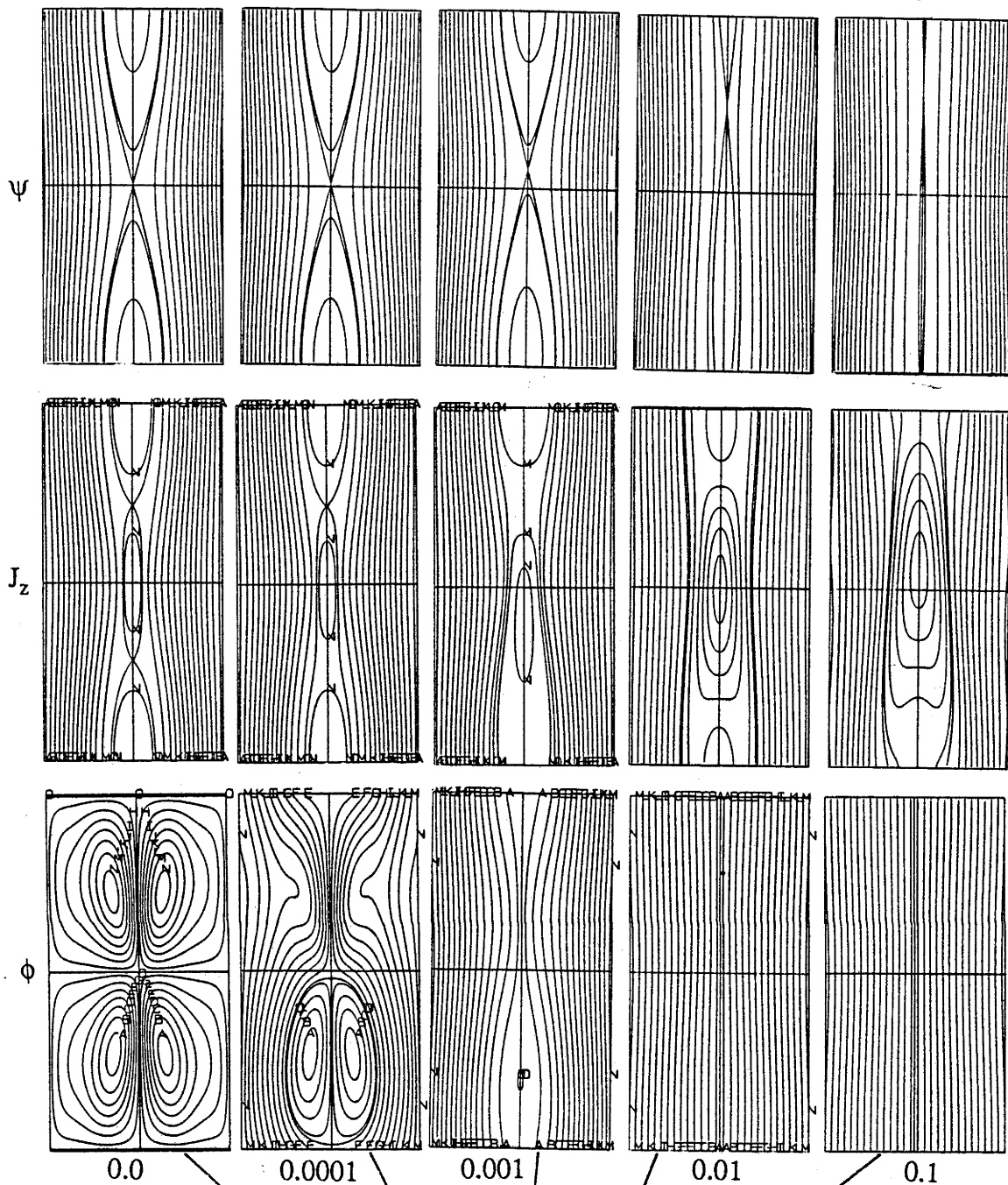
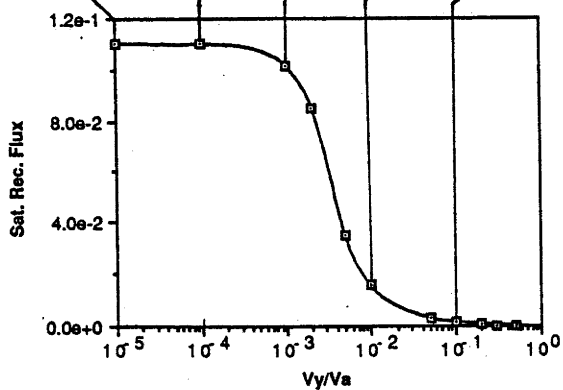


Fig.56



this. As  $V_{y0}$  is increased above the value at which the zero order flow just penetrates to the neutral line the magnetic island is shown to decrease rapidly in size, becoming a thin filament for cases when the flow is more uniformly spread across the plasma.

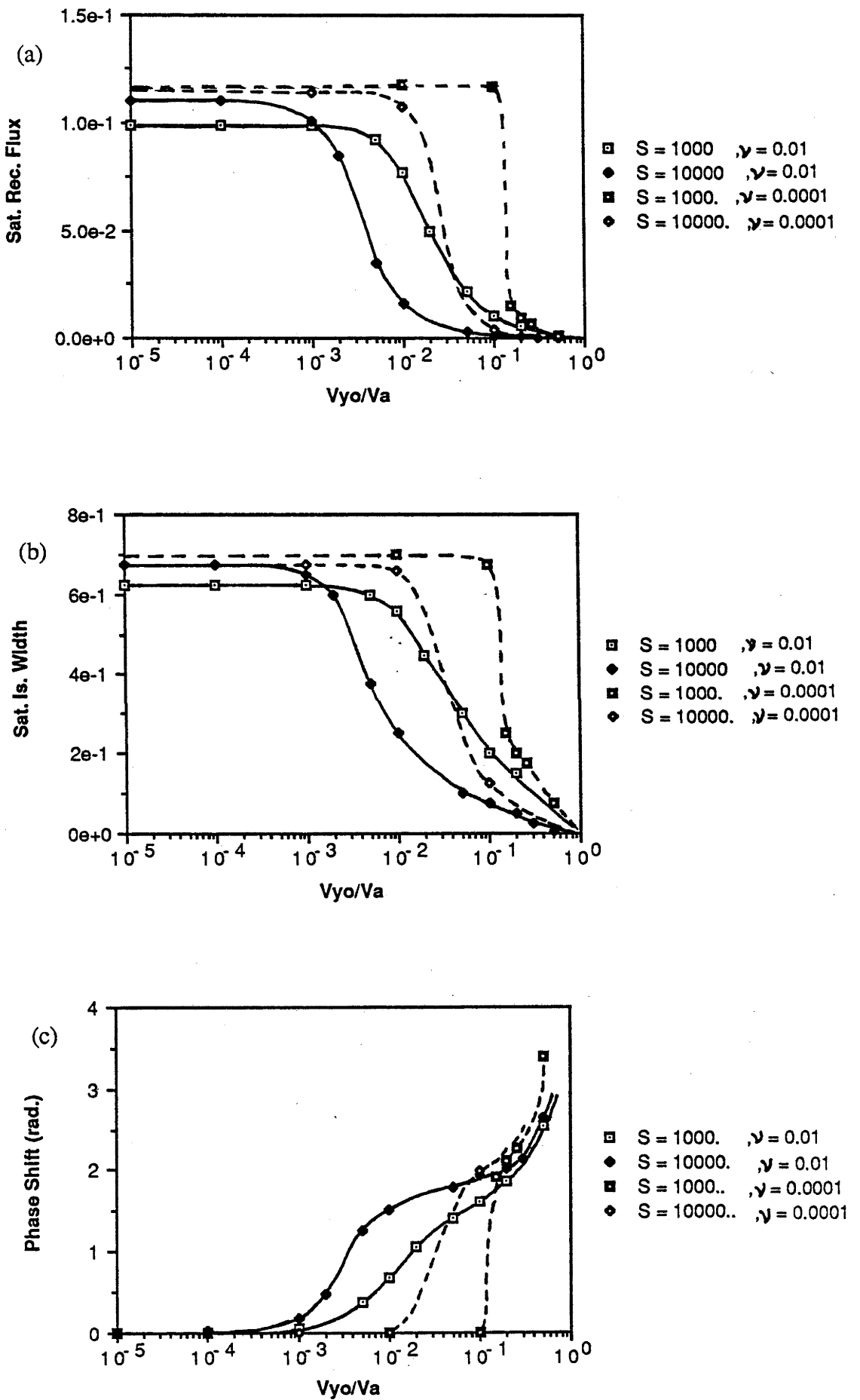
As well as decreasing in size the island forms further downstream, with the position of the x-point no longer opposite the maxima of the boundary perturbation. The variation of this phase shift with  $V_{y0}$  is shown in fig.57(c), to almost round off to a limiting value before increasing again as  $V_{y0}$  approaches  $V_A$ . It is possible that the mode may start rotating for  $V_{y0}$  close to  $V_A$  but this is not significant since then the island is negligibly small.

The effect of the flow on the current distribution is for the x-point current peak to merge with or, perhaps more accurately, be engulfed by the upstream o-point current peak so that eventually, as  $V_{y0}$  approaches  $V_A$ , there is only a single asymmetric current peak. Notice, however, that while the flux magnetic island becomes narrower with increasing zero order flow the current peak, or current island, becomes broader, covering a considerable fraction of the plasma width.

The same behaviour was exhibited by a set of runs made with  $S = 10^3$ ,  $\nu = 0.01$ , as also summarized in figs.57(a), (b) and (c), but with the penetration of the zero order flow into the island region and consequent fall in island size occurring at a higher value of  $V_{y0}$ . With  $S = 10^3$  the rate of reconnection is much higher than for  $S = 10^4$  so the fall off value of  $V_{y0}$  still corresponds to a value not much greater than the magnitude of the vortical reconnection flows (approx.  $0.002 V_A$ ). On this basis, and as long as the viscosity is high, we could expect the flow penetration and consequent fall in island size to occur at a lower value of  $V_{y0}$  the lower is the value of  $S$ .

On the other hand, with the viscosity reduced to the much smaller value of  $\nu = 0.0001$ , the viscous coupling between the plasma inside the island with that outside is greatly reduced so that, as shown in fig.57 for  $S = 10^3$  and  $10^4$ , the magnetic island is able to be maintained at its full width with the zero order flow excluded from inside the

Fig.57





separatrix for much higher values of  $V_{y0}$ . This is shown specifically for the case with  $S = 10^4$ ,  $\nu = 0.0001$ ,  $V_{y0} = 0.01$  in fig.58. Note that since the linear momentum is conserved,  $V_{y0}$  becomes equivalent to the average flow velocity in the y-direction after the plasma is perturbed. The fact that the flow does not quite vanish inside the separatrix is due to the vortical reconnection flows which, for this case, are much smaller than  $V_{y0}$ . By excluding the flow in this way the magnetic island retains many properties of the case where there was no zero order flow. For instance, the x and o point current peaks are still preserved, although a little distorted, and the phase shift is much smaller than for the higher viscosity case in which the zero order flow has completely penetrated.

As noted earlier, whether the island is large or small, the effect of flow on the current distribution is quite dramatic and the 3-D perspective plots and contour plots of  $J_z$  in fig.59 show the various forms it takes for different values of  $V_{y0}$ ,  $\nu$  and  $S$ . From them it can be seen that reducing the viscosity tends to sharpen the features of the current distribution, which at high  $V_{y0}$ , when the flow has penetrated, tend to form a line of V-shaped peaks with the arms of one rapped around the next in the line.

Fig.57 shows that as well as delaying the flow penetration and drop in island size to a higher  $V_{y0}$ , the weaker viscosity also decreases the size of the transition range. For example with  $S = 10^3$ ,  $\nu = 0.0001$  the island can be decreased from full size to a narrow filament just by doubling the zero order flow velocity, whereas for  $S = 10^3$ ,  $\nu = 0.01$  the flow velocity had to be increased by a factor of 10 or so to achieve the same end.

It has been shown that the velocity of the zero order flow at which the fall off occurs clearly depends on the viscosity and the conductivity of the plasma, decreasing with increasing  $\nu$  and  $S$ . The reason for the dependence on  $\nu$  is reasonably obvious. The dependence on  $S$  is made clearer by noting that relative motion of the plasma past the field is allowed if it is less than the resistive diffusion velocity, so the critical value of  $V_{y0}$  must at least be greater than  $S^{-1}$ , even with high viscosity. When the viscosity is weak the dependence of the fall off velocity on  $S$  and  $\nu$  is more subtle. However the determination

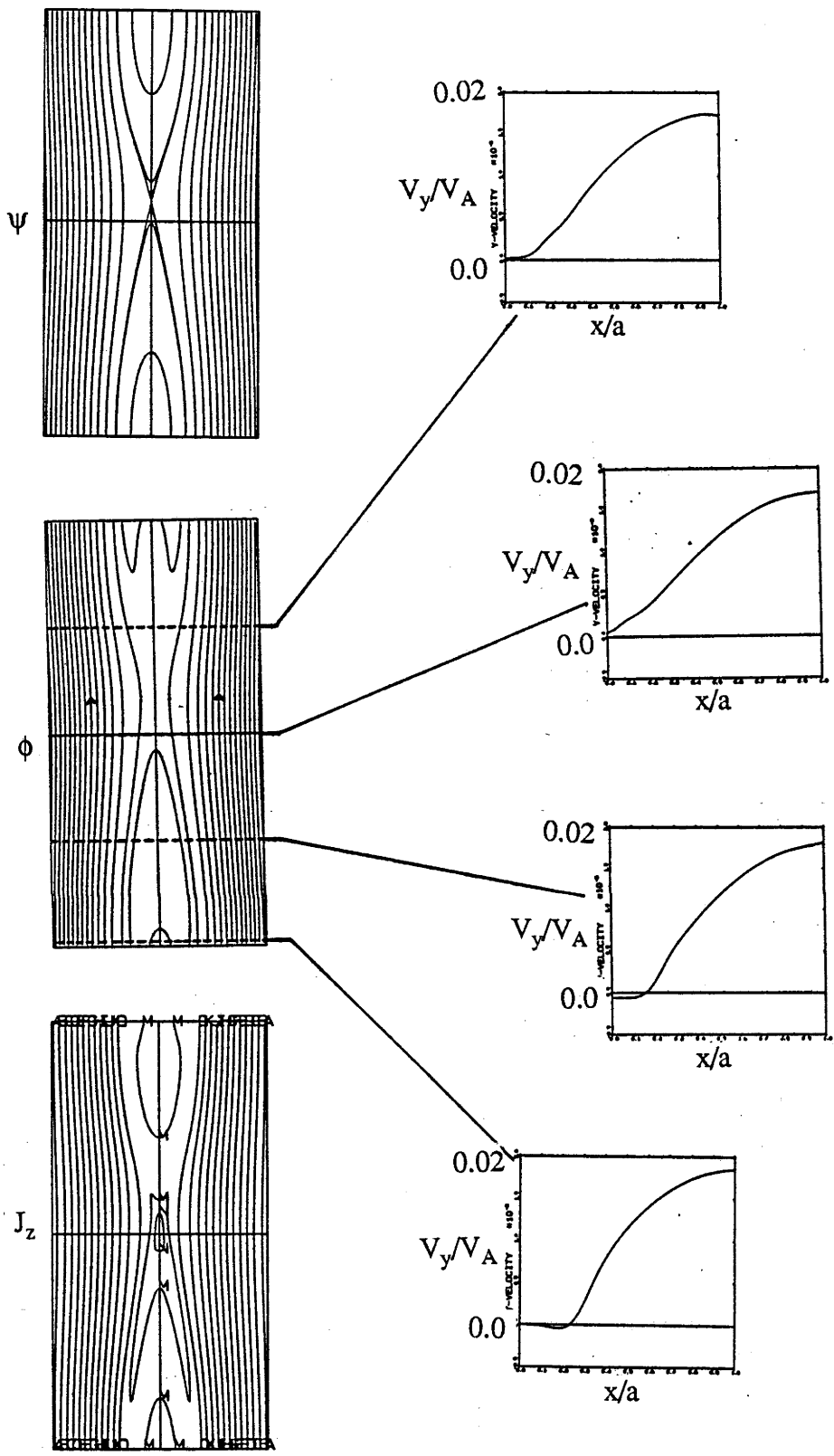


Fig.58

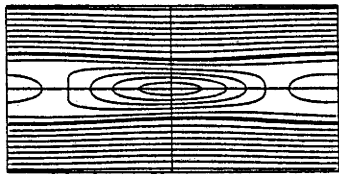
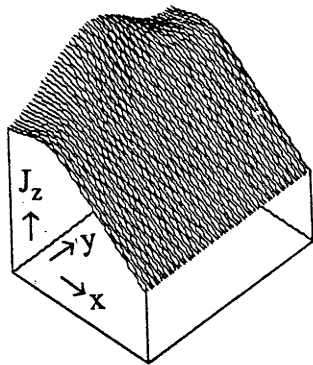
$S = 10^4$   
 $\nu = 10^{-4}$   
 $\Delta W = 0.02$   
 $V_{y0} = 0.01$

of the actual dependence will be left for a future investigation except to point out that the critical velocity appears to approach  $V_A$  in the limit that  $v \rightarrow 0$  and/or  $S \rightarrow 0$ .

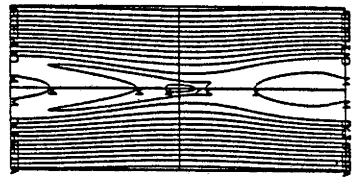
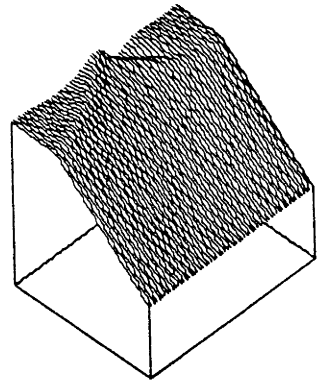
The high velocity shear that would exist just outside the separatrix in such circumstances might be expected to become unstable to the Kelvin Helmholtz instability <sup>[98,99,100,101]</sup> resulting in the onset of turbulence. This can occur in unmagnetized fluids with high Reynolds numbers <sup>[102]</sup> and in inviscid fluids when the Mach number exceeds  $2^{1/2}$  <sup>[99]</sup>. However, in a plasma with a magnetic field parallel to the flow, Sen <sup>[99]</sup> has shown that even if the plasma is completely inviscid a velocity discontinuity in excess of twice the Alfvén velocity is needed for the instability to occur. The improved stability in the presence of a magnetic field is simply derived from the increased tension of the fluid along the magnetic field lines of force due to the 'flux freezing' condition. This is not the case if the flow is transverse to the field and it was shown <sup>[99]</sup> in such cases that the magnetic field has no effect on the instability.

Given the relatively weak flows in tokamak plasmas the likelihood of a transition to turbulence via the Kelvin Helmholtz instability seems remote ; except perhaps near rational surfaces where a component of the magnetic field parallel to the flow may have a null. In the slab case discussed here this is equivalent to the neutral line where the  $B_y$  field drops to zero. We consider only flows which are sub-Alfvénic away from the neutral line and since the velocity shear occurs outside the separatrix it is unlikely that the K-H instability will occur in these simulations. It is conceivable, however, that the part of the separatrix near the x-point on the neutral line may have super-Alfvénic flows but this is where the velocity shear is weakest, see fig.58, and the instability is also stabilized by the finite viscosity. In any case for the parameter values tested,  $S = 10^3, 10^4$ ,  $v = 0.01, 0.0001$  and  $0 \leq V_{y0} < V_A$ , no turbulent activity was evident, although when the boundary corrugation was turned on suddenly an initial violent oscillation in the reconnected flux occurred when  $V_{y0}$  was close to  $V_A$ . This, however, always decayed away and is most likely just the relaxation response to the sudden change in field at the boundary.

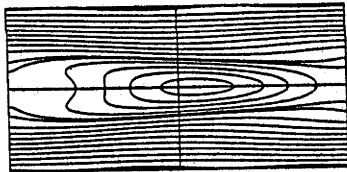
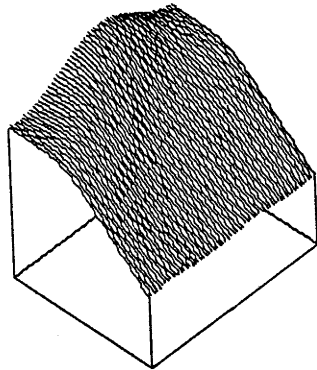
$S = 10^4$   
 $\nu = 0.01$   
 $\Delta W = 0.02$   
 $V_{y0} = 0.01$



$S = 10^4$   
 $\nu = 10^{-4}$   
 $\Delta W = 0.02$   
 $V_{y0} = 0.01$



$S = 10^4$   
 $\nu = 0.01$   
 $\Delta W = 0.02$   
 $V_{y0} = 0.1$



$S = 10^4$   
 $\nu = 10^{-4}$   
 $\Delta W = 0.02$   
 $V_{y0} = 0.1$

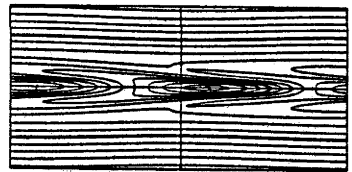
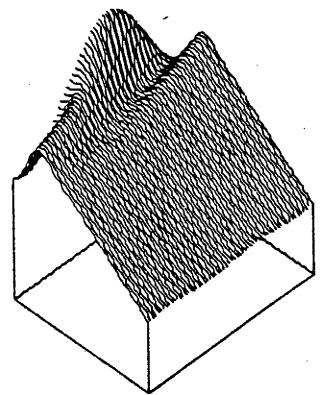
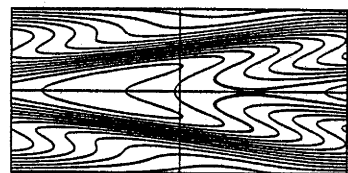
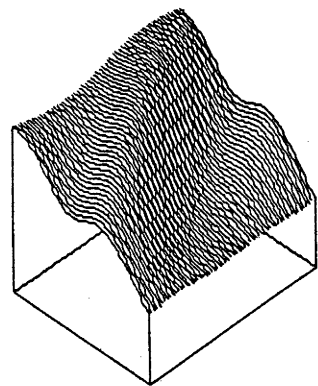


Fig.59

$S = 10^3$   
 $\nu = 10^{-4}$   
 $\Delta W = 0.02$   
 $V_{y0} = 0.5$



In summary it has been shown that a resonant boundary perturbation will still produce a magnetic island in a flowing plasma by diverting the bulk flow around the island region. This can occur as long as the flow velocity is below a critical value dependent on the viscosity and the conductivity of the plasma. Otherwise the flow will spread across the whole of the plasma with just a thin filament of an island forming.

The apparent reduced interaction of the boundary perturbation with the neutral line at high flow velocities, as signified by the reduced island width, could be interpreted as being related to the situation of reduced penetration of magnetic flux into a resistive wall when the adjacent plasma has a sufficiently high rotation frequency. The problem with this idea, however, is that even though the island may be negligibly small, fig.59 clearly shows that the effect on the current remains significant. This is especially evident for the case with  $S = 10^3$ ,  $\nu = 0.0001$  and  $V_{y0} = 0.5$ .

The conditions in a highly conducting tokamak plasma like LT-4 where  $S \sim 10^6$  are probably still such that an island would form unimpeded by the plasma rotation because of the very weak viscosity and low rotation frequency.

The dependence of the flow velocity, at which the island is suppressed, on the size of the boundary perturbation,  $\Delta W$ , will be left for a later investigation.

### II-3.3 Mode Locking : Preliminary Simulations

We now consider the effect of the boundary corrugation in a tearing unstable plasma by increasing the wall separation to  $X_w = 2.5$ . This creates an added conflict because now a tearing mode magnetic island will spontaneously form in addition to the forced-reconnected one. The difference, however, is that while the forced reconnected island is fixed in the frame of the stationary boundary corrugation, the tearing mode island is free to convect along in the frame of the plasma which, in this case, moves relative to the wall. Obviously a moving and a stationary island cannot co-exist on the same rational surface so it is expected that a competition will develop between the tendency for the island that forms to either convect along with the plasma or become mode locked onto the stationary boundary perturbation.

Such a situation is qualitatively similar to that which may occur in the LT-4 tokamak because of the asymmetric perturbing effect of the limiter and/or the single armed iron core and is, therefore, considered to be a possible mechanism for explaining the stop-start nature of the MHD activity observed, see figs.47 and 48.

The aim here is to study the basic dynamical mechanism of mode locking and for this purpose the plane slab configuration is adequate since it is far simpler than the actual tokamak geometry but still retains the essential elements of the process.

Whether mode locking occurs will depend on  $S$ ,  $v$ ,  $V_{y0}$ ,  $\Delta W$  and  $X_w$  etc.. Ideally it would be desirable to perform a systematic parameter study of the dependence of mode locking on these parameters in a similar fashion to that done in the forced reconnection study of the previous section. Unfortunately my grant for using the Cyber 205 super-computer ran out before this could be achieved and so only a handful of exploratory runs was possible. These, however, were sufficient to at least demonstrate the basic phenomenon, with results that correspond well with experimental observations.

The initial strategy was simply to test for mode locking of an already saturated tearing mode in a flowing plasma by first doing a run with unperturbed walls and then

using the resultant saturated island state as an initial equilibrium in several runs made with different corrugation amplitudes to determine the critical value.

This was based on the assumption that mode locking must occur if given a large enough boundary perturbation, which is shown to be the case in a run described in fig.60 for the case with  $\Delta W = 0.05$  and  $S = 1000.$ ,  $\nu = 0.01$ ,  $V_{y0} = 0.01$  and  $K_p = 0.35$ . The evolutions of the x and o point positions clearly show the locking of the island, while the variation in  $\psi(x=0,y=0)$  shows the corresponding disappearance in the magnetic field fluctuation. The third plot shows the additional reconnected flux produced on top of that generated by the tearing instability after the mode locking occurs. The amplitude of the perturbation was increased smoothly from  $\Delta W = 0.$  to  $\Delta W = 0.05$  over a period of  $3,000 \tau_A$  and shows mode locking occurring well before reaching full amplitude. What is more, the transition is shown to occur within one cycle, similarly to that observed experimentally, although it is possible that this may not be so for other values of  $S$ ,  $\nu$ , and  $V_{y0}$ .

Runs made with smaller corrugation amplitudes show that mode locking still occurs in the same manner with amplitudes as low as  $\Delta W = 0.012$ , but when  $\Delta W = 0.01$  the corrugation was found to be insufficient to fully lock the mode. Instead, as shown in fig.61, the island is temporarily delayed for a few cycles while it slowly squeezes past the point of maximum inward amplitude of the corrugation and then finally surges free to convect along with the rest of the plasma, only to get stuck again at the next peak in the corrugation. The process is repeated *ad infinitum*, producing a longer-cycle distorted magnetic field response similar to that recorded on LT-4 during the stage of the discharge preceding a major disruption, see fig.47. The implication of this being that the apparently isolated bursts of growth and decay often referred to as minor disruptions in LT-4<sup>[17]</sup> may actually be instances of partial mode locking of the magnetic islands. If this is so then the fact that they precede a major disruption indicates that the major disruption may also be a consequence of the same processes that induce mode locking. Each minor disruption is

MODE-LOCKED

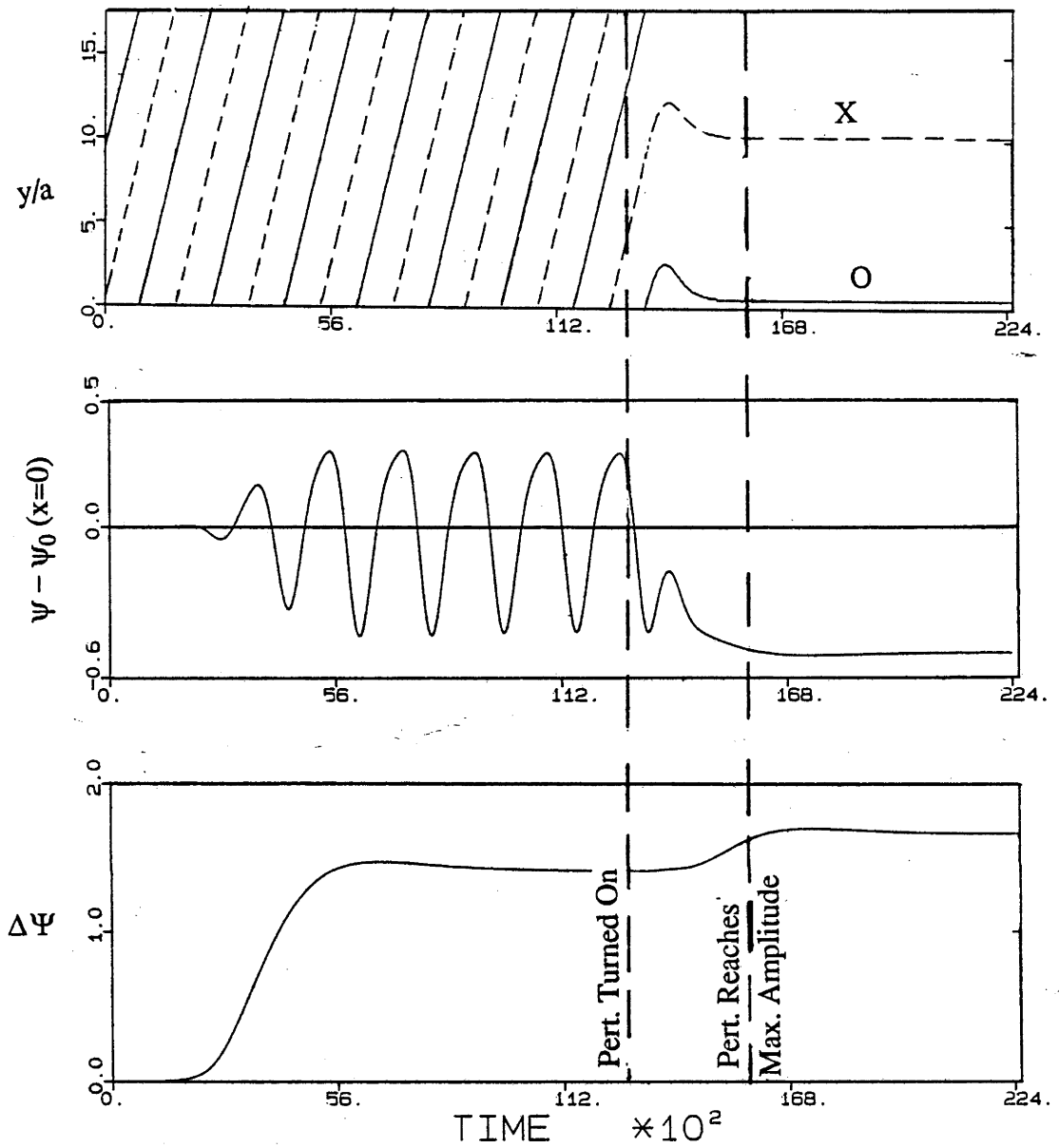


Fig.60

$S = 10^3$   
 $\nu = 0.01$   
 $\Delta W = 0.05$   
 $V_{y0} = 0.01$   
 $k_p = 0.35$   
 $X_w = 2.5$



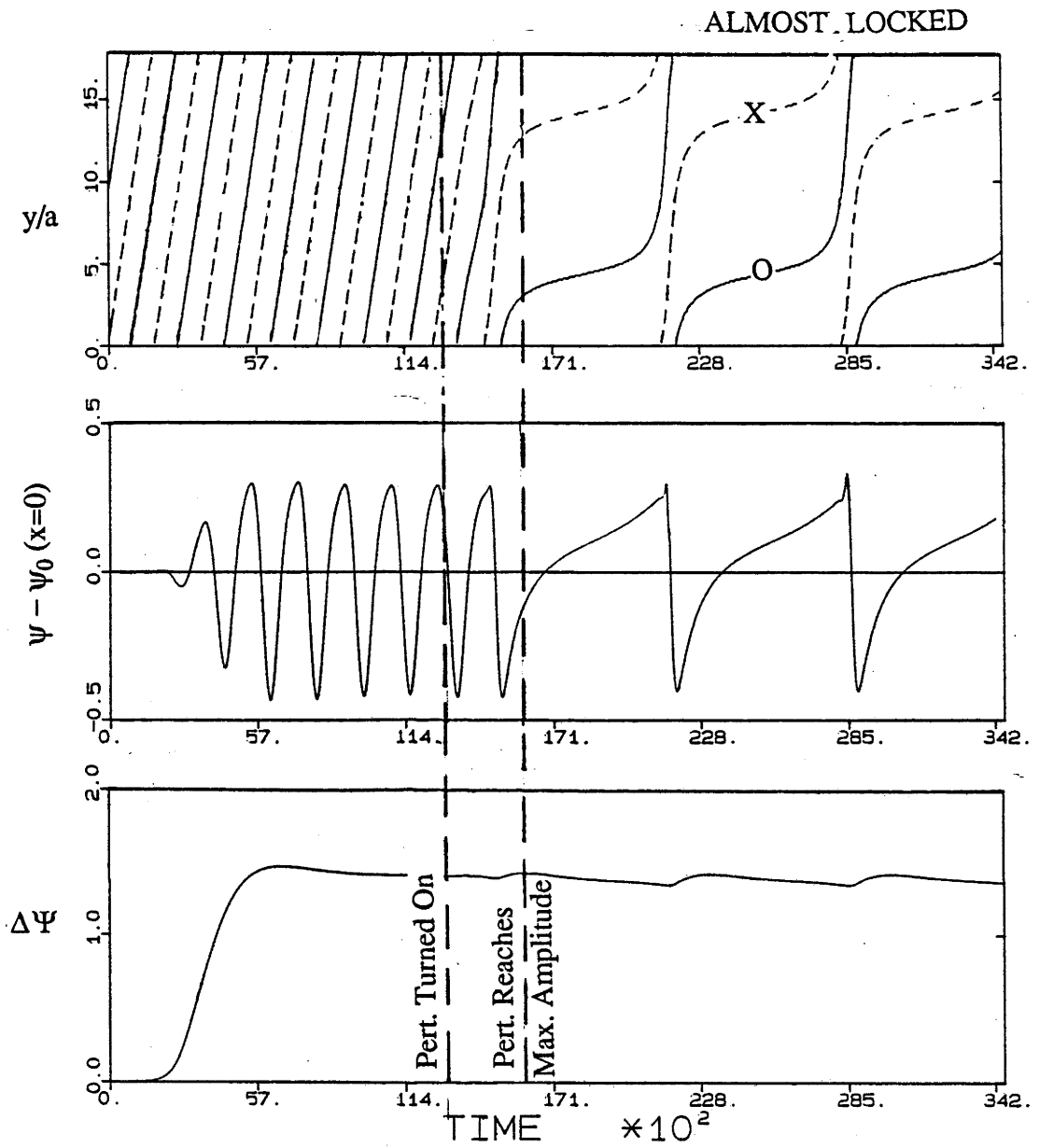


Fig.61

$$\begin{aligned}
 S &= 10^3 \\
 \nu &= 0.01 \\
 \Delta W &= 0.01 \\
 V_{y0} &= 0.01 \\
 k_p &= 0.35 \\
 X_w &= 2.5
 \end{aligned}$$

accompanied by a negative voltage spike, a burst of hard X-rays and a dip in both soft X-ray and electron cyclotron harmonic emissions, although the plasma current remains unaffected, so for this partial mode locking scenario to be valid it must be able to explain the occurrence of such phenomena.

Fig.62 shows contour plots of  $J_z$ ,  $\psi$ ,  $\phi$  and cross-section plots of  $V_y$  at two times during the process corresponding to: (a) when the island is temporarily mode locked, and (b) just after it has squeezed past a corrugation. The current and magnetic flux function contours show the magnetic field to be relatively unchanged throughout the process and generally look the same as for a tearing mode island in the absence of flow or a boundary corrugation. The plasma motion, in contrast, is dramatically altered during each cycle. When the island is locked the flow is mostly diverted around the island similar to that for the forced reconnection case of the previous section, but, because the island surges free with a velocity initially much higher than the averaged flow velocity, (which is maintained by momentum conservation) the pattern is reversed with an almost complete transfer of momentum into the island from the surrounding plasma. Although this appears quite violent, the plane slab configuration only represents the local region around a single rational surface of a toroidal plasma so such a transfer of momentum would probably not be quite such a global process in practice.

Keeping  $\Delta W = 0.012$ , several runs were made with higher flow velocities. With  $V_{y0} = 0.03$  the island remained unlocked while for  $V_{y0} = 0.015$  the island became partially locked in the same manner as when  $\Delta W = 0.01$ ,  $V_{y0} = 0.01$ . Since the island was fully locked with  $V_{y0} = 0.01$ ,  $\Delta W = 0.012$  this shows that larger amplitude corrugations are needed to lock the mode when the flow velocity is increased. This is, perhaps, not unexpected since the larger the flow velocity the greater is the momentum that has to be diverted around the island by the influence of the corrugation.

Further runs will be done later to determine the effect of  $v$  and  $S$ , although judging from the response with purely forced-reconnected islands, described in the previous

MODE-LOCKED (ALMOST)

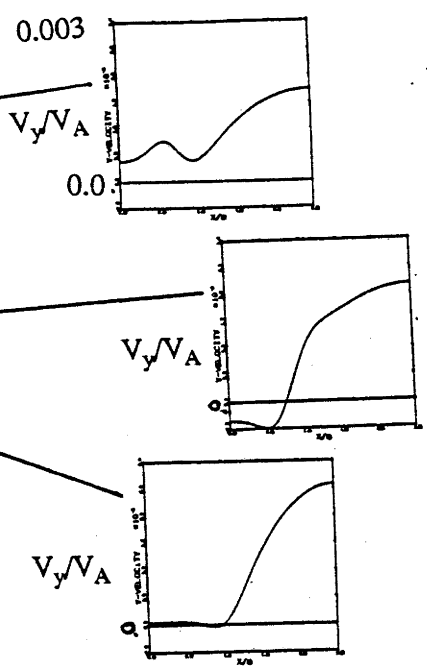
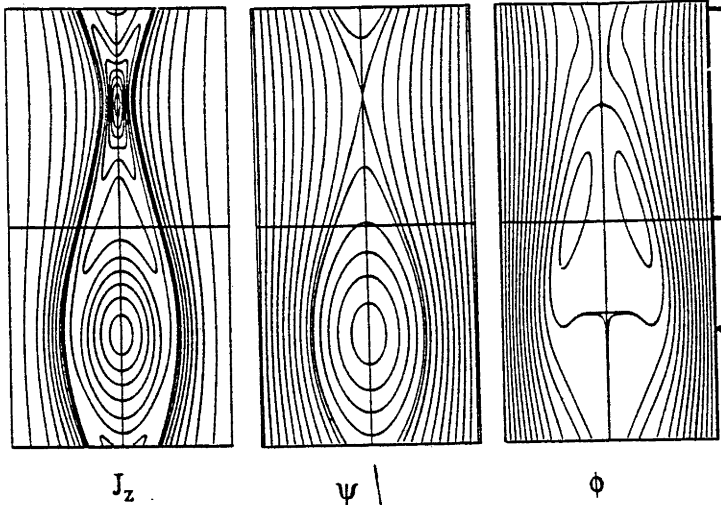
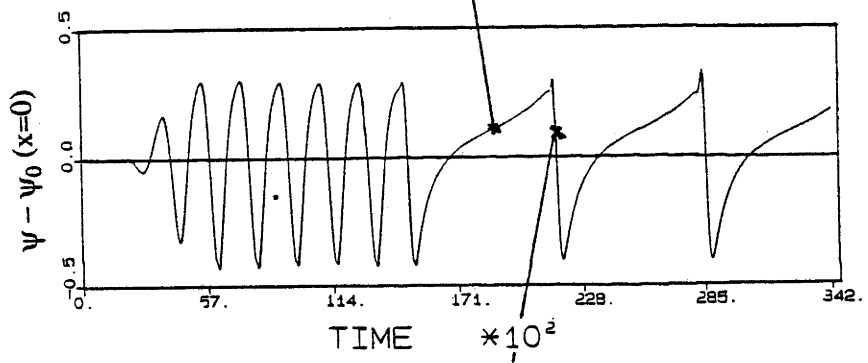
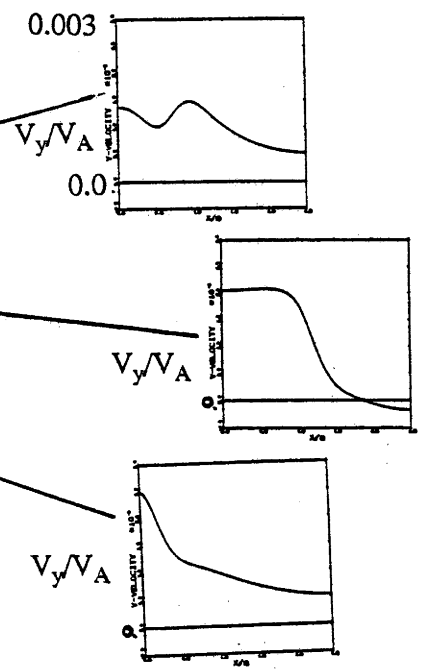
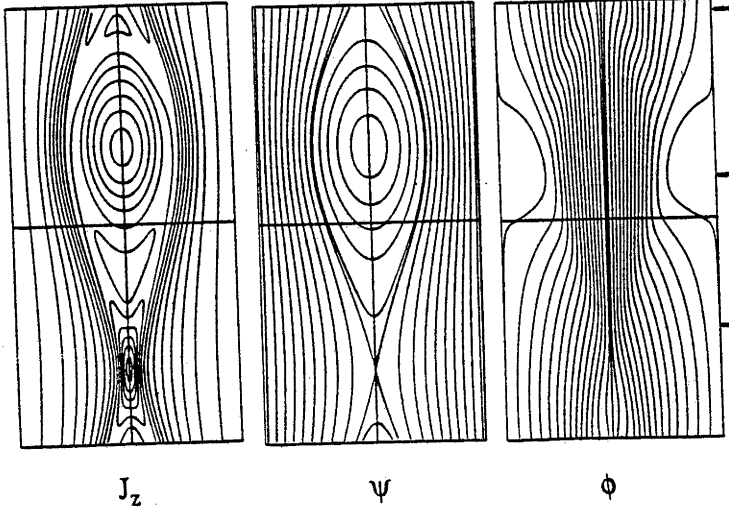


Fig.62



UNLOCKED



section, decreasing the viscosity should make it easier to lock the mode by decreasing the drag on the plasma within the island.

Although the procedure of turning on the wall perturbation after the tearing mode magnetic island has saturated is the least complicated way of examining mode locking it is not the most realistic since the effect of the limiter and/or the iron core would exist right from the beginning of the discharge, before the relevant tearing modes emerge. It would probably therefore be more realistic to reverse the procedure and test for the transition from the static forced reconnected magnetic island state to the unlocked island state as the tearing mode evolves. This could be done by introducing the full boundary perturbation right at the beginning of the run, or at least increasing the corrugation amplitude to its maximum in a time short compared to the linear growth time of the tearing mode. Such simulations could then be used to confirm whether there is a threshold island size for unlocking the mode, as suggested in the mode locking scenario described in section II-2.2, or whether mode locking is determined more by the linear phase of the tearing mode through the interaction of the linear eigenfunction with the wall corrugation.

As a matter of interest, an example of a similar type of mode locking can occur in the fluid dynamical system of the earth's atmosphere as a result of geographical effects. An example of this can be seen in the weather maps in fig.63 which show a high pressure vortex (or anti-cyclone) getting temporarily locked in the Great Australian Bight for almost a week before squeezing past the south eastern tip of the mainland to continue its journey eastwards. Note from the plot of the evolution of the centre of the High how it accelerates away from the Bight faster than it approaches it.

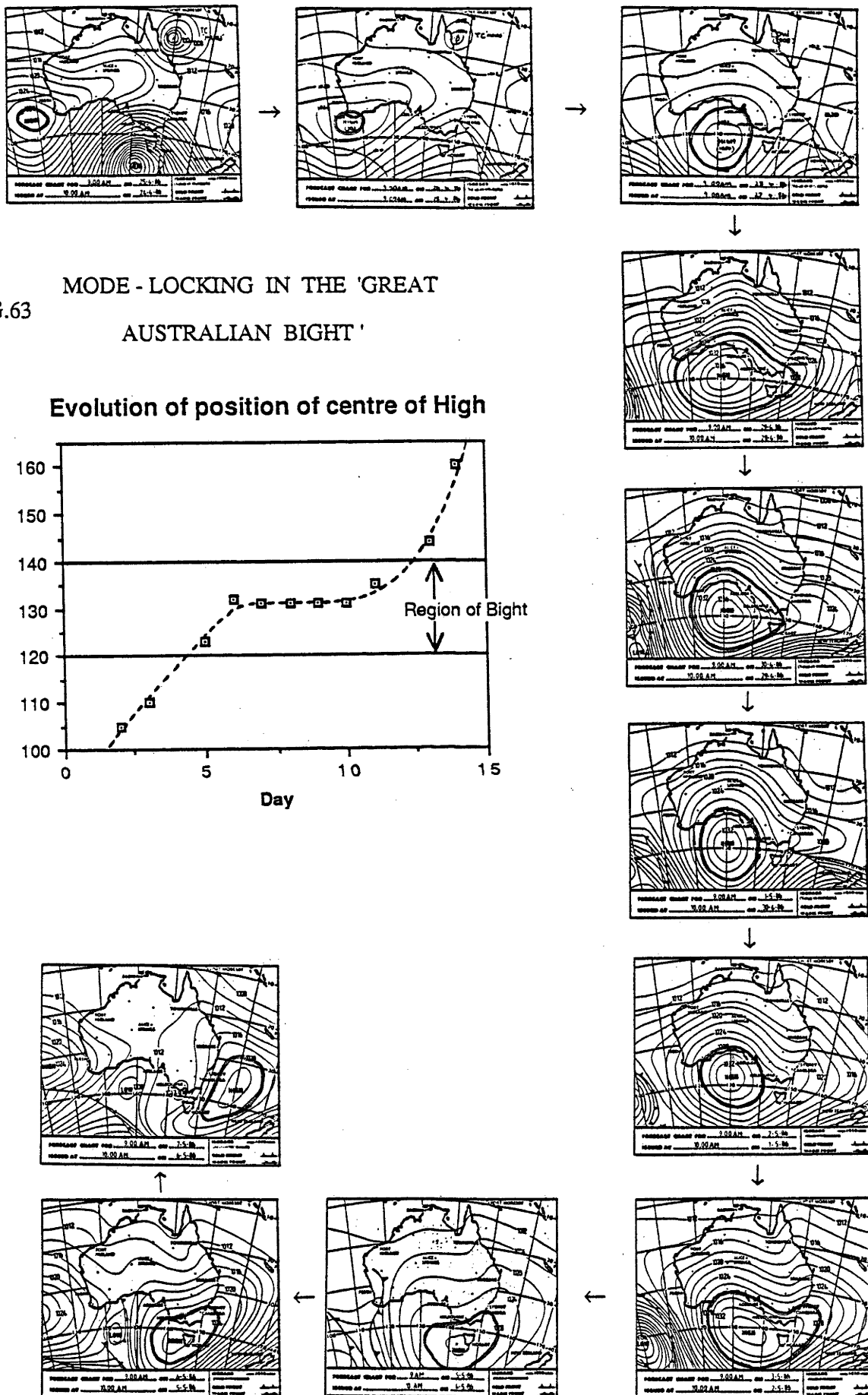


FIG.63 MODE - LOCKING IN THE 'GREAT AUSTRALIAN BIGHT'

section, decreasing the viscosity should make it easier to lock the mode by decreasing the drag on the plasma within the island.

Although the procedure of turning on the wall perturbation after the tearing mode magnetic island has saturated is the least complicated way of examining mode locking it is not the most realistic since the effect of the limiter and/or the iron core would exist right from the beginning of the discharge, before the relevant tearing modes emerge. It would probably therefore be more realistic to reverse the procedure and test for the transition from the static forced reconnected magnetic island state to the unlocked island state as the tearing mode evolves. This could be done by introducing the full boundary perturbation right at the beginning of the run, or at least increasing the corrugation amplitude to its maximum in a time short compared to the linear growth time of the tearing mode. Such simulations could then be used to confirm whether there is a threshold island size for unlocking the mode, as suggested in the mode locking scenario described in section II-2.2, or whether mode locking is determined more by the linear phase of the tearing mode through the interaction of the linear eigenfunction with the wall corrugation.

As a matter of interest, an example of a similar type of mode locking can occur in the fluid dynamical system of the earth's atmosphere as a result of geographical effects. An example of this can be seen in the weather maps in fig.63 which show a high pressure vortex (or anti-cyclone) getting temporarily locked in the Great Australian Bight for almost a week before squeezing past the south eastern tip of the mainland to continue its journey eastwards. Note from the plot of the evolution of the centre of the High how it accelerates away from the Bight faster than it approaches it.

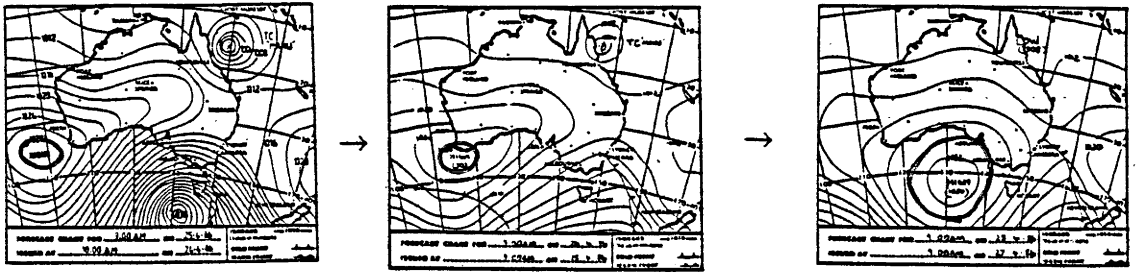
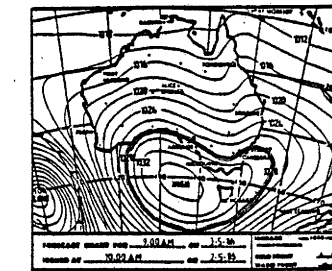
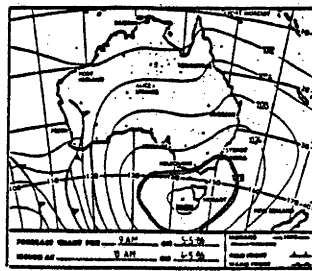
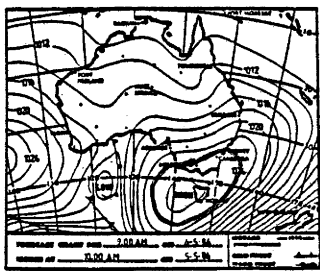
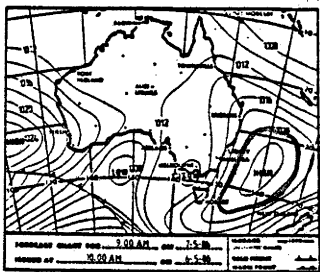
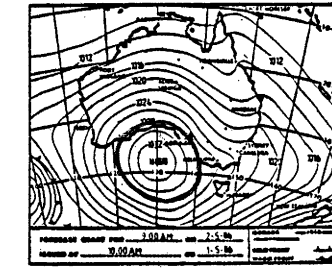
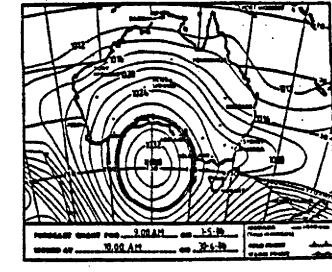
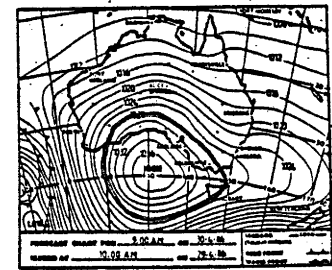
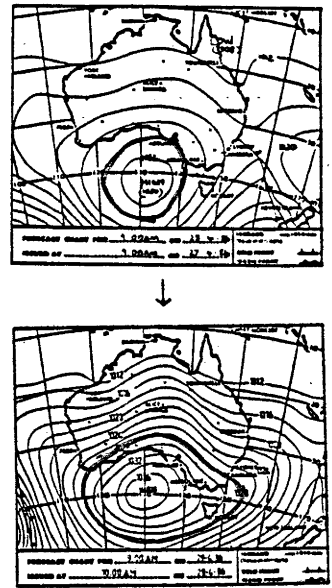
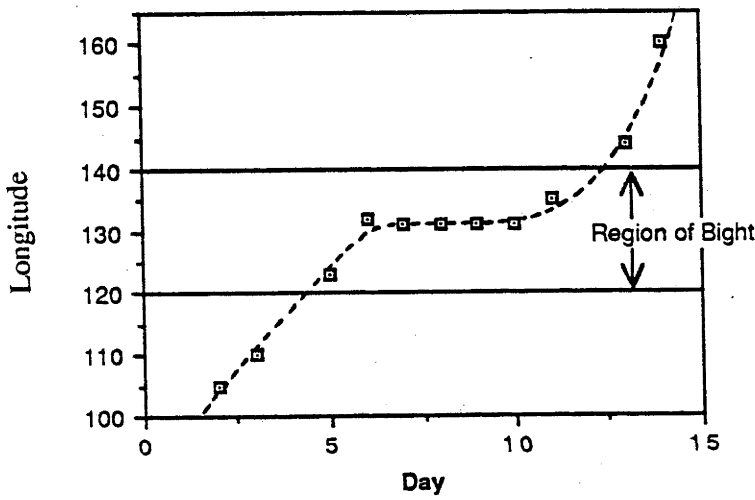


FIG.63  
MODE - LOCKING IN THE 'GREAT AUSTRALIAN BIGHT'

Evolution of position of centre of High



## II-3.4 Final Remarks

Much of the research presented in this thesis is part of an on-going study of the reconnection processes in plasmas. It is an area which has proven to be a rich source of interesting physical phenomena, and it is with anticipation that I look forward to tackling the many questions that have arisen from my work so far.



## References

- [1] J.A. Shercliff, 'A Textbook of Magnetohydrodynamics', Pergamon Press, Oxford, (1965).
- [2] J.P. Freidberg, Rev. Mod. Phys., 54, 801, (1982)
- [3] J.P. Goedbloed, 'Lecture Notes on Ideal Magnetohydrodynamics', (Fom-Instituut voor Plasafysica, Nieuwegein, Netherlands), Rijnhuizen Report 83-145, (1983), (Corrected version of notes of March 1979).
- [4] G. Bateman, 'MHD Instabilities', (MIT Press, Cambridge, Massachusetts), (1978).
- [5] H.P. Furth, J. Killeen and M.N. Rosenbluth, Phys. Fluids, 6, 459, (1963).
- [6] R.B. White, PPPL - 1655, May (1980) or Rev. Mod. Phys., 58,183,(1986).
- [7] R.B. Paris, 'Lectures on Resistive Instabilities in MHD', EUR-CEA-FC-1130, delivered at workshop on 'Hydrodynamique des Atmospheres Stellaires' at the Observatoire de Paris, Meudon, France: 18 Aug - 12 Sept 1980, (1982)
- [8] R.S. Steinolfson and G. Van Hoven, Phys. Fluids, 26, 117, (1983).
- [9] P.H. Rutherford, Phys. Fluids, 16, 1903, (1973).
- [10] R.B. White, D.A. Monticello, M.N. Rosenbluth and B.V. Waddell, Phys. Fluids, 20, 800, (1977).
- [11] B. Carreras, B.V. Waddell and H.R. Hicks, Nucl. Fusion, 19, 1423, (1979)
- [12] D.A. Monticello and R.B. White, Phys. Fluids, 23, 366, (1980)
- [13] J.M. Finn, Nucl. Fusion, 15, 845, (1975).
- [14] A.D. Cheetham, S.M. Hamberger, J.A. How, H. Kuwahara, A.H. Morton, L.E. Sharp, and C.F. Vance, Tenth International Conference on Plasma Physics and Controlled Nuclear Fusion Research, London (1984), IAEA - CN - 44 / A - V - 5, pp. 337, vol. 1.
- [15] J.M. Finn, Phys. Fluids, 20, 1749, (1977).

- [16] B.V. Waddell, B. Carreras, H.R. Hicks and J.A. Holmes, *Phys. Fluids*, 22, 896, (1979).
- [17] A.D. Cheetham, S.M. Hamberger, H. Kuwahara, A.H. Morton and D. Vender, *Nucl. Fusion*, 27, 843, (1987).
- [18] A.D. Cheetham, S.M. Hamberger, J.A. How, H. Kuwahara, A.H. Morton and L.E. Sharp, *Aust. J. Phys.*, 39, 35, (1986).
- [19] A.H. Morton, K.G. Srinivasacharya, *Nucl. Fusion*, 18, 1417, (1978).
- [20] D.B. Albert, A.H. Morton, *Nuclear Fusion*, 17, 863, (1977).
- [21] H.P. Furth, P.H. Rutherford and H. Selberg, *Phys. Fluids*, 16, 1054, (1973).
- [22] J.M. Finn and P.K. Kaw, *Phys. Fluids*, 20, 72, (1977).
- [23] P.L. Pritchett and C.C. Wu, *Phys. Fluids*, 22, 2140, (1979).
- [24] D. Biskamp and H. Welter, *Phys. Rev. Lett.*, 44, 1069, (1980).
- [25] A. Bondeson, *Phys. Fluids*, 26, 1275, (1983).
- [26] A. Bhattacharjee, F. Brunel and T. Tajima, *Phys. Fluids*, 26, 3332, (1983).
- [27] V.M. Fadeev, I.F. Kvartskhava and N.N. Komarov, *Nucl. Fusion*, 5, 202, (1965)
- [28] T. Hayashi, *J. Phys. Soc. Jpn.*, 50, 3124, (1981).
- [29] R.S. Steinolfson and G. Van Hoven, *Phys. Fluids*, 27, 1207, (1984).
- [30] D. Biskamp, *Phys. Lett.*, 87A, 357, (1982).
- [31] W.H. Matthaeus, S.L. Lamkin, *Phys. Fluids*, 28, 303, (1985).
- [32] W.H. Matthaeus, S.L. Lamkin, *Phys. Fluids*, 29, 2513, (1986).
- [33] H. Kuwahara, A.D. Cheetham and A.H. Morton, *Nucl. Fusion*, 26, 1092, (1986).
- [34] D.S. Harned and W Kerner, *Nucl. Sci. and Eng.*, 92, 119, (1986).
- [35] P.A. Sweet, *Nuovo Cimento, Suppl.* 8, Ser.X, 188, (1958).
- [36] E.N. Parker, *Astrophys. J., Suppl.* 77, 8, (1963).

- [37] H.E. Petschek, in AAS/NASA Symposium on the Physics of Solar Flares, edited by W.N. Hess (NASA, Washington, DC, 1964), p.425.
- [38] G. Van Hoven and M.A. Cross, Phys. Rev., A7, 1347, (1973).
- [39] R.G. Kleva, J.F. Drake and A. Bondeson, Phys. Fluids, 28, 2478, (1985).
- [40] B.V. Waddell, M.N. Rosenbluth, D.A. Monticello and R.B. White, Nucl. Fusion, 16, 528, (1976).
- [41] W. Park, D.A. Monticello and R.B. White, Phys. Fluids, 27, 137, (1984).
- [42] H.R. Hicks, B. Carreras, J.A. Holmes, D.K. Lee, and B.V. Waddell, J. Comp. Phys., 44, 46, (1981).
- [43] J.D. Callen, B.V. Waddell, B. Carreras, M. Azumi, P.J. Catto, H.R. Hicks, J.A. Holmes, D.K. Lee, S.J. Lynch, J. Smith, M. Soler, K.T. Tsang and J.C. Whitson, in 'PLasma Physics and Controlled Nuclear Fusion Research', Vol.I, p.415, International Atomic Energy Agency, Vienna, 1979.
- [44] J.A. Holmes, B. Carreras, H.R. Hicks, S.J. Lynch and B.V. Waddell, Nucl. Fusion, 19, 1333, (1979).
- [45] B. Carreras, H.R. Hicks and B.V. Waddell, Nucl. Fusion, 19, 583, (1979).
- [46] B. Carreras, H.R. Hicks, J.A. Holmes and B.V. Waddell, Phys. Fluids, 23, 1811, (1980).
- [47] D. Schnack and J. Killeen, J. Comp. Phys., 35, 110, (1980).
- [48] T.L. Saaty and J. Bram, 'Nonlinear Mathematics', Dover Publications, Inc. New York, (1981).
- [49] J. Killeen, Ch.5 : 'Computational Problems in Plasma Physics and Controlled Thermonuclear Research' in 'Physics of Hot Plasmas', Edited by B.J. Rye and J.C. Taylor, Oliver and Boyd Publishers Edinburgh, p.202, (1970).
- [50] R.D. Richtmyer and K.W. Morton, 'Difference Methods for Initial-Value Problems', Interscience Publishers - John Wiley and Sons, (1967).
- [51] D. Potter, 'Computational Physics', Interscience Publications - John Wiley and Sons, (1973).

- [52] H.R. Strauss, Phys. Fluids, 29, 3668, (1968).
- [53] P.J. Roache, 'Computational Fluid Dynamics', Hermosa Publications, (1982).
- [54] B.V. Waddell, M.N. Rosenbluth, D.A. Monticello, R.B. White and B. Carreras, in 'Theoretical and Computational Plasma Physics', p.79, International Atomic Energy Agency, Vienna, (1978), SMR - 31/27 - B.
- [55] R.M. Kulsrud and T.S. Hahm, Physica Scripta, T2/2, 525, (1982).
- [56] T.S. Hahm and R.M. Kulsrud, Phys. Fluids, 28, 2412, (1985).
- [57] R.K. Bullough and P.J. Caudrey, 'Solitons', Topics in Current Physics, Springer-Verlag Publishers, Berlin, pp 13 sec.1.3.
- [58] M. Hesse and K. Schindler, Phys. Fluids, 29, 2484, (1986).
- [59] E.N. Parker, 'Cosmical Magnetic Fields', Clarendon . Oxford University Press, (1979).
- [60] D. Biskamp, Phys. Fluids, 29, 1520, (1986).
- [61] M. Hazewinkel, R. Jurkovich and J.H.P. Paelinck, 'Bifurcation Analysis', D. Reidel Publishing Company, (1985).
- [62] B.V. Sonnerup, J. Plasma Phys., 4, 161, (1970).
- [63] V.M. Vasyliunas, Rev. Geophys. Space Phys., 13, 303, (1975).
- [64] F. Brunel, T. Tajima and J.M. Dawson, Phys. Rev. Lett., 49, 323, (1982).
- [65] M. Ugai and T. Tsuda, J. Plasma Phys., 17, 337, (1977).
- [66] T. Sato and T. Hayashi, Phys. Fluids, 22, 1189, (1979).
- [67] E.K. Maschke and B Saramito, Physica Scripta, vol.T2/2, 410, (1982).
- [68] B. Saramito and E.K. Maschke, 'Magnetic Reconnection and Turbulence', M.A. Dubois et al., Editor - Editions de Physique, Orsay, (1985), (Workshop Cargese, Corsica - France, July 1985 ).
- [69] E.K. Maschke and B. Saramito, 8th Europhysics Conference on Computational Physics - Computing in Plasma Physics, Eibsee, 13 - 16 May 1986, vol. 10D, Published by : European Physical Society.

- [70] E.K. Maschke and B. Saramito, 'Turbulence and Anomalous Transport in Magnetized Plasmas', D Gresillon and M.A. Dubois, Editor - Editions de Physique, Orsay, (1987), ( Workshop Cargese, 1986 ).
- [71] M.G. Bell, A.D. Cheetham, S.M. Hamberger, G.R. Hogg, M.J. Hollis, J.A. How, H. Kuwahara, A.H. Morton, L.E. Sharp, L.B. Whitbourn and C.F. Vance, *Austr. J. Phys.*, 37, 137, (1984).
- [72] B.D. Scott, A.B. Hassam, and J.F. Drake, *Phys. Fluids*, 28, 275, (1980).
- [73] D.J. Sigmar, J.A. Clarke, R.V. Neidigh and K.L. Vander Sluis, *Phys. Rev. Letters*, 33, 1376, (1974).
- [74] T.E. Stringer, *Phys. Fluids*, 13, 1586, (1970).
- [75] K.C. Shaing, *Phys. Fluids*, 27, 1567, (1984).
- [76] A.B. Hassam and R.M. Kulsrud, *Phys. Fluids*, 21, 2271, (1978).
- [77] TFR Group, EUR-CEA-FC-1151, (1982) ;  
TFR Group, EUR-CEA-FC-1196, (1983).
- [78] R.L. Dewar, ( Private communication ), 1984.
- [79] M.F.F. Nave and J.A. Wesson, 'Mode Locking in Tokamaks', 14th. European conference on Controlled Fusion and Plasma Physics, Madrid, Spain, (1987).
- [80] M. Persson and A. Bondeson, (preprint), (1987), 'Resistive Tearing Modes in the Presence of Mass Flows', Institute for Electromagnetic Field Theory and Euratom Fusion Research (SERC), Chalmers University of Technology S-41296, Göteborg, Sweden.
- [81] F. Karger et. al. (Pulsator group), IAEA Tokyo Conference, 1, 207-213, (1974) ; IAEA Berchtesgaden Conference, 1, 267-277, (1976).
- [82] W V II - A Team, *Nucl. Fusion*, 20, 1093, (1980).
- [83] Z Qinghu et. al., IAEA, London Conference, Tenth International Conference on Plasma Physics and Controlled Nuclear Fusion Research, IAEA-CN-44/A-V-5-3, (1984).

- [84] D.A. Monticello, R.B. White and M.N. Rosenbluth, PPPL-1477, Sept. 1978.
- [85] J.A. Holmes, B. Carreras, H.R. Hicks, S.J. Lynch and B.V. Waddell,  
Nucl. Fusion, 19, 1333, (1979).
- [86] A.H. Reiman, Phys. Fluids, 26, 1338, (1983).
- [87] Y. Yoshioka, S. Kinoshita, T. Kobayashi, Nucl. Fusion, 24, 565, (1984).
- [88] M.S. Chu, H. Ikezi, and T.H. Jensen, Phys. Fluids, 27, 472, (1984).
- [89] M.N. Rosenbluth, D.A. Monticello, H.R. Strauss and R.B. White, Phys.  
Fluids, 19, 1987, (1976).
- [90] L. Spitzer, Jr., 'Physics of Fully Ionized Gases', second edition, No. 3,  
Interscience Tracts on Physics and Astronomy, Division of John Wiley and  
Sons Inc., (1967).
- [91] L.E. Sharp, (Private communication), (1984).
- [92] T.H. Jensen and M.S. Chu, J. Plasma Phys., 30, 57, (1983).
- [93] P.H. Rutherford and H.P. Furth, unpublished.
- [94] J.P. Freidberg, J.P. Goedbloed and R. Rohatgi, Sherwood Theory Meeting,  
21-23 March (1983), Arlington, Virginia, University of Maryland, 2P10.
- [95] R. Nazikian, (Private communication), (1987).
- [96] M.F. Turner and J.A. Wesson, Nucl. Fusion, 22, 1069, (1982).
- [97] Pung Nien Hu, Phys. Fluids, 26, 2234, (1983).
- [98] S. Chandrasekhar, 'Hydrodynamic and Hydromagnetic Stability',  
Clarendon Press, Oxford, England, (1961).
- [99] A.K. Sen, Phys. Fluids, 6, 1154, (1963).
- [100] R.A. Gerwin, Rev. Mod. Phys., 40, 652, (1968).
- [101] S. Roy Choudhury, Phys. Fluids, 29, 1509, (1986).
- [102] H. Lamb, 'Hydrodynamics', Dover Publications Inc. New York, (1945).